Self-assembled gold nanochain based materials as building blocks to fabricate flexible devices and electrocatalysts

by
Hua Fan

A thesis
presented to the University of Waterloo
in fulfillment of the
thesis requirement for the degree of
Doctor of Philosophy
in
Chemistry (Nanotechnology)

Waterloo, Ontario, Canada, 2021

Examining Committee Membership

The following served on the Examining Committee for this thesis. The decision of the Examining Committee is by majority vote.

External Examiner	Tricia Breen Carmichael Professor
Supervisor	Vivek Maheshwari Associate Professor
Internal Members	Kam Tong Leung Professor
	Eric Prouzet Professor
Internal-external Member	Aiping Yu Professor

Author's Declaration

This thesis consists of material all of which I authored or co-authored: see Statement of Contributions included in the thesis. This is a true copy of the thesis, including any required final revisions, as accepted by my examiners.

I understand that my thesis may be made electronically available to the public.

Statement of Contributions

This thesis contains material from several published journal papers that I authored or co-authored, some of which resulted from collaboration with my colleagues in the Maheshwari group.

- Part of the content in Chapter 2 has been published in

Fan, H.; Maheshwari, V. Wearable Devices Using Nanoparticle Chains as Universal Building Blocks with Simple Filtration-Based Fabrication and Quantum Sensing. *Adv. Mater. Technol.* **2020**, *5* (6), 2000090.

H. Fan conducted the experiments including device fabrication, characterization, and testing. All authors analyzed and discussed the results and contributed to the writing of the manuscript.

This is the pre-peer reviewed version of the following article: Wearable Devices Using Nanoparticle Chains as Universal Building Blocks with Simple Filtration-Based Fabrication and Quantum Sensing which has been published in final form at DOI:10.1002/admt.202000090. This article may be used for non-commercial purposes in accordance with Wiley Terms and Conditions for Use of Self-Archived Versions.

- Part of the content in Chapter 3 has been published in

Saraf, R.; Fan, H.; Maheshwari, V. Porous Perovskite Films Integrated with Au-Pt Nanowire-Based Electrodes for Highly Flexible Large-Area Photodetectors. *Npj Flex. Electron.* **2020**, *4* (1), 1-8.

R. Saraf. and H. Fan. contributed equally to this work. V. Maheshwari and R. Saraf planned the idea, R. Saraf. and H. Fan conducted the experiments, and all authors analyzed and discussed the results and contributed to the writing of the manuscript.

- The content in Chapter 4 has been adapted from

Fan, H.; Maheshwari, V. Controlled element specific nanoscale domains by self-assembly for high performance bifunctional alkaline water splitting catalyst. *Adv. Funct. Mater.* **2021**. (No. adfm.202106149)

- The content in Chapter 5 and 6 has not been published yet. However, it is in a near-verbatim state to what is intended for submission.

Abstract

1D metal nanostructures are being actively researched as a component in next-generation electronic devices and as highly efficient electrocatalysts. 1D gold nanomaterials can be designed by controlling the aspect ratio and introducing multiple chemical elements in their structure. In this work, gold nanochains are self-assembled using electrostatic interactions by controlled addition of cations into a colloidal solution of citrate stabilized Au NPs. The UV-Vis spectrum shows the shift in the LSRP due to the assembly of the Au NPs into micrometer scale chains. The self-assembled chains have a gap of 1 to 2 nm between adjacent Au NPs. This gap can serve as a quantum tunneling barrier for the electrons transport between adjacent NPs. In part A, we study the gold chains with two kinds of morphologies: 1) the AuCa NCs with 1 to 2 nm gaps between adjacent Au NPs; 2) AuPt NWs with continuous structure and highly branched morphology. In Chapter 2, AuCa NCs are mainly investigated. The chains are used as building blocks to fabricate a range of flexible devices to monitor human physiology signals based on the modulation of the tunneling barrier, including temperature, artery pulsation, and ECG by simple filtration method.

In Chapter 3, the two kinds of 1D Au nanomaterials are researched to understand the relationship between the morphology and conductivity under tensile strain. We develop an easy process to produce stretchable devices through a filtration and transfer process. During the transfer process, microcracks are introduced, which facilitate the transport pathway for electrons under strain. AuPt NWs devices with continuous structure can endure larger strain than AuCa NCs devices because of the extended wire-like continuous morphology. We also integrate AuPt NWs as electrodes with perovskite to produce photodetectors, which are highly bendable and stretchable.

In part B, multiple elements are integrated into Au nanochains to explore their electrocatalytic performance for various applications. Stable bifunctional water splitting catalysts can simplify the development of alkaline medium electrolysers. In this work, a catalytic material with controlled nanoscale domains of Pt and Ni is formed by a self-assembly process at room temperature. The final structure of the catalyst is achieved through two stage transformation, first formation of Pt-Ni nanoscale domains and then inducing Ni to higher oxidation states. The material has a nanowire like morphology at the macroscale, which ensures rapid kinetics and mass transfer. The results prove that the nanoscale domains of Pt, Ni and Ni^{2+} and Ni^{3+} with close interfacing are crucial for

the performance of the electrocatalyst and ensure the presence of Ni in a high oxidation state, leading to both HER and OER activity. The catalyst has a low overpotential and ultralow Tafel slope for both HER and OER, 13.7 mV dec^{-1} and 32 mV dec^{-1}, respectively, crucial for high power applications.

Similarly, in Chapter 5, Pt and Ni integrated gold chains are investigated as a dopamine sensor in neutral pH. The size of Pt and Ni domain can be tuned in the range of complete homogenous mixing to 2-3 nm size nanoscale domains. The AuNiAuPt-R sample with nanoscale domains shows the best detection performance with high sensitivity of 1279.3 μA mM^{-1} cm^{-2} in the dopamine concentration range of 0.1-36.5 μM.

In Chapter 6, Ni and Cu integrated gold chains are designed as a glucose detector in 0.1 M NaOH. The AuNiAuCu-R sample with nanoscale domains demonstrates the highest sensitivity of 643.9 μA mM^{-1} cm^{-2} with high stability, high selectivity, reproducibility, and low limit of detection (LoD). The detection range fits the glucose level in saliva, sweat, and blood, which is possible for the practical analytical application. The research in part B shows that nanometer scale elemental domains are critical for efficient electrocatalysis.

This work presents two studies: first, research and understanding the electrical performance of two kinds of micron scale 1D gold nanomaterials by using a simple filtration method to fabricate their films and devices. Second, the synthesis process can control the spatial distribution of elements to design the materials for specific electrocatalytic applications. The work presents a simple method to prepare flexible and stretchable devices and a new facile self-assembly avenue for the use of electrical double layer as new composite catalysts.

Acknowledgements

First of all, I would like to express my greatest thanks to my supervisor, Professor Vivek Maheshwari, for giving me this invaluable opportunity to join his group and guide my graduate study. I gave up on myself at the beginning because of the experience of being alone in a foreign country, the feeling of discomfort, and the experience of failed experiments, but I remember he told me that the success and failure of research are just like the ups and downs of our life. With the help of my mentor, I found I am interested in flexible electrodes, and we worked together on more possible flexible applications. Our collaboration with the industry makes me realize that research is not just about publishing articles. To make the world a little bit better is my inner motivation. Additionally, my mentor's expertise, insights, problem-solving ability, and patience made me have a deeper understanding of academic research. When I have an idea, he supports me, and when I face a problem, he guides me to solve it. Once again, I would like to express my deepest appreciation to him for helping me become the person I am now.

I would also like to thank all my committee members: Prof. Kam Tong Leung, Prof. Eric Prouzet, and Prof. Aiping Yu for their encouragement, critical comments, and technical support during this work.

Also, many thanks to my fellow labmates: Avi Mathur, Long Pu, Rohit Saraf, Athulya Nambiar, William Le Boeuf, Yuheng Song, Venkatesh Gurupsarad, and Shehan Salgado for inspiring discussions and their continuous support. It was my pleasure to work with you.

Special thanks to Dr. Joseph Palathinkal Thomas, Prof. Rodney Smith, Dr. Howard Siu, and WATLab for help with materials characterization.

I would also like to thank my friends for making my life in Waterloo more colorful.

Finally, I would like to thank my parents and fiancé. With your love, tremendous support, and encouragement (both financially and mentally), I have no worries to pursue my goal. Love you!

Wish everyone be happy and stay healthy!

Table of Contents

List of Figures

List of Tables

List of Abbreviations

Abbreviations	Full names
1D	One dimensional
2D	Two dimensional
3D	Three dimensional
NPs	Nanoparticles
SPR	Surface plasmon resonance
Au NCs	Gold nanochains
DLVO theory	Derjaguin-Landau-Verwey-Overbeek theory
LSPR	Localized surface plasmon resonance
NWs	Nanowires
IoTs	Internet of things
ECG	Electrocardiogram
TEM	Transmission electron microscopy
DLS	Dynamic light scattering
XPS	X-ray photoelectron spectroscopy
XRD	X-ray diffraction
FESEM	Field emission electron microscopy
AIr	Artery augmentation index
DAI	Diastolic augmentation index
FFT	Fast Fourier Transform Algorithm
GF	Gauge factor
PET	Polyester
PBA	Prussian blue analogues
HER	Hydrogen evolution reaction
OER	Oxygen evolution reaction
HR-TEM	High resolution transmission electron microscopy
EELS	Electron energy loss spectroscopy
GCE	Glassy carbon electrode
SCE	Saturated calomel electrode
CV	Cyclic voltammetry
RHE	Reversible hydrogen electrode
iR	Ohmic drop
EIS	Electrochemical impedance spectroscopy
EDAX	Energy dispersive X-ray analysis
E^{H}_{des}	Hydrogen desorption
E^{H}_{ads}	Hydrogen adsorption
LSV	Linear sweep voltammetry

H_{UPD}	Hydrogen underpotential deposition
UA	Uric acid
AP	Acetaminophen
AA	Ascorbic acid
RSD	Relative standard deviation
LoD	Limit of detection

Chapter 1 Introduction

1 Introduction

1.1 Nanomaterials

Nanomaterials have attracted considerable interest today due to their unique physical, chemical, and biological properties compared to the bulk materials.[1] They can be classified as zero-dimensional (0D), one-dimensional (1D), two-dimensional (2D), and three-dimensional (3D) nanostructures (in Figure 1.1). 1D nanomaterials have been actively researched for various applications such as next-generation electronic devices because they can enhance electrical, optical, mechanical, and thermal properties.[2] 1D nanostructures are the smallest structures to efficiently transport electrical carriers, which can be used as wiring or device elements in the design of electronic devices. Due to their unique properties, 1D metal nanostructure has also been actively researched as highly active electrocatalysts and components in wearable devices, which is the focus of this research work in part B.

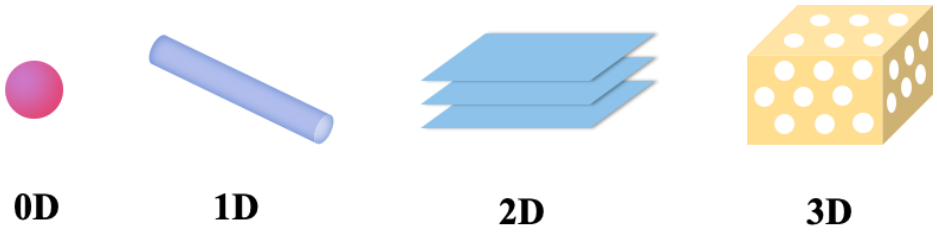

Figure 1.1 Schematic images of nanoparticles in various dimensions.

1.2 Gold nanoparticles

Gold is one of the widely studied noble metals for synthesizing and investigating 1D nanostructures, which possess high conductivity, high stability, chemical resistance, biocompatibility, etc. Furthermore, due to its intrinsic optical properties, tuning the length/aspect ratio of Au nanoparticles (Au NPs) can shift the surface plasmon resonance (SPR) peaks to enable optical monitoring, which is highly sensitive to the electronic coupling between particles (in Figure 1.2).[3] To obtain desired properties, 1D nanomaterials can be designed by controlling the aspect ratio (defined as the ratio of length to diameter) and including multiple chemical elements in their structure.

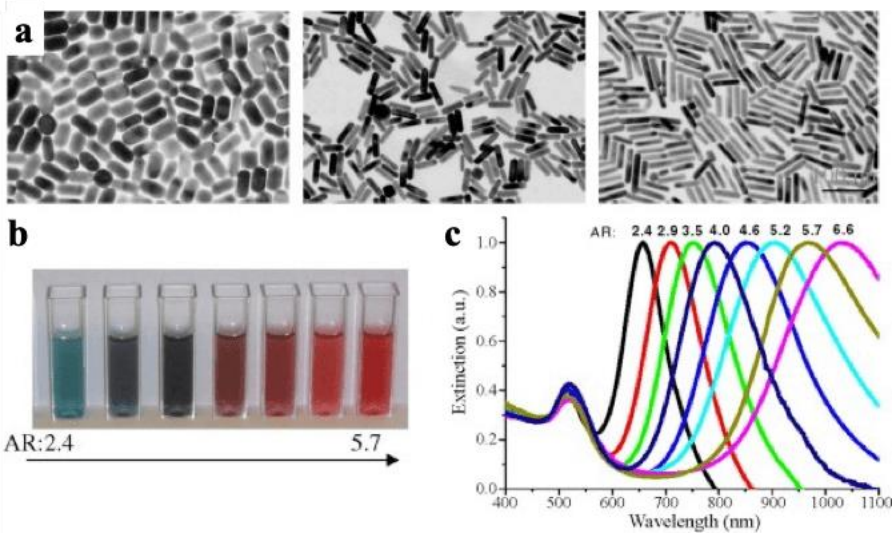

Figure 1.2 Gold nanorods with various aspect ratios show intense color and shift in surface plasmon resonance.[4,5] Copyright 2012, with permission from The Royal Society of Chemistry; Copyright 2010, with permission from Elsevier.

A critical requirement for the development of 1D nanostructures in an aqueous medium is their stability. The colloidal stability is determined by combining two main forces: electrostatic interactions and the van der Waals forces. In previous studies, Au NPs have been stabilized with low molecular weight molecules such as citrate, Biotin,[6] chitosan,[7] cetyltrimethylammonium bromide (CTAB),[8] siloxanesurfactant.[9] Specifically, in colloidal solution for electrostatic stabilization, the Zeta potential is used to assess the stability and surface charges of NPs. In this work, Au NPs stabilized by citrate acid are used as the building blocks for making 1D structures.

These Au NPs have measured Zeta potential with a value of -44 mV, which suggests that the 10-12 nm Au NPs are negatively charged and stable in water due to strong inter-particle repulsive forces from the citrate molecules.

1.3 Self-assembled nanochains

Various techniques for the synthesis of 1D metal nanomaterials have been reported, including one-pot synthesis, oriented attachment, seed-mediated growth, self-assembly, and template-assisted growth.[3] Anisotropic self-assembly of nanoparticles are widely used to synthesize 1D nanostructures, which facilitates the growth of materials in one direction.[2] This is a low-cost and easy synthesis process driven by interactions such as chemical bonding, hydrogen bonding, van der Waals forces, electrostatic forces, and others. Self-assembled gold nanochains (Au NCs) as 1D structures are an important research area in nanotechnology due to their high aspect ratio, large surface area, high stability, conductivity, flexibility, and biocompatibility.[3,10,11] Based on these features, self-assembled Au NCs have been used as building blocks for sensing devices in electrical, optical, catalytic, and biological areas, as shown in Figure 1.3.[8,12]

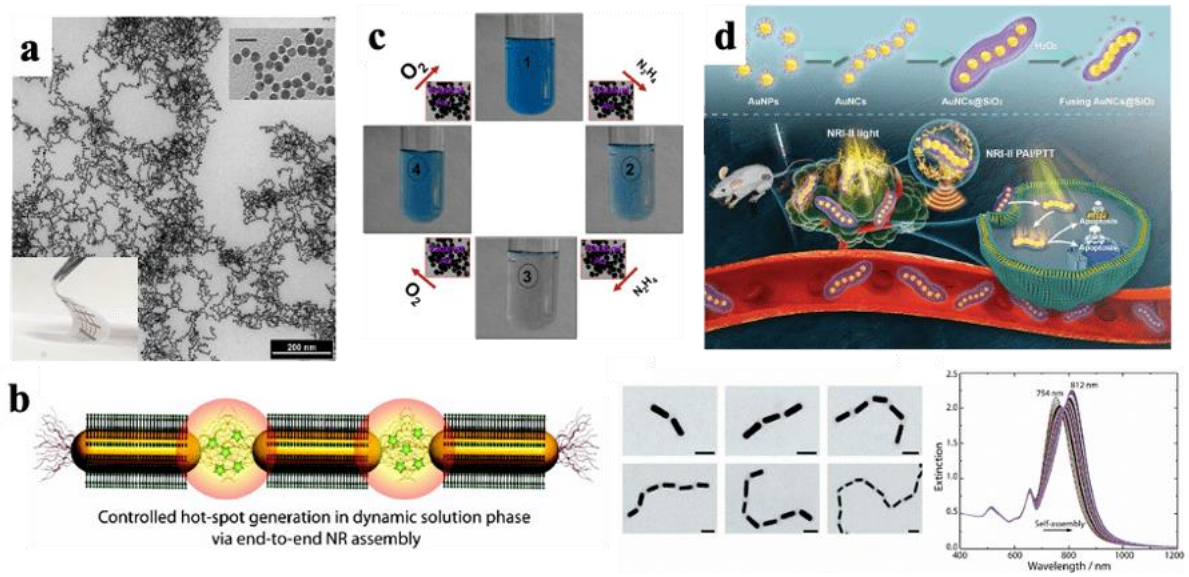

Figure 1.3 Au NCs as building blocks for sensing devices in a) electrical,[13] b) optical,[14] c) catalytic,[15] and d) biological applications.[16] © 2020 WILEY-VCH Verlag GmbH & Co. KGaA, Weinheim; Copyright © 2011 American Chemical Society; Copyright 2013, with permission from Elsevier; © 2021 WILEY-VCH Verlag GmbH & Co. KGaA, Weinheim.

Wang et al. reported the self-assembly of negatively charged Au NPs in aqueous medium. In this report, the length of the Au chains could be controlled by regulating the interparticle electrostatic repulsion.[17] The interactions between nanomaterials are typically described by the Derjaguin-Landau-Verwey-Overbeek (DLVO) theory. According to the DLVO theory, the total interaction potential (V_T) is expressed as the sum of the van der Waals attraction potential (V_{vdW}), the electrostatic repulsion potential (V_{elec}), the dipolar interaction potential (V_{dipole}), and the charge-dipole interaction potential ($V_{charge\text{-}dipole}$).

$$V_T = V_{vdW} + V_{elec} + V_{dipole} + V_{charge\text{-}dipole}$$

The assembly process is affected by concentrations of reagents, pH, and ionic strength of the solution and the interactions between molecules located at the colloidal interfaces. These involve the intermolecular forces, such as dipole-dipole interactions, hydrogen bonding, hydrophobic/hydrophilic interactions, or π-π stacking, etc.[18] Template-free self-assembly process can be triggered by adding destabilizing species (e.g., crosslinking molecules, salt, or solvent) or applying external force (thermal, electric field, or magnetic field).[9] For example, Li et al. added mercaptoethanol (MEA) into citrate capped Au NPs, resulting in a chain-like structure by producing an electrical dipole on the nanoparticle surfaces.[19] Neutral MEA was used to partially exchange with the surface citrate ions to induce the electric dipole-dipole interactions, which resulted in the growth of an anisotropic chain. The chains can maintain colloidal stability by balancing the attractive van der Waals forces, the hydrogen bond between MEA molecules, and the electrostatic repulsions between citrate acid.

Self-assembly of Au NPs with the negative surface charge by adding cations is a scalable and cost-efficient strategy for the fabrication of 1D nanochains with potential applications in electrocatalysis and wearable devices. As reported, increasing the ionic strength of the solution decreases the interparticle distance of citrate capped Au NPs resulting in a color transition due to a shift of the surface plasmon resonance.[20] Jia et al. reported that adding less than 10 mM of KCl leads to the formation of gold nanochains, while a higher concentration of KCl leads to agglomerated clusters.[9] This can be explained as the lower concentrations of the salt will not fully neutralize the surface charges (from citrate) on the Au NPs, hence will not cause aggregation of the NPs. Under this condition, the lower electrostatic repulsion between NPs leads to the formation

of nanochains. On the other hand, at higher salt concentrations, cations can fully neutralize surface potential resulting in tightly bounded aggregates.[9] Therefore, the ionic strength provides a simple method to control the assembly of the charged gold nanoparticles.

As mentioned previously, the growth of the gold nanochains can be triggered and controlled by adding salt. The mechanism is the anisotropic dipole-dipole interaction between the Au NPs. The combined effect of the short-range dipole-dipole attraction and the long-range electrostatic charge repulsion between particles play a crucial role in the process of 1D nanoparticle assembly.[9]

It has been well studied that the spherical Au NPs' surface is enclosed by several facets, like (111), (200), (220), and (311), and citrate molecules are adsorbed on Au(111), Au(110), and Au(100) surfaces. However, citrate adsorption is more favored on Au(111) than on other facets.[9,21,22] Due to the differential distribution of surface charges, the Au NPs possess a slight polarity. The addition of divalent (or higher valent) cations affects the electrostatic force and causes two Au NPs to link together to form an 'island'. As the cations partially neutralize the surface charge on the Au NP's by binding to the citrate ions, the electrostatic double layer of this 'island' is rearranged. Then, due to the asymmetrical distribution of the charges, the electrostatic repulsion at both ends of the island is weaker than the side.[23,24,25] These leads to the aggregation of Au NPs to form gold chains, as the island can attract another Au NP at the end by using the cation as a linking bridge. Again, the Au NP linked to the end of the chain experiences a weaker electrostatic repulsion than a side one, which enforces the anisotropic self-assembly process.[23,24,25] Based on the ionic strength, the solution reaches a stable state with the formation of nanochains of specific length. The Zeta potential of the Au chains is ~-30 mV, representing that they are still negatively charged due to uncompensated citrate ions on the surface. The chains are therefore stabilized by electrostatic repulsion force.[9]

1.3.1 Optical properties

Surface plasmon resonance (SPR) is a particular intrinsic optical property of gold nanomaterials that has attracted extensive interest from different fields of nanotechnology. These fields include photodynamic therapy, photothermal therapy, cancer diagnosis, drug delivery, imaging, pollutant detection, and surface-enhanced Raman spectroscopy (SERS).[11,26,27,28,29] The basic mechanism of SPR occurs when the nanoparticle diameter is smaller than the wavelength of the incident light.

The electric field of the incident light, as a result, excites the free surface electrons in Au NPs to drive their collective oscillation, referred to as localized surface plasmon (LSPR), as shown in Figure 1.4.[30,31,32]

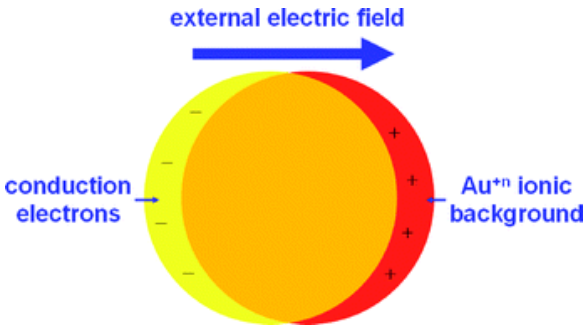

Figure 1.4 Schematic representation of a dipolar plasmon oscillation in a gold nanoparticle.[30] Copyright 2008, with permission from The Royal Society of Chemistry.

LSPR only occurs when the wavelength of the incoming light is greater than the size of nanoparticles.[33] Crystal defects cause light scattering, which adds resistance to the electron motion. The Mie theory describes the LSPR by Maxwell's equations. As for a spherical particle, the extinction coefficient, E(λ), including absorption and scattering, of the incident light, can be expressed as:

$$E(\lambda) = \frac{24\pi N_A R^3 \varepsilon_m^{3/2}}{\lambda ln\,(10)} \left[\frac{\varepsilon_i}{(\varepsilon_i+2\varepsilon_m)^2+\varepsilon_i^2}\right]$$

where N_A is the areal density of the nanoparticles, R is the radius of the gold particle, λ is the incident wavelength, ε_m is the dielectric constant of the surrounding medium, and ε_r and ε_i are the real and imaginary parts of the dielectric function of the particle material, respectively. The interaction between the incident light and a metal nanoparticle strongly depends on the dielectric function of the material and the medium.[34]

In this work, Au NCs are synthesized by self-assembly process in aqueous media, which is a low-cost and scalable approach requiring no specialized equipment. The LSPR frequency of various gold nanomaterials is determined by the shape and size of the charge distribution and the local dielectric environment.[31,35] The electrons absorb photon energy at the resonance frequency forming a strong absorption band in the UV-Vis spectrum. The effect of shape is observed on

LSPR, where Au NCs spectrum shows a red-shift of the absorption wavelength due to the larger aspect ratio (the aspect ratio of Au NPs is ~1).[31] This shift can be explained by the Au NCs having a longer length than the initial size of Au NPs (10 nm), leading to interparticle plasmon coupling, which depends on the chains' length and the separation between the NP's in the chains.[30] The resonance condition of Au NCs is satisfied at wavelengths in the visible region of light. Based on the intrinsic properties, we can monitor the change in the length of Au NCs by using UV-Vis. The absorption wavelength can be described as:[35]

$$\lambda^2 = {\lambda_p}^2 \left(\varepsilon^o + \varepsilon_m \left(\frac{1}{P} - 1 \right) \right)$$

$$\lambda_p = \sqrt{\frac{4\pi^2 c^2 m \varepsilon_0}{N e^2}}$$

where λ is the location of absorption peak, λ_p is the plasma wavelength, P is the depolarization factor, N is the electron density, m is the effective mass of electrons, and ε_0 is the dielectric constant of vacuum. As for the gold nanochains, the increased aspect ratio could cause a red-shift for λ by changing the depolarization factor. As for the 1D morphology, the depolarization factor, P, can be expressed by three axes x, y, z (where x>y=z) and aspect ratio, α, as:

$$P_x = \frac{1 - e^2}{e^2} \left[\frac{1}{2e} \ln \left(\frac{1 + e}{1 - e} \right) - 1 \right]$$

$$P_y = P_z = \frac{1 - P_x}{2}$$

$$e^2 = 1 - \alpha^{-2}$$

Therefore, the coupling or assembly of Au NPs in solution is easily observed by the change of color based on LSPR. Furthermore, the materials' surface modification and surrounding environment can also tune the wavelength. Thus, the plasmon resonance depends strongly on the particle's shape, while the absorption peak has a red-shift as the particle becomes more oblate.[32] The color can be tuned from red to dark blue, as the Au NCs length changes from 10 to 300 nm. UV-Vis spectra show that the LSPR absorbance peak of Au NPs at 525 nm red shifts to 630 nm

with a broad shoulder peak at 525 nm on assembly of 10 nm Au NPs into Au NC's with a length of 250 nm.[19]

These Au NCs can act as good 1D nanomaterials with high stability. They have tunable properties based on changing the linking ions and further surface modification. This combination of stability and tunability is applied to develop applications in the areas of electronic devices, sensing, and electrocatalysis, and is reported in the following chapters.

1.3.2 Tunneling effect

Tunneling effect is a quantum phenomenon observed in nanomaterials. The self-assembled Au NCs with several hundred nanometers in length show a nonlinear current-voltage response with Coulomb blockade behavior caused by the gaps between adjacent particles, as shown in Figure 1.5. The gaps serve as quantum tunneling barriers for the electrons to transport across neighboring Au NPs, the conductors. The basic model for this system is hence a series of conducting islands separated by energy barriers. The electrons possess wave-particle duality, behaving as waves, and exhibit the ability to tunnel through an energy barrier under applied external bias or thermal energy.[36,37,38]

In tunneling, the probability of electrons crossing an energy barrier is limited by the energy of electrons, external forces (like applied bias), and the width of tunneling junctions. As in electronic devices, there is a threshold bias, V_T, required to allow the current flow, which is called Coulomb blockade.[39] The current response initially follows a nonlinear relationship with voltage at room temperature because more electrons can tunnel through the barrier with increasing bias, as shown in the Figure 1.5.[13,36,40,41]

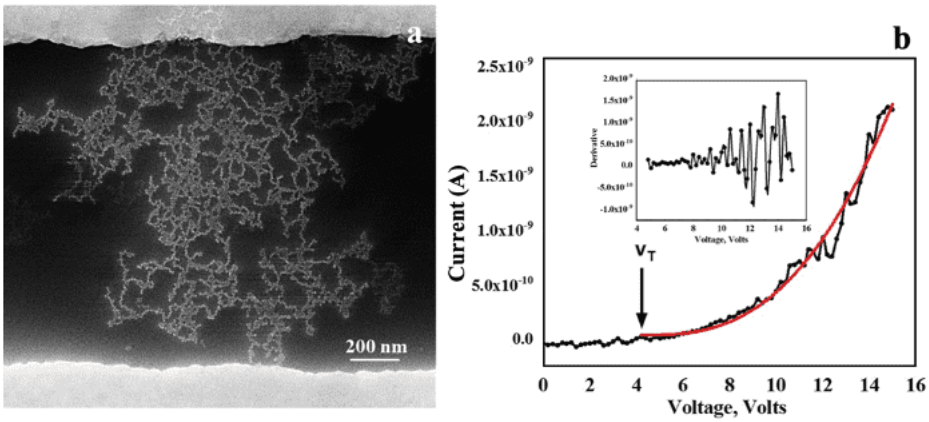

Figure 1.5 a) The FESEM image of sparse deposition of the chains across the two Au electrodes; b) The current-voltage response of the chains related to Figure 1.5 a. The current fits a typical power law with an exponent of 2.67, typical for a 2D array with defects, shown in red color. The inset is the plot of differential conductance.[13] © 2020 WILEY-VCH Verlag GmbH & Co. KGaA, Weinheim.

As mentioned before, the ability of an electron to transport in the nanochains depends on its energy and the width of the tunneling gap. Thus, for example, external force or energy-induced (such as pressure and temperature) change of gap width between neighboring nanomaterials can alter the tunneling resistance for nanomaterials. This change will be observed in the output signals as, for example, modulation in current observed at a constant voltage.[37] The tunneling current density can be expressed by:

$$J = A_0 exp(-\frac{E_c}{E})$$

where E_c is the critical electric field, E is the external electric field, and A_0 is the total electron density before tunneling.

The relationship between conductivity (σ) and temperature (T), interparticle distance (δ), and particle size (r, the radius of nanoparticles) is described as:[42]

(1) $$\sigma(\delta, T) = \sigma_o \exp(-\beta\delta) \exp\left(\frac{-E_A}{RT}\right)$$

(2) $$E_A = \frac{e^2}{8\pi\varepsilon\varepsilon_0}\left(\frac{1}{r} - \frac{1}{r+\delta}\right)$$

(3) $$\sigma_0 = ne\mu$$

where E_A is the activation energy, R is the universal gas constant, β is the electron coupling term, σ_0 is the intrinsic conductivity, ε_0 is the permittivity constant, ε is the relative permittivity, n is the number of charge carriers, μ is the mobility of the charge carriers, and e is the charge of an electron. From equation 1, the increase of temperature and the decrease of interparticle distance will cause an increase in conductivity. Therefore, an Au chains-based tunneling sensor will be presented in this work, which works on the principle that the output current signal reflects external modulation at a particular applied bias. Specifically, the gaps between adjacent Au NPs serve as quantum tunneling barriers. Their modulation is the basis of signal sensing in these devices to monitor temperature, artery pulsation, and electrocardiogram, ECG, signals (more details in Chapter 2). The sensitivity of the devices is related to the tunneling in terms of the magnitude of barrier energy and its width.[13,36]

1.3.3 Conductivity and Flexibility

Gold-based nanostructures are important research subjects in electronic devices. The 1D Au nanomaterials can act as building blocks such as circuit wires and the active layer in nanodevices, as shown in Figure 1.6. Au NCs exhibit a high aspect ratio (defined as the ratio of length to diameter) are chemically inert, biocompatible and have a threshold charging energy (the Coulomb blockade threshold for a typical ~10 nm NP is ~60 meV, for NC is ~ 1.5 eV).[36,40] In addition, the conductivity is sensitive to the mechanical force, surface potential, and temperature by modulating the interparticle spacing or local tunneling barrier. These properties support Au NCs as potential candidates for next-generation wearable electronic devices for measuring stimuli such as pulsation, ECG, and temperature sensors.[13]

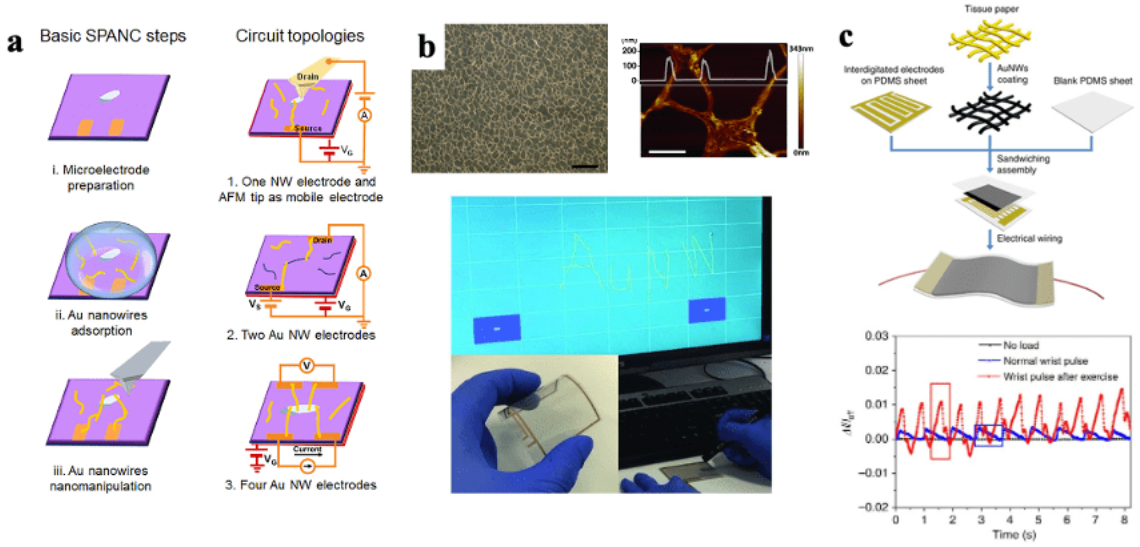

Figure 1.6 1D gold nanomaterials as a) circuits,[43] b) touch screen electrode,[44] and c) wearable devices.[45] Copyright © 2019 American Chemical Society; © 2016 WILEY-VCH Verlag GmbH & Co. KGaA, Weinheim; Copyright © 2014, Nature Publishing Group, a division of Macmillan Publishers Limited.

Due to the anisotropic morphology, self-assembled Au NCs are more effective in forming conductive pathways compared to spherical gold nanoparticles. The percolation threshold of nanochains with a larger aspect ratio is smaller than the spherical nanoparticles. The percolation threshold is the minimum concentration of the conductive particles required to form a conductive path in a nonconductive matrix. Below the threshold, there is no pathway for charge transport, while above the threshold, the conducting particles form a conductive network resulting in a sharp increase in conductivity.[3] The electrical conductivity of the network, σ, using percolation theory can be roughly expressed as:

$$\sigma = \sigma_0 (p - p_c)^t$$

where σ_0 is the conductivity of Au NCs, p is the volume fraction of Au NCs, p_c is the percolation threshold of conductive materials, σ_0 is the conductivity of composite with 100% nanomaterials, and t is a parameter that is related to the dimensionality of the conductive path: 1 for 1D, 1.3 for 2D and 1.9 for 3D.[46,47] In a 3D system, the critical volume fraction, Φ_c^{VF}, strongly depends on the aspect ratio of conductive materials.

$$\Phi_c^{VF} = 1 - e^{-(cV/V_{ex})}$$

where V is the volume of conductive particles, V_{ex} is the volume around these conductive materials, and c is a constant. $\frac{V_{ex}}{V}$ can be expressed by aspect ratio as:

$$\frac{V_{ex}}{V} = 2 + \frac{6(1+\alpha)(1+0.5\alpha)}{1+1.5\alpha}$$

$$\alpha = L/D$$

where α is the aspect ratio, *L* is the length of the nanochains, and *D* is the width. Therefore, the larger aspect ratio will lead to a larger $\frac{V_{ex}}{V}$ and a smaller Φ_c^{VF}. In other words, less amount of conductive materials is needed to achieve the percolation threshold.[3] Thus, the value of Φ_c^{VF} of Au NCs is much smaller than 10 nm Au NPs.

Based on Simmons' model, the electrical conductivity by tunneling effect within the junction is given by:[48]

$$\sigma = \frac{6.2 * 10^{10} A}{\delta^2}\left[h\, exp\left(-1.025\delta\sqrt{h}\right) - (h+eV)\ \exp\left(-0.1025\delta\sqrt{h+eV}\right)\right]$$

where A is the effective electrical tunneling area, e is the electron charge, δ is the interparticle distance, and h is the mean tunnel barrier height. The current is inversely proportional to interparticle distance and barrier height.

At high density, the large percolating clusters could act as wires, and at low density, the islands can act as sensing materials. As a promising candidate for flexible electronics, it has been demonstrated that Au NCs with mechanical flexibility perform much better than the bulk.[3] Gong et al. reported an ultrathin Au NW structure with a high aspect ratio combining great mechanical flexibility and high conductivity.[49] In addition, once the percolative network is formed by overlapping between Au NWs, applied external strain can be relieved by the rearrangement and sliding of Au NWs. Therefore, the Au NWs can maintain the connections through the percolated conductive paths.[50] As reported, the angle between the adjacent Au NPs in the chain is in the range of 120° to 180° resulting from electrostatic repulsion and attraction.[51] In this dissertation, we

develop a simple, low cost and eco-friendly filtration method to form different devices, which will be presented in Chapter 2 and 3.

1.3.4 Developing Au NC as catalysts

Catalytic properties of nanomaterials have attracted significant research attention because of their unique physical and chemical properties. Compared with traditional catalysts, the nanocomposites present better catalytic activity and selectivity due to their higher surface area and more active sites.[52] Au nanomaterials offer a promising electrocatalytic ability because of the specific catalytic activity and selectivity.[53] Recently, it has been reported that Au NCs combined with other components can provide specific electrocatalytic reacting centers on the surface.[11] For example, by mixing two or more chemical species, like alloy materials, the performance of the catalysts could be significantly improved due to synergistic effects, intrinsic chemical and physical properties, and faster charge transfer rate.[26] In Xie's work, PtNi nanoparticle-decorated Ni nanosheet arrays on carbon cloth show high water splitting catalytic performance at low overpotential of 38 mV for hydrogen evolution reaction (HER).[54] The existence of Ni modifies the Fermi level or the d-center of Pt changing the absorption/desorption energy. Meanwhile, Yu et al. reported that the nickel-iron Prussian blue analogs (PBA) exhibited a low overpotential of 283 mV for oxygen evolution reaction (OER) due to the in-situ generated nickel-iron oxy(hydroxide) active layer, which increases the activity.[55] By careful selection of the metal cations for self-assembly of the NC, a bifunctional high performance catalyst for both HER and OER is also presented in Chapter 4. This catalyst combines Au NC with Pt, Ni, and PBA.

A core-shell structure is formed by using Au NCs as the template with an ultra-thin layer of a second metal/metal oxide-hydroxide (such as Pt, $Ni(OH)_2$) covering the Au NCs surface. The resultant catalyst has a large surface area, more active sites, better conductivity, and higher stability compared to other reported materials. Our research has focused on different metal elements assembled gold nanochains and their application for sensing and electrocatalysis. First, these are obtained by controlling the assembly of gold nanoparticles in the solution phase using specific ions. Second, after forming a core-shell structure or alloy, the conducting Au core can enable fast transfer the electrons, increasing the efficiency of catalysis.[52] Also, Au NPs are chemically inert and have high stability, which is critical for catalytic applications.[56,57] The nanomaterials are also

prepared and characterized for catalytic applications like water splitting, dopamine, and glucose sensing (discussed in Chapter 4, 5, and 6, respectively).

1.4 Thesis organization

Inspired by the investigation presented above, the objectives for this dissertation are to use the effectively dispersed self-assembled Au NCs with an easy fabrication process as a template. In addition, we explore the various applications in the electronic and catalytic areas. This dissertation is organized into two parts with five chapters. The first part focuses on the optical and electrical properties of the Au NC's and their sensing application. The second part focuses on the development of composite Au NCs' with specific elements for electrocatalysis.

In part A, which includes Chapter 2 & 3, the self-assembled micrometer long Au NCs or Au NWs are used as building blocks to fabricate a range of flexible devices and stretchable devices. Using an easy filtration method to produce devices, the materials are deposited on different substrates for various applications. For example, they can serve as the basic materials for the sensing layer, interconnections, and contact pads by varying the deposition thickness and materials. In Chapter 2, the conductivity, flexibility, and optical and mechanical properties of Au NCs and their application as active materials to monitor human physiological signals based on modulation of their tunneling barrier are presented. Chapter 3 discusses stretchable devices made by Au NW's and their modulation in conductivity in response to tensile stress.

Part B of this dissertation explores using self-assembled Au NCs as a template for synthesis of electrocatalytic material and their application for water splitting (in Chapter 4) and non-enzymatic dopamine and glucose sensing (in Chapter 5 and 6). The materials are designed by the use of different chemical elements in the formation of the Au NCs'. In Chapter 4, NCs' with the controlled spatial distribution of Pt and Ni are assembled. These composite NCs present excellent catalytic performance in alkaline media OER and HER. Chapter 5 and 6 report two non-enzymatic sensors: Pt and Ni doped Au nanocomposite as the electrode to detect dopamine in neutral media in Chapter 5; and Chapter 6 investigates Cu and Ni assembled Au NCs applied to glucose sensing in alkaline solution.

Chapter 7 concludes this dissertation and lists the future work to improve materials' performance and explore the catalytic mechanism at an atomic level.

Part A Self-Assembled Au NCs as building blocks to fabricate flexible devices

Chapter 2 Wearable device using 1D Au nanomaterials as universal building blocks

1 Introduction

In recent years, significant attention has been given to the study of conductive patterns on flexible substrates. A wide range of flexible electronic applications use metal nanomaterials as the sensing layers for different stimuli, interconnects, or electrodes.[58] Examples include flexible displays, solar cells, and wearable sensors. Researchers have worked with various metals for circuits and interconnect components, including gold,[59] platinum,[60] silver,[61] and copper[62] as conductors. Although silver and copper-based nanomaterials are common today because they are much cheaper than gold, the main drawback is they are easily oxidized in ambient conditions. As an electrical conductor, this undesired oxidation decreases efficiency and increases the cost by introducing more synthesis steps and extra equipment to maintain the conductivity.[63] Therefore, gold is an ideal material for interconnections, especially for high performance applications. Among the various nanostructures, nanochains are suitable for flexible electronic devices owing to their 1D morphology. Nanochains exhibit a high surface to volume ratio, high aspect ratio, and low percolation threshold and possess the property of quantum tunneling effects due to the discontinued pathway of localized electrons to transport. This phenomenon is of use in flexible electronic devices. For example, Au NCs can be used to make connective pads in flexible devices and the active layer for sensing stimuli such as pressure and potential.

Numerous methods have been developed to fabricate device materials. The widely-used lithographic technique allows for the fabrication of precise thin layer circuits for use in flexible electronics.[64] However, this technique requires expensive facilities and a complicated and time-consuming process that generates pollution and waste. Thus, alternative manufacturing technologies have been developed, such as airbrush spraying,[65] inkjet printing,[66] and sputter coating.[67] Still, these methods are either costly or require an organic stabilizer or organic solvent, which are not eco-friendly. Furthermore, due to conductivity requirements in devices' electrodes

with low resistance, consistent response and low fabrication cost need to be developed. In order to make a simple method, we developed an easy, low-cost, repeatable, and environmental-friendly filtration method for printing large-scale electronic circuits on flexible substrates for a variety of applications.

This chapter presents a range of flexible sensors designed using two different 1D Au nanomaterials that are self-assembled using two different linker cations, Ca^{2+} and Pt^{4+}. The self-assembled micron long Au NCs in aqueous phase serve as building blocks for interconnects, electrode pads, and the active sensing layer. Moreover, the Au-Pt^{4+} NCs form continuous Au-Pt nanowires after reduction, which offers the potential to enhance electronic conductivity due to continuous pathways for electron flow. The intrinsic stability and conductivity of Pt support the nanomaterials as circuits in wearable devices. The combination of good mechanical, electronic, and transport properties make these 1D morphologies promising as interconnects for wearable devices. Meanwhile, the Au NCs can translate multiple stimuli into a signal as the active layer. Along with the simple filtration process, it makes them economically accessible for widespread use. Most devices for health monitoring and the internet of things, IoTs, will be highly applicable in the developing world. Furthermore, the use of Au and Pt allows for safe handling by users without any health hazards. The fabrication of the devices typically involves multiple steps with deposition of a variety of materials which act as the sensing layers for different stimuli, interconnects, and electrodes. Here, we show a simple wearable device where all the device components are deposited by simple vacuum filtration on a flexible polymer filter membrane. The devices can accurately measure pulse rate, pulse pressure shape, ECG, and temperature. The building materials for all the device components are self-assembled Au nanochains that are micron scale in size, but at a local scale, composed of 10-12 nm Au nanoparticles with a spacing of 1 to 2 nm between adjacent nanoparticles. This building block is used to make the sensing layer to detect all physiological signals, the electrodes and the interconnect traces by varying its deposition thickness. At limited deposition thickness, though the material is micron size in length scale, the presence of local 1 to 2 nm gaps between nanoparticles serve as quantum tunneling barrier and lead to the observed high sensitivity and real-time monitoring ability of the device in translating a variety of physiological responses to electrical signals.[68,69] The pressure palpations (pulse pressure) can be sensed as they cause a change in the conductivity by modulating the interparticle spacing. The ECG signals act as a surface potential on the chains, which alters the local tunneling barrier and hence are detected

by the device.[70] The tunneling across these multi-junction chains is temperature sensitive which forms the basis for measuring the local temperature.

2 Experimental Section

2.1 Synthesis section:

2.1.1 Preparation of AuCa NCs

Au NPs with a size of 10-12 nm, purchased from BBI Solutions OEM Limited, are capped by negatively charged citrate acid. The NPs can be stable in aqueous media without any surfactant by repulsion force. 105 µL of 1 mg/mL $CaCl_2$ (99.0%, ACP chemicals Inc.) were mixed with 1 mL of the gold solution. Then the mixture was left on the shaker at a speed of 300 rpm overnight. The nanochains were successfully assembled when the color of the solution changed to dark blue, with a length ~250 nm to 1 micron.

2.1.2 Preparation of AuPt NWs

135 µL of 4.5 mg/mL $PtCl_4$ (99.9%, Sigma Aldrich) was mixed with 1 mL gold nanoparticles, and then left on the shaker at a speed of 300 rpm until the solution color changed to dark blue. After the self-assembly process, the Pt ions were reduced by 75 µL of 4 mg/mL $NaBH_4$ (99%, Sigma Aldrich), and the color of the solution turned to dark brown. The chains can be stably suspended in solution.

2.1.3 Deposition of AuCa NCs on Au Chips

The Au chip[71] used in our previous work was first processed with piranha solution and then immersed into the AuCa NCs solution for an hour. Later, the Au chip was taken out from the solution and gently washed by Millipore water to remove the salt. In brief, the chip consists of interdigitated finger electrodes, with a gap of 2 µm between the electrodes.

2.2 Fabrication of devices

The wearable devices were prepared through the filtration process. The Polydimethylsiloxane, PDMS, masks were used to obtain the desired pattern of the active layer. For this, 2.0 g of silicon elastomer base was well mixed with 0.2 g elastomer curing agent from Dow Inc. and then cured at 75 °C for one hour. The patterns were obtained by CO_2 laser cutting with a resolution of 1200 dpi. The filter membranes (made by polycarbonate with 30 nm/200 nm pore size and polyamide

with 2 μm pore size) were purchased from Cytiva Whatman. Copper tape and silver paste were used to connect the contact gold pads and output the signals. The cost of each device is ~1-4 $USD.

2.3 Characterization section

Zeiss Ultraplus Field emission Scanning Electron Microscopy (FESEM) was used to image the morphology of samples and the deposition. Transmission electron microscopy (TEM) images were obtained with an FEI Titan 80-300 HB transmission electron microscope. The hydrodynamic size and Zeta potential were measured by Zeta Sizer Nano ZS90 from Malvern Instruments at 25 °C. The hydrodynamic diameter is calculated by the Stokes-Einstein equation. UV-Visible absorption spectra of samples were measured by Perkin Elmer Lambda 750 spectrophotometer.

2.4 Electrical measurement

Current-Voltage response of NC deposition and wearable devices were measured by 3458A Digital multimeter combined with 6614C 50 Watt system power supply from Agilent Technologies company. The measurements were conducted by using a two-probe method. For measuring the device response, one probe was connected to the Au pad, while another probe was connected to the ground. During the airflow testing, the response of devices was measured in a steady N_2 flow with different flow rates controlled by a flow meter. In addition, a precise temperature controller (ITC4020, Thorlab) was used for the temperature sensing test to mimic the temperature stimulus.

Chronoamperometry measurements of the wearable devices were done using an Ivium CompactStat Electrochemical Analyser by connecting two copper tapes using a two-electrode system to form a circuit. The additional bias for pulsation and ECG measurements are 0.01 V and 0.1 V, respectively.

3 Results and discussion

3.1 Characterization

Figure 2.1 a illustrates the scheme of the self-assembly process of Au NCs by adding calcium chloride. Briefly, Au NPs have been stabilized in solution by repulsive forces of negatively charged citrate ions. Then, an optimized volume of Ca^{2+} ions is added to trigger the assembly. Due to the divalent nature of the Ca^{2+} ion and its interaction with the citrate ions, the cations partially neutralize the negatively charged citrate acid on the Au surface. This neutralization induces the electric dipole-dipole interactions, leading to the self-assembly of Au nanoparticles into Au NCs with micron long networks.[17,71] The chains are made of 10-12 nm Au NPs with micron size assembly length and can be stable in an aqueous medium over two weeks.

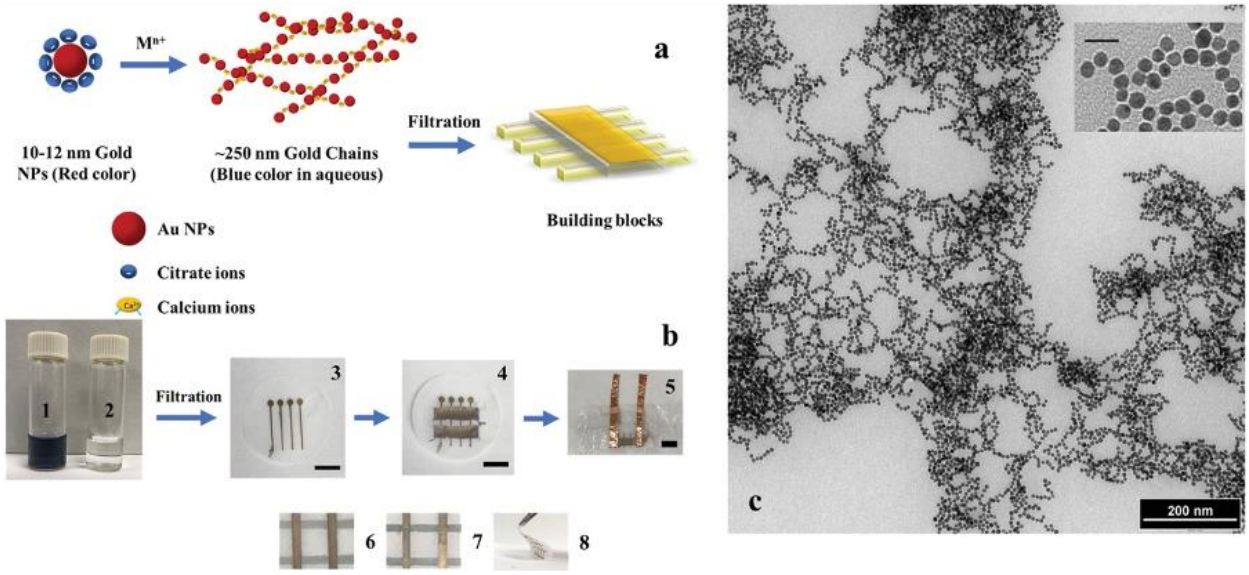

Figure 2.1 a) The schematic figure of self-assembled gold nanochains and gold pads after filtered on the flexible membrane used as building blocks with various patterns. b) The photo image of 1) the solution of self-assembled gold nanochains; 2) the solution after filtration. 3) the deposited conductive gold pads with solution volume density of 51 µL mm^{-2}. Scale bar: 10 mm; 4) an active conductive gold layer with a volume density of 9 µL mm^{-2}. Scale bar: 10 mm; 5) the final device (covered by a layer of plastic food wrap, and the copper tapes were used to connect the conductive pads to transfer the output signals). Scale bar: 10 mm; 6) and 7) the active conductive gold layer with volume density of 1.6 and 4 µL mm^{-2}, respectively. The color of the active layer with the increasing volume density changes from light blue to shiny gold; 8) Image showing the membrane flexibility after device fabrication. c) The TEM images at low magnification and high magnification (the inset image) of self-assembled AuCa NCs. At low magnification, the length of

the branched chain network is in microns. At high magnification, the gaps of 1 to 2 nm between the Au NPs are easily observed. The scale bar in the inset is 20 nm.

Transmission electron microscopy (TEM) images of Figure 2.1 c exhibit this morphology. At lower magnification, the AuCa chains are micron scale in size. As can be seen in the inset high-resolution image (the inset figure), there is a gap between two adjacent Au NPs with a distance of 1 to 2 nm. In a previous study, the thickness of the citrate layer is 8-10 Å.[22] Therefore, the gap results from steric repulsion between citrate layers and Ca^{2+} ions on NPs, helping the dispersion of Au NPs to be stable in solution.

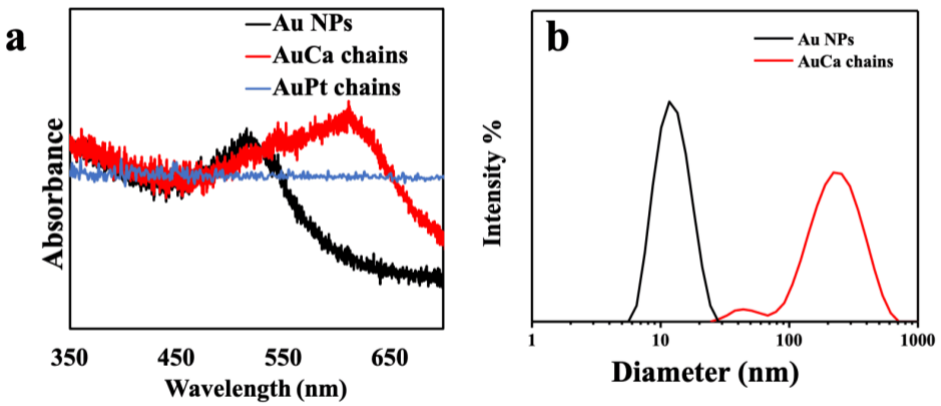

Figure 2.2 a) the UV-Vis absorption spectra of Au NPs, AuCa chains, and AuPt chains after being reduced; b) The DLS results show the particle size distribution of Au NPs and AuCa chains, labeled by black and red, respectively.

In Figure 2.2 a, UV-Vis absorption spectra present Au nanoparticles shifts from 520 nm to 620 nm due to coupling between the nanoparticles in the chains as a result of surface plasmon resonance.[71] This can also be proved by Dynamic light scattering (DLS) measurement. Following the assembly process, the hydrodynamic diameter increases from ~10-12 nm to ~250 nm (Figure 2.2 b). The Zeta potential of 10 nm Au NPs is -44 mV, which confirms that the citrate-capped Au nanoparticles suspended in an aqueous medium have a negative Zeta potential. This is caused by the layer of COO^- of citrate acid. After adding the controlled amount of Ca^{2+} cations linker, the Zeta potential decreases to -30 mV. This indicates the nanochains surface is still negatively charged, and Ca^{2+} ions only function as linking bridge and only neutralize part of the citrate acid. When Ca^{2+} ions

bind with the COO^- groups on the surface of Au NPs, the cluster became dipolar. This then leads to the cluster growth into a linear structure (more details in Chapter 1).[36]

Platinum shows extremely high conductivity and chemically inert properties with high cost. In this work, we produced 1D Pt nanowires with the same method by using Pt cations instead of calcium salt. After the reduction, the Pt forms a continuous ultrathin cover on Au NPs with a high surface area. Similar to AuCa NCs, Pt^{4+} ions first work as a linking bridge to synthesize the 1D Au NCs. The assembled AuPt chains are on a 0.5 to 2 μm length scale with 1 to 2 nm interlayer spacing between adjacent Au NPs as well. Based on a previous study, almost half the amount of Pt^{4+} ions are adsorbed on Au NPs surface or are in the electrical double layer and half remained in the solution.[9,72] Therefore, the concentration of absorbed Pt cations is much higher than the one distributed in solution due to the limited thickness of the electrical double layer. Hence, after adding $NaBH_4$, which is a strong reducing agent, due to the difference of concentration, the Pt wires preferentially nucleate and grow on the Au NPs surface due to higher concentration based on the thermodynamics. The reduction of Pt ions in the solution results in the formation of a nanowire network.[73] After the reduction, in low magnification TEM images (Figure 2.3 a), the final products chains form a highly porous network confirming the morphology of AuPt nanowires. The inset high magnification TEM image of AuPt NWs shows a continuous structure of these wires. Thus, the Au NPs are mostly covered by a continuous cover layer of metallic Pt. This ultrathin Pt layer exposes more active sites which benefit the electrocatalysis (this will be discussed more in part B). The electron energy loss spectroscopy (EELS) elemental maps exhibit this core-shell structure, as shown in Figure 2.3 b.

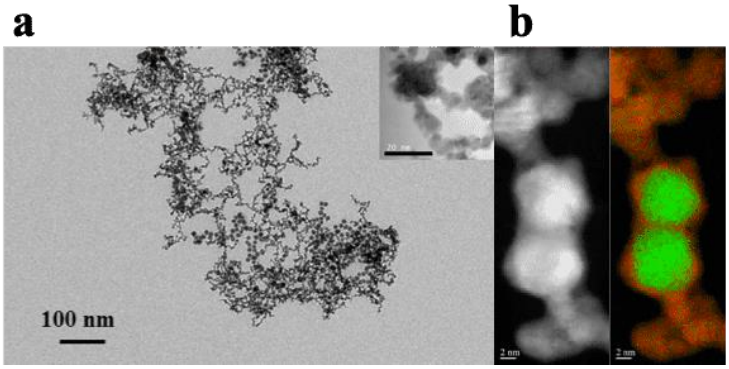

Figure 2.3 a) The low magnification TEM image of AuPt chains. The inset image is the high magnification. The scale bar in the image and inset are 100 and 20 nm, respectively. b) HRTEM

and EELS images of Pt shells (in orange color) on the Au NCs (in green color). The scale bars are 2 nm.

To better understand the formation of AuPt NWs, X-ray photoelectron spectroscopy (XPS) was carried out to examine the oxidation state of Au and Pt. After reduction (in Figure 2.4 b), the binding energies of Pt $4f_{7/2}$ are located at 71.1 eV and 71.9 eV, and for Pt $4f_{5/2}$ are located at 74.5 eV and 75.4 eV, representing metallic Pt and Pt alloy, respectively. Similarly, Au spectra also present main metallic and small alloy Au peaks (in Figure 2.4 a), which further demonstrates that a small portion of AuPt alloy formed during the reduction.

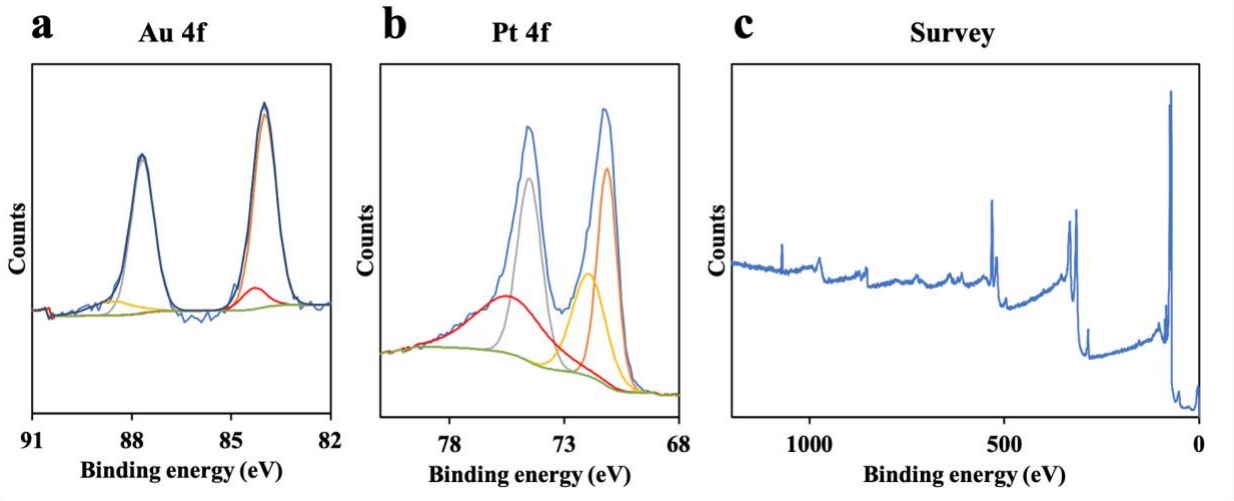

Figure 2.4 XPS spectra of a) Au, b) Pt, and c) survey of AuPt NWs.

To confirm samples' formation and crystal structures, we used the X-ray diffraction (XRD) to characterize them. Results are shown in Figure 2.5. The spectrum of Au NPs presents a prominent peak located around 38.4° (2θ), which can be ascribed to the diffraction from the (111) crystal planes of the face-centered cubic phase of Au (JCPDS no. 04-0784).[74] Similarly, Au(111) plane is observed in AuPt NWs samples at 39.0°. The small shift is due to the formation of AuPt alloy during the reduction. The XRD spectrum of AuPt NWs also observes a set of diffraction peaks presented around 40.1° and 46.7°, which can be assigned, respectively, to the Pt (111) and (200) planes. These shifts about 0.3° compared to pure Pt indicate the ultrathin layer of Pt on Au NPs. The broadness of the peaks also confirms the formation of nano-size material. Based on the Scherrer equation (Size = $K\lambda$ / (FWHM × cosθ), where K is 0.9, λ is X-ray wavelength, FWHM is

the half maximum intensity, and θ is the Bragg angle), the calculated size of the Pt in these materials is 5.8 nm.

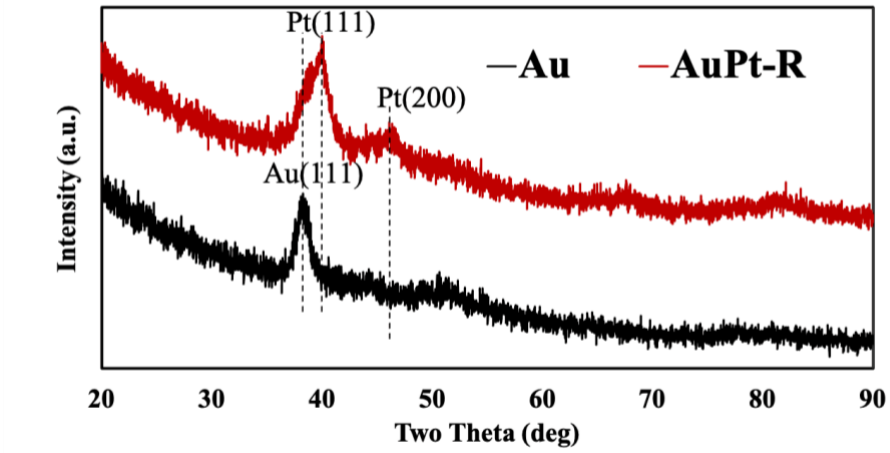

Figure 2.5 XRD spectra of Au NPs and AuPt NWs.

3.2 Current-voltage behavior of Au nanochains

A low density of AuCa NCs is deposited across two Au electrodes which have a separation of ~2 μm to investigate their conductive behavior. The deposition was checked by field emission electron microscopy (FESEM) (in Figure 2.6 a&b), which shows the sparse deposition of the AuCa NCs across the two Au electrodes. The gaps between neighbour Au NPs can be observed as well. The basic characteristics of current transport were determined by the multimeter. As shown in Figure 2.6 c, the nonlinear current-voltage behavior of Au nanochains is due to electron tunneling between the conductive particles.[75] A Coulomb blockade behaviour with a threshold voltage of V_T was also presented. The inset image is the oscillations of chains in the differential conductance due to single electron charging effects.[76,77,78,79,80,81] The current fits a power law with an exponent of 2.67 typical for a 2D nanoparticle array with defects.[77,81] These results show that the flow of electrons in these chains network is due to each isolated nanoparticle acting as a capacitor with a quantum tunneling barrier with adjacent nanoparticles. In contrast, the AuPt NWs with a similar concentration are deposited on the Au chip, as shown in Figure 2.6 d&e. Clearly, the current-voltage behavior (in Figure 2.6 f) of AuPt NWs presents a linear relationship with a much higher current response because of the absence of gaps.

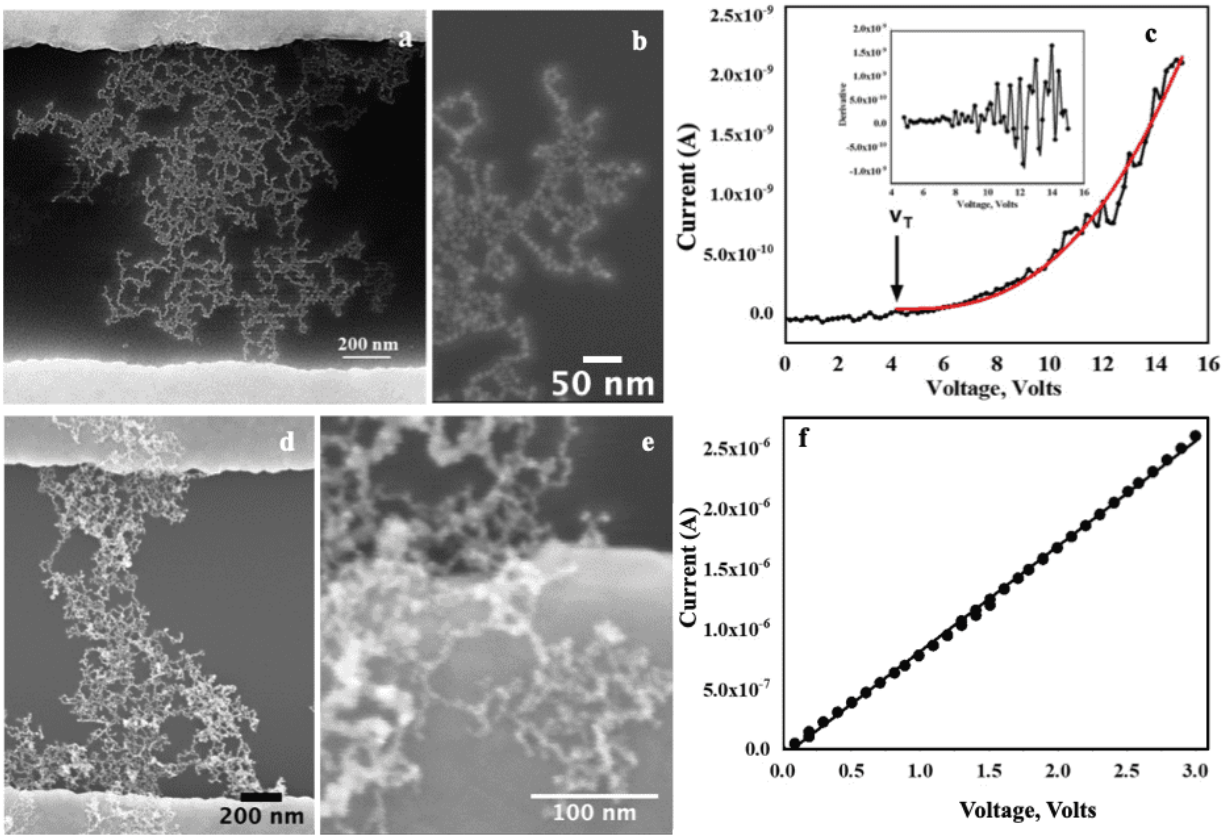

Figure 2.6 The FESEM images of the sparse deposition of a) the AuCa NCs and d) AuPt NWs across the two Au electrodes; b) and e) are the related high magnification FESEM images, respectively; The current-voltage response of c) and f) related to a) and d). The current of AuCa NCs fits a typical power law with an exponent of 2.67 typical for a 2D array with defects, which is shown in red color. The inset is the plot of differential conductance.

3.2.1 Filtration

In order to produce a flexible device, the prepared gold chains with micron scale size can be filtered out using a polymer membrane filter of pore size (~200 nm) by vacuum filtration. This simple process does not require any special deposition methods or high-cost processing. Besides, due to the basic unit being a series of nanoparticles with 1 to 2 nm gaps in between, electron tunneling is the basic process that governs the flow of current and the response from devices made with this material.[37,38,81] As seen in Figure 2.1 b, the initial blue colored Au nanochains solution becomes colorless after filtration. A layer of Au nanomaterials is deposited on the filter surface (as observed by its golden color). The formation of the device is then done by using PDMS masks that are

placed above the polymer membranes with the required patterns, and then the Au NCs are filtered through them, resulting in their deposition in pattern (schematic of Figure 2.1 a). The density of deposition is controlled by the volume of the solution filtered. At high deposition density, the patterns are shiny golden in color similar, and at lower density, they appear blue. A typical multilayer deposition of the Au NCs on the filter membrane is shown in Figure 2.7 a.

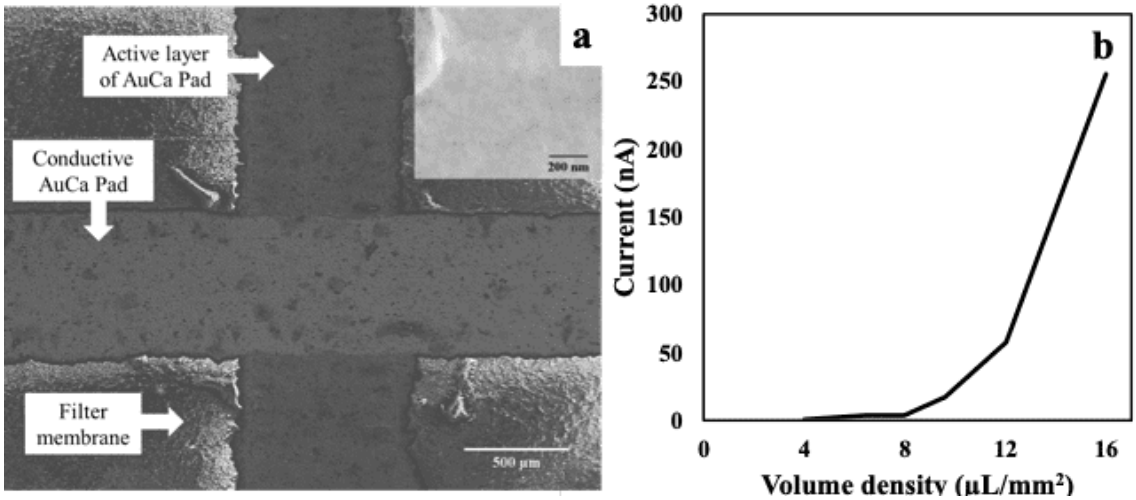

Figure 2.7 a) The FESEM image of the deposition of the Au contact electrodes (condense conductive layer) and the active layer (low density layer) on a filter membrane. The boundary between the two blocks is clearly visible. The inset image is the high magnification FESEM image of the active layer, with a volume density of ~16 µL mm^{-2}. It clearly shows the uniform deposition of the nanochains. b) The current response of devices with various deposition volume densities at 1 V applied bias.

The stacked Au NCs maintain the chains morphology. Meanwhile, due to the multilayer, the randomly dispersed chains form a highly porous network. The contact pads and the interconnect traces are made with 51 µL mm^{-2} deposition of the AuCa chains solution, while the active layer of the devices is made with 9 µL mm^{-2}-16 µL mm^{-2} of the chain solution. The density of deposition is normalized by the area of deposition. At densities lower than ~4 µL mm^{-2} of AuCa chains solution, the current levels are very low for accurate measurements. Depositing such 1D metal nanochains in 3D arrays with multilayer thickness leads to a highly conducting electrical network with a linear behavior in I-V response. The current response of devices with various deposition densities at an applied bias of 1 V is shown in Figure 2.7 b. With the increase of deposition volume, the conductivity increases overall. The device starts to show the conductivity from ~4 µL mm^{-2}

with quite high resistance. Therefore, it is considered that at the deposition of chains at ~4 µL mm$^{-2,}$ the percolation threshold is reached. The 1D morphology possesses a high aspect ratio, so less amount of gold solution is needed to obtain the conductivity. In a 3D system, the value of conductivity is proportional to the mass fraction.[83] Hence, a rapid increase in conductivity is observed above a deposition density of ~8 µL mm^{-2} due to the increase of the percolation pathways for electrons.[49,84] This simple filtration method can easily control the loading density of nanochains. This allows deposition to range from low-density arrays that have low conductivity and are sensitive to external modulations to the other extreme of high-density arrays with high conductivity that are insensitive to any external modulations. However, the electron conduction mechanism is still governed by tunneling due to local gaps in the conduction pathways, similar to other fractal systems.[68,81]

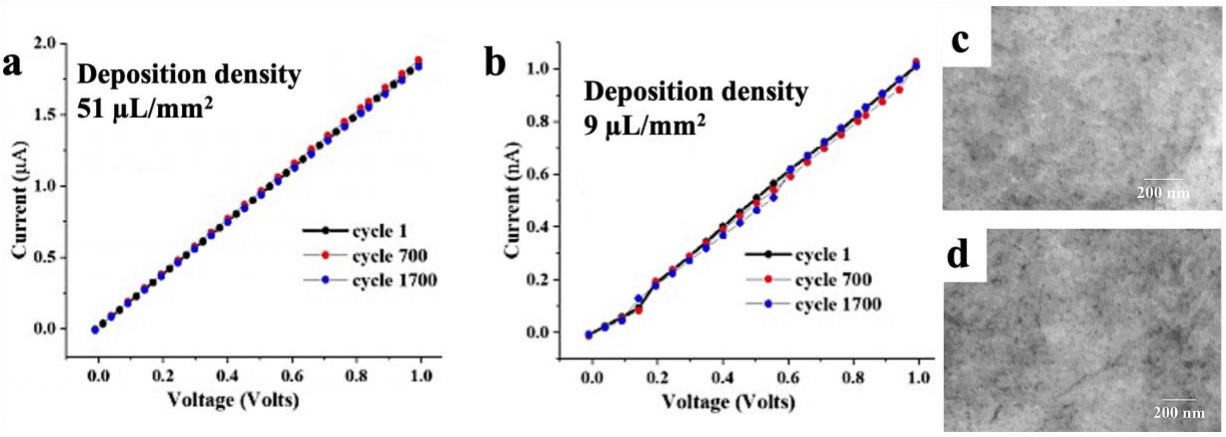

Figure 2.8 The flexibility of the device tested by cyclic bending tests where it is bent to 90°. a) The electrodes made by the process show no degradation in their conductivity even after 1700 cycles; b) The active layer also shows no change in conductivity after 1700 cycles; c) and d) the FESEM images of the electrodes and active layer after 1700 cycles bending with no obvious cracks presented, respectively.

The flexibility of deposited Au NCs is illustratedby bending at 90 degrees over 1,700 cycles. As can be seen in Figure 2.8 a&b, the conductivity of various loading densities of AuCa NCs does not show any obvious change. The FESEM images in Figure 2.8 c&d also prove that the chains are still connected with each other after the bending showing the excellent flexibility of Au NCs.

We also investigated the correlation between the filter's pore size and assembly size. The size of the chains and the pore size of the filters critically affect the fabrication of the devices. The photo images of the devices (in Figure 2.9) were made by three different pore size filter membranes, including 30 nm, 200 nm, and 2 µm, using AuCa NCs with a volume density of ~51 µL mm^{-2}. As for the 30 nm pore size membrane, the coffee ring effect is clearly observed (some part of the materials stacked at the edge of the shape) and the existence of breaks. Therefore, the conductivity decreases greatly. Also, the 30 nm filter membrane needs more time to drain the solution for the process, and it usually needs more than 12 h. While the 200 nm pore size only needs 1 to 2 minutes to obtain the device. Meanwhile, the resistance is 50 orders of magnitude higher than the device using a 200 nm filter. The longer time for draining leads to significant evaporation of the solvent (water), leading to the coffee stain effect. The 2 µm pore size device presents light blue color even for the conductive pads, and the conductivity is barely observed. This could be as the Au NCs are smaller than the pore size, so most chains are filtered through the pores. Therefore, the filter membrane with proper pore size is necessary. Also, a smaller chain size will lead to a decrease in the conductivity at the same volume. This is as the percolation threshold increases, when the aspect ratio of the chains is smaller.

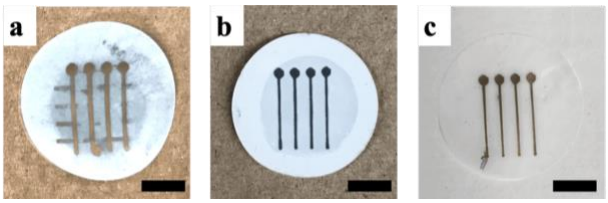

Figure 2.9 The deposited AuCa NCs with a solution volume density of 51 µL mm^{-2} using a) 30 nm, b) 2 µm, and c) 200 nm pore size filter membrane. Scale bar: 10 mm.

3.2.2 Temperature sensor

The dependence of the conductivity of films on temperature has been studied as well. The presence of a tunneling barrier in the chains also makes them sensitive to temperature at low applied bias.[85] The increase in temperature effectively increases the tunneling probability and hence the current.[86] The signal (current) hence increases directly with the stimulus (temperature).[68,69,85] This is in contrast to the decrease in current with increasing temperature (due to classical charge transport

and scattering[87]) observed in traces of metal films that are continuous in structure (e.g. of Au and Pt) and commonly used to sensing temperature in such devices.

Human body temperature is one of the vital signals, which is necessary to guarantee normal life and metabolism. However, most conventional temperature sensors are stiff and brittle with low temperature responses. Therefore, the development of soft, flexible, and real-time sensitive temperature sensors is needed. The complete device is made of 1D Au nanomaterials with micron scale size interlinked using Ca^{2+} ions or Pt, and they are safe for use and application on human skin. The filter and the deposited thin layer of Au NCs are highly flexible and can be bend without performance loss, enabling their routine use. Figure 2.10 a shows the resistance of the AuCa NCs device decreases as the temperature increases from 35 to 45 °C with a high sensitivity of 4 %/°C, which is among the best reported values for temperature sensing use in wearable devices.[88,89,90,91]

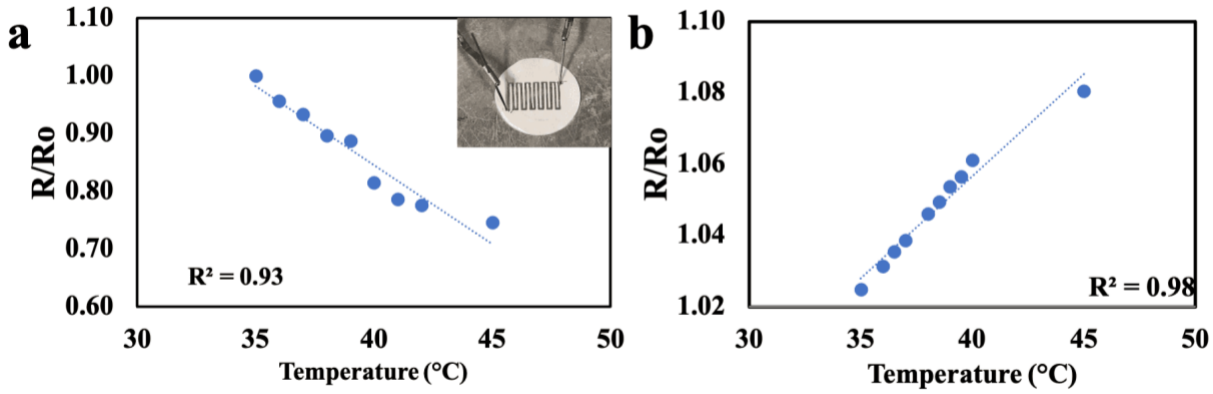

Figure 2.10 The resistance changes with the increasing temperature: a) AuCa NCs device with volume density of 19.5 µL mm^{-2} with a sensitivity of ~4% per °C, b) AuPt NWs device with volume density of 51 µL mm^{-2} with a sensitivity of ~0.2% per °C.

In contrast, the resistance increases with temperature as expected for continuous metal structures (the 51 µL mm^{-2} of AuPt deposited on filter membrane with a resistance less than thousands Ohms presents the temperature response in Figure 2.10 b), confirming the role of tunneling junctions in temperature response from the device. The temperature sensitivity of the AuPt NWs device is 0.2 %/°C. The equation can explain the effect of temperature on the tunneling behavior of the AuCa NCs:

$$\sigma \propto \exp\left(-\frac{E_A}{k_B T}\right)$$

where E_A is the activation energy and k_B is the Boltzmann constant.[83]

The volume of the filtering solution can tune the number of deposited layers. At a low count of layers, such arrays are highly sensitive to changes in any external stimuli that modulate their resistance. However, at a very high layer count, these arrays have an ohmic response with very high conductivity resulting in reduced sensitivity to external stimuli.[78,79,80] To show the basis of this strategy, devices are made with varying amounts of the Au NCs deposited, and the air is made to flow on them (normal to the device plane), which acts as a pressure stimulus.

The air flow induced pressure response was detected in the range of 1-4 liter per minute (LPM). The results from airflow testing show (in Figure 2.11) that the highest sensitivity to pressure is obtained with the lowest density of deposition (at ~4 µL mm^{-2} of the chain solution). As the deposition density increase (to ~8 µL mm^{-2}, 16 µL mm^{-2}, and then 51µL mm^{-2}), the sensitivity to the flow rate decreases. The critical point is that at the deposition of 51 µL mm^{-2} of the AuCa chains solution, the device shows almost no sensitivity to any airflow rate (less than 3.5‰ response). It could be the gold chains oscillated when applied the vertically oriented airflow pressure, so the contact area is increased. Also, the interlayer spacing is compressed with the decrease of resistance. Compared with low loading density, the space area for oscillation is much less in higher density resistance devices, which explains the much less response of the airflow. For repetitive cycles, the device shows no noticeable degradation.

As discussed in the previous chapter, external force induced change in the gap distance between neighboring nanomaterials results in a change of the tunneling resistance for nanomaterials which will modulate the output signal (current).[10] The sensing of the pressure is due to the modulation of the interparticle distance between chains that are deposited in a multilayer configuration. A typical response in current to applied load (using a load cell) is shown in Figure 2.12 d, where a decrease in resistance is observed with increasing pressure. The applied force reduces the interparticle distance, which affects electrical conductivity. This can be used as a physiological sensor to detect pressure variations due to, for example, pulse palpations. In the vertical direction, the distance was decreased because of the applied pressure, leading to more percolative conduction pathways. This reduces the resistance and increases the current.[93,94]

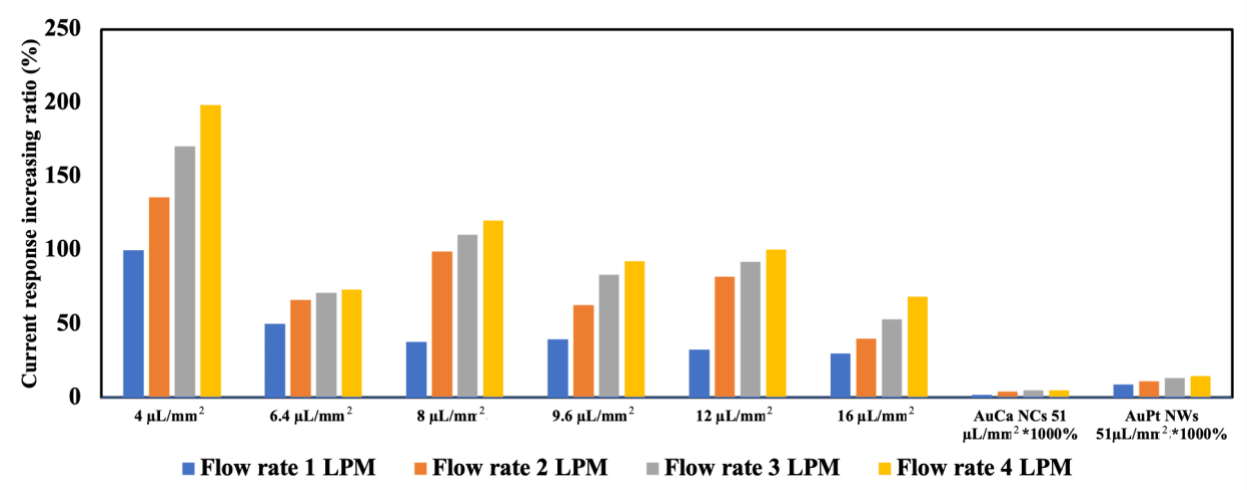

Figure 2.11 The sensitivity of devices with varying amounts of Au NCs deposited to applied airflow acts as a pressure stimulus.

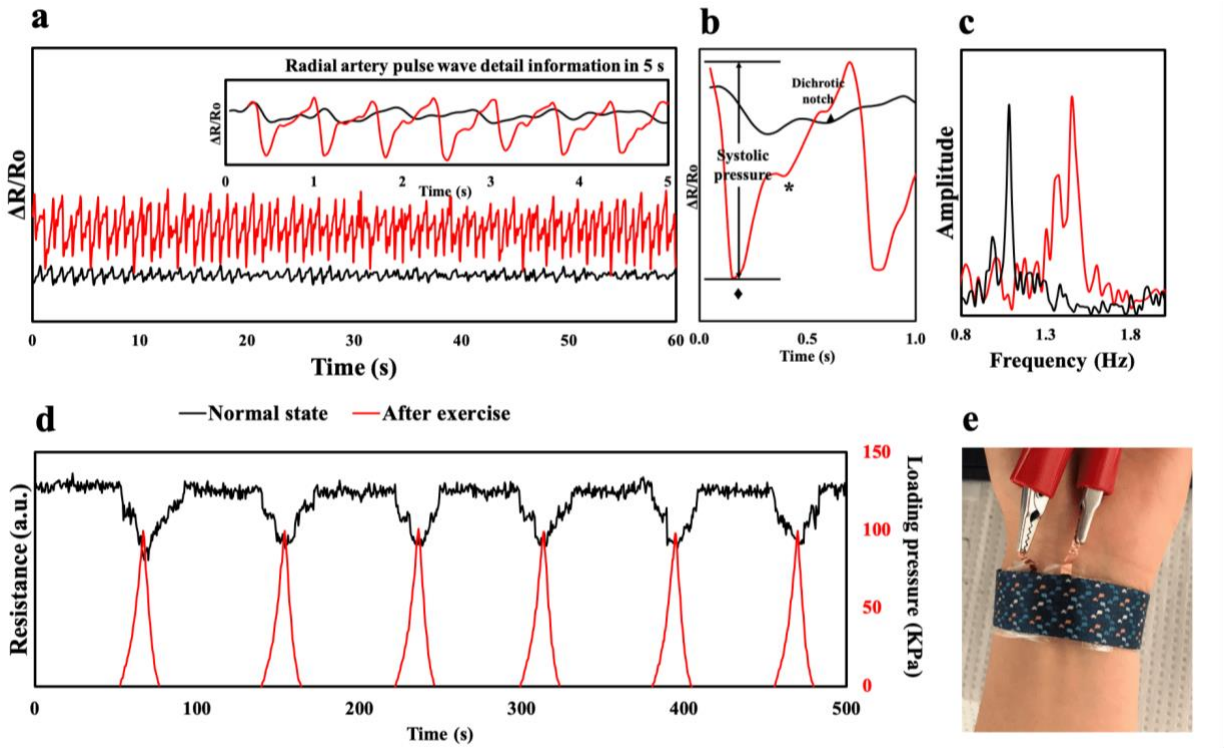

Figure 2.12 a) Radial artery pulse waves under normal state and after exercise, the pulse rate increased from ~65 to ~88 pulse/min. The inset image shows the detailed information in 5 s of the pulse wave in two situations; b) The detailed features of the pulsation wave, which shows the percussion wave (which is related to systolic pressure), the tidal wave (which refers to inflection point), and the diastolic wave (which follows the dicrotic notch) labeled as ♦, *, and ▲, respectively; c) The Fast Fourier Transform Algorithm (FFT) of the output pulsation signals; d)

The real-time response of resistance related to an external stress loading; e) A wearable monitor where the device is wrapped on the wrist by mounting it on a strap.[84]

This analysis is then used as the basis for making the device for sensing pulse pressure. A wearable device is made for sensing the pulse rate and its pressure profile. A typical configuration is made where a low density of the Au NCs is deposited between two contact pads (made by deposition of the Au NCs with ~51 μL mm^{-2} solution volume density). The top surface of the device is then covered with food-grade wrap (made from polyethylene) that is safe for human body contact. The protective layer functions to isolate the device from electrical contact with human skin. Only the pressure modulation from the pulse will be transmitted as a stimulus to the device. A typical pulse rate measurement is shown in Figure 2.12 a. We observe a typical pulse rate of ~65 pulse /min. A pressure profile of the individual pulse (Figure 2.12 b) shows the typical detailed feature of the systolic pressure, the percussion wave (which is related to systolic pressure), tidal wave (which refers to inflection point due to reflected pressure wave), and diastolic wave (which follows the dicrotic notch) labeled as ♦, * and ▲, respectively.[95,96,97,98] The ability to record the pressure profile is crucial as its shape variation is considered a marker for medical conditions. After exercising, the measured pulse rate shows a significant increase reaching ~88 pulse/min (on the same subject). In order to evaluate arterial stiffness, the radial artery augmentation index (AIr), radial diastolic augmentation index (DAI), and round-trip time of a reflected wave are commonly introduced.[98,99]

$$\text{AIr} = \text{Intensity of tidal wave/Intensity of percussion wave} \times 100\ \%$$

$$\text{DAI} = \text{Intensity of diastolic wave/Intensity of percussion wave} \times 100\ \%$$

Under the normal state, the average values (from five pulse waves) of AIr, DAI, and the cardiac cycle period are calculated to be 71, 40, and 1.08 s, respectively. After physical exercise, AIr, DAI, and the cardiac cycle period changed to 49, 23, and 0.65 s as a result of a larger contractile force is required to provide the blood to the activated muscles rapidly. Also, the reduced cardiac period after exercise was mainly because of the decreased diastolic time. All the results fit the reported range.[99,100,101]

3.2.3 ECG signals

The final set of signal monitoring is based on the ability of the device to record ECG due to modulation of the body's potential from the beating of the heart. This is fashioned as a single lead ECG placed on the wrist away from the pulse region. The two electrode pads are made with high density AuCa NCs (51 µL mm^{-2} deposition) while a thin layer of the AuCa NCs (9 µL mm^{-2}) is deposited between them. The changes in the skin potential act as a surface potential on the device layer and similar to gating leads to current modulation in the device. The change in the current through the device hence depicts the ECG signal similar to a single lead recording. A recorded signal from the device on the wrist is shown in Figure 2.13. As can be seen in Figure 2.13 a, the typical R-R wave is observed.[102,103] The width of a single pulse is ~0.85 s, which leads to a beating rate of 70 per min, which is easily calculated through the FFT Algorithm of the output ECG signals shown in Figure 2.13 b. The amplitude level difference between the three regions is small, which is a typical feature of single-lead ECG. Further to clarify that the signal is due to the gating effect on the active layer, control measurements on the device with only the contact electrodes show no significant modulation in measured potential. At the same time, recording the voltage modulation across the device instead of current also does not lead to an appreciable signal, confirming that the modulation of the surface potential on the active layer is the reason for the observed signal. The presence of a series of tunneling junctions makes the device sensitive to small modulations in the surface potential.[70,104] This is further confirmed by having a reference electrode with the device (a three-electrode set-up) in an aqueous medium and using it to act as a liquid gate.[70] The three-electrode device is fabricated with the active layer of AuCa NCs bridging the working and the counter electrode. An Ag/AgCl electrode is made and used to vary the gate potential on the Au chain active layer. With applied bias across the active layer, the change in the gate voltage modulates the current in the device. Clearly, the current response decreases with an increase of gate potential. Even a small change of 0.5 mV is enough to cause a modulation in the current in the active layer of AuCa NCs (Figure 2.14 b&c) with a sensitivity of 1.2 µA V^{-1}. A typical potential difference for a QRS complex is larger than 1 mV. This signifies the ability of the NCs to sense small changes in the surface potential.

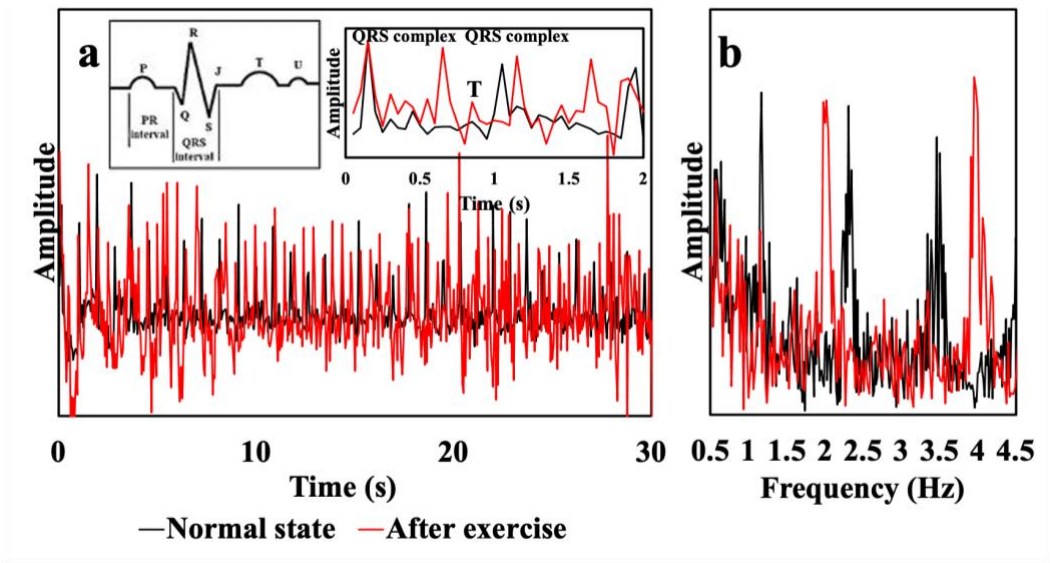

Figure 2.13 a) The output ECG signals from the device on the wrist placed away from the position of the radial artery and the inset figure on the right presenting the detail information of ECG in 2 s. The typical regions of the QRS complex (represent typically ventricular depolarization) and T wave (represents typically ventricular repolarization) are observed. The width of a single pulse under the normal state is ~0.85 s which leads to a beating rate of 70 per min. After exercise, the beating rate increased to 120 per min, ~0.55 s. The inset on the left shows the typical profile of an ECG pulse. b) FFT spectra of the ECG signals in (a) showing the dominant peaks at 1.15 Hz (normal state, black line) and 2.02 Hz (after exercise, red line), refer to the beating rate of ~70 and ~120 per min, respectively.

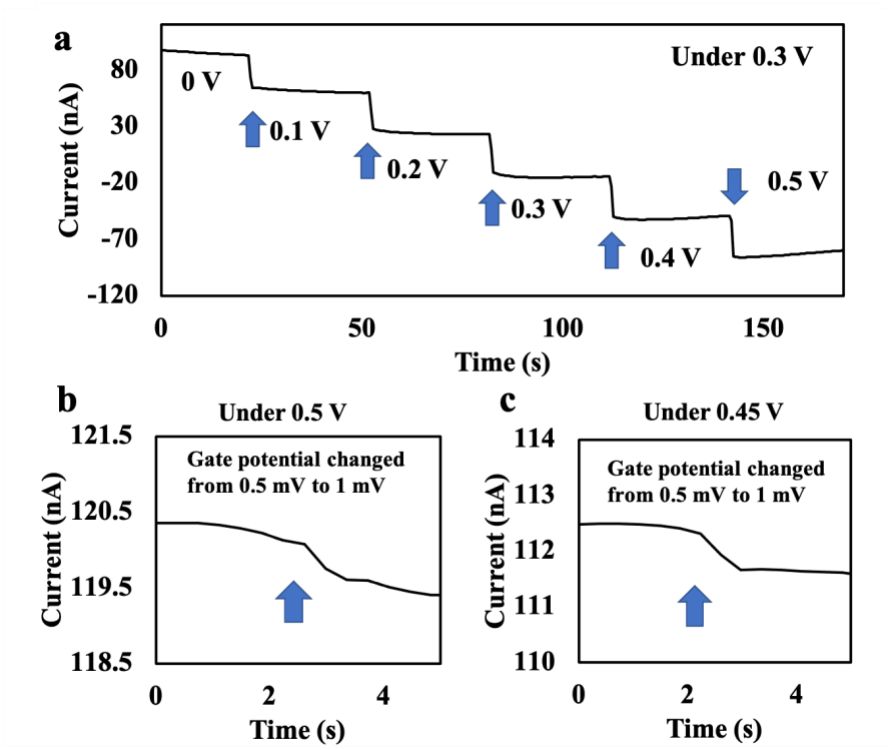

Figure 2.14 The current modulation as the change of gate potential with various applied bias across the active layer.

3.3 Conclusion

We have presented a simple method of using quantum tunneling effects in a macroscale material to record a variety of human physiological signals. The device is easy to fabricate and has a rapid response and high sensitivity with multifunction compared to other reported devices (Table 2.1). The device functioning relies on branched chain assembly of Au nanoparticles with 1 to 2 nm gaps between adjacent particles. The net effect is that the charge transport in these chains is governed by the tunneling phenomena and nanoscale capacitive (and charging) effects when deposited in low density. While at a high density of deposition, the material functions similar to a highly conductive film. The microns size scale of the assembly allows the use of simple vacuum-based filtration to make the devices. Further, as the chains have a porous network structure when deposited in low density, the device is sensitive to pressure modulations. This allows accurate measurement of the pulse pressure and shape. The sensitivity of these NCs to temperature and surface potential due to the tunneling effect allows us to measure the temperature in the physiological range and the modulation in skin's potential due to cardiac palpations.[68,69] Therefore, in a simple device configuration, all the three main human physiological signals have been incorporated. The simple process of making this macroscale material and then its fabrication into devices presents a new avenue to integrate quantum tunneling-based sensing into wearable devices in a cost-effective manner that does not require any special fabrication methods.

Table 2.1 A performance comparison of devices for measuring human physiological signals

Materials	Method	Sensing mechanism	Sensitivity	Response time	Durability	Application	Ref.
Au NCs	Self-assemble and filtration	Tunneling effect	4 %/°C; 47 Ω kPa^{-1}; 1.2 μA V^{-1}	< 50 ms	>1700 cycles 90° bending cycles	Pulse, ECG, temperature	This work
Graphene nanoplatelet network	Marangoni-flow driven convective assembly and microtopography-guided transfer technique	Resistance	Gauge factor of 1697	< 0.1 s	> 100000 cycles	Pulse, breathing, hand-motions	105
Carbon nanotube	Screen-printed, spin-coating	Field effect	~0.89 %/°C			ECG, Temperature, UV exposure	95
Multiwall carbon nanotubes-based material	Printing methods	Resistance	0.85 %/°C		100 times per 30 h of attachment	ECG, Temperature	106
3D graphene foam and carbon nanotubes	Chemical vapor deposition	Resistance	Gauge factor = 35	30 ms	>5000 cycles	Pulse, venous pressure, body motions	107
Gold nanowires	Drop casting	Resistance	Gauge factor of 6.9-9.9	< 22 ms	5000 cycles	Human motion, Pulse	49
Single-walled carbon nanotubes, Gold film	Chemical vapor deposition, sputtering	Tunneling effect	1.2 %/°C	< 60 ms	>10000 cycles	Pulse, respiration, temperature	90
Reduced graphene oxide, polyurethane	Spin-coating	Field-effect, tunneling effect	0.67 %/ °C		6000 cycles	Human motion, pulse, temperature	89

Part A Self-Assembled Au NCs as building blocks to fabricate flexible devices

Chapter 3 A simple deposition method to produce AuPt NWs based stretchable devices/electrodes

1 Introduction

High performance stretchable devices are leading to new application in the fields of IoTs and as next-generation devices to improve the quality of life. Examples of such devices are as circuits, transistors, light-emitting diodes, energy harvesters, photodetectors and stretchable energy-storage devices.[108,109] There are two primary approaches to prepare such a stretchable device: 1) embed or deposit the stretchable conductive materials on an elastomeric substrate with percolating network;[109] 2) modify the structure of non-stretchable (but flexible) materials into wrinkled configurations to create a stretchable electronic device without inducing significant strains in materials.[109,110]

Highly conductive metal-based materials are commonly used.[108] Various morphologies have been studied as conductor, including 0D sphere, 1D fibers or nanowires, and 2D sheets or crack-based thin film.[111,112] Metal nanowire percolation networks have been intensely researched due to the specific shape and high aspect ratio, which are important factors that can affect the conductivity.[110]

Although Ag and Cu are more commonly used to develop stretchable conductive composites because of the lower cost and high electrical conductivity, they are easily oxidized. Au is an excellent alternative owing to its intrinsic low resistance and high stability against oxidation.[111]

Here, we report an indirect deposition method to prepare stretchable devices. In this method, the conductive electrode materials are initially deposited on a filter membrane by a simple filtration method which can achieve large area deposition in the desired pattern at a low cost. Then the materials on the filter are transferred on the elastomeric substrate to measure the performance. We prepared two modes of stretchable devices to compare the samples' conductive performance: 1) deposit on a substrate without any pre-strain; 2) deposit on a substrate with an applied 100% pre-stretched strain. The embedded conductive materials are AuCa NCs and core-shell structured AuPt

NWs network, which are microns scale in length and are fabricated by a facile aqueous phase route. In addition, an ultrathin layer of Pt coveres10 nm Au NPs and possesses high conductivity and a high aspect ratio. The conductive behavior for all the devices depends on the morphology of the conductive filling materials. The flexible patterns can be integrated as electrodes with other devices like photodetectors.

2 Experimental section

2.1 Synthesis Section

2.1.1 Preparation of AuPt NWs

135 µL of 4.5 mg mL^{-1} $PtCl_4$ (99.9%, Sigma-Aldrich) were mixed with 1 mL gold nanoparticles, with a size of 10 to 12 nm, purchased from BBI Solutions OEM Limited, and then left on the shaker with a speed of 300 rpm until the solution color changed to dark blue. After the self-assembly process, the Pt ions were reduced by 75 µL of 4 mg mL^{-1} $NaBH_4$ (99%, Sigma-Aldrich) turned to dark brown. The chains are stable over two weeks.

2.1.2 Preparation of AuCa NCs

105 µL of 1 mg mL^{-1} $CaCl_2$ (99.0%, ACP chemicals Inc.) were mixed with 1 mL gold nanoparticles and left on the shaker at a speed of 300 rpm overnight. The nanochains were successfully assembled when the color of the solution changed to dark blue, with a length of ~250 nm.

2.1.3 Fabrication of Devices

The wearable devices were prepared through the filtration process. First, the PDMS mask was used to obtain a particular pattern of the active layer. (2.0 g of silicon elastomer base was well mixed with 0.2 g elastomer curing agent from Dow Inc., then cured at 75 °C for one hour.) Then, the desired patterns (such as a rectangle shape with 20*3 mm^2) were obtained by laser cutting. The polycarbonate filter membranes with 200 nm pore size were purchased from Structure Probe, Inc. Various loading densities of the NWs were first obtained by a simple filtration method. Then, a device was obtained by putting the PDMS mask on top of the filter membrane. Once the device was totally dried, the materials were transferred onto the stretchable substrate (3M™ VHB™ Tape 4910, acrylic adhesive foam with viscoelastic nature). This process was done by putting the material filter onto the tape such that the material was in contact with the tape. With the help of water, Ethanol, and applied pressure, the conductive materials could be fully transferred on the substrate due to the viscoelastic nature of tape. The eutectic GaIn alloy was used to connect the devices to characterize their electrical response on subjecting them to stretching cycles.

2.2 Characterization Section

Zeiss Ultraplus FESEM was used to measure the morphology of samples and the cracks under strain.

2.3 Electrical Measurement

The current-voltage response of the devices was measured by a 3458A Digital multimeter combined with a 6614C 50 Watt system power supply from Agilent Technologies Company. The measurements were conducted by using a two-probe method. First, the stretching and releasing process was precisely controlled by CONEX-MFACC linear stage with the CONEX-CC controller. Then, the devices' periodic stretching/releasing tests were performed using this linear motor to apply a tensile strain at a rate of 0.01 mm/s or 0.25 mm/s. The current response was the real-time recorded by the multimeter.

A key parameter of stretchable resistive strain sensors is gauge factor (GF), defined as:

$$GF = (\Delta R/R_0) / \varepsilon$$

$$\varepsilon = (\Delta L/L_0) \times 100\%$$

where ΔR is the relative resistance change, R_0 is the initial resistance of the electrode, ε is the tensile strain, ΔL is the relative distance change, and L_0 is the initial distance of the electrode.[113]

3 Results and discussion

The schematic images (in Figure 3.1) present the process for the fabrication of a stretchable device. First, the device pattern was made through a simple vacuum filtration process. Then the filter membrane was directly stuck on the substrate by facing the active materials to the adhesive acrylic tape. A layer of water was added on top of the filter membrane. This increases the adhesive force between the conductive filling materials and tape and expands the distance between the electrode and filter membrane due to water molecules and the capillary force. Later, with the use of ethanol, the filter membrane could be easily peeled off from the tape, while the electrode was nicely transferred on the stretchable matrix. After the transfer process, the bottom side of the electrode becomes the top surface. Thus, the flat filter substrate (the filter membrane) aids in the formation of a smooth and flat surface.[110]

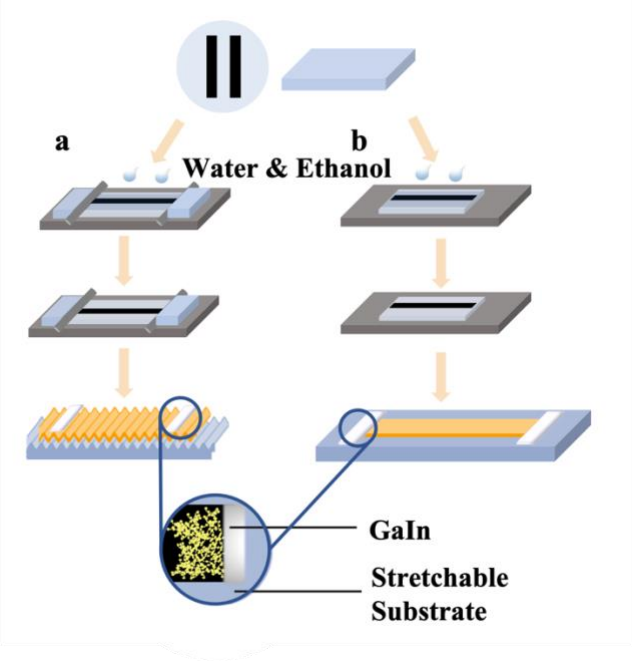

Figure 3.1 The schematic image of the stretchable device fabrication process: a) is the pre-stretched device, and b) is the scheme of a device without pre-applying any tensile strain.

As can be seen in Figure 3.2, the FESEM images illustrate the deposited AuPt NWs and AuCa NCs samples on the stretchable adhesive substrate without pre-applying any strain shows a smooth surface but with a lot of micro flakes separated by microcracks. Furthermore, as seen in the high magnification FESEM (in Figure 3.2 c), the cracks with 10-50 nm width are connected by AuPt

NWs between adjacent blocks. These kinds of interconnections could protect the film from strain induced fractures. Furthermore, this preparation method can transfer the whole electrodes and provide a simple way to fabricate a scalable stretchable device with microcracks, as is discussed below. In Figure 3.2 d, the AuCa NCs device presents cracks with 50 to 200 nm width and smaller cracks labeled in the blue circle. As seen in high-mag FESEM images, the spots on the electrode surface are caused by the pores on the filter membrane.

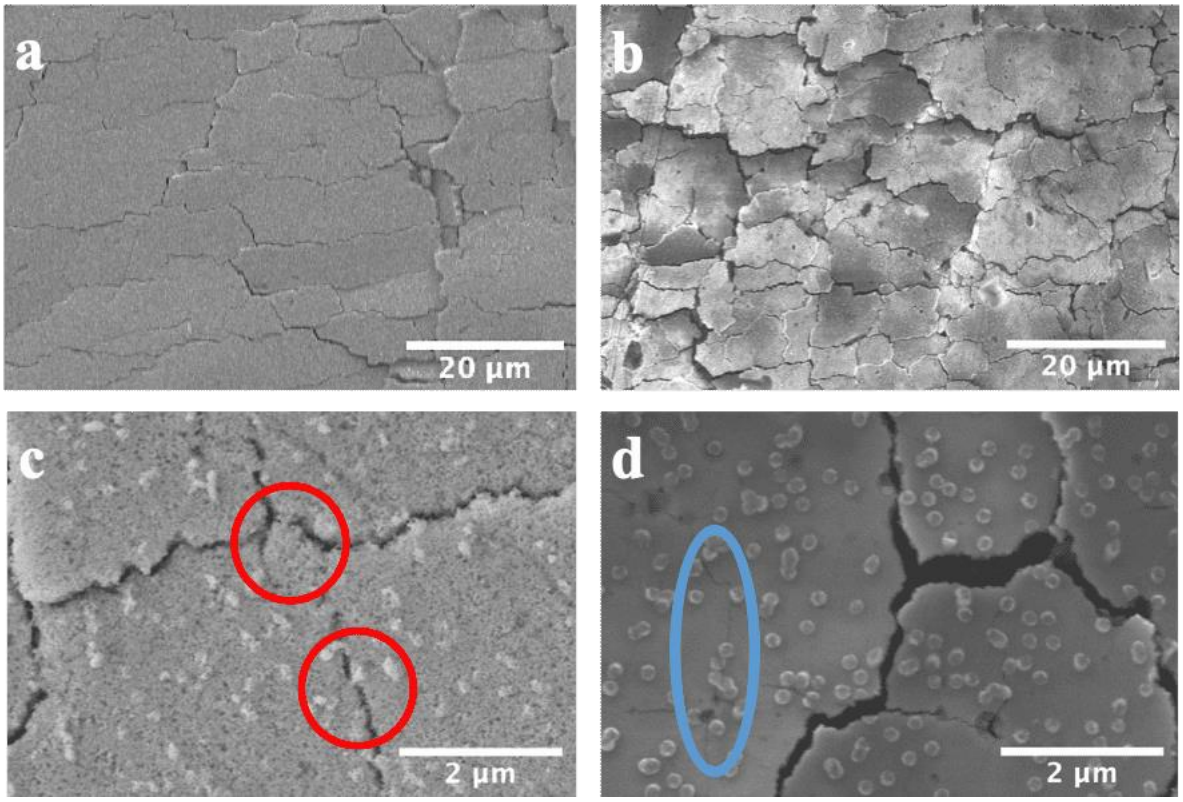

Figure 3.2 The FESEM images of a) and c) AuPt NWs and b) and d) AuCa NCs device. Red circles in image c) label the adjacent blocks that are interconnected by AuPt NWs. Blue circles in image d) label the smaller cracks in AuCa NCs.

3.1 The substrate tape without applying any pre-stretched strain

Firstly, the relationship between the loading density of conductive filling materials and the device's conductivity is investigated to show the possibility of this fabrication method. Three different loading densities of AuPt NWs are deposited in rectangle block shapes, 25.0, 16.7, and 12.5 µL mm^{-2}, respectively. The resistance of the three deposition densities is 3.57E+03, 4.00E+05,

and 7.14E+08 Ohm, respectively. The resistance is derived from two components: the resistance of each flake made of AuPt NWs and the contact resistance between neighbour flakes. The device with the lowest loading has sparsely distributed percolation networks and hence possesses the highest resistance, which is 5 orders magnitude higher than the highest loading device. Higher loading leads to higher conductivity before applying strain due to more percolated pathways. The AuPt NWs device with 25 μL mm^{-2} has high enough conductivity, which will be mainly discussed later.

Secondly, 1D gold nanochains linked by Ca^{2+} cations are used to better investigate the relationship of resistance with morphology. At the loading density of 33.3 μL mm^{-2}, the resistance of AuCa NCs is almost the same as the 25.0 μL mm^{-2} of AuPt device (7.14E+03 Ohm). Due to the presence of continuous Pt cover with extended Pt wires, less loading density of AuPt is needed to reach high conductivity compared with AuCa NCs. Even though the AuCa NCs possess a high aspect ratio, there are gaps with 1-2 nm that increase the resistance. Furthermore, AuPt NWs are longer than AuCa NCs. The AuPt NWs possess the percolation networks with fewer junctions, resulting in a lower total junction resistance. Au and Pt present chemical stability and high electrical conductivity. However, too much loading causes the formation of bulk chunks after the filtration process, decreasing the conductivity. Therefore, the high density in loading is limited to ensure the stability of the device structure.

Then, the current response was recorded as a function of time under various tensile strains to study the performance of stretchable devices. The stretched length was precisely controlled by a motor controlled stage. We measured the current response of devices in two modes: first, the responses were recorded after the devices were stretched to specific strain; second, the response with repetitive stretching/releasing cycles was continuously measured.

The current response of AuPt NWs device with 25.0 μL mm^{-2} loading density was recorded as a function of increasing strain until the device resistance increases to 100 kOhm. The strain sensor of the devices can be characterized by:[114,115,116]

$$\frac{\Delta R}{R_o} = e^{g\varepsilon} - 1$$

where g is the gauge factor (GF), and ε is the strain. From the equation, the AuPt NWs device presents GF=110 in the range of 0-6.67% strain. Then the current response to a tensile stress of the AuCa NCs device with the loading density of 33.3 μL mm^{-2} was measured. The GF is 243 in the range of 0-2.5%, as demonstrated in Figure 3.3. This confirms the continuous networks and extended nanowires can enhance the conductive performance of the 1D gold nanochains. The resistance of these two devices increases with the increase in applied strain. Typically, the devices using an elastomer matrix show immediate response with external strain. However, the matrix needs a longer relaxation time to restore to the initial state at high moving speed (of the stage for application of the strain).

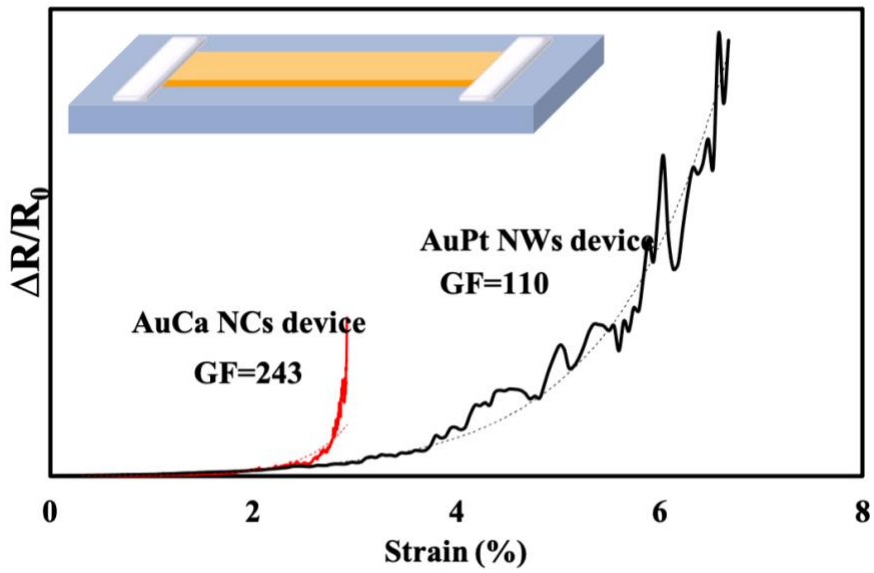

Figure 3.3 Relative resistance change as a function of the strain of AuPt NWs device and AuCa NCs device. Fitting results (in dashed lines) of strain sensing calibration curves are according to the exponential law.

We also prepared a device made by sputtering a layer of gold with a thickness of 30 nm (Au film). From the FESEM images (Figure 3.4 a&b), it is a continuous film without any obvious cracks. The initial resistance is ~12 Ohm. This initial high conductivity is attributed to the absence of microcracks. In comparison with the Au film, the AuPt NWs devices have a thicker thickness (~150-200 nm) due to the highly porous networks.

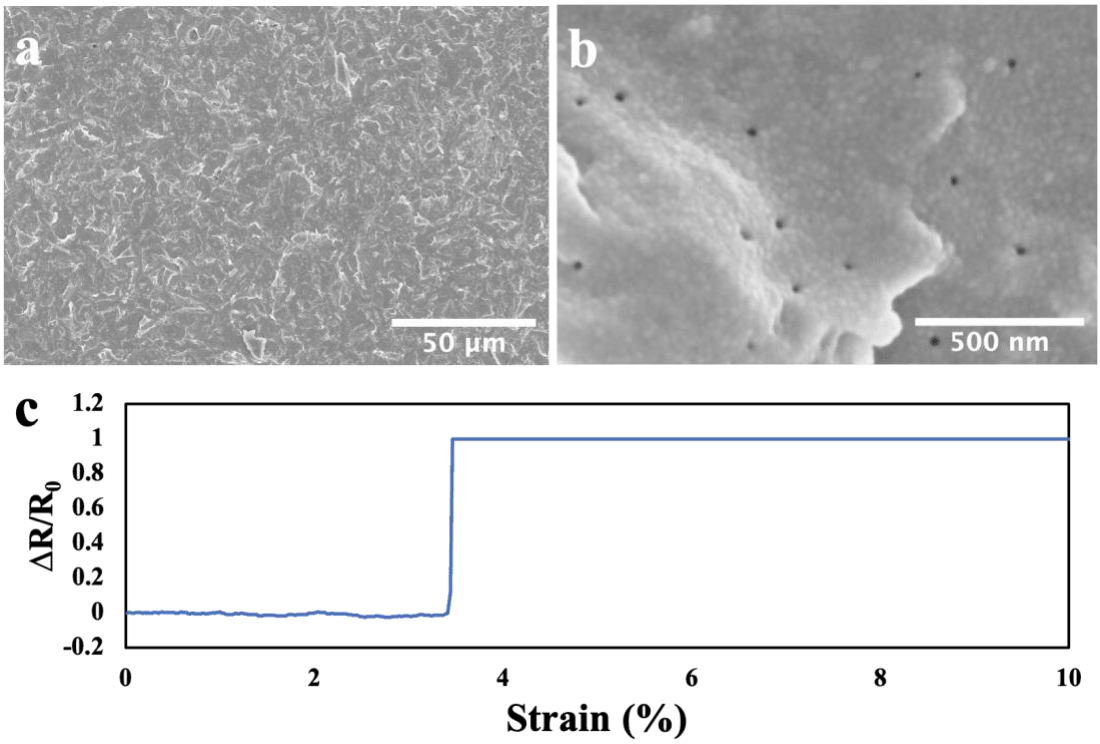

Figure 3.4 FESEM images of Au film on the substrate in a) low magnification and b) high magnification; c) Relative resistance change as a function of the strain of Au film device.

From the data, AuPt NWs device can endure the highest strain compared with AuCa NCs device and Au film. This makes them suitable as flexible electrodes. In this work, after the filtration process, AuPt NWs form a condense film that presents outstanding conductivity. After the transfer process onto a stretchable substrate from the FESEM images (in Figure 3.5) it is observed that short and narrow microcracks form both parallel and perpendicular to the tensile stress direction. The length and width of the cracks are about 10 to 30 µm and ~10 to 50 nm, respectively. As shown in low magnification FESEM images (Figure 3.5 b), the cracks, that are perpendicular to strain direction, change from several nanometer scales to ~1 µm under 6.67% strain. The strain-induced change of gaps is responsible for reducing conductive pathways, reflected by the output current response.[49] The flakes are ~10-20 µm large but stay connected parallel to the direction of strain force. Additionally, under high magnification FESEM images (inset image in Figure 3.5 b), the interconnections made by AuPt NWs are clearly observed, which help to maintain the pathway for charge carriers. Thus, when the matrix has been stretched, the micro flakes remain connected due to the NWs. The contact between two adjacent gold flakes also plays a role as the transfer

bridge for charge carriers. Therefore, inter-crack conduction dominates the resistance with applied strain.[114]

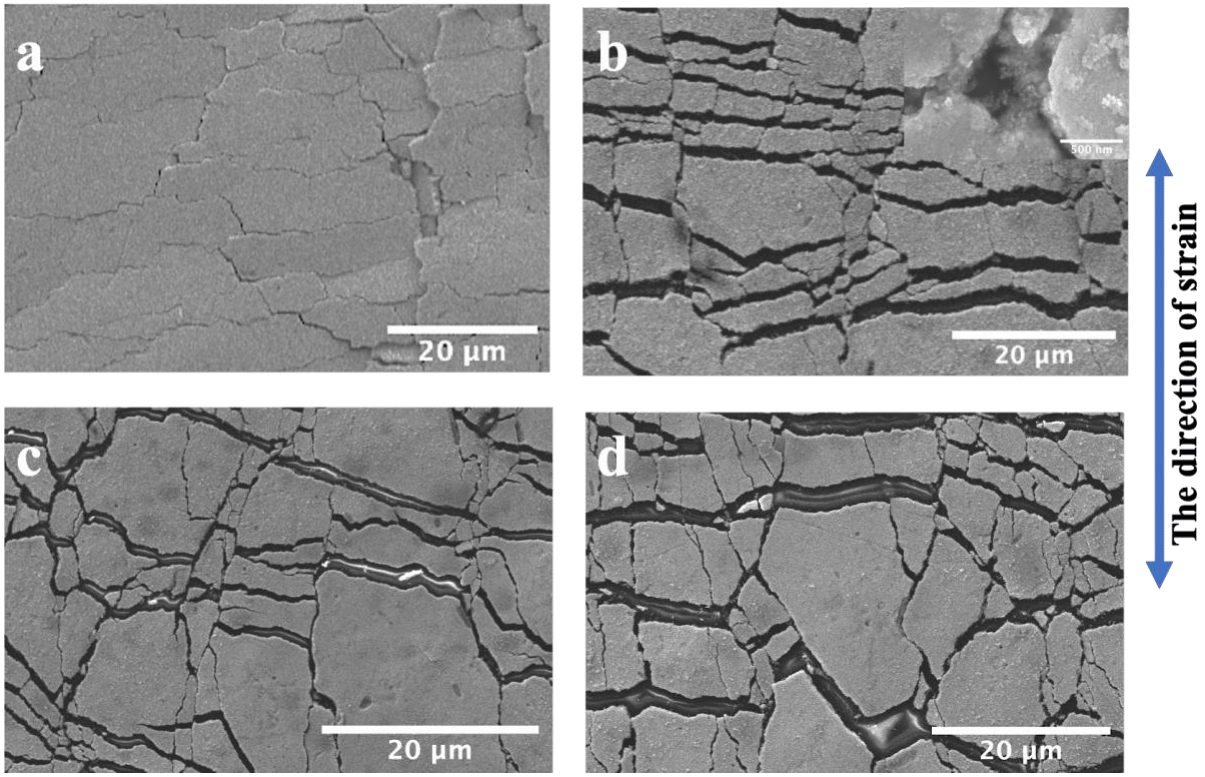

Figure 3.5 FESEM images of AuPt NWs device: a) 0% strain, b) 6.7% strain, c) 12.5% strain and d) 25% strain, with gap sizes of ~10 to 50 nm, ~1 µm, ~1.5 µm, and ~2 µm, respectively. Higher strain applied on the devices results in larger crack formation. The inset is the high magnification FESEM image under 6.7% strain which presents the interconnections by AuPt NWs.

Then, the current-voltage response was measured to calculate the resistance after releasing the strain to test the reproducibility. All the I-V curves present a linear relationship, indicating the devices show an ohmic property. After releasing the strain, the gaps between the adjacent islands decrease when the device is under strain. Thus, the device's conductivity can be fully recovered after application of 12.5% strain, and it retains ~65% conductivity after application of 37.5% strain. The FESEM image in Figure 3.6 a shows that the cracks for a fresh device are in the range of 10 to 50 nm. After releasing the strain, the size of the gaps increases to microns, but the flakes are still connected as labeled in red cycles Figure 3.6 b. At higher strains, the density of the cracks increases, and smaller micro flakes are observed.

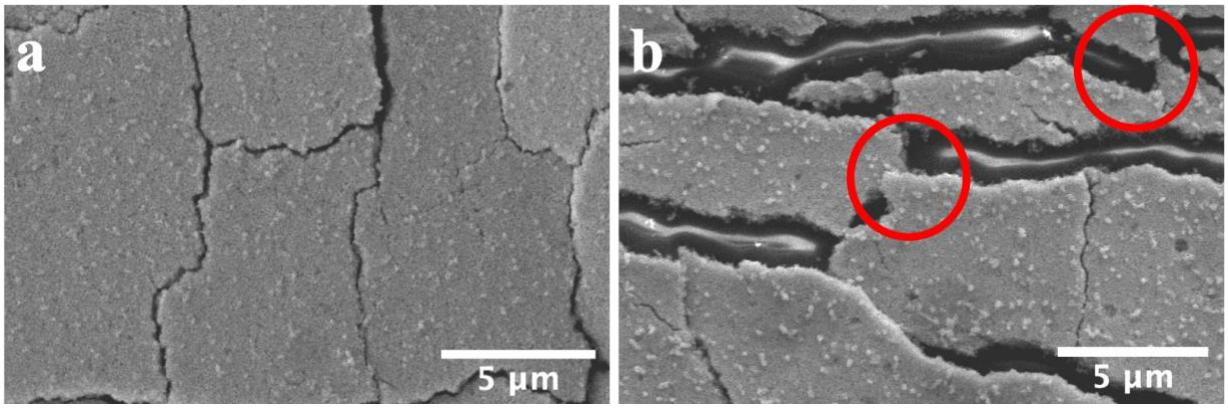

Figure 3.6 FESEM images of AuPt NWs a) before and b) after releasing 100% strain. The red circles in b) show the flakes are connected.

The gauge factor of AuCa NCs device is larger than AuPt NWs device because of their non-continuous 1D nanochains morphology. From Figure 3.7 a&c, even though the cracks with less than 200 nm width, there are hardly any interconnection presented. Thus, when a strain force is applied on the AuCa NCs sensor, the adjacent flakes are gradually separated, and less contact and interconnection lead to a less current pathway.[112] Thus, the conductivity of AuCa NCs device is more sensitive to external strain. When a small strain is applied, the neighboring islands are separated with fewer connections, while at larger strains, the joints between the islands and the flow of current are hindered. Similarly, once the strain on the device is fully removed, the contact between adjacent flakes is recovered, and the current pathway is reformed, restoring the current flow. However, there is still a slight decrease of conductivity as a not complete recovery of the connection is achieved.[110]

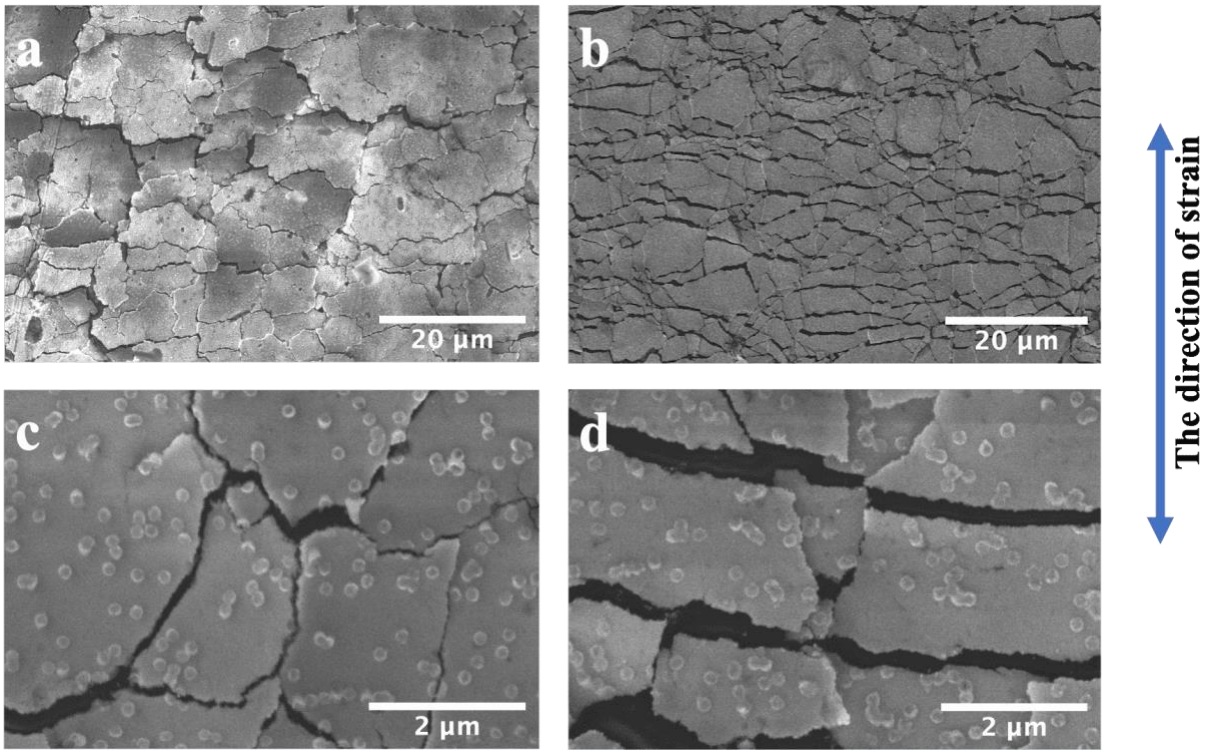

Figure 3.7 FESEM images of AuCa NCs device: a) and c) 0% strain, b) and d) 6.7% strain with a gap size of 50 to 200 nm and 200 to 300 nm, respectively. Higher applied strain on the device results in the formation of larger crackers.

As for the Au film, the external strain force leads to the forming of 3 to 5 μm width cracks at 3.5% strain (proved by Figure 3.4 c and FESEM image Figure 3.8 b), resulting in a sharp decrease to nearly 0 current. This could be because no interconnections are formed between the cracks, which lose the connection under the stain. Meanwhile, once the strain is released, the current response bounces back to the initial state. As a result, the gap size of cracks decreases, and separated islands begin to contact again with overlapped flakes, which recovers the conductivity. However, after total recovery, application of a higher strain (7%) leads to a decrease in contact area between adjacent islands and wider cracks are formed. This leads to an increase in the film's resistance by 5 orders magnitude higher.[117] Thus, higher tensile strain causes the decrease of contact area between adjacent islands and wider cracks are present.[117] All the samples can endure thousands of cycles and remain conductive within a certain range after releasing the strain. Relevant data are listed in Table 3.1.

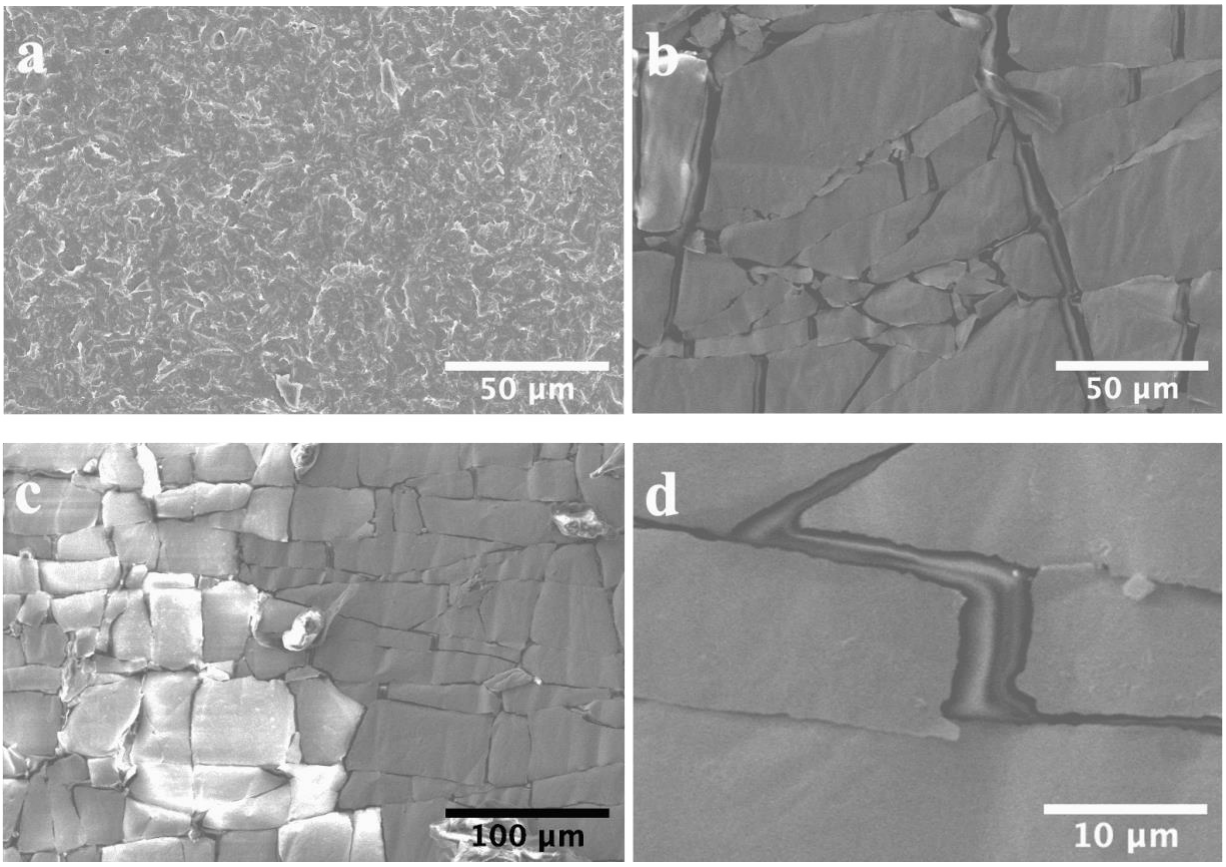

Figure 3.8 FESEM images of Au film at a) 0% strain and b) 3.5% strain; c) The low magnification and d) high magnification FESEM image of Au film device after releasing the 7% strain.

Table 3.1 Relevant conductivity change under tensile strain and repeated cycles.

	Strain i%	I_i/I_0	$I_{i\text{-back}}/I_0$	Repeated Cycles	$I_{i\text{-cycles}}/I_{back}$
AuPt NWs	1.25	0.552	0.793	100	0.959
	3.13	0.207	0.655	100	0.974
	6.25	0.014	0.621	100	0.953
	9.38	0.003	0.690	100	0.948
	12.5	0.000	0.683	100	0.999
	37.5	0.000	0.655	100	0.973
AuCa NCs	1.25	0.053	1.405	100	0.927
	2.5	0.001	0.800	100	1.008
	5	0.000		100	1.151
	10	0.000		100	1.046
	30	0.000		100	0.825

Au film	2.5	1.034	1.036	3	1.167
	5	0.000	1.069		
	10	0.000	0.000		

I_i is the conductivity with the device under strain;

I_0 is the conductivity before application of any strain;

$I_{i\text{-back}}$ is the conductivity after the applied strain is removed;

$I_{i\text{-cycles}}$ is the conductivity after repeated stretching/releasing cycles at certain strain.

Thus, the electrical properties of stretchable electronic devices mainly depend on the morphology of embedded conductive materials. In addition, the generated microcracks with interconnections facilitate the free movements of carriers, unlike bulk cracks which cause full loss of conduction.[108]

3.2 The substrate with 100% pre-stretched strain

We also deposited the AuPt NWs, AuCa NCs blocks, and Au film on a 100% pre-stretched substrate (AuPt NWs-pre, AuCa NCs-pre, and Au film-pre device), with 25.0 and 33.3 μL mm^{-2} loading density and 30 nm thickness, respectively. From the FESEM images (Figure 3.9), it is observed that after releasing the strain, AuPt NWs-pre, AuCa NCs-pre, and Au film-pre device form wrinkles that are uniformly aligned perpendicular to the direction of strain over the whole film. These wrinkles are formed due to the compressive force in the longitude direction. The distance between adjacent wrinkles is ~5 to 10 μm. As for AuPt NWs-pre and AuCa NCs-pre device, the edge of each wrinkle can be clearly observed on the cross-section of the flakes. Meanwhile, the formed microcracks are aligned parallel to the strain direction with relatively uniform size (~2 μm) due to the tensile stress in the lateral direction.[117] The difference between the two kinds of devices is that the AuPt NWs-pre device presents interconnections between the neighbouring flakes. In contrast, the AuCa NCs-pre device does not present any obvious linking bridges. As a result, the Au film-pre device only shows wrinkles with larger flakes without microcracks.

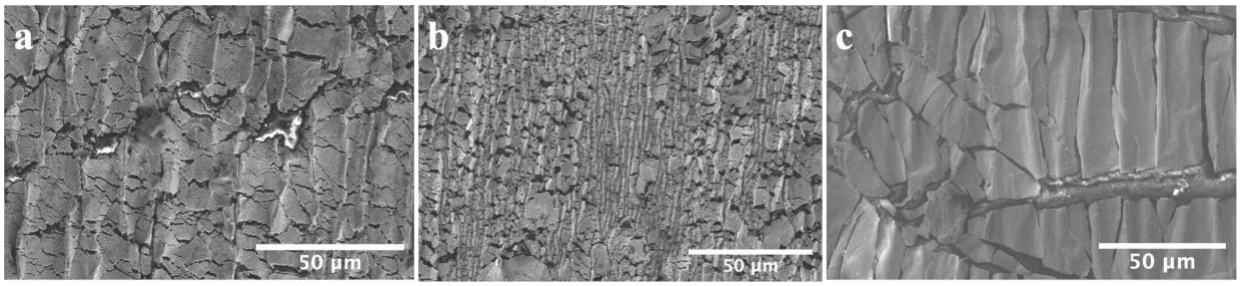

Figure 3.9 FESEM images of a) AuPt NWs-pre device, b) AuCa NCs-pre device, and c) Au film-pre device.

The current response of the three devices with continuously applied strain presents different conduction modes. Notably, the AuPt NWs-pre device remains conductive with currents in µA range up to 325% tensile strain. The relative resistance change over strain has been exhibited in Figure 3.10. The strain shows an exponential relationship with relative resistance change. The calculated GF is 1.4 in the range of 0-255% strain, while GF is 4.7 in the range of 255-325%. The FESEM images in Figure 3.11 present the AuPt NWs-pre device at various strains. The significantly smaller gauge factor of the AuPt NWs-pre device compared with the AuPt NWs devices is caused by a higher density of interconnections. These interconnections are formed during the preparation process from the wrinkles, as seen in high magnification FESEM images in Figure 3.11 b, d, f, and h. Meanwhile, after releasing the pre-applied strain, the micro flakes fold at the edges and also overlap. Once the tensile strain is applied on the device, the flakes can still maintain connections with each other with a larger interior angle, as shown in the scheme (in Figure 3.11 i).

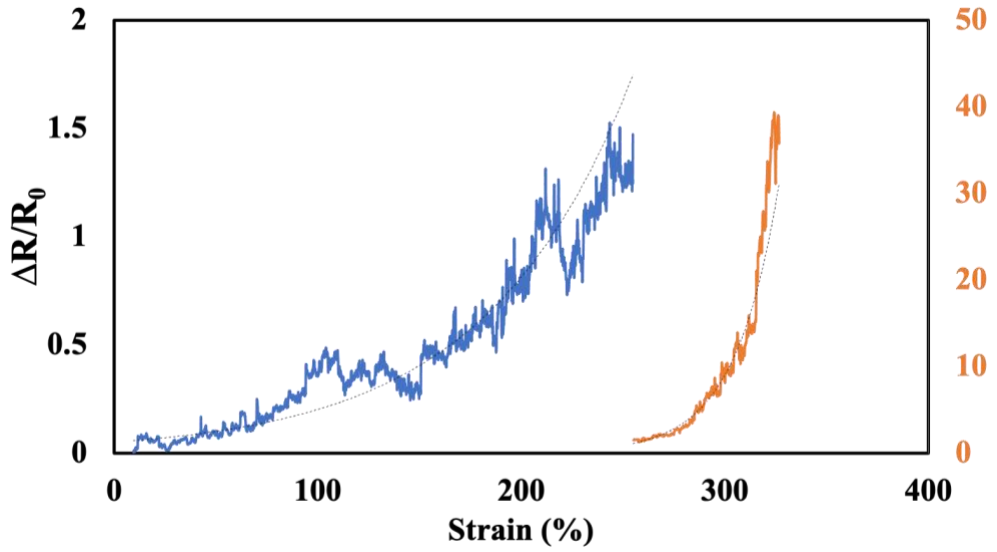

Figure 3.10 Relative resistance change as a function of the strain of AuPt NWs-pre device. Two exponential curves (in dashed lines) are used to fit the experiment results. GF at 0-255% strain is 1.4 (in blue line) and at 255-325% strain is 4.7 (in orange line by using secondary Y-axis).

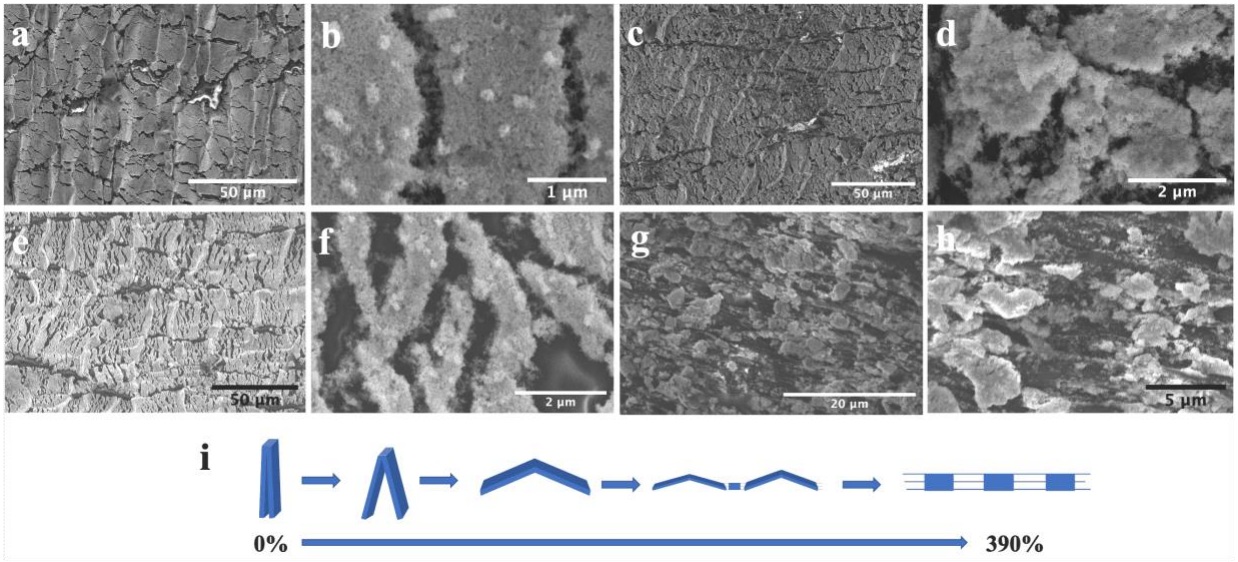

Figure 3.11 The low magnification FESEM images of AuPt NWs-pre device at a) 0% strain, c) 100% strain, e) 255% strain and g) 390% strain and b), d), f) and h) are the respective high magnification FESEM images; i) the scheme of the change of micro flakes under application of strain.

However, the AuCa NCs-pre device presents three different stages. In the first stage as seen in Figure 3.13, the current response increases with applied strain up to 20%, with GF=0.14. In the

second stage, which is from 20 to 53% strain, the GF is ~17 and the current response decreases with the strain. Finally, at higher strains (up to 59%), the GF is 50. The possible reason of this behavior could be as the flakes near wrinkles are first folded, so the stretching process could lead to the flakes sliding to increase the contact areas under 20% strain, as shown in Figure 3.12 a-d. In contrast, at higher applied strain (up to 65 %) on the device, the gaps between the neighboring flakes increase from 150 nm to into micron range, which leads to loss of the conductivity. As a result, Au film-pre can only endure 55.6% strain. All the pre-stretched devices can endure higher strain compared to the devices without stretching.

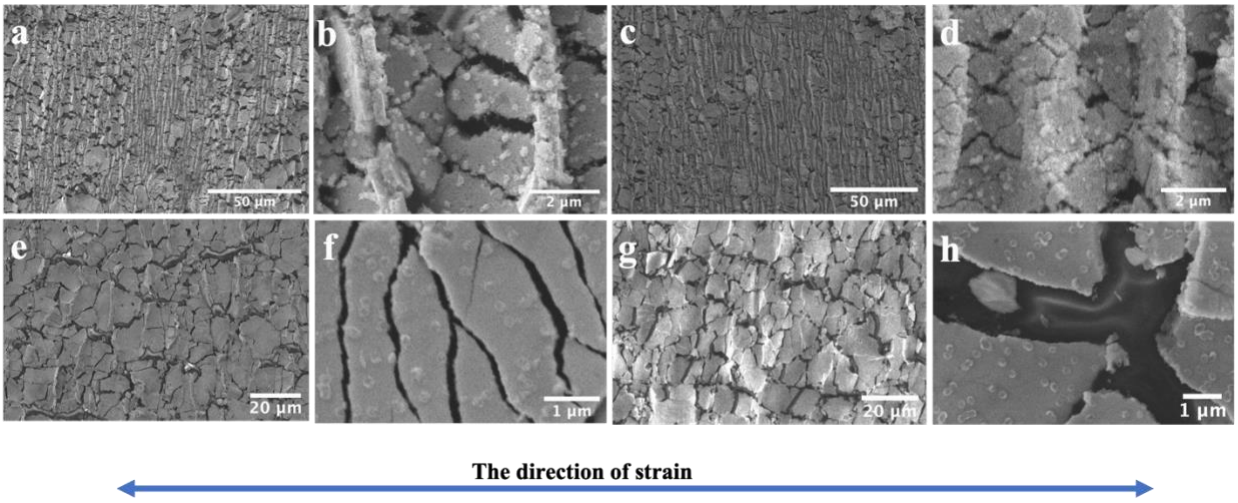

Figure 3.12 The low magnification FESEM images of AuCa NCs-pre device at a) 0% strain, c) 20% strain, e) 45% strain and g) 65% strain and b), d), f) and h) are the respective high magnification FESEM images, respectively.

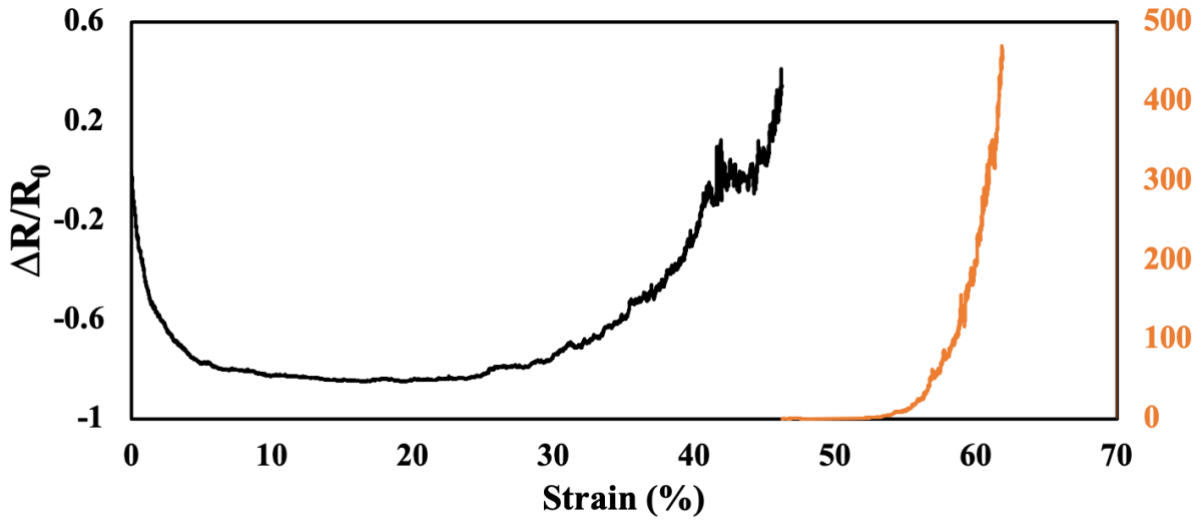

Figure 3.13 Relative resistance change as a function of the strain of AuCa NCs-pre device. GF is separated into three stages: at low strain (0-20% strain) is 0.14, at 20-53% strain is 17 and at high strain (57-65% strain) is 50 (in orange line by using secondary Y-axis).

In Figure 3.14, the electrical stability of the AuPt NWs-pre device is demonstrated by a real-time recording of the current response with repeated cyclic strain at 50%, 75%, 100%, 133%, and 166% over thousands of cycles, respectively. Overall, the device presents long-term reliability, and the output signals exhibit a reproducible and stable response. Additionally, there are no obvious changes in the morphology of the cracks and flakes even after thousands of cycles (in Figure 3.15). During the long-term cycling test, the small drift could be due to transient change, rearrangement of flakes, and slow redistribution of the strain on the polymer matrix.[108,190,114] This confirms the AuPt NWs-pre device possesses excellent consistency and durability during the repeated cycles. It also proves a strong adhesive force between polymer matrix and AuPt NWs, as no peeling of devices is observed.[116] Table 3.2 exhibits the relative resistance change under various applied strains.

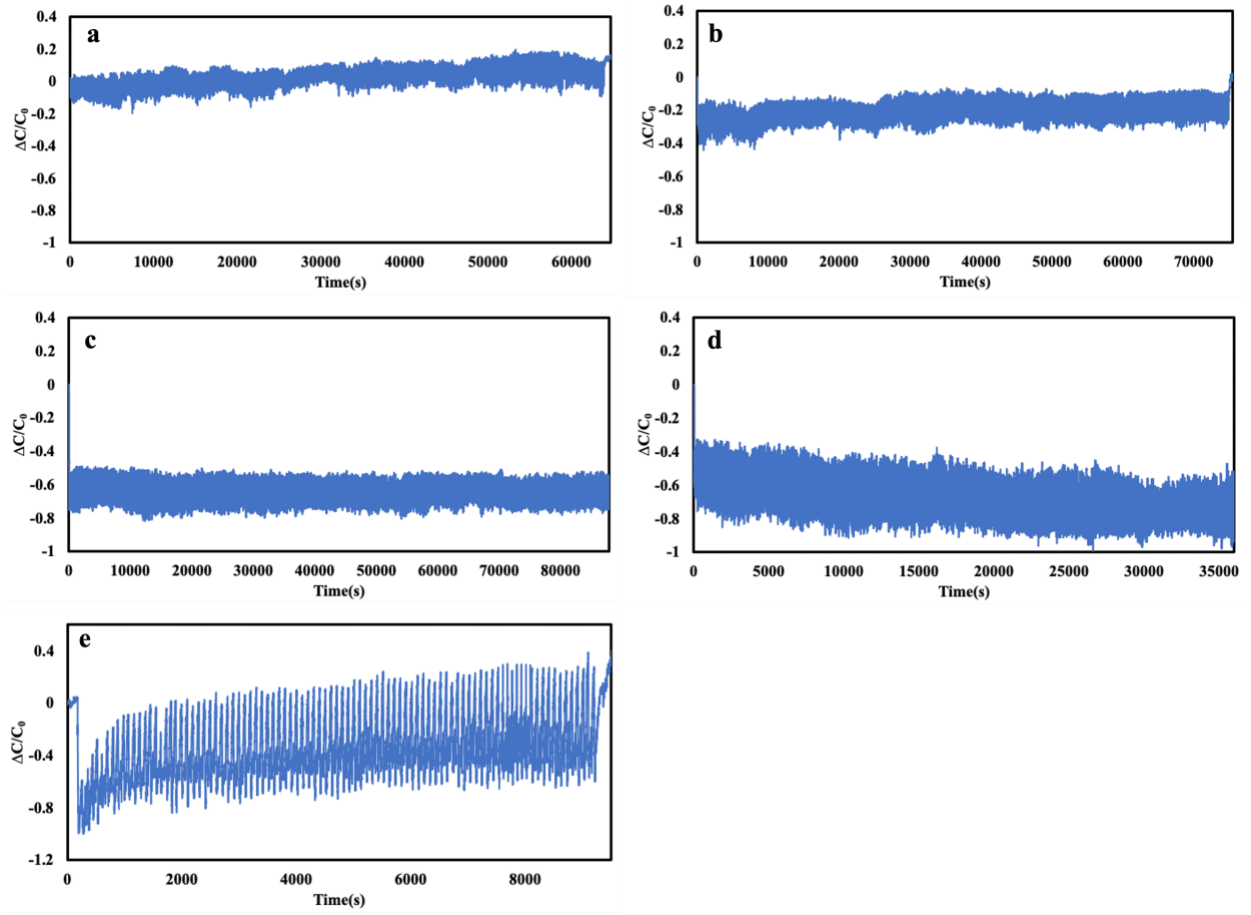

Figure 3.14 Durability test of AuPt NWs-pre strain sensor a) 50% strain under 2000 cycles, b) 75% strain under 2000 cycles, c) 100% strain under 2000 cycles, d) 133% strain under 1000 cycles and e) 166% strain under 200 cycles.

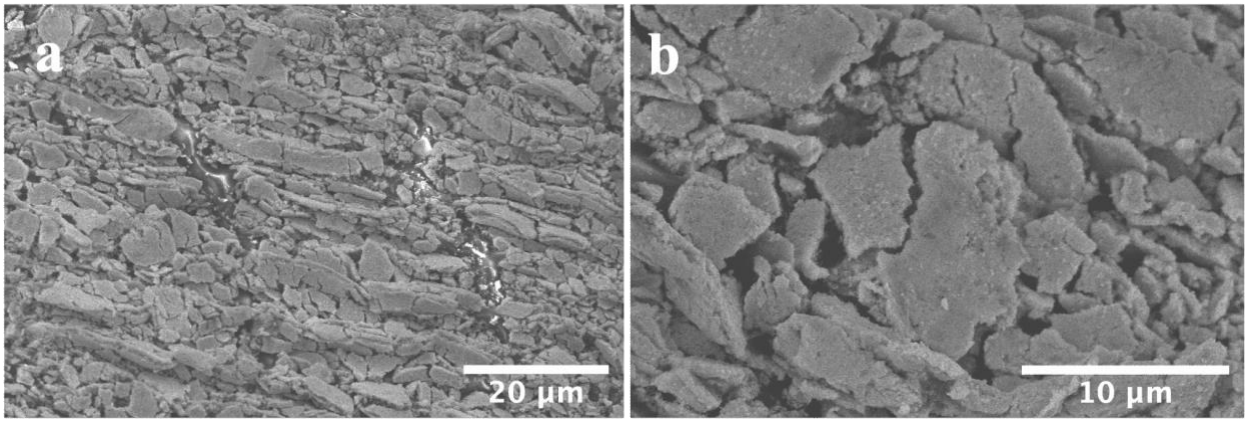

Figure 3.15 FESEM images of AuPt NWs-pre device a) before and b) after releasing 166% strain.

Table 3.2 Relevant conductivity change under tensile strain and repeated cycles.

	Strain i%	I_i/I_0	Repeated Cycles	$I_{i\text{-cycles}}/I_{beg}$
AuPt NWs-pre device	50	1.057	2000	1.207
	83	0.957	2000	1.018
	100	0.847	2000	1.219
	133	0.856	1000	0.878
	166	0.765	200	0.721
	390	0.000	5	0.330
AuCa NCs-pre device	6.25	4.931	200	1.426
	18.75	6.471	200	0.807
	37.5	1.916	200	1.175
	50	0.551	200	1.260
	62.5	0.002	200	0.957
	100	0.000	200	1.192
	175	0.000	200	1.042
Au film-pre device	25	0.999		
	55.6	0.000	1	0.000

I_{beg} is the initial conductivity at 0% strain before each repeated cycle.

The detailed information at the 1st, 50th, and 100th cycles is presented in Figure 3.16 for stretching to 167 % strain. This particular strain is presented as the AuPt NWs-pre device starts to suffer the loss of performance at this threshold. In the first cycle of stretching from 0 to 167% tensile strain, the current response of the AuPt NWs-pre device decreased along with the increasing tensile strain. When the device is kept at 167% strain, the conductivity gradually increases due to the slow reformation of the interconnections. On releasing the strain, the conductivity recovers.[116] The resistance under 167% tensile strain is 1.4 times higher than the initial resistance. Furthermore, after removing the strain, the conductivity loss is ~60%. This implies that the flakes rearrange, and the connections are partially restored during this stretching/releasing process. However, the device does not fully recover after such high applied strains.

The profiles are significantly different when comparing the 50th and 100th cycles to the 1st cycle, as shown in Figure 3.16. As for the 50th and 100th cycles' profiles, the conductivity decreases with increased tensile stress. During release of strain the current response first decreases. Once the strain reaches ~75%, the conductivity starts to increase. When the strain is completely removed, after 30 s, the conductivity reaches its initial state. This behavior may be caused by the substrate which needs a much longer time to release the applied strain. It also demonstrates that the repeated long-term cyclic test makes the device and the interconnections between the flakes more stable. Therefore, after the stretching process, the device presents higher conductivity. Thus, the cyclic process is a manner of conditioning the device to reach a stable configuration. As a result, the device presents high stability and durability under thousands of stretching/releasing cycles.

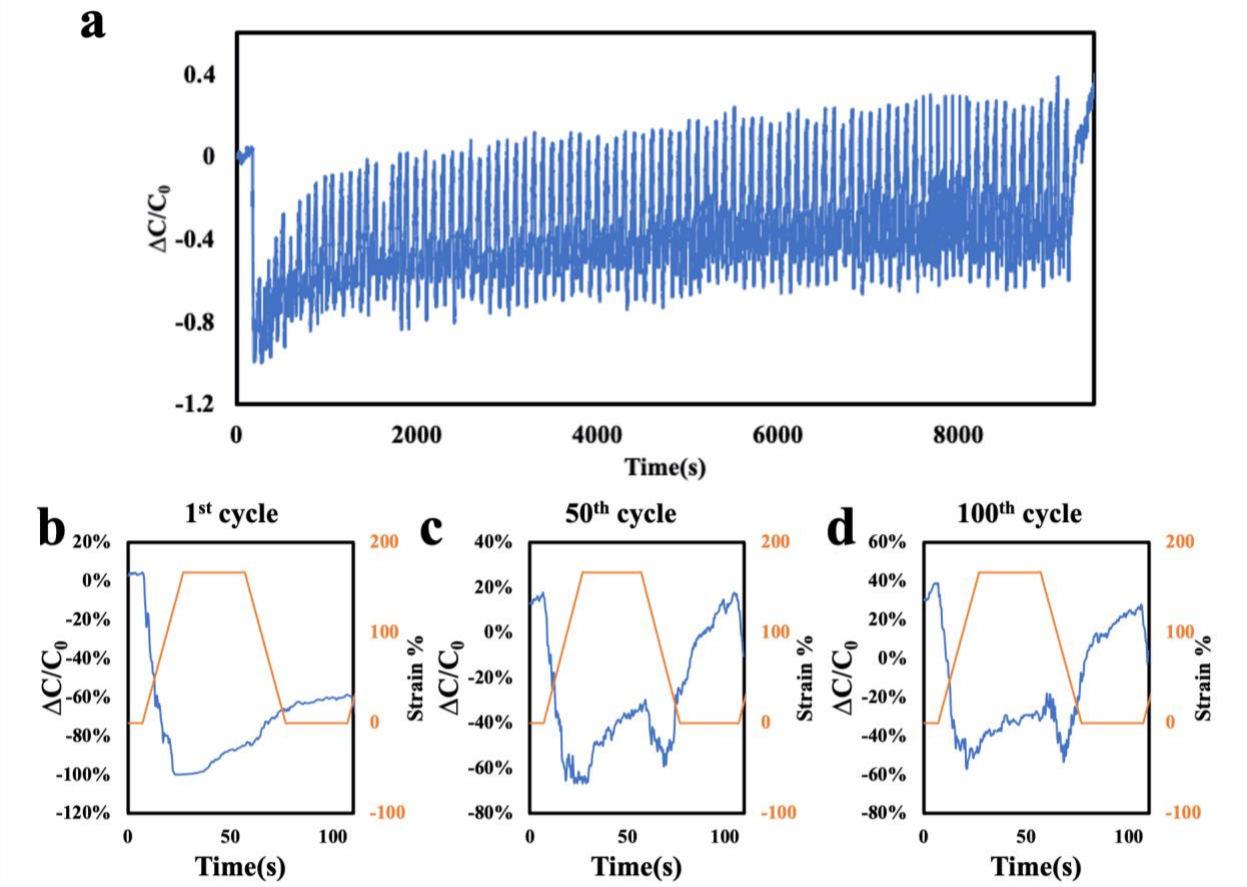

Figure 3.16 Electromechanical response of strain sensor based on AuPt NWs-pre device, which shows the details about the $\Delta C/C_0$ values on gradual release of strain from 0-166%.

The AuCa NCs-pre device presents quite different performance during strain cycling. From the cyclic plot, at 12.5% strain with higher stretch speed, 0.25 mm/s, the current response is not stable due to the slow response from the polymer matrix (tape). Therefore, a lower speed of 0.01 mm/s at 12.5% tensile strain is investigated. The consistent current response during the cyclic process is demonstrated in Figure 3.17 a. Moreover, the detailed profile of the 1^{st}, 50^{th}, and 100^{th} cycles is illustrated in Figure 3.17 b-d. Same with AuPt NWs pre-stretched device, the first cycle presents differences compared to 50^{th} and 100^{th} cycles. As can be seen, the conductivity decreases with the increase of strain. After reaching the maximum of 12.5% strain, the decrease in conductivity is 70%. When the strain is kept at 12.5%, the conductivity rises back by ~5% and then continuously increases as the cycling decreases the strain. The device loses ~30% conductivity after the first cycle. This could be due to a loss in interconnections between the flakes. However, the 50^{th} and 100^{th} cyclic plot presents similar profiles. For these two, the conductivity still shows a decrease with the increase in strain and an increase with the decrease in strain, but when the strain is kept constant at 12.5%, no obvious rise can be observed. Furthermore, they can recover to their initial state on complete removal of the applied strain. Therefore, in the AuCa NWs- pre device, there is also the initial rearrangement of the NWs during cycling. The device reaches a final equilibrium state that leads to a stable response on repeated strain cycling.

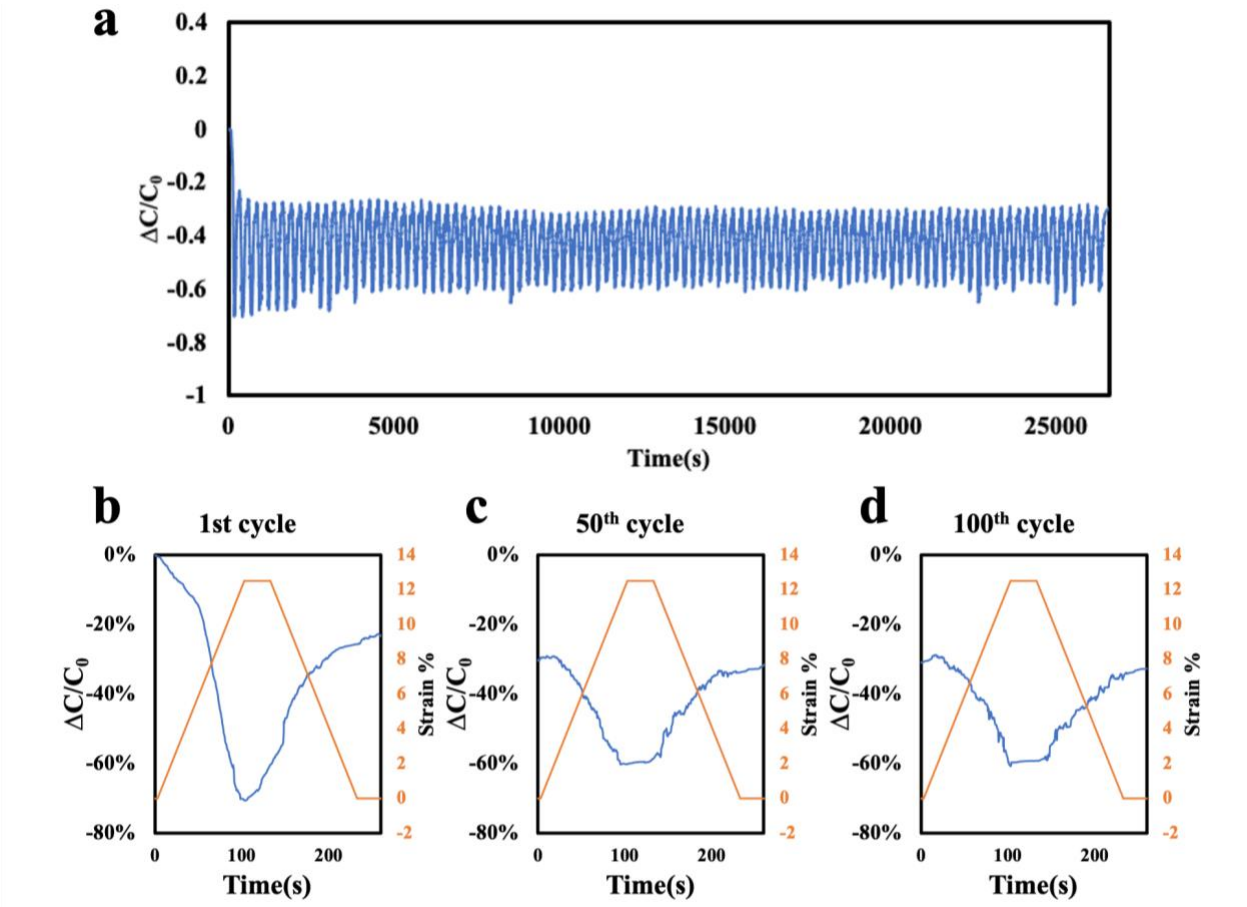

Figure 3.17 a) Durability test of AuCa NCs-pre sensor at 12.5% strain under 100 cycles; Electromechanical response of strain sensor based on AuCa NCs-pre device which shows the details about the $\Delta C/C_0$ values on gradual release of strain from 0-12.5% for b) 1st, c) 50th and d) 100th cycle. Each state was held for 10 s.

Additionally, flexible, large-area and stable perovskite photodetectors have drawn increasing research attention for next-generation wearable and portable optoelectronic devices. Therefore, we integrated the AuPt NWs as electrodes with perovskite to fabricate two kinds of photodetectors. The first photodetector is highly bendable and flexible. The devices are fabricated based on a polyamide filter substrate (with 0.2 µm pore size), as shown in Figure 3.18. The polystyrene (PS) incorporated $CH_3NH_3PbI_3$ ($MAPbI_3$) photodetector can maintain 85% of its original photocurrent value after 10,000 bending cycles at a bending angle of 120°.[119] In contrast, the plain $MAPbI_3$ device's photocurrent dropped to 50% of its initial value after the bending.

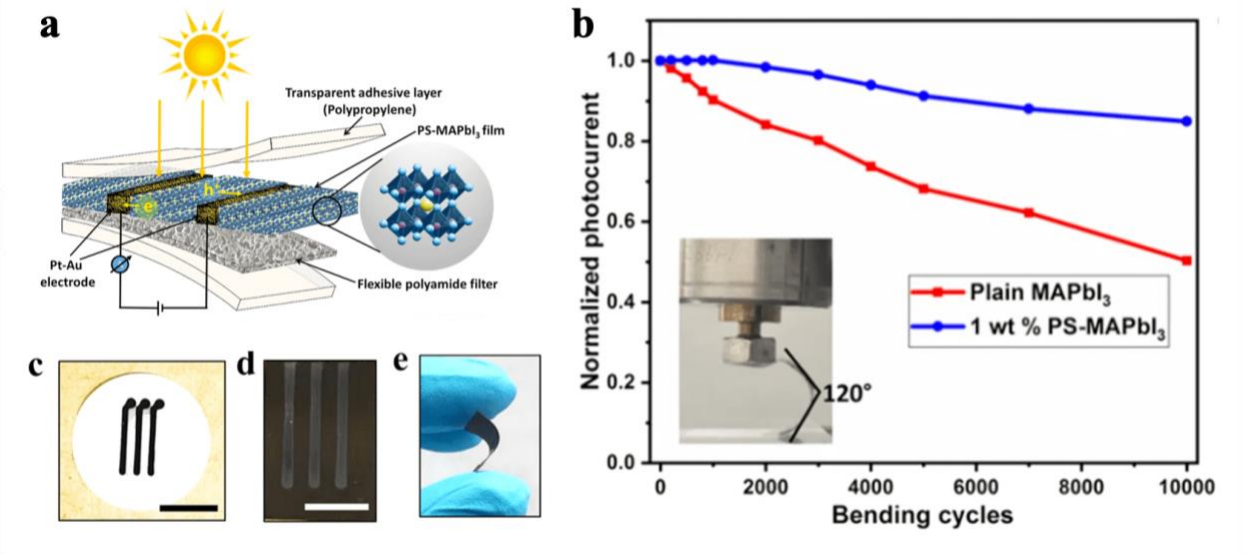

Figure 3.18 a) Schematic diagram showing the current generation by light irradiation from the flexible PS-$MAPbI_3$ photodetector; b) Normalized photocurrent of the flexible devices after bending cycles at a bending angle of 120° showing the mechanical stability and durability of 1 wt % PS-$MAPbI_3$ device even after 10,000 bending cycles; Photograph of the c) Pt-Au electrodes on the flexible substrate with the 1 cm scale bar, d) final PS-$MAPbI_3$ device with a 4 mm scale bar, and e) bending (or flexibility) of the device.

The second device is a highly stretchable photodetector made of the AuPt electrode and perovskite on a pre-stretched substrate. The schematic is presented in Figure 3.19. The samples are first depositing on a Polyester (PET) film and then attached to a pre-stretched substrate. The AuPt electrodes can endure over 10,000 stretching/releasing cycles under 50% strain and maintain the resistance of less than 1 kOhm. Meanwhile, the device can still show photoresponse after over 10,000 stretching cycles.

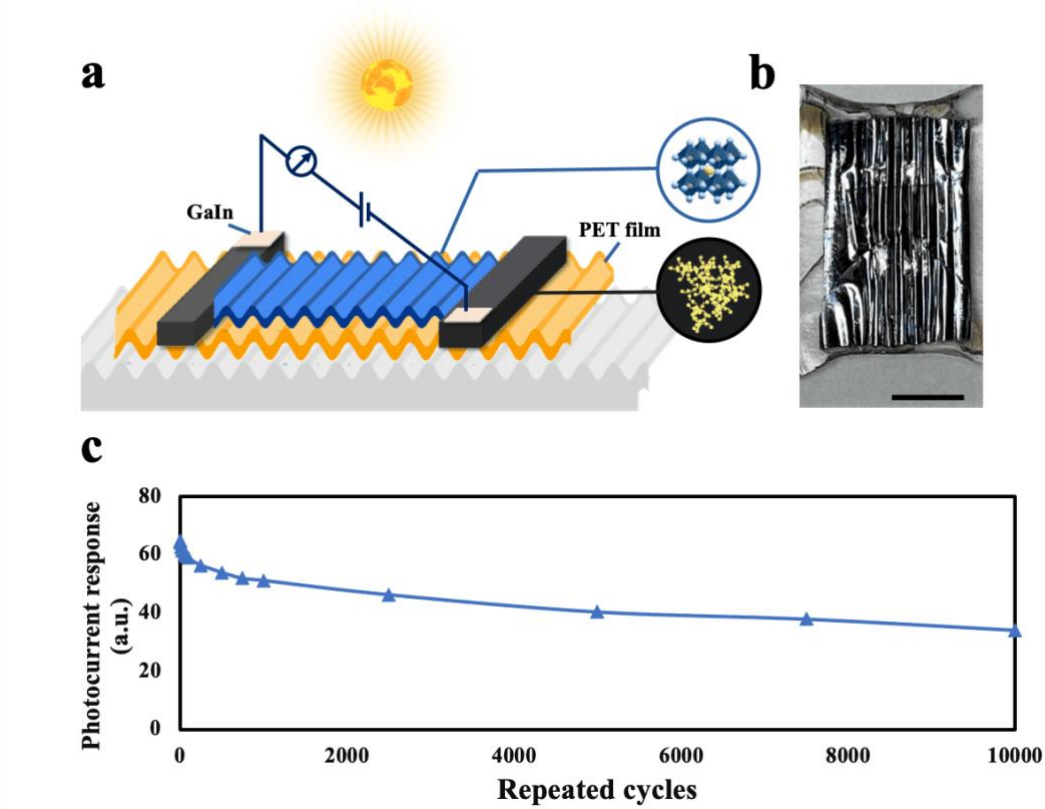

Figure 3.19 a) The schematic image of a highly stretchable photodetector; b) The photo image of the device. The scale bar is 5 mm; c) The photocurrent response of stretchable device for repeat cycles at 50% strain.

4 Conclusion

In this work, we have developed an easy filtration-transfer production method, which can be scaled up to prepare stretchable devices. Two kinds of 1D nanomaterials are investigated. The samples are first filtrated on a polycarbonate filter and then transferred onto a flexible substrate (polymer matrix). Devices are made with both pre-stretched substrate and also without any pre-stretch. The conductive behavior of these devices is studied on being subjected to tensile strains. The transfer process introduces numerous interconnected micro-cracks, which facilitate current pathways in the devices even under strain. Specifically, the AuPt NWs devices have extended continuous nanowires as interconnections between adjacent flakes. In contrast, the AuCa NCs device only has a few interconnections as the nanochains do not have a continuous structure but rather have 1 to 2 nm gaps between adjacent nanoparticles. This allows the AuPt NWs devices to endure higher tensile strains than AuCa NWs devices. The AuPt NWs devices show high reproducible and stable response on being subjected to 1000's stretching/releasing strain cycles, which confirms their ability to act as a stretchable electrode for devices.

Part B Self-Assembled Au NWs doped with various elements as electrocatalysts

Chapter 4 Au-Pt-Ni-Fe-PBA nanocomposites as water splitting catalyst

1 Introduction

Bifunctional catalyst that can be effective for both hydrogen evolution reaction (HER) and oxygen evolution reaction (OER) in alkaline medium will simplify the development of electrolysers for the hydrogen economy.[120,121,122] A key challenge lies in developing effective catalysts for HER and OER and then combining them at nanoscale to achieve effective bifunctionality. HER in alkaline medium is specially challenging and has a large overpotential and high Tafel slope. A common observation is that the inclusion of Ni based oxides and hydroxide compounds improves both HER and OER.[123,124,125,126] While in OER it is proposed to be due to the direct involvement of the hydroxide group in the reaction.[127] In HER it has been proposed to, ease the rearrangement of the water layer for the transport of OH^- (a reaction by product)[128] and also lower the barrier for adsorption of the water molecule for cleavage of the O-H bond (in H_2O).[129,130] Recent researches have also shown that use of Pt-Ni combination leads to lower overpotential for HER in alkaline medium along with lowering of the Tafel slope.[124,131,132,133] They were reported that surface segregation between Pt and Ni improves the HER performance,[134] similarly Nitrogen doping of Pt-Ni nanowire structures also improves the HER performance.[135] Different polymorphs of NiOOH also exhibit dissimilar electrochemical characteristics.[132]

We show here a simple ion-based, room temperature, self-assembly method to develop a bifunctional HER-OER catalyst. It combines a Pt-Ni nanowire network (HER active, 5-7 nm in diameter) with nanoscale regions of Ni-Fe-Prussian blue analog (Ni-Fe-PBA, OER active). The combined composite catalyst shows excellent properties towards both HER and OER due to synergistic effects and effective transport of reaction species between the distinct nanoscale regions. The observed HER overpotential for the best catalyst (in alkaline medium) is 37.9 mV and 49.8 mV at current densities of 10 mA cm^{-2} and 30 mA cm^{-2}, respectively. Further the Tafel slope (for HER) is just 13.7 mV dec^{-1}. After 27 hours of continuous operation the HER

overpotential increases marginally to 38 mV (at 10 mA cm^{-2}). A synergistic effect is observed for OER where the presence of the Pt-Ni regions improves the performance of the Ni-Fe-PBA regions. For OER the composite catalyst shows an overpotential of 256 mV at current density of 10 mA cm^{-2} and the Tafel slope is 32 mV dec^{-1}. After 27 hrs. of continuous operation the Tafel slope increases to 44 mV dec^{-1} and the over potential increases to 276 mV. These performance values are among the best reported when compared to HER specific and OER specific catalyst and are achieved in a single composite structure.[55,133,136,137,138] The excellent catalytic performance is attributed to the close interaction between Pt, Ni and the Ni-Fe-PBA nanoscale domains and the nanowire like morphology also ensures effective electron transport in the catalyst structure. The high concentration of defects and Ni^{3+} states in the catalyst due to the effect of PBA leads to more effective adsorption of H_2O molecules, which results in the low Tafel slopes for HER.[55] Further the catalyst effectively desorbs OH^- species which is required for progression of HER (after cleavage of the O-H bond in H_2O).[139,140,141]

2 Experimental section

2.1 Material fabrication

2.1.1 Synthesis of the Au-Ni, Au-Pt, Au-Ni-R, and Au-Pt-R composite

80 μL of 4 mg/mL $NiCl_2$ and 135 μL of 4.5 mg/mL $PtCl_4$ were added into 1 mL 10 nm Au NPs (purchased from BBI company), respectively, and then left on the shaker. Once the solution color changed to dark blue, the Au-Ni and Au-Pt, with a chain like structure, were obtained. Then 75 μL of 4 mg/mL $NaBH_4$ solution was added drop by drop to reduce the composite (named Au-Ni-R and AuPt-R).

2.1.2 Synthesis of the Au-Pt-Ni_{beg} and Au-Pt-Ni_{end} composite

As for the preparation of Au-Pt-Ni_{beg}, 195 μL of 4.5 mg/mL $PtCl_4$ and 40 μL of 4 mg/mL $NiCl_2$ were mixed well firstly, and then the mixed solution was added into 2 mL 10 nm Au NPs and then left on the shaker. After the solution color turned to dark blue, 150 μL of 4 mg/mL $NaBH_4$ solution was added drop by drop into the solution.

As for the Au-Pt-Ni_{end} sample, 0.5 mL Au-Ni was mixed with 1.5 mL of Au-Pt, and then 150 μL of 4 mg/mL $NaBH_4$ solution was added drop by drop to reduce the composites.

2.1.3 Synthesis of the Au-Pt-Ni_{beg}-Fe-PBA and Au-Pt-Ni_{end}-Fe-PBA composite

2 mL Au-Pt-Ni_{beg}-Fe or Au-Pt-Ni_{end} sample was first dissolved into 5 mL H_2O, and then 3 mL of 0.5 mg/mL $K_3Fe(CN)_6$ (dissolved in 0.5:0.5 v/v H_2O: Ethanol) were added. The mix solutions are left on the shaker at 500 rpm for 24 h to react. The final composites were washed by H_2O and Ethanol and dried at 60 °C. Finally, the Au-Pt-Ni_{beg}-Fe-PBA or Au-Pt-Ni_{end}-Fe-PBA powder was obtained.

2.1.4 Preparation of electrode materials

The glassy carbon electrode, GCE, with a diameter of 3 mm, was polished using 0.05 µm alumina suspension on a polishing cloth. Commercial platinum on carbon (Pt/C, 20 wt% Pt) and RuO_2 samples were utilized as benchmark catalysts to compare the electrocatalytic performances.

5.0 mg powder was dispersed into 1 mL of 0.5:0.5 v/v H_2O: Ethanol along with 5 µL Nafion solution to prepare the ink. The mixture was sonicated for 30 min. Then 3 µL of prepared ink was drop-casted on the glassy carbon electrode.

2.2 Characterization section

Zeiss Ultraplus Field-emission Scanning Electron Microscopy (FESEM) was used to measure the morphology of samples and the deposition. Transmission electron microscopy (TEM) images were obtained with an LEO 912ab energy filtered transmission electron microscope (EFTEM). UV-Visible absorption spectra of samples were detected by Perkin Elmer Lambda 750 spectrophotometer. The powder X-ray diffraction (XRD) pattern was measured by the PANalytical Empyrean diffractometer with Cu Kα radiation ($\lambda = 1.54$ Å). X-ray Photoelectron Spectra, XPS, characterization was performed on VGS ESCALab 250. Raman measurements were performed using a Horiba HR800 spectrometer in the backscattering configuration. Fourier-transform infrared, FT-IR, spectra were obtained by using Bruker Tensor 27.

2.3 Electrochemical measurement

All electrochemical measurements were performed on an Ivium CompactStat Electrochemical Analyser at room temperature. The standard three-electrode system was used where the composites are the working electrode, Pt wire as a counter electrode, and saturated calomel electrode as a reference electrode in a 0.1 M aqueous KOH electrolyte. Before HER/OER measurements, the electrodes were electrochemically pretreated with continuous cyclic voltammetry (CV) from 0.1 V to -0.09 V (.vs reversible hydrogen electrode, RHE)/1.2 V to 1.6 V (vs. RHE) in 0.1 M KOH until a stable response was achieved. This process helped to activate the Ni-Fe-PBA to $Ni(OH)_2$ or NiOOH. The CV curves were recorded with a scan rate of 5 mV/s. HER and OER polarization curves were obtained by linear sweep voltammetry (LSV) at a scan rate of 5 mV/s. Polarization curves were corrected for an ohmic drop (iR) tested by electrochemical impedance spectroscopy

(EIS). EIS was measured by AC impedance spectroscopy within the frequency range from 0.1 to 30 kHz in 0.1 M KOH. The long-term durability test was conducted without iR-correction at the potential of 1.46 V.

All potentials were converted to RHE, using the equation:

$$E(RHE) = E(SCE)+0.241 +0.059\times pH,$$

where E(RHE) is the potential referred to as reversible hydrogen electrode, E(SCE) is the tested potential against the reference electrode.

Tafel slope was calculated by the following equation:

$$\eta = b\ log|j| + a,$$

where η is the overpotential, j is the current density, b is the Tafel slope, and a is the intercept related to the current exchange density.

3 Results and Discussion

The formation of Pt-Ni nanowire network is based on self-assembly of citrate capped Au nanoparticles (in an aqueous medium) with Pt^{4+} and Ni^{2+} cations. A controlled addition of the cations leads to formation of long chains of Au nanoparticles due to coupling between the metal cations and the nanoparticles. Following that the reduction of the cations leads to the formation of a continuous nanowire network (schematic image, Figure 4.1). The nanowire networks can be made in two distinct configurations: one, where the two cations are added simultaneously to the Au nanoparticle solution and reduced after the self-assembly of the chains. This leads to the formation of a nanowire network with highly homogenous Pt-Ni domains (Figure 1a, Au-Pt-Ni_{beg}). In the second case, the cations are separately mixed with the Au nanoparticles and allowed to undergo self-assembly into chains. Following this, the self-assembled chains are mixed and then reduced to form nanowire network with segregated domains (~2-5 nm) of Pt and Ni (Figure 1b, Au-Pt-Ni_{end}). In both the cases samples can be made with different ratios of Pt:Ni.

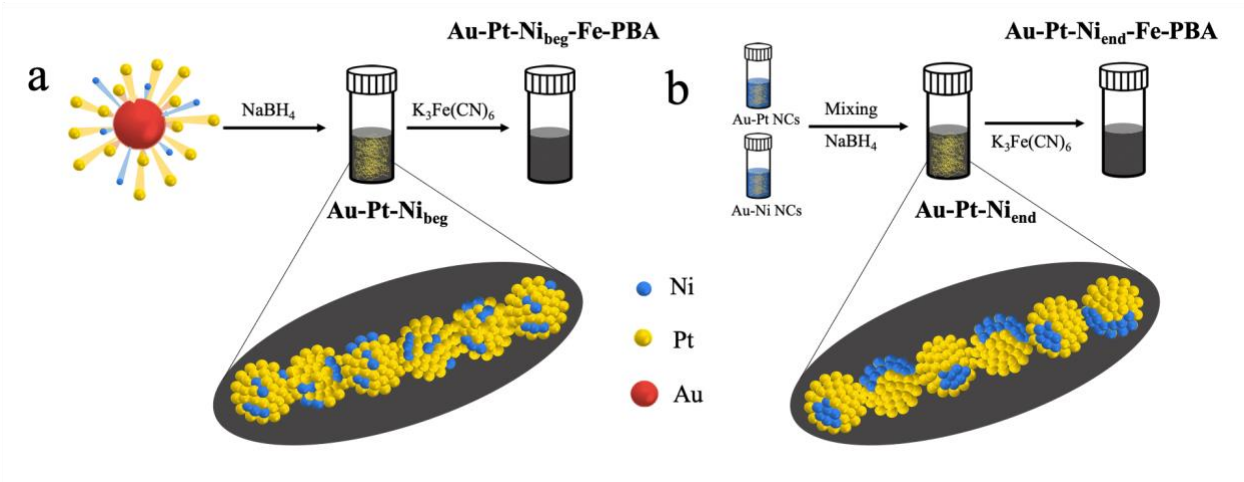

Figure 4.1 The schematic image showing the fabrication of the material in two distinct configurations. (a) Au-Pt-Ni_{beg} (or Au-Pt-Ni_{beg}-Fe-PBA) with homogenous distribution of the domains. (b) Au-Pt-Ni_{end} (or Au-Pt-Ni_{end}-Fe-PBA) with segregated domains.

The self-assembly of the Au nanoparticles into chains due to the addition of the metal cations leads to the red shift in their surface plasmon resonance from 525 nm (for the nanoparticles) to ~ 620 nm (for the chains) (Figure 4.2 a). In transmission electron microscopy (TEM) image, the chain

like structures are clearly visible with a spacing of 1-2 nm between adjacent nanoparticles (Figure 4.2 b).

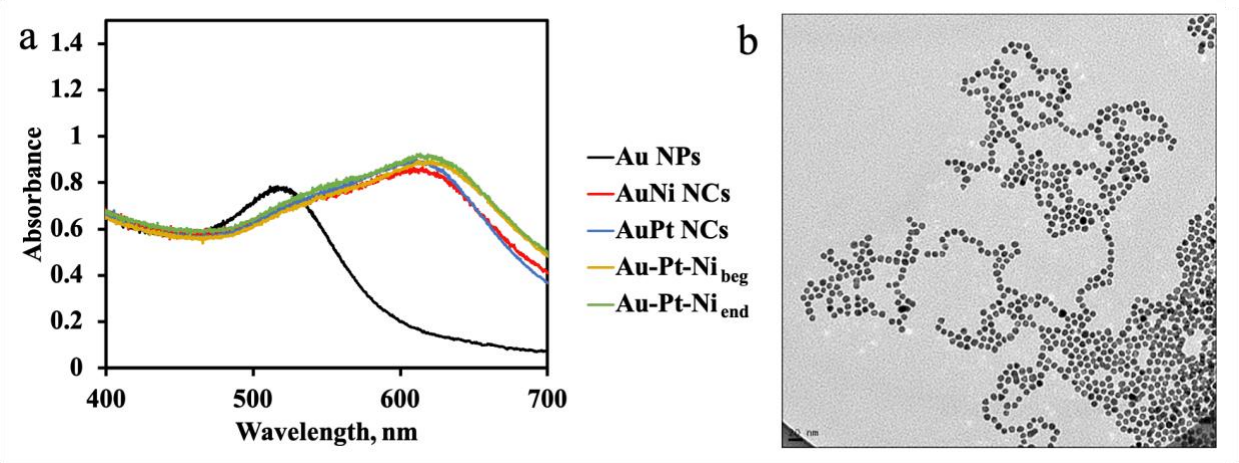

Figure 4.2 a) UV-Vis absorbance spectra of Au NPs and self-assembled Au NCs; b) a typical TEM image of self-assembled gold chains with metal cations shows a gap of 1-2 nm between neighbouring nanoparticles. The scale bar is 20 nm.

The samples are made with the Pt:Ni ratio of 3:1 (precursor ratio) for optimized catalytic performance. On reduction, formation of Pt and Ni occurs on the Au nanoparticle chains. This is due to preferential nucleation caused by the higher concentration of the respective ions in the electrical double layer around the nanoparticles.[72] As a result the formation of a continuous nanowire network can be seen in the TEM images of Figure 4.3 a (and its inset). The Au-Pt-Ni$_{beg}$ network shows a homogenous distribution of Pt and Ni, as seen in the Electron energy loss spectroscopy (EELS) mapping (Figure 4.3 b). Further we observe the formation of the Pt-Ni over the Au nanoparticles. In case of Au-Pt-Ni$_{end}$, we observe a more distinct nanoscale distribution of Pt and Ni as seen in the EELS maps (Figure 4.3 c). The X-ray diffraction (XRD) results for Au, Pt, Au-Pt, Au-Pt-Ni$_{beg}$ and Au-Pt-Ni$_{end}$ are presented in Figure 4.3 d. Due to the smaller atomic radius of the Ni, the Pt diffraction peaks are shifted to larger angles in the Au-Pt-Ni$_{beg}$ and Au-Pt-Ni$_{end}$ samples. We observe that the shift is greater in the Au-Pt-Ni$_{beg}$ sample due to its more homogenous distribution of Pt and Ni, than Au-Pt-Ni$_{end}$. For example, the Pt (111) peak in Au-Pt is observed at 39.90^{o} and this is shifted to 40.25^{o} in the Au-Pt-Ni$_{end}$ and to 40.62^{o} in the Au-Pt-Ni$_{beg}$. Whereas no significant changes are observed in the Au peak (111). From Vegard's law (for approximate estimation) the ratio of Pt:Ni is calculated as 4:1 for the Au-Pt-Ni$_{beg}$ sample.[134,142]

The overall ratio of Pt:Ni in both the samples from Energy dispersive X-ray analysis (EDAX) is also 4:1. This shows that the Pt and Ni form a relatively homogenous alloy in the Au-Pt-Ni_{beg} sample. For the Au-Pt-Ni_{end} sample, the calculated Pt:Ni ratio from Vegard's law is 11:1, in line with the formation of nanoscale Ni regions distinct from the Pt regions and limited alloying. The distinct nature of the two samples is hence confirmed by TEM and XRD results. The spectra of the binding energy (Ni $2p_{3/2}$) from X-ray photoelectron spectroscopy (XPS) (Figure 4.3 e) further shows the distinctness of the two composites, Au-Pt-Ni_{end} and Au-Pt-Ni_{beg}. Peaks corresponding to Ni^0 (852.4 eV, metallic Ni), Ni^{2+} (855-856.5 eV, NiO and $Ni(OH)_2$) and Ni^{3+} (860-864 eV, NiOOH) are observed.[143,144,145,146,147,148,149,150] However, there are key differences between the two materials, for Au-Pt-Ni_{end} clear peaks in the three Ni states are observed, with the ratio of peak height for Ni^{2+}/Ni being 0.84 and for Ni^{3+}/Ni being 0.43. In case of Au-Pt-Ni_{beg}, clear and distinct peaks are only observed for Ni^o and Ni^{2+} states, with the ratio of Ni^{2+}/Ni being 0.40. This shows that a minimum domain size of Ni is required to form stable Ni^{3+} states. This is critical as Ni^{3+} states are needed for effective catalysis of the HER.[139]

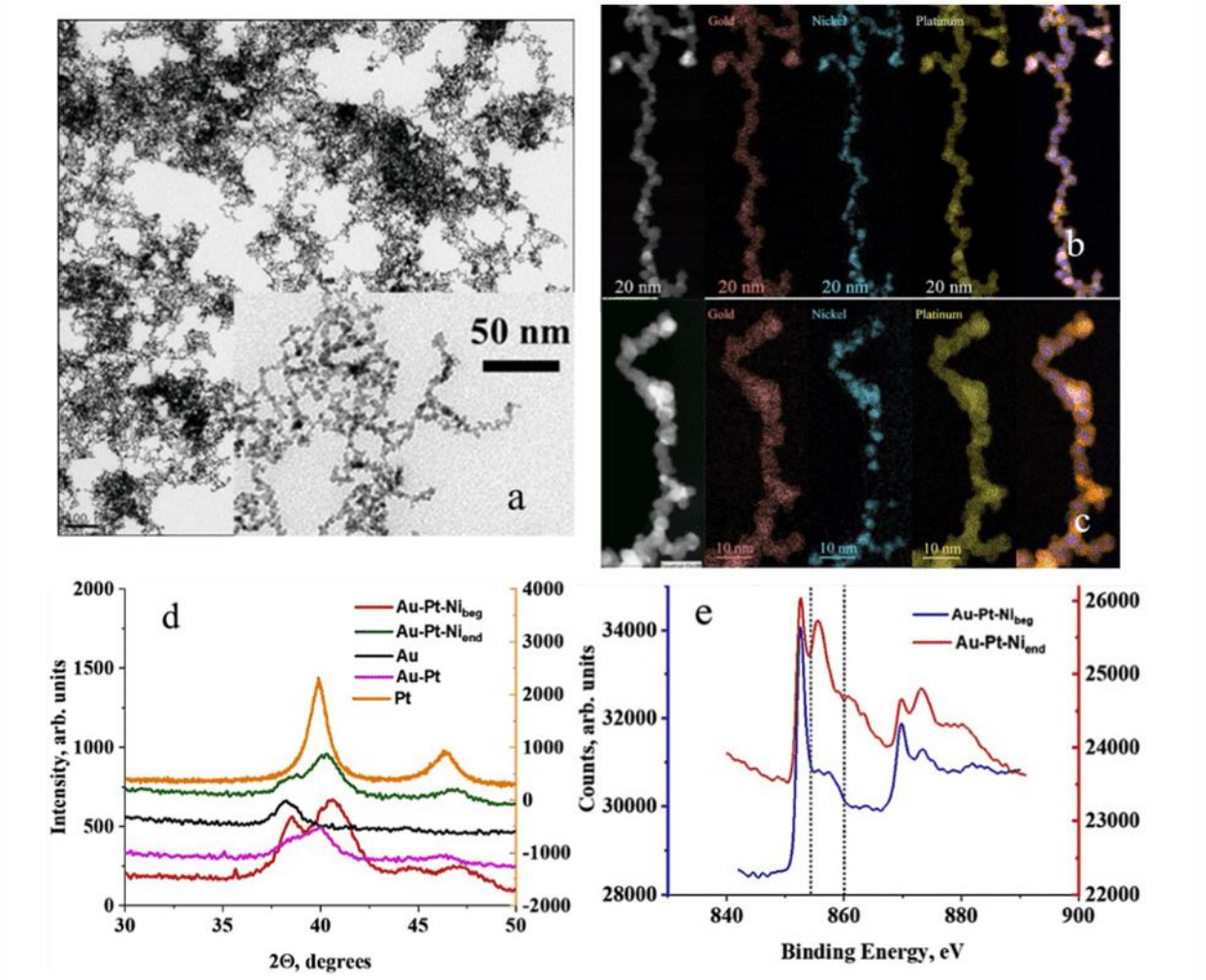

Figure 4.3 a) The TEM image of a continuous nanowires network. The scale bar is 100 nm. The inset image is the high magnification TEM image of the continuous nanowires. EELS mapping of b) Au-Pt-Ni_{beg} and c) Au-Pt-Ni_{end}; d) X-ray diffraction spectra of self-assembled chains after reduction. Pt sample uses second y axis; e) XPS spectra of Ni region for Au-Pt-Ni_{end} and Au-Pt-Ni_{beg} (by using second Y-axis) composites.

Electrochemical cyclic voltammetry (CV) curves for the Au-Pt-Ni materials performed in 0.1 M KOH show the typical peaks for under potential hydrogen adsorption and desorption (H_{upd}) (Figure 4.4 a). The steps for the HER in alkaline medium consist of both adsorption of Hydrogen (the Volmer step, due to splitting of the adsorbed water molecule into H_{ads} and OH^-_{ads}) and its subsequent desorption (Heyrovsky or Tafel step, in molecular form).[151] The equations are as followed:

The Volmer step: $H_2O + M + e^- \rightarrow M\text{-}H_{ad} + OH^-$

The Heyrovsky step: $H_2O + M\text{-}H_{ad} + e^- \rightarrow H_2 + M + OH^-$

The Tafel step: $2M\text{-}H_{ad} \rightarrow H_2 + 2M$

where M denotes catalyst surface here.[152,153,154] Given that both adsorption and desorption of hydrogen is required for HER, therefore for effective catalysis low potential for hydrogen desorption (E^H_{des}) and high potential for hydrogen adsorption (E^H_{ads}) is preferable. The effectiveness of the catalyst for HER can be therefore be ascertained by E^H_{ads} - E^H_{des} (ΔE^H). The E^H_{des} values for Pt/C, Au-Pt, Au-Pt-Ni_{beg}, Au-Pt-Ni_{end} are 0.267 V, 0.251 V and 0.249 V. While the E^H_{ads} values for them are respectively 0.20 V, 0.187 V and 0.223 V. Among the four catalysts we observe that Au-Pt-Ni_{end} has the highest ΔE^H of -0.026 V, while for Pt/C and Au-Pt-Ni_{beg} it is -0.067 V and -0.064 V, respectively. This signifies that Au-Pt-Ni_{end} has the lowest barrier for HER. The other important factor is the rapid desorption of OH^-_{abs} (adsorbed during Volmer step) to maintain the HER activity, as it can poison the active sites on the catalyst. From the hydroxyl desorption region in the Figure 4.4 a (above 0.6 V), we find that Au-Pt-Ni_{end} has the most favorable (highest) positive potential (0.692 V) compared to Au-Pt-Ni_{beg} (0.687 V) and Pt/C (0.658 V).

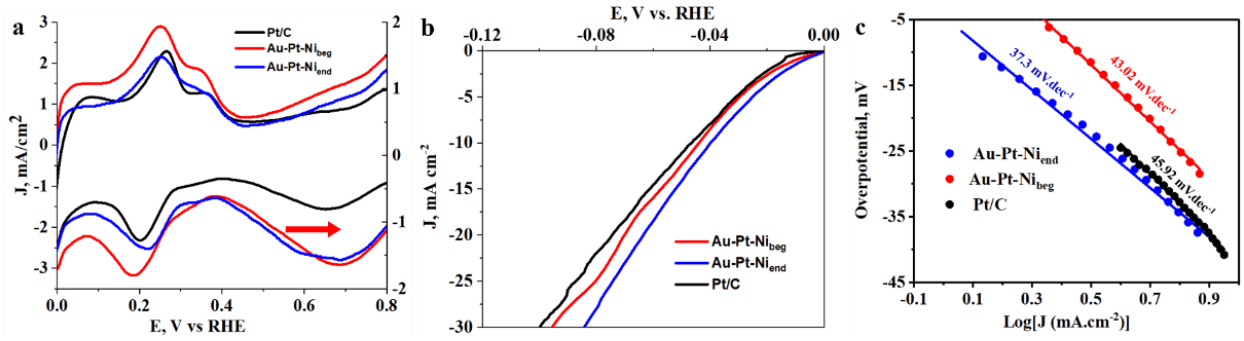

Figure 4.4 a) The cyclic voltammetry (CV) of Au-Pt-Ni_{beg} (in red), commercial Pt/C nanoparticles (in black) and Au-Pt-Ni_{end} (in blue, by using second y axis). All measurements were obtained at 100 mV s^{-1} in N_2 saturated 0.1 M KOH at room temperature. HER performance in KOH solution b) LSV curve of Au-Pt-Ni_{end}, Au-Pt-Ni_{beg} and commercial Pt/C nanoparticles and c) the corresponding Tafel slopes.

The cumulative effect of these factors is confirmed by HER activity as seen in linear sweep voltammetry (LSV) curves of Figure 4.4 b. The HER overpotential at 10 mA cm^{-2} (and 30 mA cm^-

^{2}) is 40.1 mV (84.3 mV) for Au-Pt-Ni_{end} and 44.1 mV (95.4 mV) for Au-Pt-Ni_{beg}, in comparison the corresponding values of Pt/C is 47 mV (100.5 mV). The Tafel slopes (Figure 4.4 c) for Au-Pt-Ni_{end} and Au-Pt-Ni_{beg} are observed to be 37.3 mV dec^{-1} and 43.02 mV dec^{-1}, while for Pt/C it is 45.92 mV dec^{-1}. The close values for Tafel slopes signify a very similar HER mechanism for the three catalysts. The lower Tafel slopes and smaller overpotentials for the composite catalyst compared to Pt/C signify that the presence of Ni does improve the HER performance. The better performance of Au-Pt-Ni_{end} compared to Au-Pt-Ni_{beg} arises from the fundamental difference in their structure both in terms of the size of the Ni domains and its oxidation state, which leads to differences in their ability to desorb H_2 and OH^-.

However, this HER performance in alkaline medium is still lacking compared to typical performance in acidic medium. Based on the Tafel slopes it seems that the Heyrovsky step is the rate limiting step in the Au-Pt-Ni catalysts.[153] We worked with the hypothesis that further enhancement in density of oxyphilic Ni^{3+} sites will be required to improve the HER performance, by inducing faster dissociation of the adsorbed water molecule. At the same time close interfacing between the Ni^{3+} and Pt regions must be maintained for formation of H_2 from H_{ads}. Such a transition is possible given the presence of Ni^0 (metallic Ni) domains in the composite catalysts (as seen from XPS data, Figure 4.3 e) which can be converted to Ni^{3+}. To achieve this by a simple synthesis process, Prussian blue analogues (PBA) are formed by addition of a controlled amount of $K_3Fe(CN)_6$ to the Au-Pt-Ni_{end} and Au-Pt-Ni_{beg} solutions. The formation of Ni-Fe-PBA structure occurs as the Ni domains react with the $[Fe(CN)_6]^{3-}$. The XPS spectra in Figure 4.5A a for Fe shows that the Au-Pt-Ni_{end}-Fe-PBA has a much higher signal from Fe^{2+} $2p_{3/2}$ and $2p_{1/2}$ corresponding to the PBA structure.[55] While in the Au-Pt-Ni_{beg} the prominent signal is from Fe^{3+} $2p_{3/2}$ and $2p_{1/2}$ (marked by dashed lines),[155] which indicates that its transformation to PBA structure is limited. For comparison spectra from Ni-PBA is also shown. The alloying of Ni with Pt in Au-Pt-Ni_{beg} limits the ability of Ni to react and form the PBA structures. A corresponding transformation is also seen in the XPS spectra of Ni (Figure 4.5 b). The Au-Pt-Ni_{end}-Fe-PBA now has a prominent signal from Ni^{3+}, while in Au-Pt-Ni_{beg}-Fe-PBA this signal is much lower. The Ni^{3+} signals in these PBA nanowire structures are also much higher than their counter part Au-Pt-Ni_{beg} and Au-Pt-Ni_{end} wires. The PBA formed is highly disordered as can be seen from absence of any signature in XRD (Figure 4.5B i). The EELS scans (Figure 4.5A c) show that in Au-Pt-Ni_{end}-Fe-PBA the signal from Ni, Fe and N occurs from same regions, along with distinct regions of Pt.

The Fe and N signals correspond to PBA like regions. While EELS scans for Au-Pt-Ni$_{beg}$-Fe-PBA show only a faint signal for Fe and N (Figure 4.5A d). The TEM images shows that both Au-Pt-Ni$_{end}$-Fe-PBA and Au-Pt-Ni$_{beg}$-Fe-PBA (Figure 4.5B e&f) have a nanowire web like morphology. The nanowire diameter is ~ 2-5 nm, with their length being in microns and they have an open structure. From the HR-TEM images (Figure 4.5B g) we see that Au-Pt-Ni$_{end}$-Fe-PBA structure is made up of distinct crystalline (circled in blue) and amorphous regions (circled in red) that are 2-5 nm in size and are adjacent to each other. The spacing of the crystalline regions matches with that of Pt and Au. This further confirms the structure of the Au-Pt-Ni$_{end}$-Fe-PBA material. While for the Au-Pt-Ni$_{beg}$-Fe-PBA we observe that the structure is mostly made of highly crystalline domains corresponding to Au and Pt, with limited amorphous regions (Figure 4.5B h).

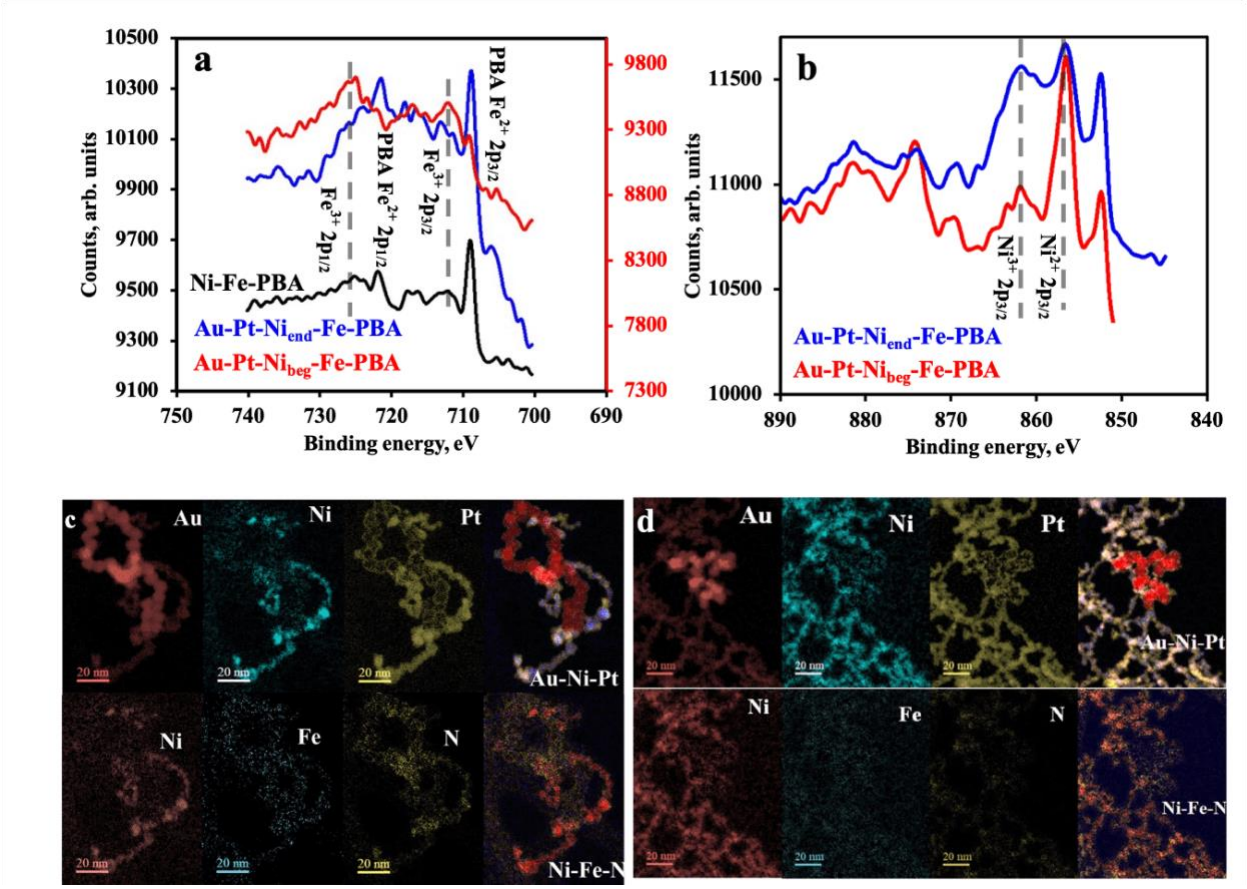

Figure 4.5A a) XPS spectra of Fe region for Au-Pt-Ni$_{end}$-Fe-PBA (in blue), Au-Pt-Ni$_{beg}$-Fe-PBA (in red, by using second y axis) and Ni-Fe-PBA composites (in black); b) XPS spectra of Ni region for Au-Pt-Ni$_{end}$-Fe-PBA (in blue) and Au-Pt-Ni$_{beg}$-Fe-PBA (in red) composites; EELS mapping of c) Au-Pt-Ni$_{end}$-Fe-PBA, and d) Au-Pt-Ni$_{beg}$-Fe-PBA.

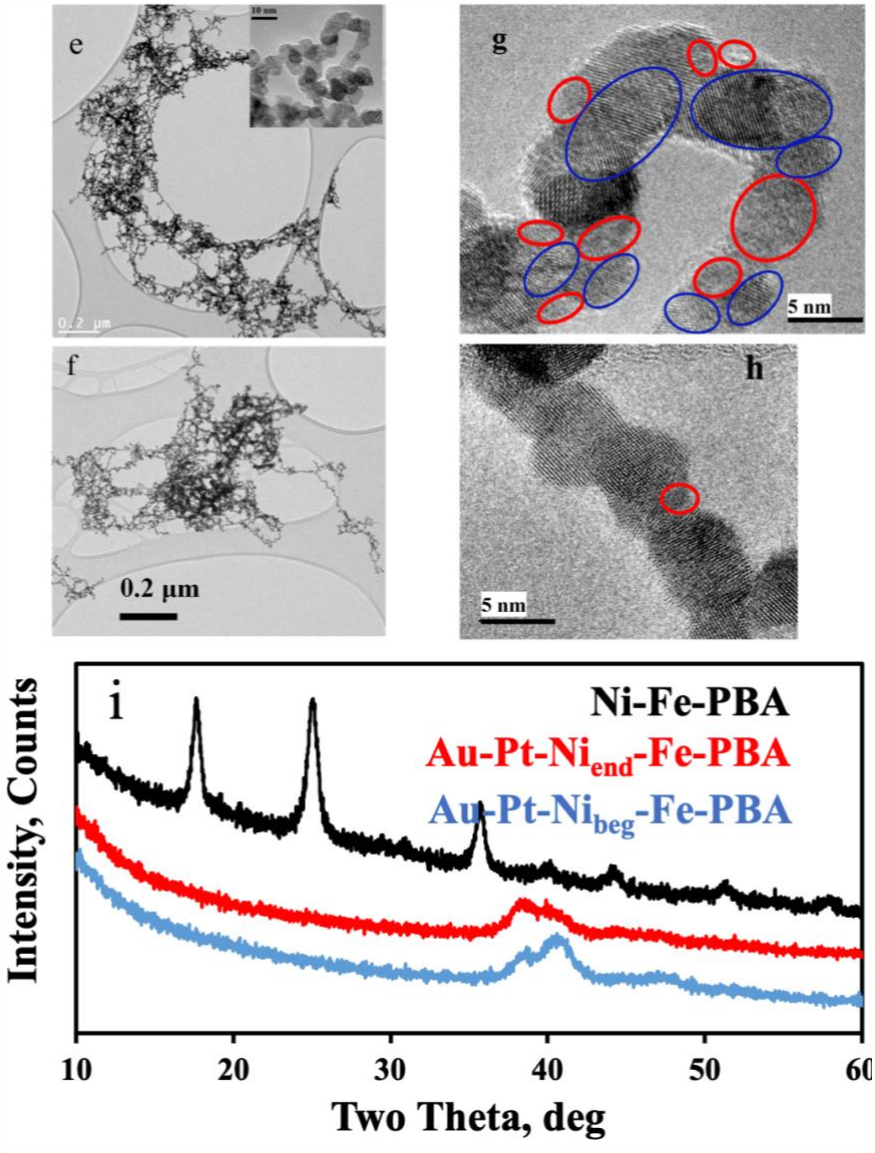

Figure 4.5B TEM images of e) Au-Pt-Ni$_{end}$-Fe-PBA and f) Au-Pt-Ni$_{beg}$-Fe-PBA; HR-TEM images of the inset image of e) is shown in g) Au-Pt-Ni$_{end}$-Fe-PBA, in h) Au-Pt-Ni$_{beg}$-Fe-PBA, and i) XRD spectra of Au-Pt-Ni$_{end}$-Fe-PBA (in red), Au-Pt-Ni$_{beg}$-Fe-PBA (in blue) and Ni-Fe-PBA (in black).

In the FESEM images for Au-Pt-Ni$_{end}$-Fe-PBA (Figure 4.6 a) and Au-Pt-Ni$_{beg}$-Fe-PBA (Figure 4.6 b) also we observe long entangled NW's with highly porous structure. To observe the formation of the PBA structures more clearly, a higher ratio of Ni:Pt was used (1:1). For Au-Pt-Ni$_{end}$-Fe-PBA, now we clearly observe the formation of the typical cubic structures associated with Ni-Fe-PBA (Figure 4.6 c), with NW's wrapping around their surface. This signifies that during the transformation close interfacing between different regions is maintained. Similarly, for Au-Pt-

Ni_{beg}-Fe-PBA, (Figure 4.6 d) again formation of cubic structures with wrapping of NW's is observed. However, in this case the size of the cubes is smaller, and they are more sparsely located. To verify the generality of this process, Au-Pt-Co chains were made through identical process and then transformed to Au-Pt-Co-Fe-PBA structures. At high ratio of Co:Pt, as seen in FESEM images (Figure 4.6 e) a clear formation of cubic PBA structures is observed with inter-dispersed NW's.

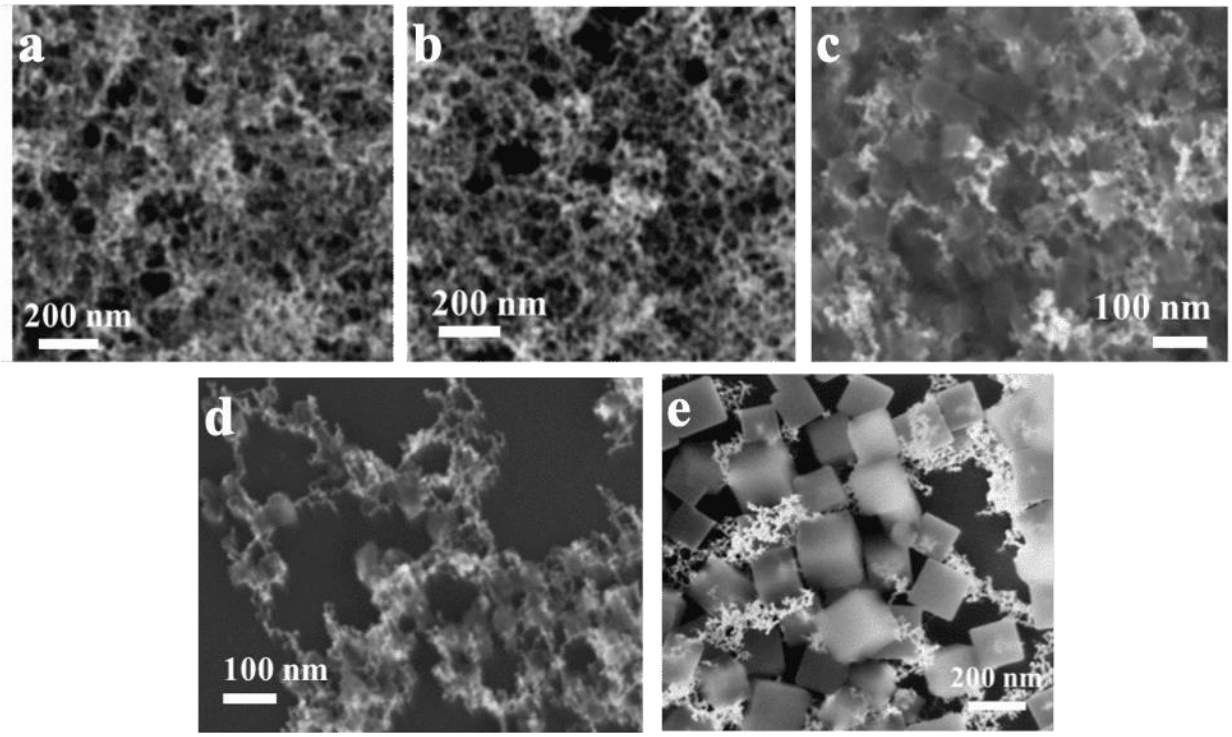

Figure 4.6 SEM images of a) Au-Pt-Ni_{end}-Fe-PBA, b) Au-Pt-Ni_{beg}-Fe-PBA, c) Au-Pt-Ni_{end}-Fe-PBA (at higher Ni:Pt ratio=1:1), d) Au-Pt-Ni_{beg}-Fe-PBA (at higher Ni:Pt ratio=1:1) and e) Au-Pt-Co-Fe-PBA.

Both the Au-Pt-Ni_{end}-Fe-PBA and Au-Pt-Ni_{beg}-Fe-PBA are then tested for their HER performance (Figure 4.7). The Au-Pt-Ni_{end}-Fe-PBA shows better performance than Au-Pt-Ni_{beg}-Fe-PBA, consistent with higher density of Ni^{3+} in its structure. The overpotential for HER for Au-Pt-Ni_{end}-Fe-PBA at 10 mA cm^{-2} and 30 mA cm^{-2} is 38.3 mV and 50.4 mV respectively (Figure 4.7 a). While for Au-Pt-Ni_{beg}-Fe-PBA at identical current densities the overpotential is 38.7 mV and 56.1 mV (Figure 4.7 a). The Tafel slopes for Au-Pt-Ni_{end}-Fe-PBA is 13.7 mV dec^{-1}, while for Au-Pt-Ni_{beg}-

Fe-PBA it is 13.9 mV dec^{-1} (Figure 4.7 b). To reiterate, the overpotential for Pt/C at similar current densities is 47 mV and 100.5 mV while its Tafel slope is 45.9 mV dec^{-1}. Based on the Electrochemically active surface area (ECSA) the specific activity for the Pt/C, Au-Pt-Ni_{beg}-Fe-PBA and Au-Pt-Ni_{end}-Fe-PBA samples at an overpotential of 50 mV is 0.39 mA $cm^{-2}{}_{ECSA}$, 0.6 mA $cm^{-2}{}_{ECSA}$ and 1.5 mA $cm^{-2}{}_{ECSA}$. Au-Pt-Ni_{end}-Fe-PBA achieves ~3.8 times higher than Pt/C. The stability of the catalyst is a key parameter to ensure its viability for practical applications, this is tested by running the catalysts continuously for 27 hrs. (see Figure 4.7 c). On retesting, the Au-Pt-Ni_{end}-Fe-PBA overpotential increases marginally to 39.0 mV (at 10 mA cm^{-2}) and 51.7 mV (at 30 mA cm^{-2}), (Figure 4.7 a). Similarly, for the Au-Pt-Ni_{beg}-Fe-PBA the overpotential increases to 39.4 mV and 60.6 mV. In contrast for Pt/C the overpotential increases significantly to 116 mV (at 10 mA cm^{-2}) from initial 47 mV.

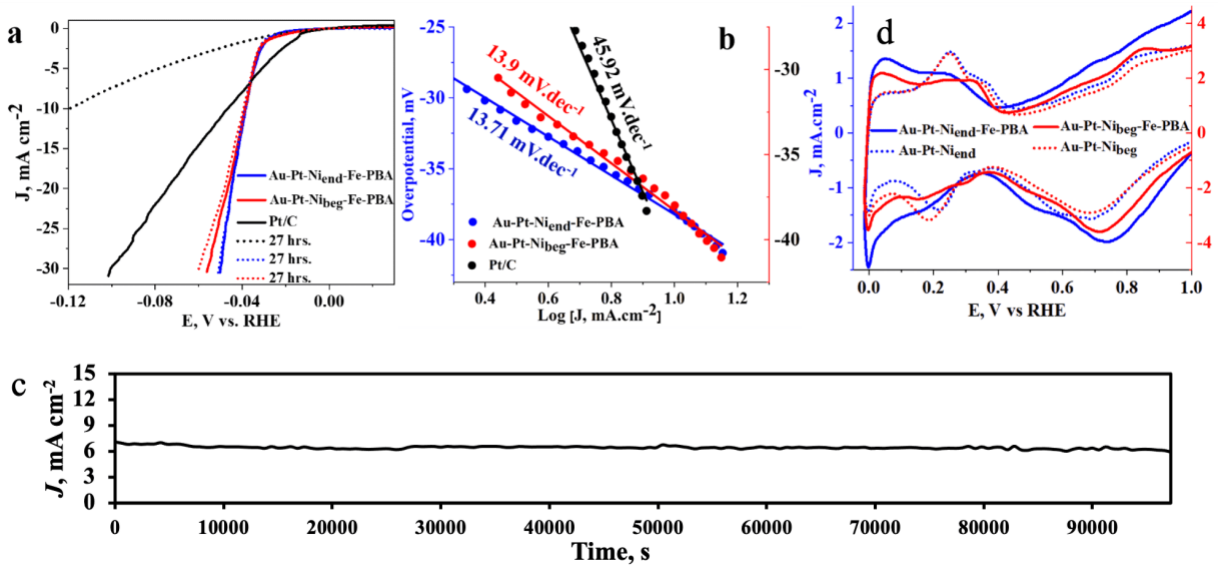

Figure 4.7 HER performance in KOH solution a) LSV curve of Au-Pt-Ni_{end}-Fe-PBA (in blue), Au-Pt-Ni_{beg}-Fe-PBA (in red) and commercial Pt/C nanoparticles (in black) before and after 27 hrs. and b) the corresponding Tafel slopes; c) Durability tests (27 hrs.) recorded at a constant voltage of 1.46 V in 0.1 M KOH; d) The cyclic voltammetry (CV) of hydrogen underpotential deposition (H_{UPD}) region with Au-Pt-Ni_{end}-Fe-PBA, Au-Pt-Ni_{end}, Au-Pt-Ni_{beg}-Fe-PBA, and Au-Pt-Ni_{beg}. All measurements were obtained at 100 mV s^{-1} in N_2 saturated 0.1 M KOH at room temperature.

We observe that the Au-Pt-Ni_{end}-Fe-PBA provides better performance than Au-Pt-Ni_{beg}-Fe-PBA, consistent with its structural characterization results. Also, the catalysts with incorporated PBA

structure provide significantly better performance than the plain catalyst (Au-Pt-Ni_{beg} and Au-Pt-Ni_{end}) and Pt/C. The performance of Au-Pt-Ni_{end}-Fe-PBA for HER is exceptional in terms of the overpotential and the Tafel slop, which relates to its interaction energy with the reactants and intermediates, and kinetics.[153] This performance is the result of the structure of the catalyst that is first initiated by formation of nanoscale domains of Pt and Ni in a nanowire like network. This provides for the crucial high-density interfacing between Pt and Ni for effective catalysis. The structure ensures effective adsorption of the water molecule on the Ni domains and then the transfer of H_{ads} and formation of molecular H_2 on the adjoining Pt domains.[135,151] The addition of $Fe(CN)_6^{3-}$ leads to formation of PBA like structure on the Au-Pt-Ni NW's, by reacting with Ni domains. The process is controlled to have Ni as the limiting reactant, which leads to a high concentration of Ni^{3+} states, along with a high defect density. This significantly improves the performance of the HER by enhancing the critical water splitting Heyrovsky step. The Tafel slope of ~14 mV dec^{-1} points to a fundamental change in the HER mechanism compared to traditional Pt/Ni catalyst, which show a significantly higher slopes in the range of 40-120 mV dec^{-1}.[135,153]

The exceptional performance of the Au-Pt-Ni-Fe-PBA catalysts is further supported by the results of CV curves performed in 0.1 M KOH, which show the typical peaks for under potential hydrogen adsorption and desorption (H_{upd}) and the OH^- adsorption and desorption (Figure 4.7 d). For both the PBA samples we observe that the H_{upd} region is shifted significantly to lower potential and has a broad distribution. The Au-Pt-Ni_{end}-Fe-PBA shows a small peak at 0.247 V and a more prominent peak at 0.051 V. While in the case of Au-Pt-Ni_{beg}-Fe-PBA the region extends from 0.325 V to 0.039 V. In contrast in Pt/C the two prominent desorption peaks are observed at 0.368 V and 0.269V. For the plain chain samples these two peaks lie at ~ 0.354 V and 0.253 V. The presence of a broad low potential H_{upd} region in the PBA chain catalyst further confirms the basis of their HER performance that is attributed to the presence of Ni^{3+} states and a highly disordered structure which affects the interaction of Pt with 'H'.[132,156,157] The other crucial parameter for HER is the OH^- desorption. For the Au-Pt-Ni_{end}-Fe-PBA a broad OH^-_{des} peak is observed at 0.738 V, while for Au-Pt-Ni_{beg}-Fe-PBA this lies at 0.715V. For Pt/C, Au-Pt-Ni_{beg} and Au-Pt-Ni_{end} the same is observed at 0.658 V, 0.687 V and 0.692 V. The shift to more positive potential signifies that desorption of OH^- occurs with greater ease on the PBA samples and hence enhances their HER performance.

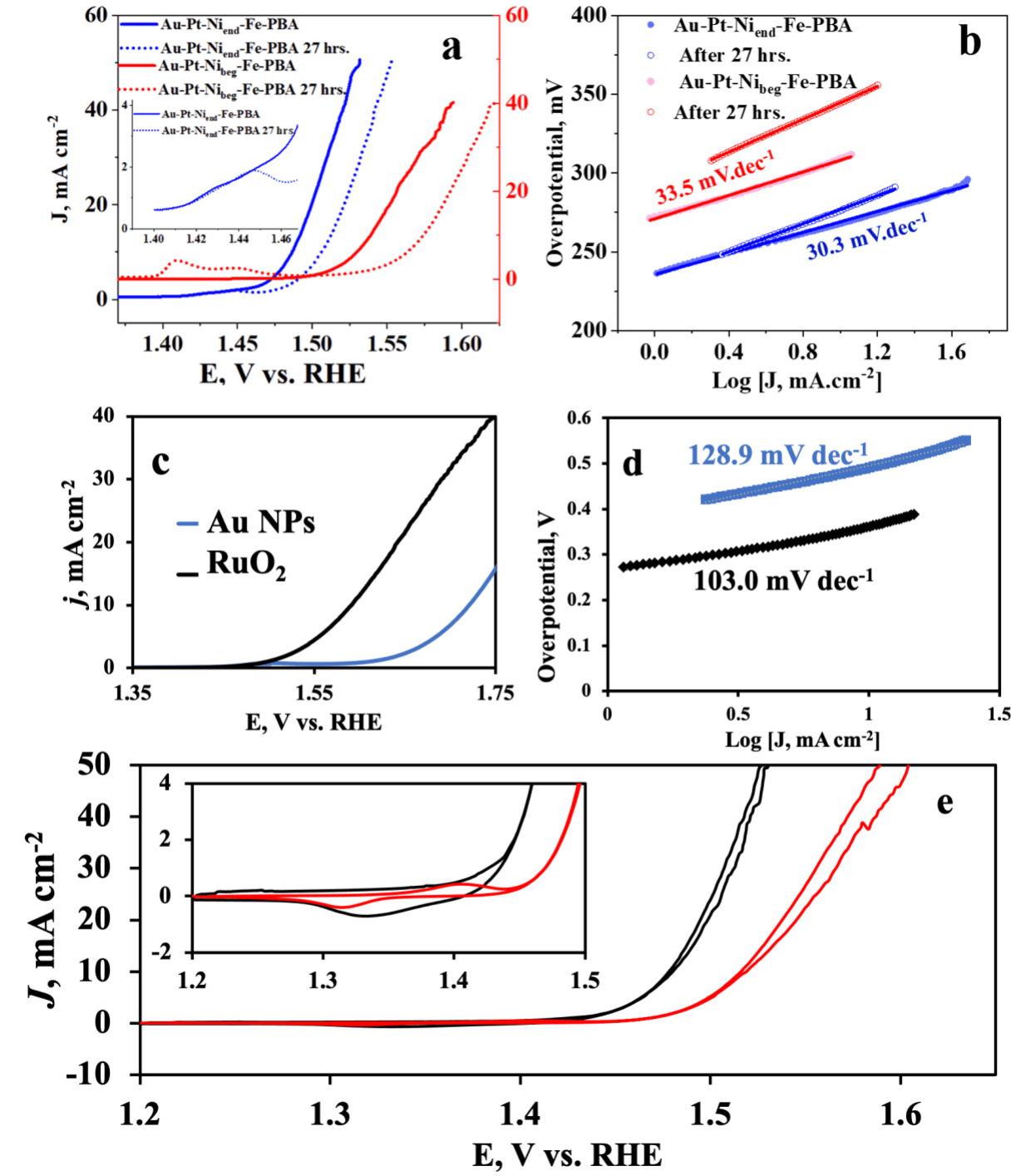

Figure 4.8 OER performance in KOH solution a) LSV curve of Au-Pt-Ni$_{end}$-Fe-PBA (in blue), Au-Pt-Ni$_{beg}$-Fe-PBA (in red) before (in solid line) and after 27 hrs. (in dashed line) and b) the corresponding Tafel slopes; c) the LSV curve of 10 nm Au NPs and commercial RuO_2, d) the corresponding Tafel slopes; e) The CV curves of OER for Au-Pt-Ni$_{end}$-Fe-PBA (in black line) and Au-Pt-Ni$_{beg}$-Fe-PBA (in red line) with a scan rate of 5 mV s^{-1}.

The OER performance of the PBA catalysts is tested in 0.1 M KOH using the three-electrode system (Figure 4.8). The LSV curves (Figure 4.8 a) show that Au-Pt-Ni_{end}-Fe-PBA has the lowest overpotential of 256 mV at current density of 10 mA cm^{-2}, while the Au-Pt-Ni_{beg}-Fe-PBA shows an overpotential of 314 mV. The Tafel slope (Figure 4.8 b) for Au-Pt-Ni_{end}-Fe-PBA is 30.3 mV dec^{-1}, and for Au-Pt-Ni_{beg}-Fe-PBA it is 33.5 mV dec^{-1}. After 27 hrs. of chronoamperometric run at a constant voltage of 1.46 V, the overpotential of the samples increase to 276 mV and 344 mV, respectively. While their Tafel slopes increase to 44.59 mV dec^{-1} and 52.15 mV dec^{-1}. Without the PBA treatment the Au-Ni-Pt wires have poor performance due to limited presence of OER active sites and they show an overpotential of 443 mV (Au-Pt-Ni_{end}) and 367 mV (Au-Pt-Ni_{beg}). While their Tafel slopes are 104.1 mV dec^{-1} and 84.4 mV dec^{-1}, respectively. Additionally, in the PBA composites (and others with Ni) a clear oxidation peak is observed at ~1.45 V, which is due to surface oxidation of Ni from low valence states to higher oxidation states (Ni^{2+} to Ni^{3+}).[158] For comparison commercial RuO_2 electrocatalyst shows as overpotential of 362 mV (at 10 mA cm^{-2}), with a Tafel slope of 103 mA dec^{-1} (Figure 4.8 c&d). To further confirm that the underling Au nanoparticles do not contribute towards the electrocatalytic performance, their OER performance is tested. They show an overpotential of ~ 489 mV for a current density of 10 mA cm^{-2} and a Tafel slope of 129 mV dec^{-1} (Figure 4.8 c&d). The excellent performance and stability of the Au-Pt-Ni_{end}-Fe-PBA hence is attributed to multiple factors: namely high density of Ni^{3+} states, a nanowire like structure with highly conductive core of Au-Pt which provides facile electron transfer and a porous structure for effective mass transfer. To confirm that oxidation of other species does not contribute to the signal from OER, CV curves were also recorded (Figure 4.8 e). These curves confirm that the observed signal in the potential range is from OER.[159,160] Further overall water splitting is performed with Au-Pt-Ni_{end}-Fe-PBA catalyst and compared with commercial catalyst to show its better performance (Figure 4.9). The calculated Faradaic efficiency for Au-Pt-Ni_{end}-Fe-PBA towards HER is ~ 98.8 % and for OER is 98 %. The Au-Pt-Ni_{end}-Fe-PBA parameters are also compared to other reported electrocatalyst to show its high performance (Table 4.1).

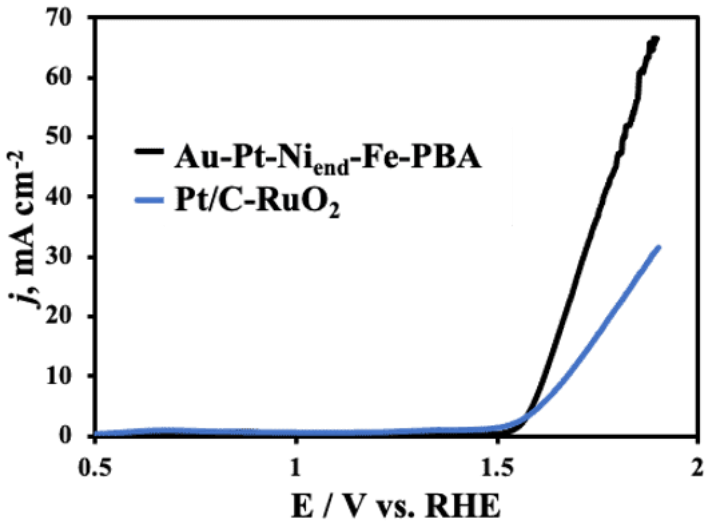

Figure 4.9 Overall water splitting is performed in a two-electrode system, Au-Pt-Ni_{end}-Fe-PBA serves as bifunctional catalyst for both OER and HER. With a scan rate of 5 mV s^{-1} at current density of 30 mA cm^{-2}, the water splitting of cell voltage is 1.7 V, which is better than the commercial benchmark samples. The cell voltage using RuO_2 as anode and Pt/C as cathode for overall water splitting needs 1.9 V to deliver a 30 mA cm^{-2} current density.

The HER and OER activity is measured in samples after activation cycles (100) and their stability is tested in chronoamperometry for 27 hrs. A key factor during such testing is the transformation of the catalyst structure that can further enhance its performance. For the PBA samples, we observe that their activity increases in the initial period. Raman spectroscopy (Figure 4.10) was conducted on both fresh samples and after the 100 CV conditioning cycles. In the fresh Au-Pt-Ni_{end}-Fe-PBA a signature for CN^- is observed is observed at 2100-2150 cm^{-1}.[55] This shows effective transformation of Ni to Ni-Fe-PBA on treatment with $[Fe(CN)_6]^{3-}$. However, on conditioning on the OER side (100 cycles from 1.2V to 1.6V), this CN^- band disappears and new the bands corresponding to $Ni(OH)_2$ becomes more prominent.[161,162] This change is not observed on conditioning on the HER side, as oxidation is only possible at positive potentials. This transformation is consistent with previous reports and further improves the performance for the catalyst. To further confirm the effect of domain size and characterize the Ni oxidation states Fourier transform infrared spectroscopy (FT-IR) was conducted (Figure 4.11 a&c). A sample made by mixing partially assembled Au-Pt^{4+} and Au-Ni^{2+} chains and then allowing them to assemble completely, followed by the reduction of the metal cations and PBA treatment (Au-Pt-Ni_{mid}-Fe-

PBA) was also tested. This sample will have domain size in between that of Au-Pt-Ni_{beg}-Fe-PBA and Au-Pt-Ni_{end}-Fe-PBA. We observe that as prepared samples of Au-Pt-Ni_{beg}-Fe-PBA and Au-Pt-Ni_{mid}-Fe-PBA, show a greater signal from the Ni^{2+}-O (region around 460 cm^{-1}) and Ni^{2+}-OH (region around 530 cm^{-1}) with relatively weak signal from Ni^{3+} (broad region around 600 cm^{-1}).[170,171,172,173] After cycling (100) first for HER and then OER, we observe that in both the samples the signal from Ni^{3+} region increases, however the signal from Ni^{2+} regions is still dominant. However, for the Au-Pt-Ni_{end}-Fe-PBA catalyst even in the fresh sample the dominant signal is from Ni^{3+} region compared to Ni^{2+} region. After cycling there is no discernable signal from the Ni^{2+} region and only a broad peak in the Ni^{3+} region is observed. This further confirms the that HER and OER performance of Au-Pt-Ni_{end}-Fe-PBA catalyst is correlated to its structure and high density of disordered Ni^{3+} regions. The macroscale structure of the catalyst as a web of nanowires (Figure 4.11 d) is still maintained after the 27 hrs. of continuous use in both HER (Figure 4.11 e) and OER (Figure 4.10 f), which further ensures a stable response from the catalysts.

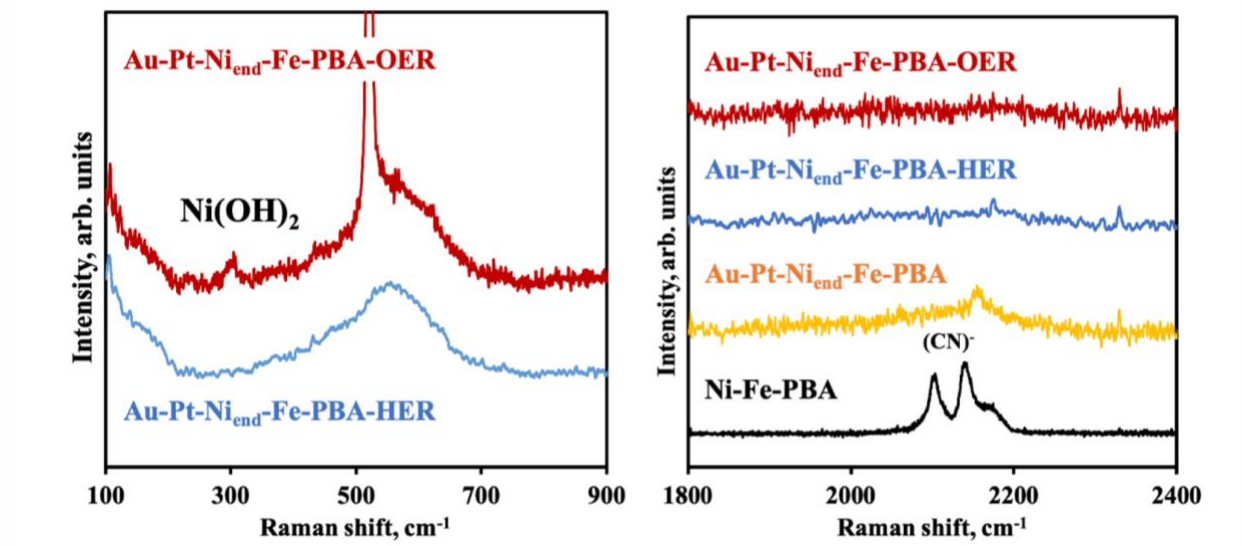

Figure 4.10 Raman spectra of Au-Pt-Ni_{end}-Fe-PBA conditioning on the OER side (in red line), Au-Pt-Ni_{end}-Fe-PBA conditioning on the HER side (in blue line), Au-Pt-Ni_{end}-Fe-PBA (in yellow line) and Ni-Fe-PBA (in black line);

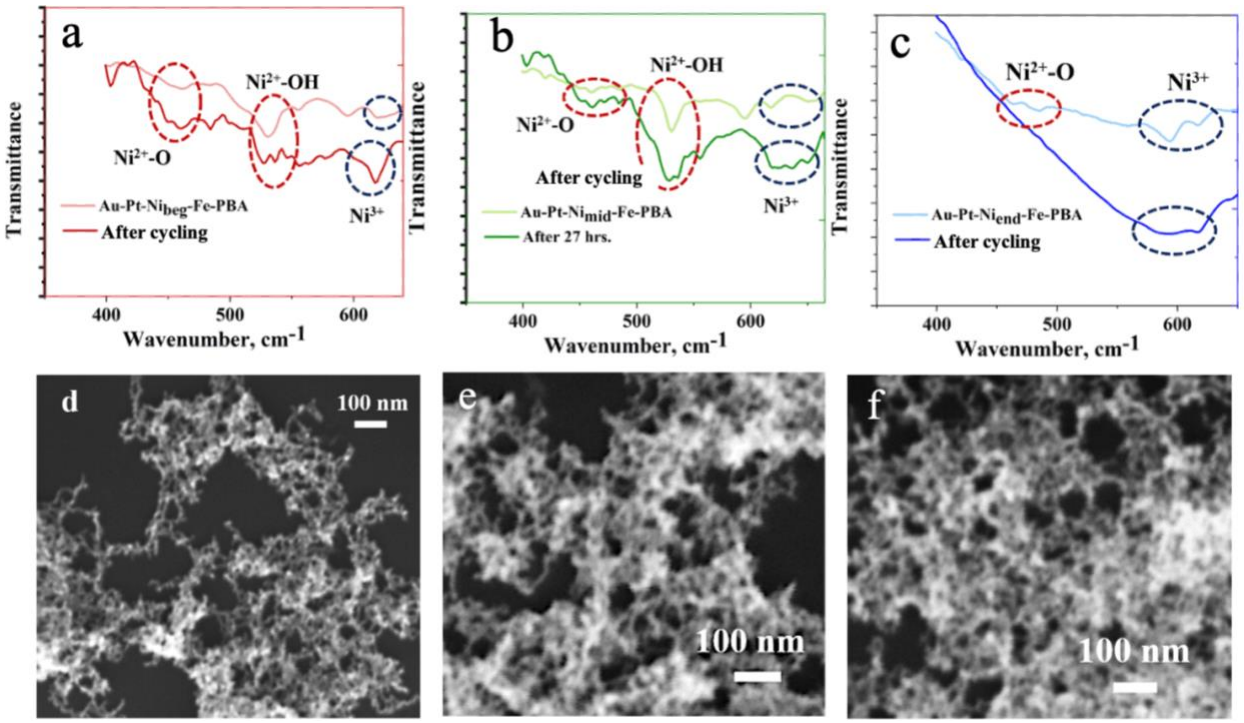

Figure 4.11 FT-IR data of spectrum for as prepared a) Au-Pt-Ni_{beg}-Fe-PBA and cycled samples, b) Au-Pt-Ni_{mid}-Fe-PBA and cycled samples, and c) Au-Pt-Ni_{end}-Fe-PBA and cycled samples; FESEM image showing that the nanowire like morphology of: d) Au-Pt-Ni_{end}-Fe-PBA and after operation for 27 hrs. of e) HER and f) of OER. From the images, the samples maintain the nanowires like structure with highly porous morphology without any aggregation.

Table 4.1 A performance comparison of water splitting catalysts

Sample	Overpotential mV	Current density mA/cm^2	Tafel slope mV/dec	Electrolyte	Reaction	Ref.
O-CNT/NiFe	279	10	42.8	1.0 M KOH	OER	138
Ni-PBA	285	50	53.1	1.0 M KOH	OER	137
Ni-Fe-PBA	283	10	54	1.0 M KOH	OER	55
CFHC	330	10	57	1.0 M KOH	OER	163
NF-PBA	258	10	46	1.0 M KOH	OER	164
Pt-Ni	65	10	78	0.1 M KOH	HER	133
β-$Ni(OH)_2$/Pt	42	10	92	0.1 M KOH	HER	132
N modified Pt-Ni nanowires	13	10	29	1.0 M KOH	HER	135
Pt-NC/Ni-MOF	25	10	42.1	1.0 M KOH	HER	165

$Pt/Ni(HCO_3)_2$	27	10	45	1.0 M KOH	HER	166
Ni5Fe LDH@NF	210	10	59	1.0 M KOH	OER	167
	133	10	92	1.0 M KOH	HER	
0.6 Ni-Fe-Pt nanocubes	333	10	65	1.0 M KOH	OER	168
	463	10	81	1.0 M KOH	HER	
Co-Fe-PBA	220	10	55	1.0 M KOH	OER	169
	155	10	60	1.0 M KOH	HER	
$Ni/Ni(OH)_2$	310	10	74.8	1.0 M KOH	OER	125
	168	10	95.7	1.0 M KOH	HER	
Au-Pt-Ni-Fe-PBA	256	10	30	0.1 M KOH	OER	This work
	37	10	14	0.1 M KOH	HER	

4 Conclusion

A nanoscale multidomain catalyst is engineered for excellent bifunctional performance towards HER and OER. The structure of the catalyst is made by the use of a self-assembly process that is based on the ion distribution in the electrical double layer around the surface of nanoparticles. The self-assembly process leads to the critical features that are needed to achieve the high performance in HER and OER. A high-density interfacing is achieved between regions with Ni in high oxidation states (Ni^{2+} and more crucially Ni^{3+}) and Pt-Ni (Ni metallic) regions. This is crucial to ensure rapid adsorption and splitting of the water molecules on the Ni^{2+} and Ni^{3+} regions and subsequently the formation of molecular H_2 on the adjacent Pt-Ni (metallic) regions. The structure also ensures rapid OER performance. A key is also the underlying nanowire like porous structure of the catalyst that leads to rapid electron and mass transfer for electrocatalytic activity. All these combined features lead to the observed performance in the bifunctional catalyst. The ease of the presented synthesis process with the ability to incorporate different metal species and control the structure, will provide new avenues for use of the electrical double layer to develop highly efficient composite catalyst.

Part B Self-Assembled Au NWs doped with various elements as electrocatalysts

Chapter 5 Au-Pt-Ni-R nanocomposites as dopamine catalyst in neutral media

1 Introduction

Dopamine is a crucial neurotransmitter in the human nervous system which affects cognitive and behavioral functions.[174] The abnormal concentration of dopamine is related to neurological diseases like Parkinson's and Alzheimer's. Therefore, intense research activities have been devoted to developing sensors with highly sensitive and reliable detection of dopamine. Several analytical techniques include enzyme-based detection, liquid chromatography, mass spectrometry, and electrochemical detection for measuring dopamine.[174] However, the non-enzymatic electrochemical method provides a simple, rapid, and straightforward detection of dopamine. Electrochemical detection is based on the oxidation reaction process of dopamine which involves 2 electrons. Electrochemical detection can be done using chronoamperometry, differential pulse voltammetry, and cyclic voltammetry. The response in current can have a linear relation with the concentration of dopamine, which enables easy quantification of dopamine in real samples. Researchers have put in efforts to solve the problem of interfering compounds, which co-exist in the biosystem. For example, uric acid (UA), glucose, acetaminophen (AP), and ascorbic acid (AA) are specifically important due to the similar oxidation potentials with dopamine.[174]

However, the electrochemical process has some limitations. For example, the bare electrode requires a quite high potential to operate the electrochemical oxidation reaction of dopamine. The formation of phenoxy radicals during the process can result in subsequent coupling and formation of a polymeric film, leading to the fouling of the electrodes.[174]

Noble metal nanomaterials are promising in the electrochemical field because of their excellent electrocatalytic properties, high conductivity, and high stability, for example, Pt,[175,176,177] Au,[178,179] and their alloy.[143,180] However, these materials are expensive. To reduce cost, nanomaterials have been used, or they have been combined with Earth-abundant elements, like Ni,[181,182,183,184]

Co,[185,186] Fe,[178] or carbon composites[175,187] while increasing the catalytic performance based on the synergistic effects.[144,184,188] 1D nanochains are a class of nanomaterials that also possess a large surface area, and the overlapped chains can form the 3D highly porous structure on the glassy carbon electrode (GCE). This porous structure improves catalytic activity and stability due to effective mass transfer.

This work assembles Pt, Ni, and Au-based nanochains using a facile, cost-effective, and controllable process. We developed two kinds of micron length 1D nanowires by controlling the spatial distribution of Pt/Ni bimetallic nanoclusters coated on gold chains to detect dopamine at neutral pH. The spatial distribution of catalytic elements can be controlled within the nanometer scale, which modifies the materials' absorption and desorption energy of intermediates or final products.[72] This work achieved spatial distribution of Pt/Ni by mixing the metal cation or mixing the chains at different stages during the self-assembly process. The metal cations are then reduced to form the active materials for electrochemical catalysis. The size of Pt and Ni domain can be tuned in the range of complete homogenous mixing to 2-5 nm size nanoscale domains. The results exhibit that the nanoscale domain area is necessary for better performance than the homogenous mixing of the Pt and Ni.

2 Materials and methods

2.1 Materials

2.1.1 Preparation of AuPt and AuNi NCs

135 µL of 4.5 mg/mL $PtCl_4$ (99.9%, Sigma Aldrich) and 80 µL of 4 mg/mL $NiCl_2$ (99.9%, Sigma Aldrich) were mixed with 1 mL gold nanoparticles separately and then left on the shaker with a speed of 300 rpm until the solution color changed to dark blue. After the self-assembly process, the chains were reduced by 75 µL of 4 mg/mL $NaBH_4$ (99%, Sigma Aldrich) (samples labeled as AuPt-R and AuNi-R), and the color turned to black or pink. The stocked samples are stable in aqueous media over two weeks.

2.1.2 Preparation of $AuPt_3Ni$/AuPtNi/$AuPtNi_3$ (mixing ions) NCs

202.5/135/67.5 µL of 4.5 mg/mL $PtCl_4$ and 40/80/120 µL of 4 mg/mL $NiCl_2$ were mixed first, and then added into 2 mL gold solution. When the color turned to dark blue, the solution was reduced by 150 µL of 4 mg/mL $NaBH_4$, which turned the color black (samples labeled as $AuPt_3Ni$/AuPtNi/$AuPtNi_3$-R). The stocked samples are stable in aqueous media over two months.

2.1.3 Preparation of $AuNi_3AuPt$/AuNiAuPt/AuNi$AuPt_3$ (mixing chains) NCs

1.5/1/0.5 mL of AuNi chains solution before reduction and 0.5/1/1.5 mL of AuPt chains solution before reduction were well mixed first. Then 2 mL mixture was reduced by 150 µL of 4 mg/mL $NaBH_4$, which turned the color to black (samples labeled as $AuNi_3AuPt$/AuNiAuPt/AuNi$AuPt_3$-R). The stocked samples are stable in aqueous media over two months.

2.2 Characterization section

Zeiss Ultraplus Field-emission Scanning Electron Microscopy (FESEM) was used to measure the morphology of samples and the deposition. Transmission electron microscopy (TEM) images were obtained with an LEO 912ab energy filtered transmission electron microscope (EFTEM). UV-

Visible absorption spectra of samples were detected by Perkin Elmer Lambda 750 spectrophotometer. The powder X-ray diffraction (XRD) pattern was measured by the PANalytical Empyrean diffractometer with Cu Kα radiation (λ = 1.54 Å). X-ray Photoelectron Spectroscopy (XPS) was performed on VGS ESCALab 250. Raman measurements were performed using a Horiba HR800 spectrometer in the backscattering configuration.

2.3 Electrical measurement

Cyclic voltammetric (CV) and chronoamperometric experiments were performed with an Ivium CompactStat Electrochemical Analyzer electrochemical workstation. A conventional three-electrode system was adopted using GCE as working electrode, Ag/AgCl (1 M KCl) as reference electrode, and Pt wire as a counter electrode. 15 μL gold chain solution was drop-cast on GCE and dried under at 60 °C to do measurements. The electrolyte is 0.01 M Phosphate buffered saline (PBS, Sigma Aldrich). The concentrations of dopamine (Sigma Aldrich) in 0.01 M PBS were varied between 0.1 μM and 10 mM. All the dopamine detection experiments are operated under a stirrer with 500 rpm speed at room temperature. CV scans were recorded in 0.01 M PBS from -0.5 to 0.5 V vs. reference electrode at different scan rates. For chronoamperometry measurements, the amperometric response of the electrode toward successive additions of dopamine is recorded. A calibration curve is established using the readout current versus dopamine concentration (the detection current is averaged over the last 15 s range). During the measurements, it was ensured that the baseline current (in the absence of dopamine) was stabilized before adding dopamine. The current change with time is tracked with increasing dopamine concentration. Interference tests measured electroactive compounds, such as 10 μM ascorbic acid (AA), 10 μM uric acid (UA), 10 μM acetaminophen (AP) and 250 μM glucose, which are commonly present in physiological samples and cause problems in the determination of dopamine (10 μM). The LoD was determined from the relationship, expressed as:[189]

$$LoD = 3.3\sigma/S$$

where σ is the standard deviation of the baseline and S is the slope of the sensor's linear calibration curve. Sensitivity was defined as the slope of the sensor's calibration curve normalized to the geometrical area of the electrode. EIS was measured by AC impedance spectroscopy within the frequency range from 0.1 to 30 kHz in PBS.

3 Results and discussion

3.1 Characterization

The schematic image in Figure 5.1 shows the self-assembly process of Au nanoparticles by Pt^{4+} and Ni^{2+} cations. Then they are chemically reduced by $NaBH_4$ to obtain the continuous morphology of 1D Au-Ni-Pt nanochains. In Figure 5.2 a, the SEM images present the morphology of these nanochains. A highly porous network is created with overlapping micron length chains. At high magnification, it clearly exhibits the chains morphology with high structural uniformity. UV-Vis spectrum, in Figure 5.2 b, illustrates the self-assembly process of the chains. The initial 10 nm Au nanoparticles show a plasmon resonance peak at 525 nm. After fully assembled, the Au NCs' UV-Vis absorption peak shifts to 620 nm, confirming the formation of ~250 nm 1D chains. Based on our previous study, ~50% of the added metal cations are adsorbed on the surface of Au NPs, which might cover the surface or play a role as a linking bridge.[72] After adding $NaBH_4$, the metal cations are reduced to metallic form, and they form an ultrathin continuous covered layer on top of Au NPs. Their surface exposes more active sites, which benefits the electrocatalysis of dopamine.

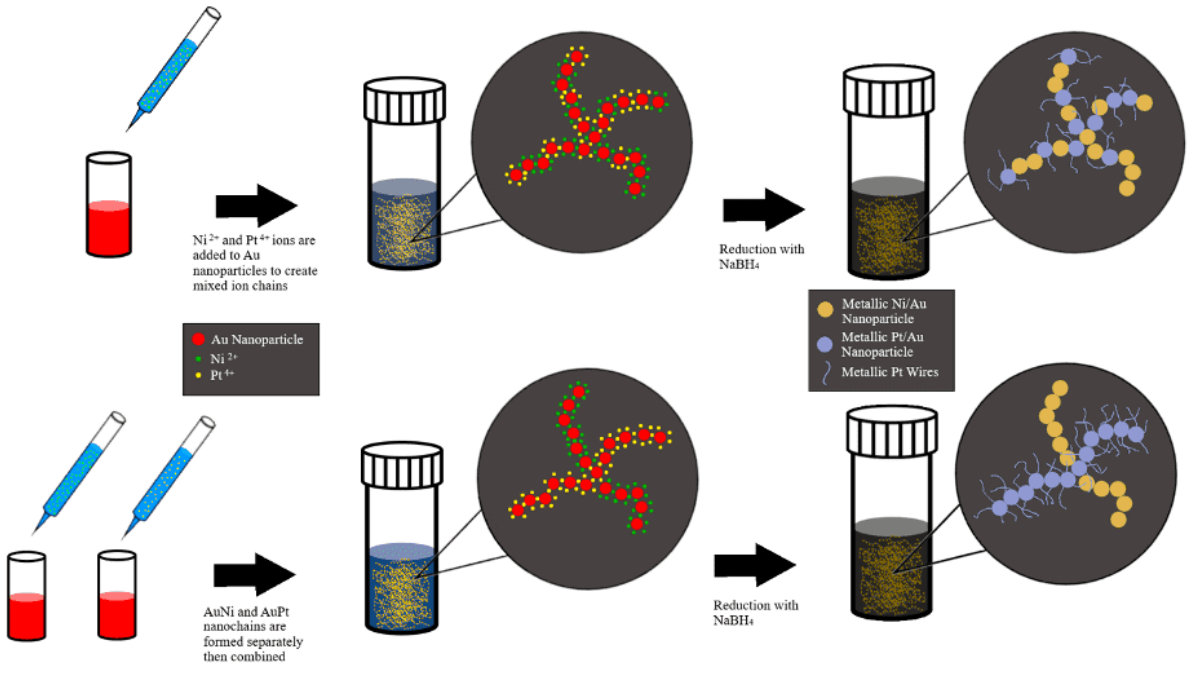

Figure 5.1 Schematic image of the preparation process of 1D Au-Ni-Pt nanochain.

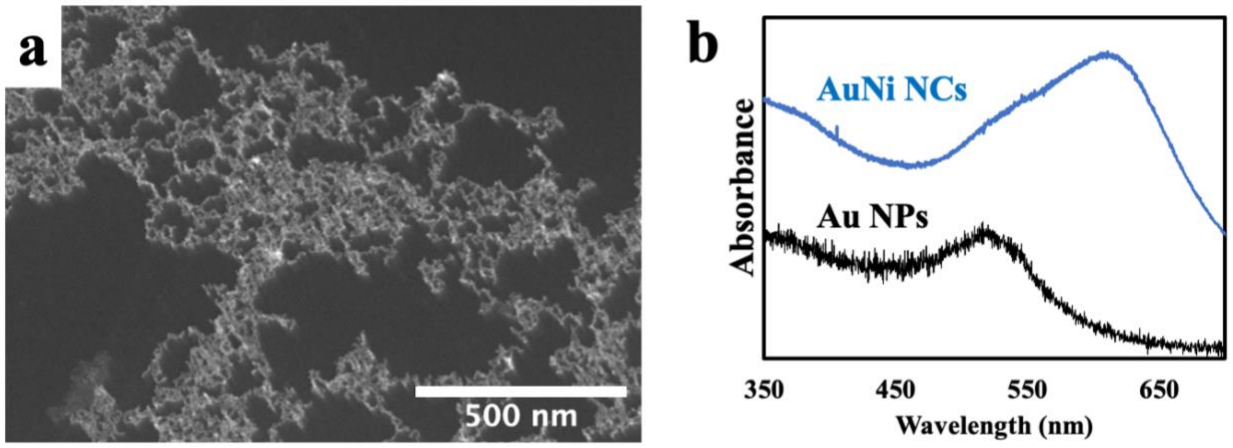

Figure 5.2 a) Typical SEM image of self-assembled Au-Ni-Pt NWs; b) Typical UV-Vis spectrum of Au NPs and self-assembled Au NCs. The wavelength UV-Vis absorption shifts from 520 nm to ~620 nm.

To confirm the formation and crystal structures of samples, XRD is used. As shown in Figure 5.3, it is observed that a prominent peak is located around 38.4° (2θ), which can be ascribed to the diffraction from the (111) crystal planes of the face-centered cubic phase of Au (JCPDS no. 04-0784).[74] Similarly, this peak is also observed in the AuNi-R and AuPt-R samples at 38.5° and 39.0°. The small shifts could be caused by the formation of AuNi or AuPt alloy during the reduction.[72] To better investigate the crystal structure of Ni after the reduction, we characterized the Ni-R sample without Au NPs. Surprisingly, the Ni-R is amorphous. This could be due to the formation of an extremely thin disordered $Ni(OH)_2$ layer.[190] As for the AuPt-R sample, the XRD spectrum also shows a set of diffraction peaks presented around 40.1° and 46.7°, which can be assigned, respectively, to the Pt (111) and (200) planes. These shifts about 0.3° compared to pure Pt indicate the ultrathin layer of Pt on Au NPs with limited alloy formation. The broadness of the peak corresponds to the smaller size of the material. Because the AuNiAuPt-R sample has the best electrocatalytic performance among the synthesized materials, in this work we mainly focus on AuNiAuPt-R and AuPtNi-R samples for characterization. The AuNiAuPt-R sample presents the Au(111) and Pt (111) peaks at 39.0° and 41.1°. In contrast, the AuPtNi-R sample's peaks exhibit at 38.6° and 41.6°, respectively, Therefore, according to the Bragg's Law, which provides an estimation of the actual structure (the greater shift in the peaks), mixing ions sample possesses a greater degree of alloy formation compared to mixed chains ones. Ni atoms are also plausibly at a higher chemical state than surrounding Pt atoms because the electronegativity of Ni is lower than

Pt. The EDX results show the atomic ratio of Pt/Ni of AuNiAuPt-R and AuPtNi-R samples are ~1.8:1. In comparison, theoretical results are ~1.5:1, which is similar to experimental results. The atomic ratio of $AuNi_3AuPt$-R, $AuNiAuPt_3$-R, $AuPtNi_3$-R, and $AuPt_3Ni$-R samples are 0.93, 4.59, 0.92, and 5.62, respectively, measured by EDX.

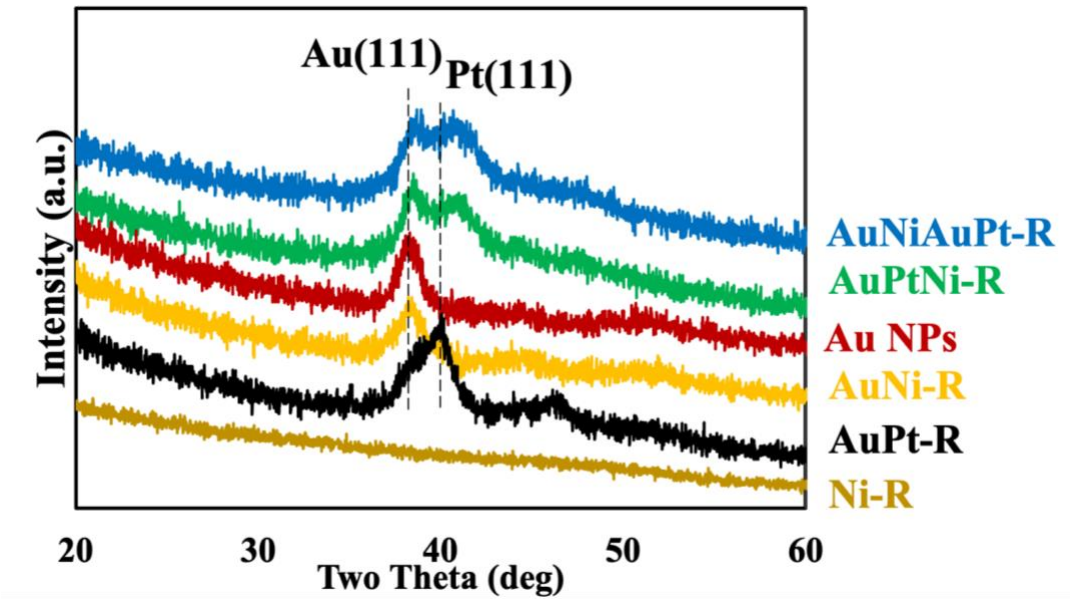

Figure 5.3 XRD spectra of assembled Au chains after reduction, including AuNiAuPt-R, AuPtNi-R, AuPt-R, AuNi-R, Au NPs, and Ni^{2+} salt after reduction.

To better understand the chemical state of elements, X-ray photoelectron spectroscopy (XPS) was carried out to examine the surface of the composites. The high-resolution XPS spectra of the Pt 4f region of the samples, as shown in Figure 5.4, the binding energies of Pt $4f_{7/2}$ for the AuPt-R, AuNiAuPt-R, and AuPtNi-R samples are mainly located at 71.1 eV, and the $4f_{5/2}$ binding energies are located at 74.4 eV. These prove the Pt ions are transferred in a metallic state. Meanwhile, the Pt $4f_{7/2}$ spectra were best fitted by two peaks that could be assigned, respectively, to Pt metal and Pt alloy. More detailed information about the alloy peak shift is summarized in Table 5.1. Thus, Au binding energy decreases a bit when Ni is introduced into AuPt alloy, as the electronegativity of Ni is lower than Pt and Au. The binding energy of Ni in the AuNiAuPt-R sample is slightly higher than AuPtNi-R representing the higher oxidation state of Ni that exists in the AuNiAuPt-R sample. This can assist the mixing chains samples electrocatalysis of dopamine compared to the mixing ions samples. In Figure 5.4 a, the Ni 2p spectrum of the AuNiAuPt-R sample was

deconvoluted by 3 peaks identifying the presence of Ni^0, Ni^{2+}, and Ni^{3+} (NiOOH).[143,144,145] As for AuPtNi-R, the spectrum exhibits the presence of Ni^0, and $Ni(OH)_2$, while AuNi-R only show the peak for NiO.[146,147,148,149,150]

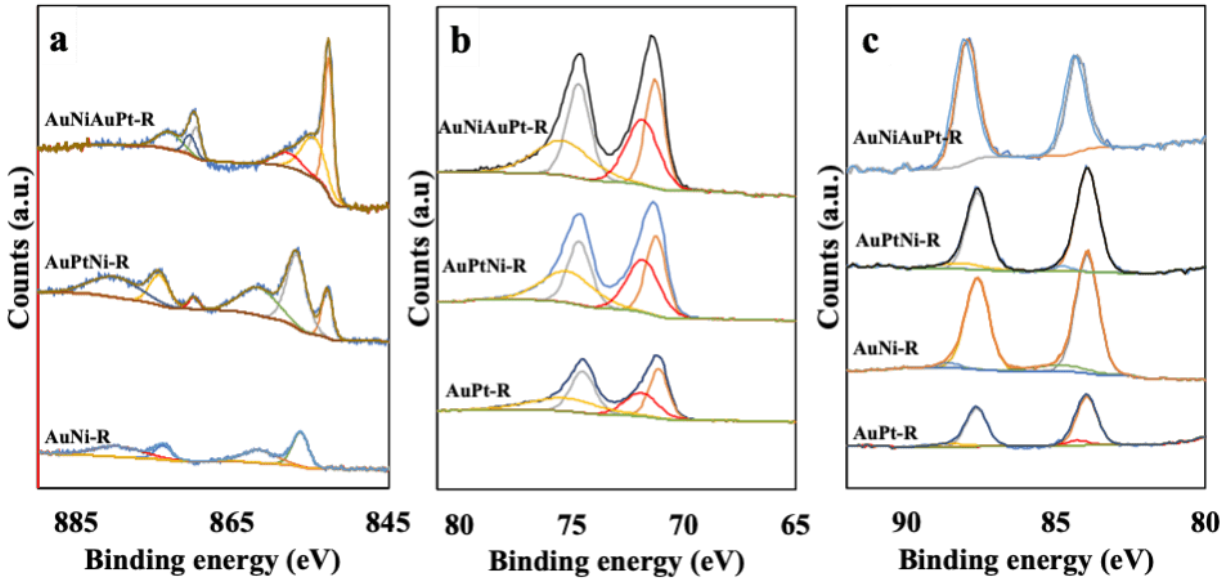

Figure 5.4 XPS spectra in the a) Ni 2p regions, b) Pt 4f regions and c) Au 4f regions for AuNiAuPt-R, AuPtNi-R, AuNi-R and AuPt-R samples.

Table 5.1 The summary of Au, Pt, and Ni peak location from XPS

Samples	Au $4f_{7/2}$ (eV)		Pt $4f_{7/2}$ (eV)		Ni $3d_{5/2}$ (eV)		
AuNiAuPt-R	84.0	84.9	71.2	71.9	852.7	854.6	858.0
AuPtNi-R	84.0		71.3	72.0	852.8	856.8	861.7
AuNi-R	84.0	85.0				856.3	861.5
AuPt	84.0	84.4	71.1	71.9			

Furthermore, the morphology and crystal structure of materials are characterized by TEM. Figure 5.5 a-d confirm the growth of 1D chains. The low magnification TEM images of the Au nanowires exhibit the highly porous chain-like structures, which is crucial for improving the electrocatalytic

activity. Our previous study reported that the self-assembled Au chains are 0.5 to 2 μm in length. After reduction, a continuous layer of the crystalline cover is formed. As shown in Figure 5.5 e&f, the electron energy loss spectroscopy (EELS) elemental maps of AuNiAuPt-R and AuPtNi-R and samples further prove this morphology. The combination of the TEM and XRD results suggest that Pt or Ni are formed on the surface of Au NPs to form a core-shell structure.[191] Comparing the Pt/Ni domains, AuNiAuPt-R shows a larger domain sized from 2-5 nm, where AuPtNi-R sample possesses highly homogenous Pt-Ni domains. Therefore, the system can successfully achieve atomic spatial control by varying the synthesis process.

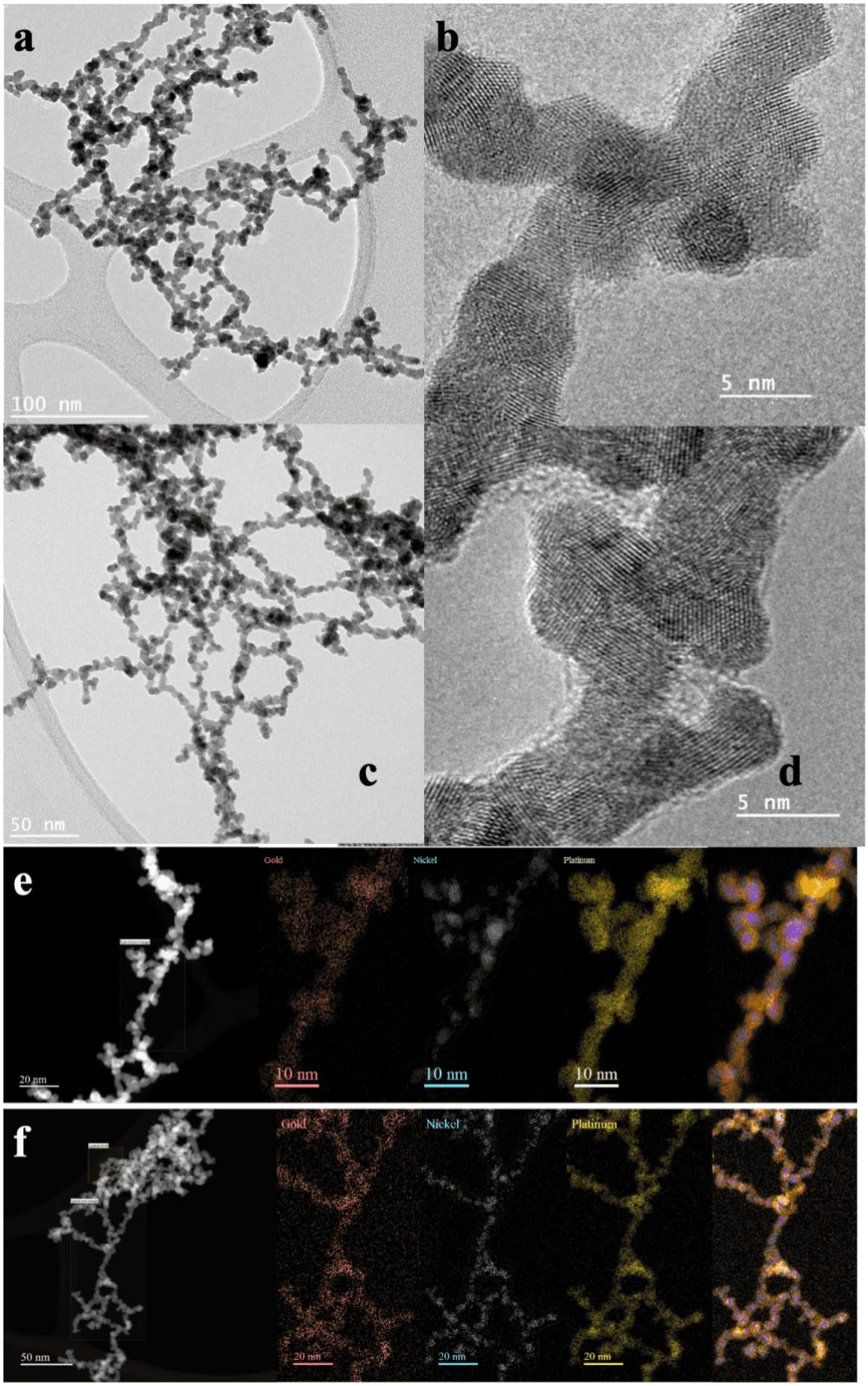

Figure 5.5 The TEM image of a) AuNiAuPt-R and c) AuPtNi-R, and the related HRTEM image b) and d) respectively, which presents a highly crystalline structure. TEM image with EELS map

of elemental distributions in the green region of e) AuNiAuPt-R and f) AuPtNi-R samples, that AuNiAuPt-R shows larger domain sized from 2-5 nm and AuPtNi-R sample possesses highly homogenous Pt-Ni domains.

3.2 Electrochemical measurement

3.2.1 Cyclic voltammograms (CVs)

Figure 5.6 presents the CV curves of hybrid electrodes in dopamine free PBS solution in a neutral pH environment. The samples of AuNi-R, AuPt-R, AuNiAuPt-R, and AuPtNi-R were subjected to CV at 20 mV/dec scan rate for 50 cycles for activation. As shown in Figure 5.6 a, the CV profile of AuNi-R sample demonstrates a pair of wide redox peaks located at -0.25 V (vs. Ag/AgCl) and -0.15 V. The cycles can also result in activation by transforming the Ni^0 or Ni^{2+} to $Ni(OH)_2$ or NiOOH by the following possible reactions:[143]

(1) $Ni + 2H_2O \rightarrow Ni(OH)_2 + 2e^- + 2H^+$

(2) $Ni^{2+} + 2H_2O \rightarrow Ni(OH)_2 + 2H^+$

(3) $Ni(OH)_2 + H_2O \rightarrow NiOOH + e^- + H_3O^+$

(4) $NiOOH + H_2O + e^- \rightarrow Ni(OH)_2 + OH^-$

As for AuPt-R samples in plain 0.01 M PBS solution, OH_{ads} species obtained from the water dissociation are first absorbed on the Pt surface in the positive scan. These OH_{ads} can accelerate the electrooxidation of the vicinity bonded carbohydrate (e.g., dopamine) by breaking the C-O-C bond.[192] At even higher potential (> 0.3 V), OH_{ads} can form a monolayer of oxygen-containing species PtO.[193] As for AuNiAuPt-R and AuPtNi-R, both CV profile presents three cathodic peaks at 0.15 V, and -0.12 V could represent the reduction of Pt, and -0.35 V could be Ni compounds reduction.[194,195,196]

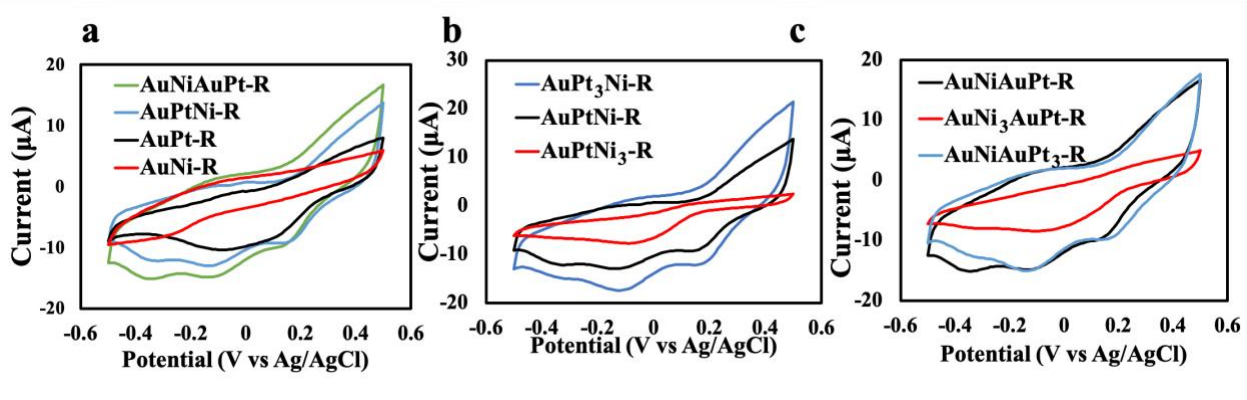

Figure 5.6 Cyclic voltammetry profiles of various samples in 0.01 M PBS.

In mixing chains or mixing ions series (in Figure 5.6 b&c), when the Ni ratio is increased by changing the additional volume, the conductivity decreases, and the peak at 0.15 V disappears. In contrast, samples with more Pt show an opposite trend. We can obtain several important information from the curve: First, when the CV program ran to higher potential, the Ni, Ni^{2+}, and $Ni(OH)_2$ can be oxidized into NiOOH corresponding to reversible reactions 3 and 4. This can be deduced by the presence of a cathodic peak at -0.2 V. However. Once the $Ni(OH)_2$ domain is formed, it would not be electrochemically reduced back to metallic Ni since reaction (1) is irreversible.[190] The NiOOH/$Ni(OH)_2$ domain formation reaches a steady state after 50 cycles. To prove the formation of NiOOH, the AuNiAuPt-R sample was first run 50 cycles in PBS, and then the materials were collected and analyzed by Raman measurement. From Figure 5.7, the peaks present at ~480 and 560 cm^{-1}, which belong to NiOOH, are observed in the sample after cycling.[197]

Additionally, the influence of the scan rate on the redox peak currents was then studied by cyclic voltammetry. The measurements were conducted at several scan rates from 10 to 200 mV s^{-1} in PBS without dopamine (Figure 5.8). The current of redox peak increases with the increase of scan rate. Furthermore, a linear relationship between the current and the scan rate (v) is observed. This suggests that the electron transfer process is a surface adsorption controlled reaction.[198,199,200] Besides, with the scan rate increase, oxidation/reduction peaks are slightly shifted to positive/negative potential due to the higher scan rate, which leads to a slower electron transfer process.

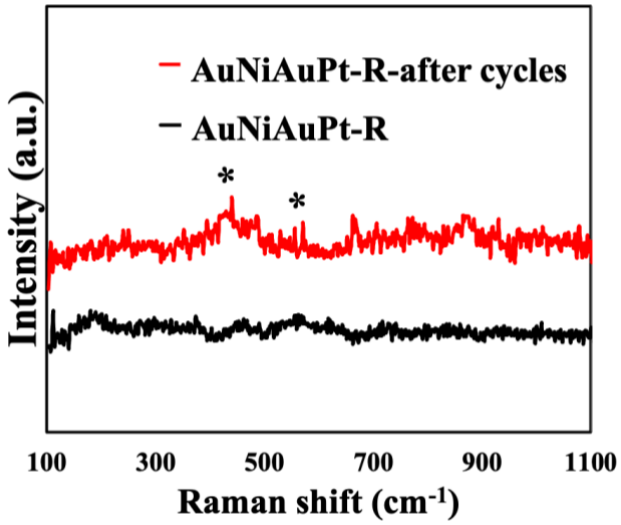

Figure 5.7 Raman spectra recorded the AuNiAuPt-R samples before and after electrochemically modification in PBS. The places labeled as * represent the formation of NiOOH after the cyclic voltammetry program.

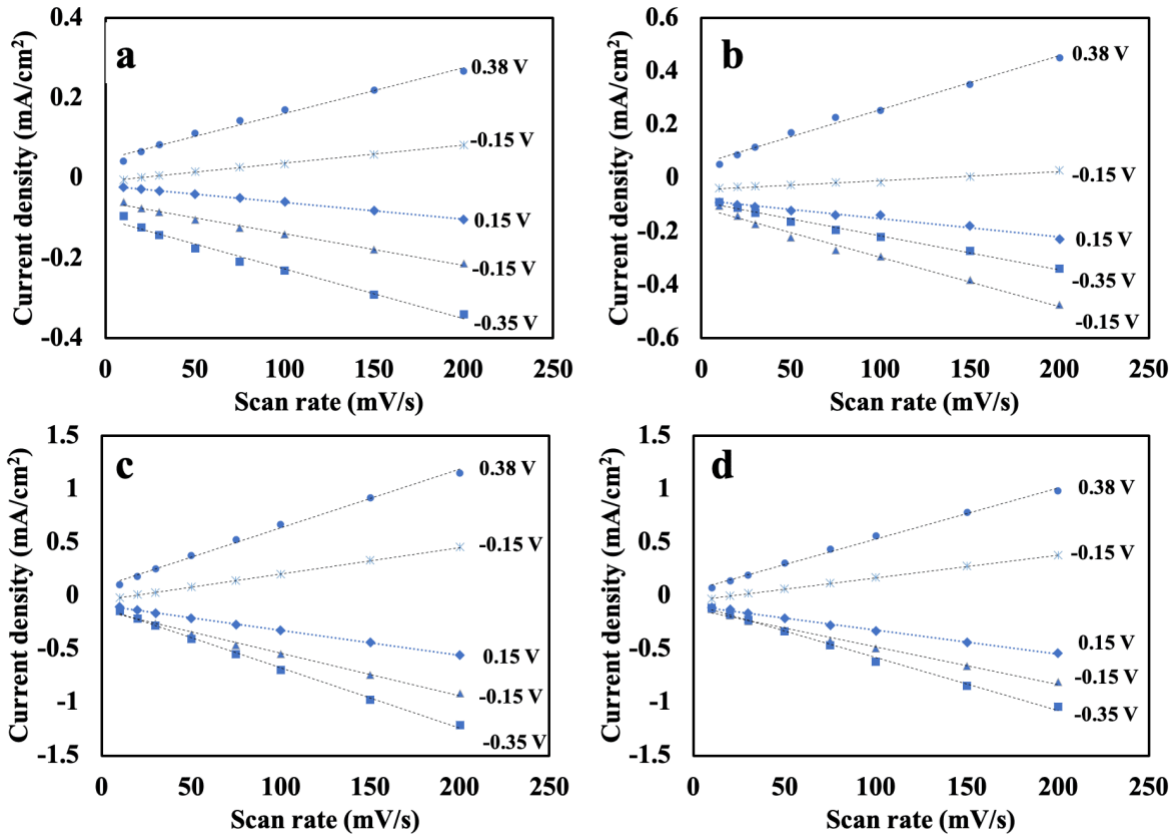

Figure 5.8 Variation of anodic and cathodic peak currents vs. scan rate for a) AuNi-R, b) AuPt-R, c) AuNiAuPt-R, and d) AuPtNi-R in PBS.

3.2.2 Dopamine detection

The synthesis has been designed to tune the atomic ratio of Pt:Ni from 0.7 to 5.6 to find the best sample by adjusting the volume ratio of $PtCl_4$ and $NiCl_2$ during the assembly process. Figure 5.9 presents the CV curves of hybrid electrodes in 0.5 mM dopamine in PBS solution in a neutral pH environment. As shown in the figure, compared with the CV scan without dopamine in solution (in Figure 5.6), the CV curves of all electrode materials present a pair of reversible prominent redox peaks related to the oxidation of dopamine where oxidation peaks locate at ~0.2 V and reduction peaks exhibit at 0.1 V. To better understand the dopamine oxidation reaction, cyclic voltammetry measurements were performed at several scan rates from 10 to 200 mV/s in PBS pH 7 containing 0.5 mM dopamine. Figure 5.9 b&c presents the redox peak current increases with the scan rate, and redox peaks are assigned to the reversible reaction of dopamine to dopaminoquinone. Furthermore, a linear relationship of the reduction peak potential and the scan rate and oxidation peak potential and $v^{1/2}$ are observed. These confirmed the electrooxidation of dopamine is a diffusion-controlled process, and reduction reaction is surface adsorption controlled.

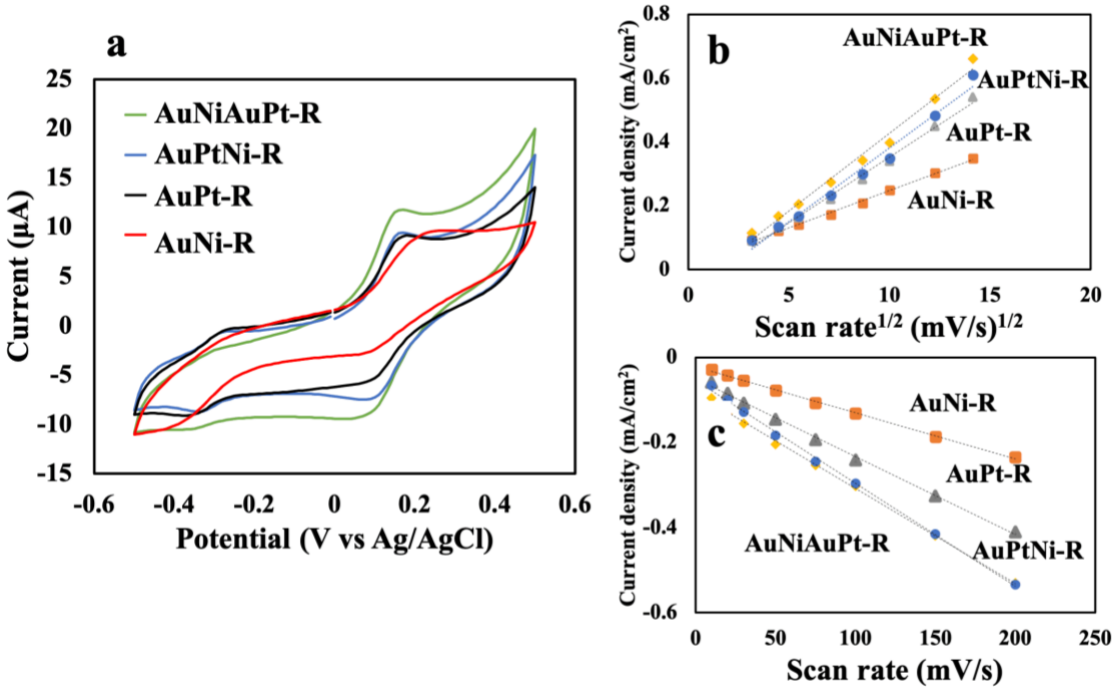

Figure 5.9 Cyclic voltammograms recorded for AuNi-R, AuPt-R, AuNiAuPt-R, and AuPtNi-R sample in PBS with 0.5 mM dopamine; b) Variation of anodic peak currents vs. square root of scan rate and c) variation of cathodic peak currents vs. scan rate in PBS with 0.5 mM dopamine.

On the other hand, to investigate more about the electrochemical materials, we calculated the redox peak difference, Δ*E*p. More details are presented in Table 5.2. For the AuPt-R sample, the cathodic peak current is almost the same with anodic peak current, and Δ*E*p is 0.07 V. Meanwhile, for the AuNi-R sample, the cathodic peak current is much smaller than the current value of the anodic peak with a 0.14 V Δ*E*p. This indicates that the reactions that occur on the AuNi-R material are semi-reversible. The decrease in peak cathodic current is attributed to unstable oxidation products. Besides the redox peaks of oxidation of dopamine to dopaminoquinone, another pair of peaks located around -0.35 V are observed, which is related to further oxidation of dopaminoquinone. As shown in Scheme 5.10, this is a fast cyclization reaction.[201]

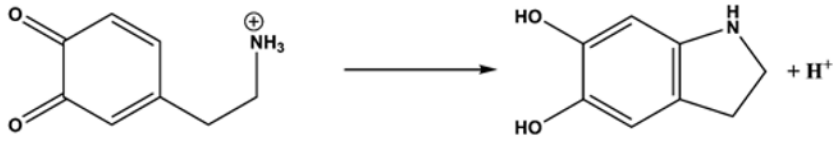

Figure 5.10 The scheme of electrocatalytic oxidation of dopaminoquinone.

Table 5.2 The redox peak difference, ΔE_p, of various samples

Sample	E_o (V)	E_r (V)	ΔE_p (V)
AuNi-R	0.24	0.1	0.14
AuPt	0.17	0.1	0.07
$AuPtNi_3$-R	0.21	0.1	0.11
$AuNi_3AuPt$-R	0.18	0.1	0.08
AuPtNi-R	0.17	0.1	0.07
AuNiAuPt-R	0.17	0.1	0.07
$AuPt_3Ni$-R	0.18	0.1	0.08
$AuNiAuPt_3$-R	0.18	0.1	0.08

* E_o, E_r, and ΔE_p are the potential of oxidation peak, reduction peak, and the redox peak difference.

However, all mixed chains samples possess ΔEp of less than 0.1 V. This suggests that Pt domains can improve the electron transfer rate. As can be seen in Figure 5.9 a, the pair of electrochemical

redox peaks of the AuNiAuPt-R sample presents the highest current response compared to AuNi, confirming a higher current response due to the presence of Pt domains. Comparing AuPtNi-R and AuPt-R samples, the Ni domain can increase dopamine absorption, facilitating the reaction. Therefore, mixing Ni and Pt could lead to higher catalytic ability due to synergistic effect and higher electron transfer rate. There could be competitive adsorption between anions and dopamine. However, when dopamine was added into the solution, the absorption peak of HPO_4^{2-} in negative scan gradually decreased. In this work, alloy nanocomposites show better response compared to the corresponding monometallic nanoparticles because of the higher conductivity and faster electron transfer rate.[183] In addition, the porous morphology of Au chains provides a higher surface area with more active sites. This helps the faster mass transport of the reactants and products. On the other hand, dopamine contains catechol and amine functional groups, which show excellent affinity with inorganic surfaces and organic groups, like the carboxylic group.[183] This reduces the effect of interferent molecules and also increases the oxidation current.[174,183]

3.2.3 Effect of deposition

To obtain the critical deposition mass, successive volume addition of the active materials on GCE was investigated in PBS without dopamine. As shown in Figure 5.11, a greater mass of the catalyst increases the current response. In addition, the stacked porous structure can help the diffusion of reactants to reach the active sites.[179] At 15 µL of samples, the materials can completely cover the active area on the GCE surface, and further addition does not increase the current response. Meanwhile, the material might peel off from the electrode at a higher loading density.[194]

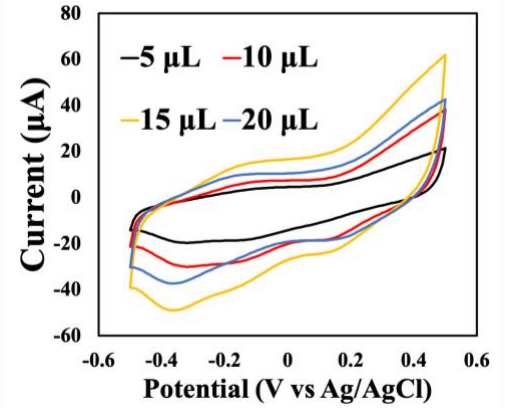

Figure 5.11 Cyclic voltammograms profile of successive volume addition of the active materials on GCE in PBS.

3.2.4 Calibration line

The dopamine detection performance is evaluated using amperometry. The calibration curves (as shown in Figure 5.12 b) are obtained from amperometric responses of the materials deposited on GCE upon the successive injection of dopamine at an applied potential. From Figure 5.12 a, it is clearly observed that after adding the dopamine, the current response increases sharply within few seconds and then decreases a little at low concentrations (less than 0.5 μM). Overall, the Au NWs' current response increases with the dopamine concentration. Furthermore, the change in response is observed in less than 15 sec. These results show that the Au NWs provide fast electron transfer, with high density of active sites and a porous structure which leads to effective mass transfer. The AuNiAuPt-R materials show the highest electrochemical activity. The Pt, Ni, and Au form domains with a nanometer scale according to the XRD spectrum. These not only modify the electronic properties of Pt and Ni to form a suitable bond strength with the adsorbate (dopamine) but also enhances the electron transfer rate. Furthermore, the nanochains have a large surface area and a porous structure, which helps to improve the catalysis performance. Due to the diffusion process and ultrafast oxidation, the response current is recorded after 45 s following the addition of dopamine. The AuNiAuPt-R presents the best performance where the current density increases linearly with dopamine concentration, from 0.14 to 36.5 μM (R=0.994). The sensitivity was calculated to be 1279.3 μA mM^{-1} cm^{-2} at 0.16 V vs. Ag/AgCl, an ultrahigh sensitivity compared with other works.[179,183,185,201]

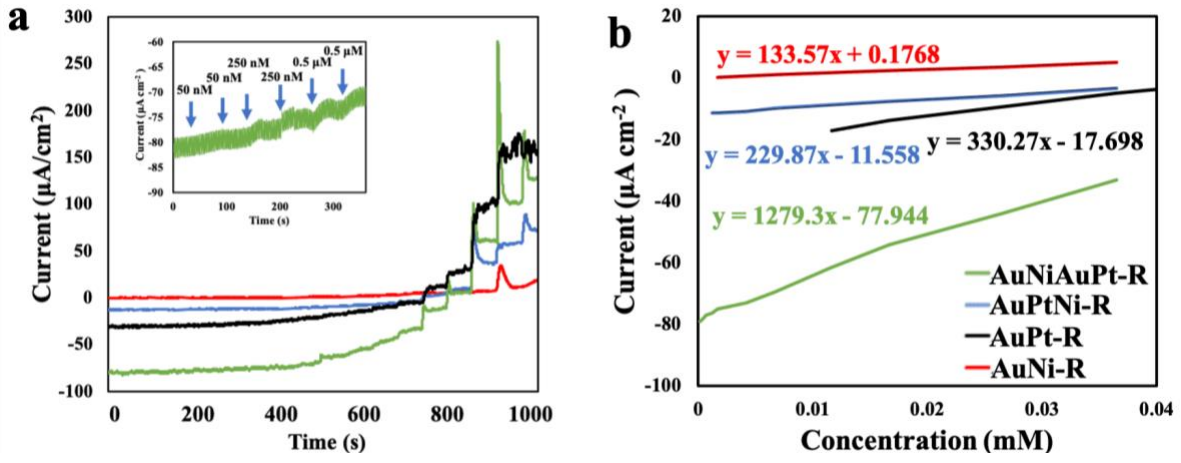

Figure 5.12 a) Amperometric current-time responses for different samples to successive addition of dopamine; b) Variations of current densities against Dopamine concentrations in PBS.

The detection limit is 0.01 μM with a signal-to-noise ratio of 3. Based on the excellent electrochemical characteristics, the AuNiAuPt-R is an excellent electrochemical detection material for dopamine. The properties of electrochemical sensors for all involved Au chains for dopamine detection are compared in Table 5.3.

The AuNiAuPt-R has a relatively wider linear range, higher sensitivity, and lower detection limit. The excellent performance can be attributed to the large surface area and fast transfer rate of charges which improves the electrocatalytic activity of the AuNiAuPt-R sample towards the sensing of dopamine. Thus, the combination of both Pt and Ni based composites provides excellent electrocatalytic performance and superior electronic conductivity compared to the plain AuPt-R and AuNi-R samples. Meanwhile, the presence of Ni nanocomposites facilitates the adsorption and oxidation of the dopamine molecule and desorption of final products on nanomaterials surface. The electron-injection mechanism also further supports the better catalytic performance of AuNiAuPt-R than AuPt-R and AuNi-R.[182] The electrons from Au NPs and metallic Pt can be injected into $Ni(OH)_2$ or NiOOH phase. This injection builds an electric field at the interface, which can accelerate the transfer of electrons.[190] It explains that AuNiAuPt-R samples have better output current density for the oxidation of dopamine than AuPt-R and AuNi-R.[190]

Table 5.3 The detailed information of the dopamine detection performance of various composites

Sample	Sensitivity ($\mu A\ mM^{-1}\ cm^{-2}$)	Range (μM)		R^2	LoD (μM)
AuNi-R	133.6	1.7	36.5	0.996	0.012
AuPt	330.3	11.6	371.8	0.996	0.019
$AuPtNi_3$-R	368.9	0.4	134.5	0.998	0.003
$AuNi_3AuPt$-R	430.1	0.2	85.8	0.993	0.002
AuPtNi-R	229.9	1.2	36.5	0.993	0.011
AuNiAuPt-R	1279.3	0.1	36.5	0.994	0.010
$AuPt_3Ni$-R	555.2	0.4	134.5	0.993	0.034
$AuNiAuPt_3$-R	574.1	0.7	134.5	0.994	0.029

A series of experiments have been done to improve the oxidation performance by changing Pt/Ni ratio. The final optimized Pt/Ni ratio is 1:1. The relationship between the catalytic activity and elemental domain size is studied by mixing two elements at the different assembly processes. From the previous section, the mixing ions samples form a relatively homogeneous structure without clear boundaries of each elemental domain. However, in the AuNiAuPt-R sample, we can observe distinguishable domains. Our previous study proved that the relative spatial placement of domains could affect the catalyst performance.[72]

From Table 5.3, AuNiAuPt-R with well-defined domains of Pt and Ni performs better than AuPtNi-R catalyst. With the Pt/Ni ratio of 1:1, the dopamine oxidation sensitivity of the mixed chains sample is 5.5 times higher than the AuPtNi-R samples with homogeneous elements distribution. The performance of the AuNiAuPt-R catalyst for dopamine oxidation is also 3.8 times that of AuPt-R and 9.6 times of AuNi-R. All the samples with Ni ions inside show better performance, which could be due to the synergistic effect of Pt and NiOOH. We also observed that for the mixing ions samples higher Pt/Ni ratio improves the sensitivity. When the Pt/Ni ratio is varied from 1:3 to 3:1, the sensitivity increased 1.5 times. NiOOH domains with neighboring Pt sites are required to oxidize dopamine molecules effectively.[72] Therefore, the spatial distribution of elements plays a crucial role in the catalyst's performance due to the scale of elemental domains.

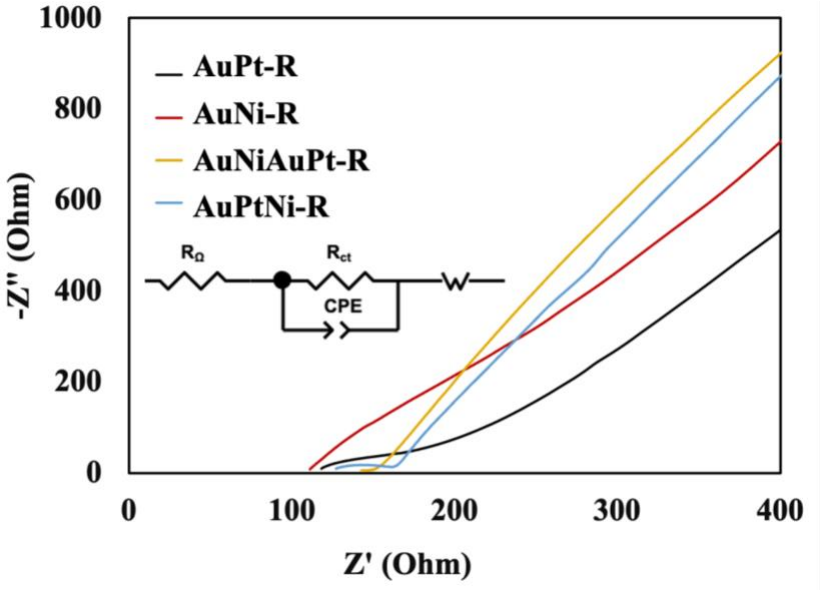

Figure 5.13 Electrochemical impedance spectroscopy (EIS) spectra of AuPt-R, AuNi-R, AuPtNi-R, and AuNiAuPt-R. The inset is the equivalent circuit.

As shown in Figure 5.13, compared with the AuPt-R sample (~39 Ohm), AuNi-R (~65 Ohm) presents a much lower charge-transfer resistance (R_{ct}). Furthermore, AuNiAuPt-R (~35 Ohm) and AuPtNi-R (~43 Ohm) both show lower R_{ct} than even AuNi-R. This confirms the involved Ni facilitates charge transfer. Meanwhile, the AuNiAuPt-R sample exhibits the lowest R_{ct}, proving that nanoscale domains improve electrical conductivity at the electrode surface.[203,204]

3.2.5 Selectivity, reproducibility, stability, and reusability of device

Selectivity, reproducibility, and stability of electrodes are also important parameters to evaluate the practical performance. Some organic compounds such as uric acid (UA), ascorbic acid (AA), acetaminophen (AP), and glucose can strongly adhere to the electrode surface and severely reduce the selectivity of active material.

As seen in Figure 5.14, the chronoamperometry measurements of the AuNiAuPt-R sample with the interference of UA, AP, glucose, and AA at the applied potential of 0.16 V were performed. The current responses to successive addition of UA, AP, glucose, and AA were negligible. Meanwhile, the electrode presents a significant electrochemical response to 10 μM dopamine.

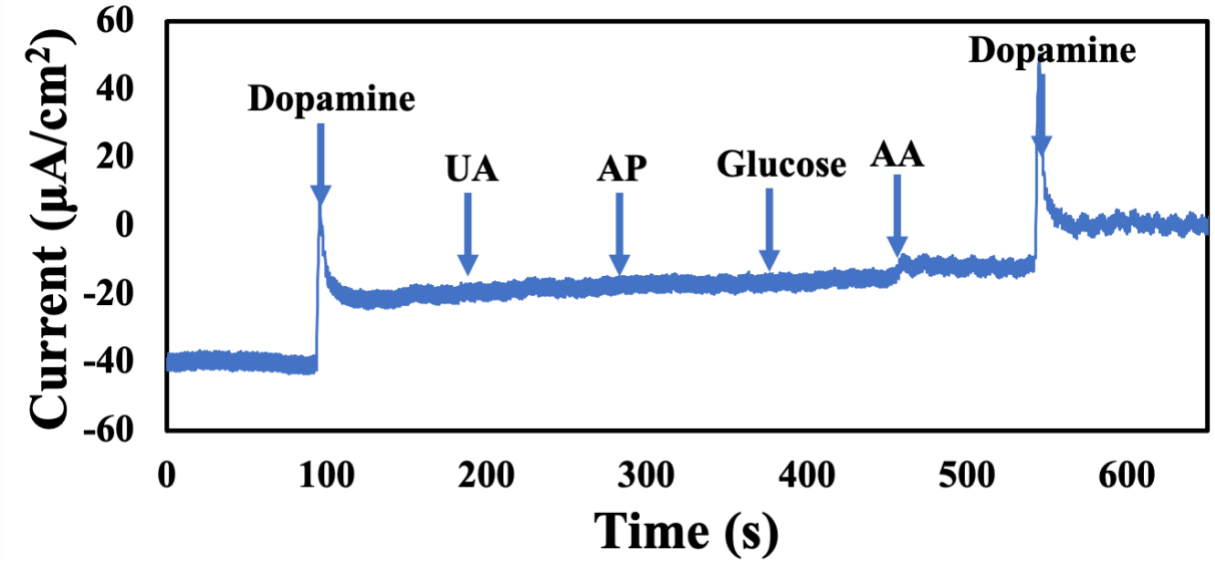

Figure 5.14 The chronoamperometry measurements with the interference of 10 μM UA, 10 μM AP, 250 μM glucose, and 10 μM AA with 10 μM Dopamine.

3.2.6 Reproducibility and stability of electrodes

The stability and reproducibility of the Au chains were tested to determine the efficiency of the active materials. Three different AuNiAuPt-R deposited on GCE prepared independently were tested to characterize the reproducibility. The relative standard deviation (RSD) is 7%. This suggests that the AuNiAuPt-R presents excellent reproducibility. Moreover, the shelf-life of materials was measured as well. Only a decrease of 6% was found for active materials after being stored in the ambient environment over four months, indicating good stability and reproducibility of the Au chains system.

4 Conclusion

The self-assembled 1D gold nanochains with the controlled spatial distribution of elements were developed to detect dopamine. The AuNiAuPt-R sample shows the best performance with high sensitivity of 1279.3 μA mM^{-1} cm^{-2} in the range of 0.1-36.5 μM. Compared with homogeneously distributed elements, nanometer scale domain size is necessary to improve the electrocatalytic sensitivity. In addition, this synthesis process provides a simple way to fabricate multi-element composite for electrocatalytic applications.

Part B Self-Assembled Au NWs doped with various elements as electrocatalysts

Chapter 6 Au-Ni-Cu nanocomposites as glucose catalyst

1 Introduction

The World Health Organization claims that about 422 million people worldwide have diabetes, a chronic disease that can seriously damage vital organs. Diabetes is usually monitored by the level of blood glucose. In a conventional way, this is done via an invasive finger-stick procedure. However, the patients suffer pain and stress during the time. Thus, a non-invasive method to precisely monitor glucose levels is highly desirable. The glucose level in sweat is in a lower range 0.25-1.5 mM while in the blood is 3-8 mM.[189]

Electrochemical sensors play an important role in clinical diagnostics owing to their high sensitivity and fast response. Overall, there are two main categories: enzymatic sensor and non-enzymatic sensor. Even though enzymatic glucose sensors remain commercially unchallenged, they are impacted by ambient conditions (like oxygen, pH, temperature, and humidity) and enzyme activity and stability. In this respect, non-enzymatic electrodes have been attracting significant attention, which can directly oxidize glucose in the sample and free from oxygen limitation with high stability and sensitivity. Various glucose biosensors have been investigated including noble metal (e.g. Au,[205,206] Pt[194,196]), transition metal (e.g. Ni,[207] Cu[208,209]), metal-oxide (NiO, CuO, Co_3O_4)[209,210,211,212,213], conductive polymer (PANI), carbon nanotubes and graphene.[189,194] Although the noble metals perform excellent catalysis behavior, they are still limited by the high cost and low sensitivity. Transition metal or metal oxides can lower the cost but have poor conductivity, which impedes the electron transport resulting in low performance.[210]

This chapter presents research results from integrated Au NCs with a cover layer of Cu and Ni composites to produce electrochemical glucose sensors using the synthesis method developed in previous chapters. This core-shell nanowire-like glucose sensor displays high electrocatalytic activity with a large active surface area, electroconductivity, and stability.

2 Materials and methods

2.1 Materials

2.1.1 Preparation of AuCu and AuNi nanochains

55 µL of 4 mg/mL $CuCl_2$ (99.9%, Sigma Aldrich) and 80 µL of 4 mg/mL $NiCl_2$ (99.9%, Sigma Aldrich) were mixed with 1 mL gold nanoparticles separately and then left on the shaker with a speed of 300 rpm until the solution color changed to dark blue. After the self-assembly process and mixing the chains, they are reduced by 75 µL of 4 mg/mL $NaBH_4$ (99%, Sigma Aldrich), which color turned to black first and then pink (samples labeled as AuCu-R and AuNi-R). The stocked samples are stable in aqueous media over two months.

2.1.2 Preparation of $AuCuNi/AuCu_3Ni/AuCuNi_3$ (mixing ions) nanochains

55/82.5/27.5 µL of 4 mg/mL $CuCl_2$ and 80/40/120 µL of 4 mg/mL $NiCl_2$ were mixed first and then added into 2 mL gold solution, respectively. When the color turned to dark blue, the solution was reduced by 150 µL of 4 mg/mL $NaBH_4$, which color turned to black (samples labeled as $AuCuNi/AuCu_3Ni/AuCuNi_3$-R). The stocked samples are stable in aqueous media over two months.

2.1.3 Preparation of $AuNiAuCu/AuNi_3AuCu/AuNiAuCu_3$ (mixing chains) nanochains

1/1.5/0.5 mL of AuNi chains solution before reduction and 1/0.5/1.5 mL of AuCu chains solution before reduction were well mixed first. Then 2 mL mixture was reduced by 150 µL of 4 mg/mL $NaBH_4$, which color turned to black (samples labeled as $AuNiAuCu/AuNi_3AuCu/AuNiAuCu_3$-R). The stocked samples are stable in aqueous media over two months.

2.2 Characterization

Zeiss Ultraplus Field-emission Scanning Electron Microscopy (FESEM) was used to measure the morphology of samples and the deposition. Transmission electron microscopy (TEM) images were obtained with an LEO 912ab energy filtered transmission electron microscope (EFTEM). UV-Visible absorption spectra of samples were detected by Perkin Elmer Lambda 750

spectrophotometer. The powder X-ray diffraction (XRD) pattern was measured by the PANalytical Empyrean diffractometer with Cu Kα radiation (λ = 1.54 Å). X-ray Photoelectron Spectra (XPS) was performed on VGS ESCALab 250.

2.3 Electrical measurement

The electrolyte is 0.1 M NaOH. Concentrations of β-+-glucose (Sigma Aldrich) in 0.1 M NaOH were varied between 10 μM and 100 mM. Cyclic voltammetric (CV) and chronoamperometric experiments were performed with an Ivium CompactStat Electrochemical Analyzer electrochemical workstation. A conventional three-electrode system was adopted using GCE as working electrode, SCE as reference electrode, and Pt wire as a counter electrode. 15 μL gold chains solution was drop-cast on GCE to do measurements. All experiments were performed at room temperature. All the glucose detection experiments are operated under a stirrer with 500 rpm speed. CV scans were recorded in basic solution from 0.2 to 0.8 V vs. reference electrode at different scan rates. For chronoamperometry measurements, the amperometric response of the electrode toward successive additions of glucose is recorded. A current response versus glucose concentration calibration curve is established using the readout current (the detection current averaged over the last 15 s range). During the measurements, it was ensured that the baseline current (in the absence of glucose) was stabilized before adding glucose. The current change with time is tracked at the working electrode as a function of increasing glucose concentration. Interference tests were performed with electroactive compounds, such as ascorbic acid (AA), uric acid (UA), acetaminophen (AP), and dopamine (DA) (added to a concentration of 0.5 mM), which are commonly present in physiological samples and cause problems in the accurate determination of glucose (0.5 mM). The LoD was determined from the relationship, expressed as:[189]

$$LoD = 3.3\sigma / S$$

where σ is the standard deviation of the baseline and S is the slope of the sensor's linear calibration curve. Sensitivity was defined as the slope of the sensor's calibration curve normalized to the geometrical area of the electrode.

3 Results and discussion

3.1 Characterization

From the Figure 6.1 a, the SEM image shows the 1D morphology of $AuCu_3Ni$-R, AuCuNi-R, $AuCuNi_3$-R, $AuNi_3AuCu$-R, AuNiAuCu-R and $AuNiAuCu_3$-R samples. Clearly, all of them present a wire-like structure. The scheme is presented in Figure 6.1 b. The samples are deposited on the substrate, and the wires have a stacked structure resulting in a connected porous network that can form a continuous pathway for electrons. The ratio of Ni/Cu of 1 presents the best performance. Thus, the later characterization will mainly focus on AuNiAuCu-R and AuCuNi-R.

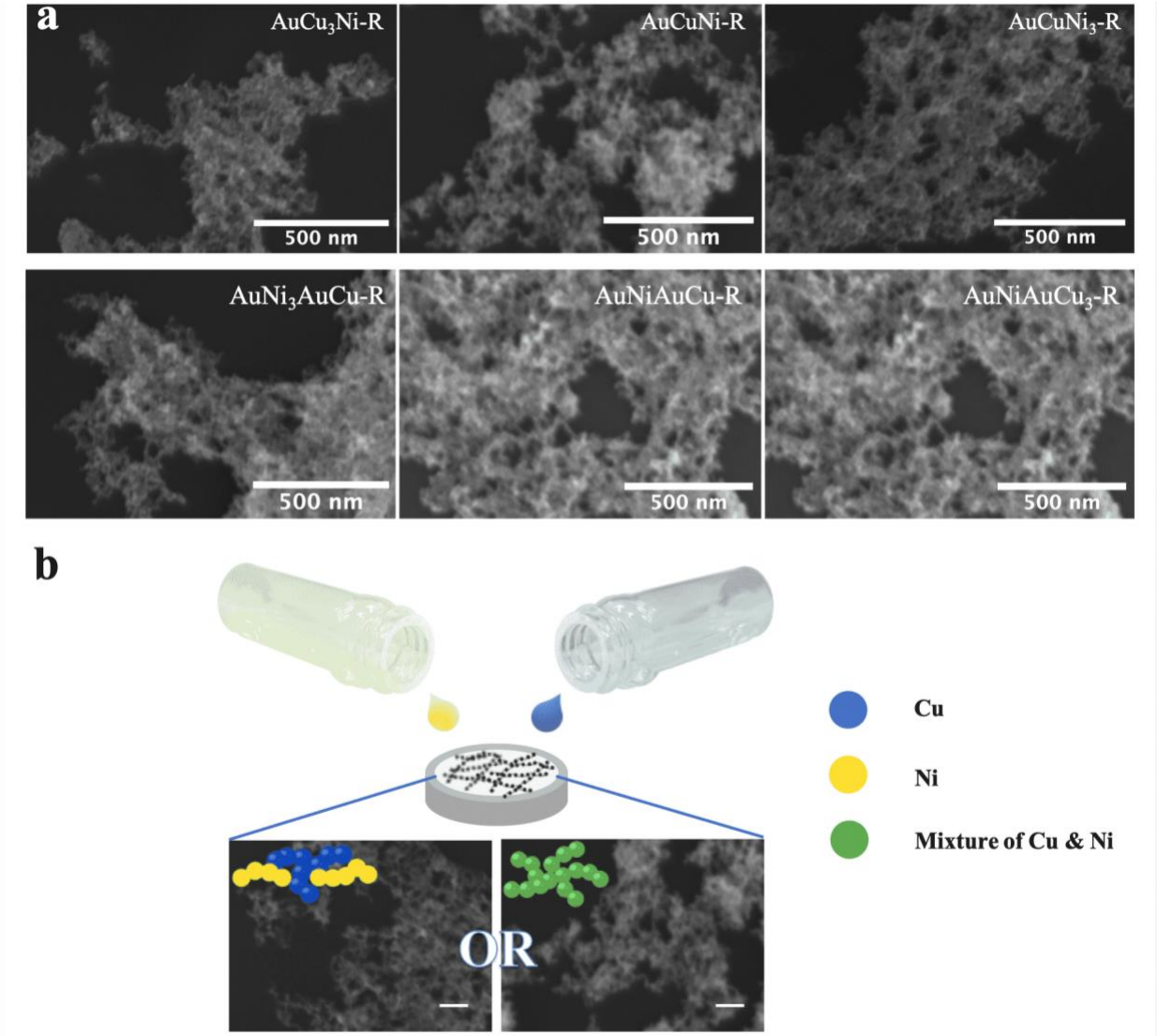

Figure 6.1 a) The FESEM images of various samples shows that all have nanochain based porous structure; b) The schematic image of two kinds of gold nanowires. The scale bar is 100 nm.

The elemental mapping of the TEM images (in Figure 6.2 b&c) present Cu or Ni covers the Au NPs surface with a thickness of 1 to 2 nm. The synthesis methods can control the domain size element achieving spatial distribution. As discussed in chapter 4, the samples with mixing the ions have homogenous elemental placement, while AuNiAuCu-R samples present nanometer scaled domain size (the schematic image in Figure 6.1 b illustrates the difference). However, there are small Cu-Ni segregations around the chains, as shown in elemental mapping images. It could be due to dislocation of Au and Cu/Ni during the synthesis process to reduce the epitaxial strain. As shown in Figure 6.2 a, the XRD pattern of all reduced composites displays the main peak of Au (111). The XRD spectrum of Au NPs has a broad peak around 38.4° which represents the size of Au is small. However, AuNi presents a dominant peak at 38.5° and in AuCu, the peak shifts to 38.6°, which indicates the formation of Ni or Cu alloy with Au. The spectra do not show any obvious peak for Ni or Cu, which might be due to formation of amorphous or ultrathin layer of Ni/Cu compounds.[214] Comparing the XRD spectra of AuCuNi-R and AuNiAuCu-R samples, the mixed ions one has a slightly wider peak, indicating a smaller domain size for the mixed ions chains.

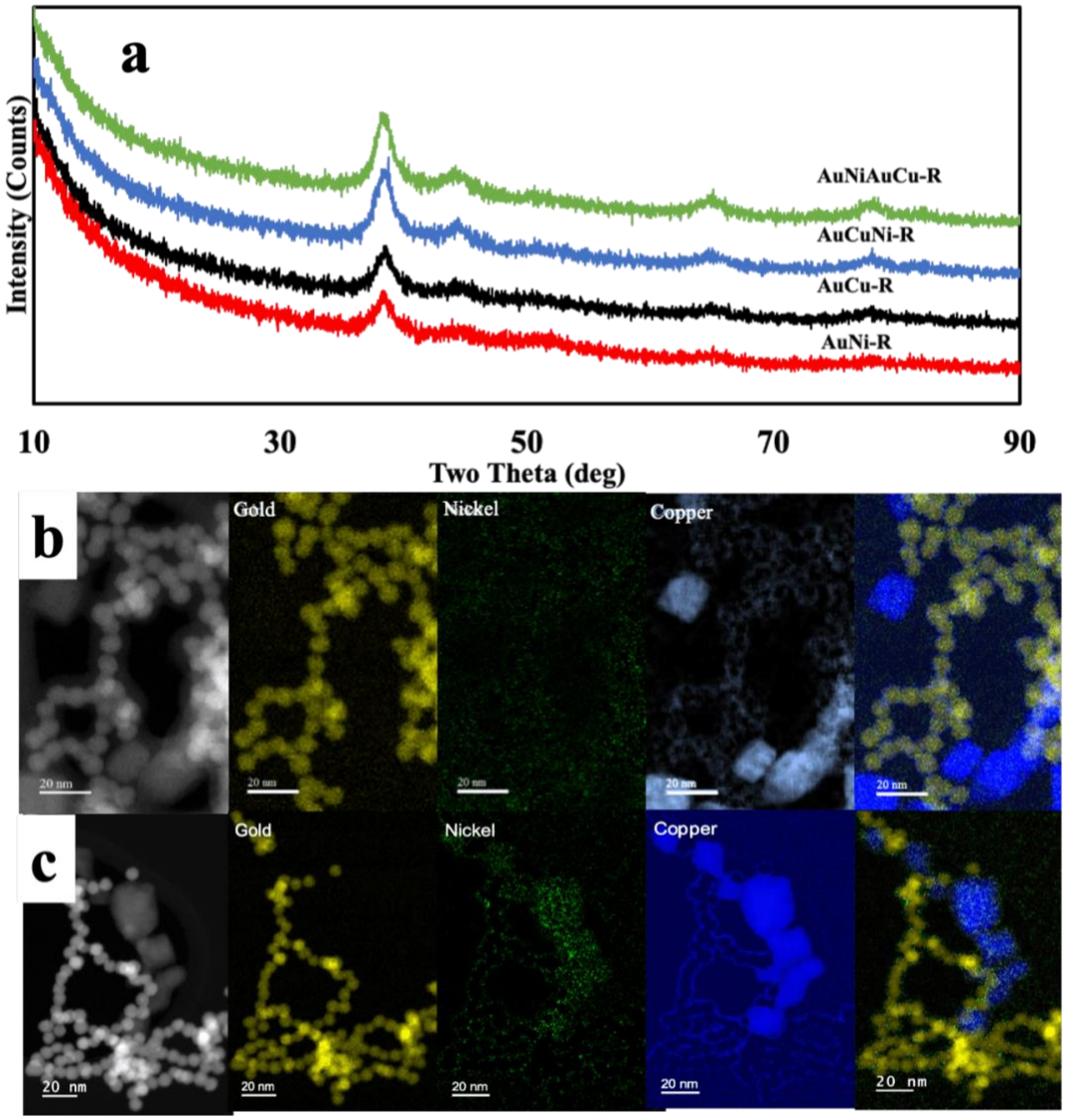

Figure 6.2 a) XRD spectra of of AuCu-R, AuNi-R, AuCuNi-R and AuNiAuPt-R; the TEM images and EELS of b) AuNiAuCu-R and c) AuCuNi-R samples present Cu and Ni shells on the Au nanoparticle chains.

The chemical compositions were confirmed by XPS measurement. All Au 4f XPS spectra of AuCu-R, AuNiAuCu-R, and AuCuNi-R samples (Figure 6.3 a) exhibit the binding energies of 83.9 and 87.6 eV attributed to Au $4f_{7/2}$ and Au $4f_{5/2}$, respectively, which are metallic gold.[215] There are also another pair of peaks located at 84.2 and 87.8 eV, representing the formation of alloy.[215] The Cu $2p_{3/2}$ spectrum of AuCu-R (Figure 6.3 b) can be resolved into two components at 931.7 and 934.2 eV assigned to metallic Cu and Cu^{2+}, respectively.[216] The peaks are accompanied by two broad satellite peaks at 940.2 and 943.1 eV ascribed to Cu^{2+} and CuO.[208,217,218] As for the

AuNiAuCu-R sample, the Cu^{2+} peak at 934.2 eV shifted to 933.6 eV might be explained by the presence of Ni. In comparison, the Cu^{2+} peak of the AuCuNi-R sample shifts to 933.8 eV. These could be due to the existence of highly homogenous distributed Cu and Ni domains. The Ni 2p spectrum of AuCuNi-R sample (Figure 6.3 c) is fitted with a dominant peak at 855.6 eV, and a small peak at 857.2 eV from NiO and $Ni(OH)_2$.[219] The AuNiAuCu-R sample Ni 2p spectrum is only consistent with NiO peaks at 855.2 eV for the Ni $2p_{3/2}$.[220] The AuNiAuCu-R, therefore, is dominated by Ni^{2+} state. In contrast, the AuNi-R sample only presents $Ni(OH)_2$ at 856.3 eV.[221] The atomic ratio of Ni/Cu measured by EDX for $AuNi_3AuCu$-R, AuNiAuCu-R, $AuNiAuCu_3$-R, $AuCuNi_3$-R, AuCuNi-R and $AuCu_3Ni$-R is 2.4, 1.2, 0.5, 3.0, 1.5 and 0.8, respectively.

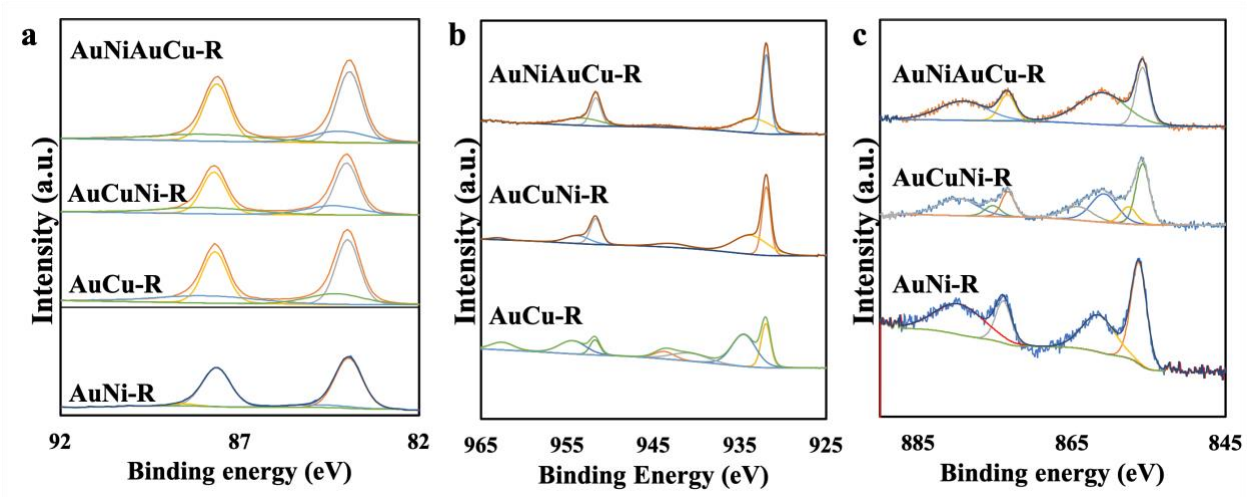

Figure 6.3 XPS spectra of assembled Au chains in a) Au 4f region, b) Cu 2p region, and c) Ni 2p region.

Figure 6.4 shows the UV-Visible spectra of Au NPs, AuCu-chains, and AuNi-chains. As for the Au NPs, it presents a maximum absorption peak, λ_{max}, at 520 nm. Au NCs exhibit a similar spectrum with λ_{max} at 620 nm and a broad shoulder at ~520 nm. For mixed ions samples, with the increase of Ni/Cu ratio inside, the λ_{max} has a slight red-shift. In contrast, mixed chains samples do not show an obvious shift. The red-shift in the absorbance maxima confirms that Au NPs are physically linked before the reduction.[222,223] After the reduction by $NaBH_4$, Au NCs present a single peak ~530 nm. After the reduction, the spacing between the Au nanoparticles has increased due to an ultrathin layer Cu-Ni cover formed on each Au NPs, which is similar to the presenting in EELS mapping (as shown in Figure 6.2 b&c).

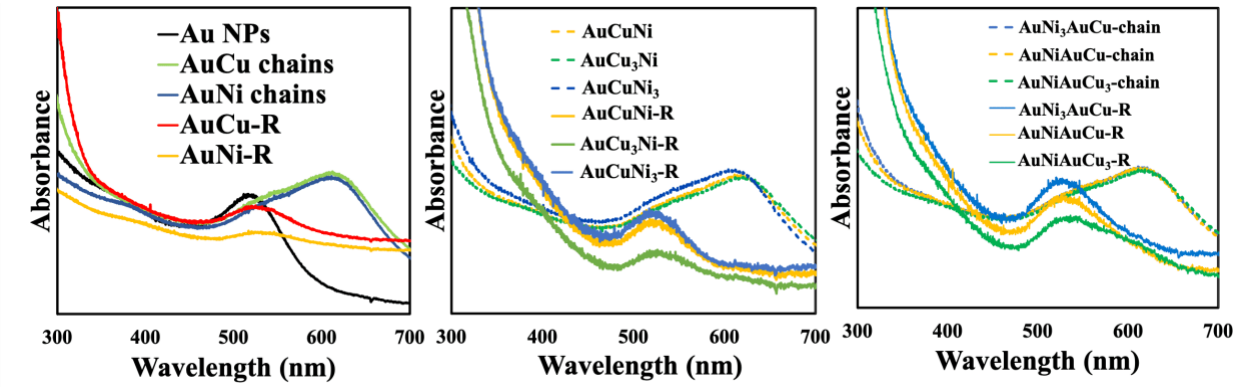

Figure 6.4 UV-Vis spectrum of self-assembled Au nanochains and the samples after reduction.

3.2 Electrocatalytic activity

Using 0.1 M NaOH as the electrolyte, the spatial distribution of Cu and Ni composites on the surface of Au NPs can be transformed to Cu/Ni hydroxide or (oxy)hydroxide by cyclic voltammetric activation (in Figure 6.5). Ni and Cu based nanomaterials can be oxidized into NiOOH and CuOOH in 0.1 M NaOH solution with a confined crystalline size during the CV scanning. After CV scanning for 50 cycles, stable redox peaks appear for all the samples. As for the AuNi-R sample, a pair of redox peaks are observed, with an anodic peak at 0.45 V and a cathodic peak at 0.35 V, which might be the conversion of Ni^{2+} to NiOOH.[207] The relevant mechanism is:[184]

(5) $Ni + 2OH^- \rightarrow Ni(OH)_2 + 2e^-$

(6) $Ni(OH)_2 + OH^- \leftrightarrow NiOOH + H_2O + e^-$

(7) $NiO + OH^- \leftrightarrow NiOOH + e^-$

Even though AuCu-R experienced the same process, the cathodic peak shifts to 0.6 V, and the anodic current continuously increases without presenting any obvious peak. During the cycling, the following possible electrochemical reaction could happen:[224,225]

(8) $Cu + 2OH^- \rightarrow Cu(OH)_2 + 2e^-$

(9) $Cu(OH)_2 + OH^- \leftrightarrow CuOOH + H_2O + e^-$

(10) $CuO + OH^- \leftrightarrow CuOOH + e^-$

As shown in Table 6.1, with different atomic ratios of Ni/Cu, the redox peak's location shifts differently.

Table 6.1 The redox peaks location of various composites in 0.1 M NaOH

Sample	Anodic peak (V)	Cathodic peak (V)
AuCu-R	N/A	0.60
AuNi-R	0.45	0.35
$AuCu_3Ni$-R	0.45	0.34
AuCuNi-R	0.45	0.33
$AuCuNi_3$-R	0.45	0.33
$AuNiAuCu_3$-R	0.60	0.35
AuNiAuCu-R	0.55	0.43
$AuNi_3AuCu$-R	0.51	0.31

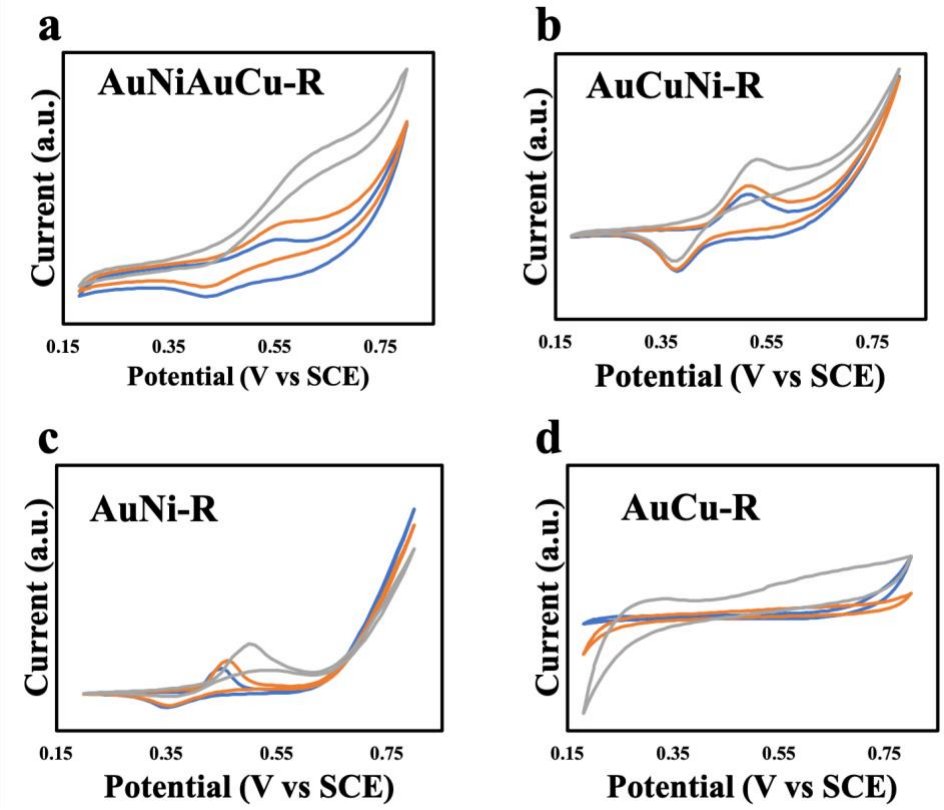

Figure 6.5 Cyclic voltammetric profile of a) AuNiAuCu-R, b) AuCuNi-R, c) AuNi-R and d) AuCu-R samples in 0.1 M NaOH with 0 mM (in blue line), 0.5 mM (in orange line) and 2.5 mM (in grey line) glucose.

As can be seen, the mixed ion samples' redox peaks do not shift much. The possible reason could be the ions are homogeneously distributed on Au NPs surface. In contrast, the redox peaks of mixed chains samples with nanometer domains separation show an obvious shift. For example, the difference between the anodic peak of $AuNiAuCu_3$-R and $AuNi_3AuCu$-R is 0.09 V. Compared with AuNi-R, whose anodic peak is located at 0.45 V, it can be clearly noticed that when more Ni is introduced into the samples, the location of anodic peak shifts closer to the AuNi-R peak position, due to the domination by oxidation of Ni during the CV cycling. Therefore, the oxidation potential shift depends on the ratio of Ni/Cu.

The cyclic voltammogram for the AuNiAuCu-R electrodes in 5 mM NaOH and 5 mM glucose solution is presented in Figure 6.6. A pair of redox peaks at 0.66/0.53 V is the activation of Ni and Cu into a higher state. A higher current response at 0.85 V represents the oxidation of glucose. Base on a previous study, the glucose oxidation mechanism could be expressed as:[226,227]

(11) $Ni(OH)_2 + OH^- \rightarrow NiO(OH) + H_2O + e^-$

(12) $NiO(OH) + \text{glucose} \rightarrow Ni(OH)_2 + \text{glucolactone}$

(13) $Cu(OH)_2 + OH^- \rightarrow CuO(OH) + H_2O + e^-$

(14) $CuO(OH) + \text{glucose} \rightarrow Cu(OH)_2 + \text{glucolactone}$

The probable mechanism could be that NiOOH/CuOOH receives an electron from glucose and becomes Ni^{2+}/Cu^{2+} while glucose is oxidized into gluconolactone. Then Ni^{2+}/Cu^{2+} releases an electron to the Pt wire to regenerate NiOOH/CuOOH. Thus, the potential of glucose oxidation depends on the potential of redox couples. To prove that Cu and Ni have been first oxidized into a higher state and then catalyzed glucose oxidation, the cyclic voltammetric of AuNiAuCu-R in 5 mM NaOH with 5 mM glucose was measured. The figure presents that the activation of Ni/Cu into a higher state happened at a lower potential compared to the oxidation of glucose. Therefore, the Ni/Cu would be oxidized into Ni^{3+}/Cu^{3+} before the oxidization of glucose. On the other hand, the oxidation peak of glucose presents a higher potential in low pH. Thus, the electrodes present higher catalytic performance in high pH media. This could be due to the fact that it is easier to form OH_{ads} radicals on the surface at high pH hence facilitating the oxidation of glucose.[194] In the first step of glucose oxidation, the glucose C-1 hydrogen is abstracted at the Ni^{3+} and Cu^{3+} sites (NiOOH and CuOOH), followed by further oxidizing dehydrogenated radical intermediates into

glucono-δ-lactone.[194] In the absence of glucose, the ratio of the current for the redox peaks is one. When a low concentration of glucose is added, the anodic current rises, whereas the cathodic peak remains unchanged (in Figure 6.5). This suggests that oxidation of glucose happens quickly without the blocking of active sites and rapid electron transfer. From the CV plot, the glucose oxidation potential shifts to a higher positive potential on increasing glucose concentration. This could be due to 1) higher concentration of glucose may impede the diffusion of reaction products from the electrode; 2) formation of greater amounts of intermediates can block the active sites leading to higher resistance for electron transfer. Hence higher potential is needed with higher glucose concentration.[209]

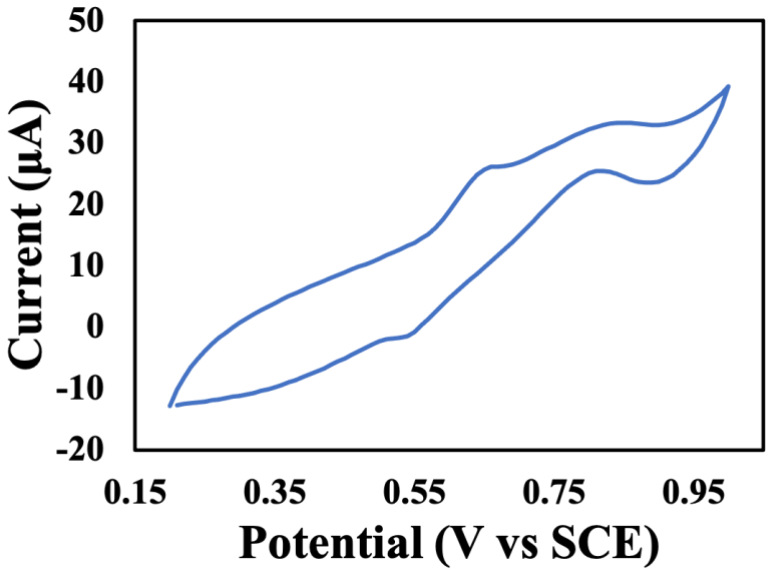

Figure 6.6 Cyclic voltametric profile of AuNiAuCu-R sample in 5 mM NaOH and 5 mM glucose.

3.3 Glucose detection

3.3.1 Calibration line

The glucose detection performance is evaluated using chronoamperometry. The calibration curves (as shown in Figure 6.7) are obtained from current responses of the electrode upon the successive injection of glucose at a fixed applied potential. From Figure 6.7 a, it is clearly observed that after the glucose injection, the current response rapidly increases and stabilizes quickly within 5 s. This ultra-fast glucose electrooxidation results from the higher surface area and porous structure. The

AuNiAuCu-R electrode shows high electrochemical activity due to its synergistic effects of the two metal components (discussed below) and nanowires morphology, which is ideal for a kinetically controlled surface bond reaction such as glucose oxidation. Due to the diffusion process and ultrafast oxidation, the response current is calculated as the average response over the last 15 s for each addition. The detection limit is calculated at S/N=3. The response to glucose concentration changes demonstrates that the chains show very sensitive detection ability. The linear relationship between the current response and glucose concentration fits a double linear profile for composite chains and a linear profile for single metal chains, with details presented in Table 6.2.

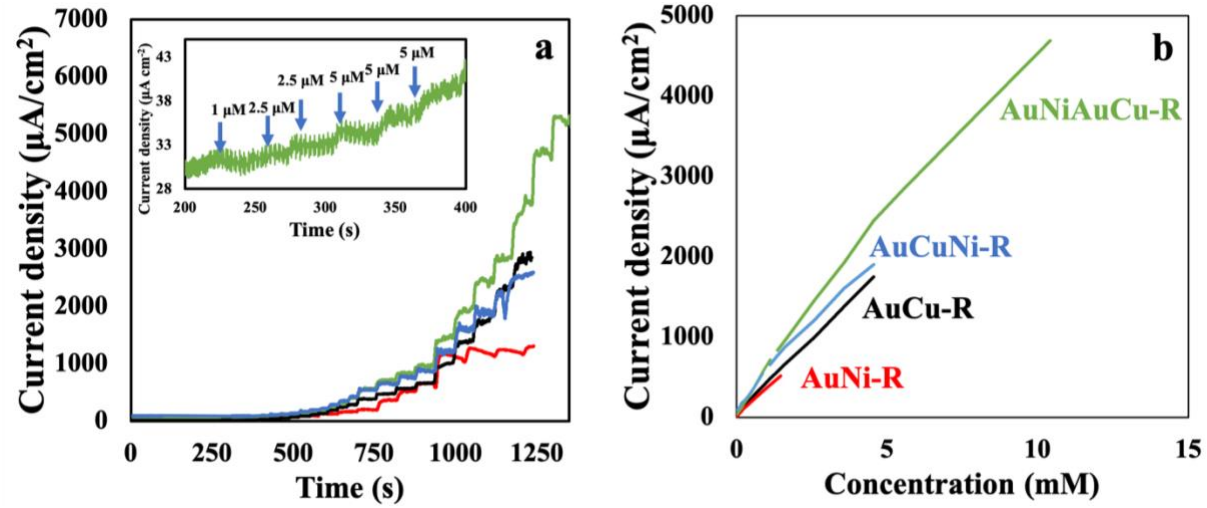

Figure 6.7 a) Amperometric current-time responses for different samples on successive addition of glucose in 0.1 M NaOH; b) Variations of current densities against glucose concentrations in 0.1 M NaOH.

As for AuCu-R, the sensitivity is 380.7 μA mM^{-1} cm^{-2} in the 5 μM to 4.55 mM range (R^2 = 0.999), and for AuNi-R is 353.7 μA mM^{-1} cm^{-2} in the 5 μM to 0.39 mM range (R^2 = 0.997). Comparing the samples with the same Ni/Cu=1, the AuNiAuCu-R performs better in sensitivity (643.9 μA mM^{-1} cm^{-2} in the 5 μM to 4.55 mM range, R^2 = 0.998, and 464.4 μA mM^{-1} cm^{-2} in the 4.55 mM to 12.85 mM range, R^2 = 0.997) than AuCuNi-R (516.2 μA mM^{-1} cm^{-2} in the 3 μM to 0.86 mM range, R^2 = 0.999, 363.7 μA mM^{-1} cm^{-2} in the 1.11 μM to 4.55 mM range, R^2 = 0.998). We also compared the sensitivity of AuNiAuCu-chains before (193.0 μA mM^{-1} cm^{-2} in the range from 8 μM to 0.49 mM range, R^2 = 0.997) and after reduction (643.9 μA mM^{-1} cm^{-2}). After the reduction, the

sensitivity is higher, confirming that the formation of Ni and Cu nanosize domain (and their hydroxides) is necessary for effective glucose oxidation. Additionally, the domain size does play a crucial role as a catalyst. Comparing the samples with the same Ni/Cu ratio, the mixing chains samples with a larger domain size perform better than the mixing ions one, which possess smaller domain sizes. Specifically, we observe that AuNiAuCu-R can be operated to detect glucose from 5 μM to 12.85 mM fitting the glucose level in saliva, sweat, and blood.

Table 6.2 The detail information of the glucose detection performance of various composites in 0.1 M NaOH

Sample	Sensitivity in Range A μA mM^{-1} cm^{-2}	Linear Range A mM	R^2	LoD μM	Sensitivity in Range B μA mM^{-1} cm^{-2}	Linear Range B mM	R^2
$AuCuNi_3$-R	513.3	0.004-0.46	0.997	4	325.9	0.49-1.6	0.998
AuCuNi-R	516.2	0.003-0.86	0.997	5	363.7	1.11-4.55	0.998
$AuCu_3$Ni-R	471.9	0.02-0.86	0.999	7	315.0	1.11-5.52	0.997
$AuNi_3$AuCu-R	406.9	0.005-1.59	0.998	5	244.8	1.59-4.55	0.994
AuNiAuCu-R	643.9	0.005-4.55	0.998	5	464.4	4.55-12.85	0.997
AuNiAuCu_3-R	516.1	0.02-0.86	0.997	10	362.7	1.11-4.55	0.998
AuCu-R	380.7	0.005-4.55	0.999	3			
AuNi-R	353.7	0.005-0.39	0.999	5			
AuCa	47.4	0.025-1.46	0.999	20			

To further investigate the role of the gold template in this work, an electrode made by gold nanochains assembled by calcium ions is examined. In Figure 6.8, even though it presents the oxidation performance, it takes a longer time to show the response, over 30 s. This suggests that Ni and Cu possess suitable adsorption and desorption energy toward glucose oxidation.

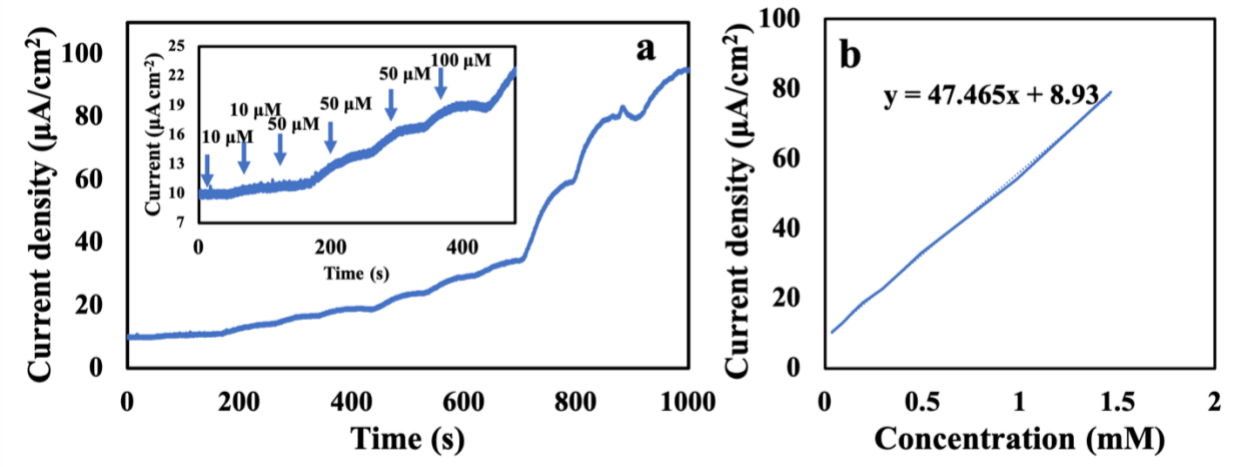

Figure 6.8 Amperometric current-time responses for AuCa samples on successive addition of glucose in 0.1 M NaOH; b) Current densities against glucose concentrations in 0.1 M NaOH.

Table 6.3 shows that our 1D Au nanomaterials with porous networks do possess a high sensitivity, a low detection limit, and a wide linear range than other works. This is attributed to an interconnected porous network which improves the mass transfer by enabling more analytes to approach the active sites due to the larger surface area and facilitating a higher electron transfer rate.[227] The wide linear range is attributed to the nanoscale combination of Ni and Cu domains that could lead to effective detection at low concentrations on the Ni domains and higher concentrations at Cu domains.

Table 6.3 Performance comparison with some previously reported glucose detection materials.

Material	LoD	Liner range	Sensitivity	Electrolyte	Ref
AuNiAuCu-R	5 μM	0.005-4.55 mM and 4.55-12.85 mM	643.9 $\mu Acm^{-2}mM^{-1}$ and 464.4 $\mu Acm^{-2}mM^{-1}$	0.1 M NaOH	This work
Ni/Cu-MOFs	0.51 μM	1 μM-20 mM	26.05 $\mu Acm^{-2}mM^{-1}$	PBS	228
Cu, Mn, Ni, or Zr - benzene-1,4-dicarboxylic acid nanosheets	6.68 μM	0.01 mM-0.8 mM	635.9 $\mu Acm^{-2}mM^{-1}$	0.1 M NaOH	212
CuO/NiO-Carbon	37 nM	100 nM-4.5 mM	586.7 $\mu Acm^{-2}mM^{-1}$	0.1 M NaOH	229
CuO/$Ni(OH)_2$/carbon cloth	0.31 μM	0.05-8.50 mM	598.6 $\mu Acm^{-2}mM^{-1}$	0.1 M NaOH	211
CuO/screen printed carbon electrode	0.1 μM	0.5 μM -4.03 mM	308.71 $\mu Acm^{-2}mM^{-1}$	0.1 M NaOH	230

CuO decorated CeO_2	10 μM		2.77 $\mu Acm^{-2}mM^{-1}$	PBS	213
CuO nanoleaf/ZnO nanorods	18 μM	0.1-1 mM	408 $\mu Acm^{-2}mM^{-1}$	0.1 M NaOH	231
Au@Cu_2O	18 μM	0.05-2.0 mM	715 $\mu Acm^{-2}mM^{-1}$	0.05 mM NaOH	206
Ni/NiO/nitrogen doped carbon spheres	0.31 μM	2 μM-600 μM and 800 μM-2500 μM	219.19 $\mu Acm^{-2}mM^{-1}$ and 87. $\mu Acm^{-2}mM^{-1}$	0.1 M NaOH	232
Au@Ni	0.0157 mM	0.5-10 mM	23.17 $\mu Acm^{-2}mM^{-1}$	0.1 M NaOH	233

3.3.2 Selectivity, reproducibility, and stability of device

Selectivity, reproducibility, and stability of electrodes are also important parameters to evaluate the practical performance. Organic compounds such as uric acid (UA), ascorbic acid (AA), acetaminophen (AP), and dopamine (DA) can strongly adhere to the surface and severely reduce the activity of the electrode. The normal physiological glucose levels in the blood for non-diabetics range from 4 mM to 7 mM, and the levels of UA, AA, AP, and DA range from 0.1 mM to 0.3 mM. The physiological concentrations of interfering substances are tens of times smaller than the blood glucose level. The selectivity of the sensor to detect 0.5 mM glucose over other interference agents, such as 0.5 mM UA, AA, AP, and DA. As seen in Figure 6.9, we clearly observe that the current responses to AA, UA, AP, and DA (after 30 s) were negligible, presenting good selectivity of the electrode materials. This might be due to the Au nanochains that are still negatively charged, as proved by their Zeta potential values in the range of -30 to -40 mV.[234] At the same time, the high pH condition helps to retain the negative charge of the metal-based electrode. Therefore, the glucose electrodes possess high selectivity by repelling negatively charged interference agents like AA and UA. The selectivity of the non-enzymatic sensor is also related to the proper working potential required for the oxidation of the specific chemical species. The oxidation peak for the interference occurs at a higher potential while the glucose detection is performed at a lower potential, which also improves selectivity.

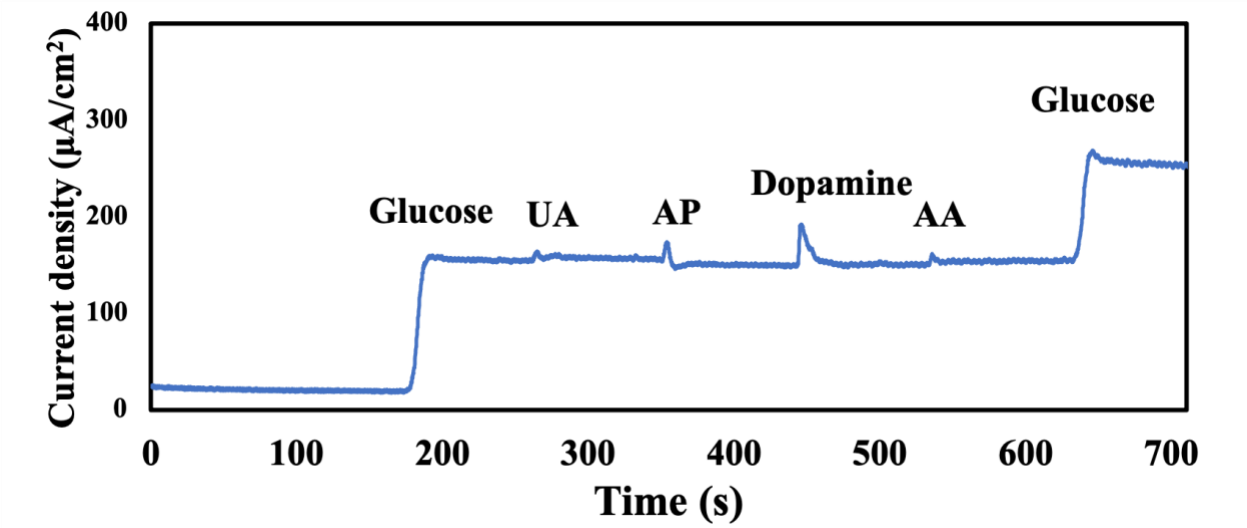

Figure 6.9 The chronoamperometry measurements of AuNiAuCu-R with the interference of 0.5 mM UA, AA, AP, and DA with 0.5 mM glucose.

Reproducibility and reusability of the electrode materials are evaluated. The AuCuAuNi-R electrode maintained 95% of its initial performance four months after fabrication which electrode solution has been stored in ambient condition. Meanwhile, the response from three identical devices provides that the relative standard deviation is less than 8%. These results confirm that the as-prepared materials are highly reproducible and stable.

4. Conclusion

We have presented a facile strategy to achieve spatial distribution of elements on 1D gold nanochains surface. In this work, Ni and Cu are involved as active elements for glucose oxidation in basic media. Using 0.1 M NaOH as the electrolyte, the spatial distribution controlled gold nanochains deposited on GCE can be transformed into Ni/Cu oxyhydroxide by cyclic voltammetric activation. The as-prepared electrode materials were used to investigate the electrochemical response of glucose. Mixing Ni and Cu improves the detection sensitivity by synergistic effect. Additionally, the proper size of the domain is needed to obtain the best performance. The AuNiAuCu-R sample demonstrates the highest sensitivity of 643.9 μA mM^{-1} cm^{-2} with high stability, reproducibility, and low limits. This offers a promising feature for practical analytical application.

Chapter 7 Conclusions and Future Work

1 Summary of contributions

Nanostructured materials are being intensely researched due to their properties that are distinct from bulk material. 1D gold nanomaterials are suitable candidates for circuit interconnections, flexible sensors, and electrochemical devices due to their high aspect ratio, unique morphology, stability, and intrinsic conductive nature. A template-free self-assembly based synthesis method has been developed with the use of cations, that is easy and cost-effective for the production of 1D NWs and NC. Additionally, different kinds of metal cations can be integrated into the 1D structure to design their use for various applications.

Macroscale assemblies of nanomaterials can play a role as building blocks for fabricating flexible devices and human-electronic interfaces to translate multiple stimuli into electrical signals. In part A, Chapter 2, a simple filtration method is developed to fabricate various wearable devices to monitor human physiological signals, including temperature, artery pulsation, and ECG signals. The micron scale AuCa NCs with gaps of 1-2 nm between neighbor Au NPs are the basic materials in these devices. The gaps are crucial to translate the physiological responses by the quantum tunneling effect. In Chapter 3, an easy filtration-transfer production method is developed to prepare a series of stretchable devices. In this work, two kinds of 1D gold nanomaterials are studied to investigate the relationship between morphology and conductive behavior under tensile strain. After the transfer process, numerous micrometer scale cracks with interconnections develop in the devices, facilitating charge carriers' transport under strain. AuPt NWs devices can endure higher strain than AuCa NCs devices because the AuPt NWs devices are made by extended continuous nanowires, which also act as interconnections between adjacent micro flakes. In contrast, AuCa NCs devices barely present this kind of interconnection. In addition, the AuPt NWs devices show high reproducible and stable responses on the application of thousands of repeated strain cycles. This simple method provides a universal way to prepare scaled-up stretchable devices. Additionally, due to the unique morphology and conductive performance of AuPt NWs, we integrate them as circuit elements with perovskites to fabricate highly bendable and stretchable photodetectors.

In part B, various metal cations as linking bridges are developed to assemble 1D gold nanochains as multi-element electrocatalysts with the controlled spatial distribution of elements. The distribution of the ions in the electrical double layer around the chains is used to control the spatial distribution of the catalytic elements. In Chapter 4, Pt and Ni-PBA are designed as bifunctional water splitting electrocatalytic material. The metallic Pt and Ni and Ni with a higher oxidation state (+3) are obtained during the synthesis process. These improve the performance of HER and OER. The best electrocatalytic material presents the lowest overpotential of 256 mV for OER with a Tafel slope of 30.3 mV dec^{-1} and for HER an overpotential of 37.9 mV with a Tafel slope of 13.7 mV dec^{-1}.

In Chapter 5, Pt and Ni based gold nanochains are designed to detect dopamine at neutral pH. With nanometer scale spatial distribution of catalyst elements, the AuPtAuNi-R sample shows the best performance for dopamine detection. The sensitivity is 1279.3 μA mM^{-1} cm^{-2} in the detection range of 0.14-36.5 μM, and the detection limit is 0.01 μM. The electrode presents a negligible current response to the interference of UA, AP, glucose, and AA. The samples also show good stability and reproducibility. In Chapter 6, Au NCs with Ni and Cu cover layer are presented as a glucose sensor. The highly conductive and porous networks lead to fast mass transfer, facilitate electron transportation, and provide more active sites for glucose detection. The best sample can achieve high sensitivity, a low detection limit, and a wide linear range from 5 μM to 12.85 mM, which fits the glucose level in sweat and blood.

2 Future Work

In Chapter 2, the devices present high flexibility compared to most commercial products. Further optimizing the loading density and morphology can improve the sensitivity of the devices and lead to their commercialization. More research is also needed for detailed testing of the devices for sensing of other critical signals such as Electroencephalogram (EEG), Electromyogram (EMG), Electrooculogram (EOG), electroencephalogram (EEG), etc. The early adoption of the device could be for sensing EEG and EOG signals, for example, to detect the rapid eye movement (REM) sleep for accelerating the recovery of post-traumatic stress disorder (PTSD).[235,236] EMG signals could help evaluate the muscle activity and health status of a baby, for example, in case of compromised spinal development and the central nervous system.[237,238] The correlation between

the signal details in EEG, EOG, and EMG and health conditions is well developed, which makes such applications well suited to advance healthcare. Meanwhile, designing a device with multifunctionality (for example, a wireless device patch that can in real-time monitor temperature, pulsation, ECG, and other crucial physiological signals) can be beneficial for the development of remote clinical diagnosis. This will also require integration with a wireless data collection and transfer interface.

In Chapter 3, for stretchable sensors, more effort is required to make the device commercially viable. Even though we integrated the AuPt NWs as an electrode with perovskite to fabricate flexible photodetector, the effect of biaxial strain and torsion forces are critical to evaluate the possibility of practical application. The substrate used in this work can show a real-time response under strain but still faces the challenge of relaxation. Therefore, a more suitable substrate is required for possible application, like circuits and interconnections in healthcare devices.

In Chapters 4, 5, and 6, we need to conduct a further study for a complete understanding of the materials at the atomic level, including the synthesis process and the reactions. For example, Density functional theory (DFT) computations can help investigate the electronic structure to better under the effect of the domain size and the relevant mechanism of each reaction step for HER and OER. Furthermore, the data presents quite a low Tafel slope, so using a rotating disk electrode would help us study the performance at higher overpotential, which is required for larger power application and the mechanism of electron transfer and mass transfer on the catalyst surface.

As for the glucose sensor, the performance is studied as materials deposited on the GCE in this work. We can integrate the materials on a flexible substrate by simple filtration method to produce a device that can monitor the glucose level in sweat or saliva. This is a non-invasive way for potential use as a diabetes monitor. Regarding dopamine devices, a chip-like product can be designed to meet the requirements of testing dopamine in urine. Moving technology from lab to market will be a huge improvement to make life better.

Letters of Copyright Permission

Your confirmation email will contain your order number for future reference.

Printable Details

License Number	5087801497732
License date	Jun 14, 2021

Licensed Content

Licensed Content Publisher	Elsevier
Licensed Content Publication	Journal of Advanced Research
Licensed Content Title	Gold nanoparticles: Optical properties and implementations in cancer diagnosis and photothermal therapy
Licensed Content Author	Xiaohua Huang,Mostafa A. El-Sayed
Licensed Content Date	Jan 1, 2010
Licensed Content Volume	1
Licensed Content Issue	1
Licensed Content Pages	16

Order Details

Type of Use	reuse in a thesis/dissertation
Portion	figures/tables/illustrations
Number of figures/tables/illustrations	1
Format	electronic
Are you the author of this Elsevier article?	No
Will you be translating?	No

About Your Work

Title	Self-assembled gold nanochains based materials as building blocks to fabricate flexible devices and as electrocatalysts
Institution name	University of Waterloo
Expected presentation date	Aug 2021

Additional Data

Portions	Figure 3

Requestor Location

Requestor Location	UWaterloo QNC 200 University Avenue West Waterloo, ON N2L3G1 Canada Attn: UWaterloo

Tax Details

Publisher Tax ID	GB 494 6272 12

Licensed Content

Licensed Content Publisher	Elsevier
Licensed Content Publication	Journal of Colloid and Interface Science
Licensed Content Title	Synthesis of gold nanochains via photoactivation technique and their catalytic applications
Licensed Content Author	Arun Kumar Sinha,Mrinmoyee Basu,Sougata Sarkar,Mukul Pradhan,Tarasankar Pal
Licensed Content Date	May 15, 2013
Licensed Content Volume	398
Licensed Content Issue	n/a
Licensed Content Pages	9

Order Details

Type of Use	reuse in a thesis/dissertation
Portion	figures/tables/illustrations
Number of figures/tables/illustrations	1
Format	electronic
Are you the author of this Elsevier article?	No
Will you be translating?	No

About Your Work

Title	Self-assembled gold nanochains based materials as building blocks to fabricate flexible devices and as electrocatalysts
Institution name	University of Waterloo
Expected presentation date	Aug 2021

Additional Data

Portions	Scheme 3

Requestor Location

Requestor Location	UWaterloo QNC 200 University Avenue West Waterloo, ON N2L3G1 Canada Attn: UWaterloo

Tax Details

Publisher Tax ID	GB 494 6272 12

Your confirmation email will contain your order number for future reference.

Printable Details

License Number	5087810545021
License date	Jun 14, 2021

Licensed Content

Licensed Content Publisher	John Wiley and Sons
Licensed Content Publication	Advanced Materials
Licensed Content Title	Activatable NIR-II Plasmonic Nanotheranostics for Efficient Photoacoustic Imaging and Photothermal Cancer Therapy
Licensed Content Author	Chunyu Zhou, Liang Zhang, Tao Sun, et al
Licensed Content Date	Dec 6, 2020
Licensed Content Volume	33
Licensed Content Issue	3
Licensed Content Pages	11

Order Details

Type of use	Dissertation/Thesis
Requestor type	University/Academic
Format	Electronic
Portion	Figure/table
Number of figures/tables	1
Will you be translating?	No

About Your Work

Title	Self-assembled gold nanochains based materials as building blocks to fabricate flexible devices and as electrocatalysts
Institution name	University of Waterloo
Expected presentation date	Aug 2021

Additional Data

Portions	Scheme 1

Requestor Location

Requestor Location	UWaterloo QNC 200 University Avenue West Waterloo, ON N2L3G1 Canada Attn: UWaterloo

Tax Details

Publisher Tax ID	EU826007151

Publication Title	Chemical Society reviews	**Country**	United Kingdom of Great Britain and Northern Ireland
Author/Editor	Royal Society of Chemistry (Great Britain)	**Rightsholder**	Royal Society of Chemistry
Date	01/01/1972	**Publication Type**	e-Journal
Language	English	**URL**	http://www.rsc.org/csr

REQUEST DETAILS

Portion Type	Image/photo/illustration	**Distribution**	Canada
Number of images / photos / illustrations	1	**Translation**	Original language of publication
Format (select all that apply)	Electronic	**Copies for the disabled?**	No
Who will republish the content?	Academic institution	**Minor editing privileges?**	No
Duration of Use	Life of current edition	**Incidental promotional use?**	No
Lifetime Unit Quantity	Up to 499	**Currency**	CAD
Rights Requested	Main product		

NEW WORK DETAILS

Title	Self-assembled gold nanochains based materials as building blocks to fabricate flexible devices and as electrocatalysts	**Institution name**	UWATERLOO
		Expected presentation date	2021-08-03
Instructor name	Vivek Maheshwari		

ADDITIONAL DETAILS

Order reference number	N/A	**The requesting person / organization to appear on the license**	Hua Fan

REUSE CONTENT DETAILS

Title, description or numeric reference of the portion(s)	Modelling the optical response of gold nanoparticles	**Title of the article/chapter the portion is from**	N/A
Editor of portion(s)	N/A	**Author of portion(s)**	Royal Society of Chemistry (Great Britain)
Volume of serial or monograph	9	**Issue, if republishing an article from a serial**	N/A
Page or page range of portion	1793	**Publication date of portion**	2008-06-27

AFM Manipulation of Gold Nanowires To Build Electrical Circuits

Author: Miriam Moreno-Moreno, Pablo Ares, Consuelo Moreno, et al
Publication: Nano Letters
Publisher: American Chemical Society
Date: Aug 1, 2019

Your confirmation email will contain your order number for future reference.

License Number	5087820021189
License date	Jun 14, 2021

Printable Details

Licensed Content

Licensed Content Publisher	John Wiley and Sons
Licensed Content Publication	Advanced Electronic Materials
Licensed Content Title	Fabrication of Highly Transparent and Flexible NanoMesh Electrode via Self-assembly of Ultrathin Gold Nanowires
Licensed Content Author	Wenlong Cheng, Hemayet Uddin, Daniel T. H. Lai, et al
Licensed Content Date	May 23, 2016
Licensed Content Volume	2
Licensed Content Issue	7
Licensed Content Pages	8

Order Details

Type of use	Dissertation/Thesis
Requestor type	University/Academic
Format	Electronic
Portion	Figure/table
Number of figures/tables	2
Will you be translating?	No

About Your Work

Title	Self-assembled gold nanochains based materials as building blocks to fabricate flexible devices and as electrocatalysts
Institution name	University of Waterloo
Expected presentation date	Aug 2021

Additional Data

Portions	Figure 1, Figure 5

Requestor Location

Requestor Location	UWaterloo QNC 200 University Avenue West Waterloo, ON N2L3G1 Canada Attn: UWaterloo

Tax Details

Publisher Tax ID	EU826007151

Your confirmation email will contain your order number for future reference.

License Number	5087820234732
License date	Jun 14, 2021

Printable Details

Licensed Content

Licensed Content Publisher	Springer Nature
Licensed Content Publication	Nature Communications
Licensed Content Title	A wearable and highly sensitive pressure sensor with ultrathin gold nanowires
Licensed Content Author	Shu Gong et al
Licensed Content Date	Feb 4, 2014

Order Details

Type of Use	Thesis/Dissertation
Requestor type	academic/university or research institute
Format	electronic
Portion	figures/tables/illustrations
Number of figures/tables/illustrations	2
High-res required	no
Will you be translating?	no
Circulation/distribution	1 - 29
Author of this Springer Nature content	no

About Your Work

Title	Self-assembled gold nanochains based materials as building blocks to fabricate flexible devices and as electrocatalysts
Institution name	University of Waterloo
Expected presentation date	Aug 2021

Additional Data

Portions	Figure 1. Figure 6

Requestor Location

Requestor Location	UWaterloo QNC 200 University Avenue West Waterloo, ON N2L3G1 Canada Attn: UWaterloo

Tax Details

Wearable Devices Using Nanoparticle Chains as Universal Building Blocks with Simple Filtration-Based Fabrication and Quantum Sensing

Author: Vivek Maheshwari, Hua Fan
Publication: Advanced Materials Technologies
Publisher: John Wiley and Sons
Date: May 4, 2020

Order Completed

Thank you for your order.

This Agreement between UWaterloo -- Hua Fan ("You") and John Wiley and Sons ("John Wiley and Sons") consists of your license details and the terms and conditions provided by John Wiley and Sons and Copyright Clearance Center.

Your confirmation email will contain your order number for future reference.

License Number	5083421382583
License date	Jun 07, 2021

Printable Details

Licensed Content

Order Details

Licensed Content Publisher	John Wiley and Sons
Licensed Content Publication	Advanced Materials Technologies
Licensed Content Title	Wearable Devices Using Nanoparticle Chains as Universal Building Blocks with Simple Filtration-Based Fabrication and Quantum Sensing
Licensed Content Author	Vivek Maheshwari, Hua Fan
Licensed Content Date	May 4, 2020
Licensed Content Volume	5
Licensed Content Issue	6
Licensed Content Pages	8

Type of use	Dissertation/Thesis
Requestor type	Author of this Wiley article
Format	Electronic
Portion	Full article
Will you be translating?	No

About Your Work

Title	Self-assembled gold nanochains as building blocks to fabricate flexible devices and as electrocatalysts
Institution name	University of Waterloo
Expected presentation date	Aug 2021

Additional Data

Requestor Location

Requestor Location	UWaterloo QNC 200 University Avenue West Waterloo, ON N2L3G1 Canada Attn: UWaterloo

Tax Details

Publisher Tax ID	EU826007151

Price

Total	0.00 USD

Reference

(1) Kitching, H.; J. Shiers, M.; J. Kenyon, A.; P. Parkin, I. Self-Assembly of Metallic Nanoparticles into One Dimensional Arrays. *J. Mater. Chem. A* **2013**, *1* (24), 6985-6999.

(2) Walter, M. V.; Cheval, N.; Liszka, O.; Malkoch, M.; Fahmi, A. Hybrid One-Dimensional Nanostructures: One-Pot Preparation of Nanoparticle Chains via Directed Self-Assembly of in Situ Synthesized Discrete Au Nanoparticles. *Langmuir* **2012**, *28* (14), 5947-5955.

(3) Huo, D.; Kim, M. J.; Lyu, Z.; Shi, Y.; Wiley, B. J.; Xia, Y. One-Dimensional Metal Nanostructures: From Colloidal Syntheses to Applications. *Chem. Rev.* **2019**, *119* (15), 8972-9073.

(4) Dreaden, E. C.; Alkilany, A. M.; Huang, X.; Murphy, C. J.; El-Sayed, M. A. The Golden Age: Gold Nanoparticles for Biomedicine. *Chem. Soc. Rev.* **2012**, *41* (7), 2740-2779.

(5) Huang, X.; El-Sayed, M. A. Gold Nanoparticles: Optical Properties and Implementations in Cancer Diagnosis and Photothermal Therapy. *J. Adv. Res.* **2010**, *1* (1), 13-28.

(6) Murphy, C. J., Sau, T. K., Gole, A. M., Orendorff, C. J., Gao, J., Gou, L., Hunyadi, S. E. and Li, T., Anisotropic metal nanoparticles: synthesis, assembly, and optical applications. *J. Phys. Chem. B* **2005,** *109*(29), 13857-13870.

(7) Wu, L.; Shi, C.; Tian, L.; Zhu, J. A One-Pot Method to Prepare Gold Nanoparticle Chains with Chitosan. *J. Phys. Chem. C* **2008**, *112* (2), 319-323.

(8) Zhu, H.; Prince, E.; Narayanan, P.; Liu, K.; Nie, Z.; Kumacheva, E. Colloidal Stability of Nanoparticles Stabilized with Mixed Ligands in Solvents with Varying Polarity. *Chem. Commun.* **2020**, *56* (58), 8131-8134.

(9) Jia, H.; Bai, X.; Li, N.; Yu, L.; Zheng, L. Siloxane Surfactant Induced Self-Assembly of Gold Nanoparticles and Their Application to SERS. *CrystEngComm* **2011**, *13* (20), 6179-6184.

(10) Zhang, Y.; Chu, W.; Foroushani, A. D.; Wang, H.; Li, D.; Liu, J.; Barrow, C. J.; Wang, X.; Yang, W. New Gold Nanostructures for Sensor Applications: A Review. *Materials* **2014**, *7* (7), 5169-5201.

(11) Saldan, I.; Dobrovetska, O.; Sus, L.; Makota, O.; Pereviznyk, O.; Kuntyi, O.; Reshetnyak, O. Electrochemical Synthesis and Properties of Gold Nanomaterials. *J. Solid State Electrochem.* **2018**, *22* (3), 637-656.

(12) Zhu, B.; Gong, S.; Cheng, W. Softening Gold for Elastronics. *Chem. Soc. Rev.* **2019**, *48* (6), 1668-1711.

(13) Fan, H.; Maheshwari, V. Wearable Devices Using Nanoparticle Chains as Universal Building Blocks with Simple Filtration-Based Fabrication and Quantum Sensing. *Adv. Mater. Technol.* **2020**, *5* (6), 2000090.

(14) Lee, A.; Andrade, G. F. S.; Ahmed, A.; Souza, M. L.; Coombs, N.; Tumarkin, E.; Liu, K.; Gordon, R.; Brolo, A. G.; Kumacheva, E. Probing Dynamic Generation of Hot-Spots in Self-Assembled Chains of Gold Nanorods by Surface-Enhanced Raman Scattering. *J. Am. Chem. Soc.* **2011**, *133* (19), 7563-7570.

(15) Sinha, A. K.; Basu, M.; Sarkar, S.; Pradhan, M.; Pal, T. Synthesis of Gold Nanochains via Photoactivation Technique and Their Catalytic Applications. *J. Colloid Interface Sci.* **2013**, *398*, 13-21.

(16) Zhou, C.; Zhang, L.; Sun, T.; Zhang, Y.; Liu, Y.; Gong, M.; Xu, Z.; Du, M.; Liu, Y.; Liu, G.; Zhang, D. Activatable NIR-II Plasmonic Nanotheranostics for Efficient Photoacoustic Imaging and Photothermal Cancer Therapy. *Adv. Mater.* **2021**, *33* (3), 2006532.

(17) Zhang, H.; Wang, D. Controlling the Growth of Charged-Nanoparticle Chains through Interparticle Electrostatic Repulsion. *Angew. Chem. Int. Ed.* **2008**, *47* (21), 3984-3987.

(18) Grzelczak, M., Vermant, J., Furst, E. M. and Liz-Marzán, L. M., Directed self-assembly of nanoparticles. *ACS nano* **2010**, *4*(7), 3591-3605.

(19) Li, M.; Johnson, S.; Guo, H.; Dujardin, E.; Mann, S. A Generalized Mechanism for Ligand-Induced Dipolar Assembly of Plasmonic Gold Nanoparticle Chain Networks. *Adv. Funct. Mater.* **2011**, *21* (5), 851-859.

(20) Burns, C.; Spendel, W. U.; Puckett, S.; Pacey, G. E. Solution Ionic Strength Effect on Gold Nanoparticle Solution Color Transition. *Talanta* **2006**, *69* (4), 873-876.

(21) Gisbert-González, J. M.; Cheuquepán, W.; Ferre-Vilaplana, A.; Herrero, E.; Feliu, J. M. Citrate Adsorption on Gold: Understanding the Shaping Mechanism of Nanoparticles. *J. Electroanal. Chem.* **2020**, *875*, 114015.

(22) Park, J. W.; Shumaker-Parry, J. S. Structural Study of Citrate Layers on Gold Nanoparticles: Role of Intermolecular Interactions in Stabilizing Nanoparticles. *J. Am. Chem. Soc.* **2014**, *136* (5), 1907-1921.

(23) Batista, C. A. S.; Larson, R. G.; Kotov, N. A. Nonadditivity of Nanoparticle Interactions. *Science* **2015**, *350* (6257).

(24) Zhang, H.; Fung, K. H.; Hartmann, J.; Chan, C. T.; Wang, D. Controlled Chainlike Agglomeration of Charged Gold Nanoparticles via a Deliberate Interaction Balance. *J. Phys. Chem. C* **2008**, *112* (43), 16830-16839.

(25) Liao, J.; Zhang, Y.; Yu, W.; Xu, L.; Ge, C.; Liu, J.; Gu, N. Linear Aggregation of Gold Nanoparticles in Ethanol. *Colloids Surf. Physicochem. Eng. Asp.* **2003**, *223* (1), 177-183.

(26) He, R.; Wang, Y. C.; Wang, X.; Wang, Z.; Liu, G.; Zhou, W.; Wen, L.; Li, Q.; Wang, X.; Chen, X.; Zeng, J.; Hou, J. G. Facile Synthesis of Pentacle Gold-Copper Alloy Nanocrystals and Their Plasmonic and Catalytic Properties. *Nat. Commun.* **2014**, *5* (1), 4327.

(27) Elahi, N.; Kamali, M.; Baghersad, M. H. Recent Biomedical Applications of Gold Nanoparticles: A Review. *Talanta* **2018**, *184*, 537-556.

(28) Saha, K.; Agasti, S. S.; Kim, C.; Li, X.; Rotello, V. M. Gold Nanoparticles in Chemical and Biological Sensing. *Chem. Rev.* **2012**, *112* (5), 2739-2779.

(29) Zeng, S.; Baillargeat, D.; Ho, H. P.; Yong, K. T. Nanomaterials Enhanced Surface Plasmon Resonance for Biological and Chemical Sensing Applications. *Chem. Soc. Rev.* **2014**, *43* (10), 3426-3452.

(30) Myroshnychenko, V.; Rodríguez-Fernández, J.; Pastoriza-Santos, I.; Funston, A. M.; Novo, C.; Mulvaney, P.; Liz-Marzán, L. M.; Abajo, F. J. G. de. Modelling the Optical Response of Gold Nanoparticles. *Chem. Soc. Rev.* **2008**, *37* (9), 1792-1805.

(31) Takahata, R.; Yamazoe, S.; Koyasu, K.; Imura, K.; Tsukuda, T. Gold Ultrathin Nanorods with Controlled Aspect Ratios and Surface Modifications: Formation Mechanism and Localized Surface Plasmon Resonance. *J. Am. Chem. Soc.* **2018** *140* (21), 6640-6647.

(32) Kelly, K. L.; Coronado, E.; Zhao, L. L.; Schatz, G. C. The Optical Properties of Metal Nanoparticles: The Influence of Size, Shape, and Dielectric Environment. *J. Phys. Chem. B* **2003**, *107* (3), 668-677.

(33) Rycenga, M., Cobley, C. M., Zeng, J., Li, W., Moran, C.H., Zhang, Q., Qin, D. and Xia, Y., Controlling the synthesis and assembly of silver nanostructures for plasmonic applications. *Chem. Rev* **2011**, *111*(6), 3669-3712.

(34) Haes, A. J.; Haynes, C. L.; McFarland, A. D.; Schatz, G. C.; Van Duyne, R. P.; Zou, S. Plasmonic Materials for Surface-Enhanced Sensing and Spectroscopy. *MRS Bull.* **2005**, *30* (5), 368-375.

(35) Pérez-Juste, J.; Pastoriza-Santos, I.; Liz-Marzán, L. M.; Mulvaney, P. Gold Nanorods: Synthesis, Characterization and Applications. *Coord. Chem. Rev.* **2005**, *249* (17), 1870-1901.

(36) Maheshwari, V.; Kane, J.; Saraf, R. F. Self-Assembly of a Micrometers-Long One-Dimensional Network of Cemented Au Nanoparticles. *Adv. Mater.* **2008**, *20* (2), 284-287.

(37) Albrecht, T. Electrochemical Tunnelling Sensors and Their Potential Applications. *Nat. Commun.* **2012**, *3* (1), 829.

(38) Schreiner, P. R. Tunneling Control of Chemical Reactions: The Third Reactivity Paradigm. *J. Am. Chem. Soc.* **2017**, *139* (43), 15276-15283.

(39) Tricard, S.; Said-Aizpuru, O.; Bouzouita, D.; Usmani, S.; Gillet, A.; Tassé, M.; Poteau, R.; Viau, G.; Demont, P.; Carrey, J.; Chaudret, B. Chemical Tuning of Coulomb Blockade at Room-Temperature in Ultra-Small Platinum Nanoparticle Self-Assemblies. *Mater. Horiz.* **2017**, *4* (3), 487-492.

(40) Wilson, P.; Ong, J. K. Y.; Prasad, A.; Saraf, R. F. Quantitative Visualization of Topology and Morphing of Percolation Path in Nanoparticle Network Array Exhibiting Coulomb Blockade at Room Temperature. *J. Phys. Chem. C* **2019**, *123* (32), 19999-20005.

(41) Maheshwari, V. C. Large Area Electro-Optical Tactile Sensor: Characterization and Design of a Polymer, Nanoparticle Based Tunneling Device. 113.

(42) Wang, G. R.; Wang, L.; Rendeng, Q.; Wang, J.; Luo, J.; Zhong, C. J. Correlation between Nanostructural Parameters and Conductivity Properties for Molecularly-Mediated Thin Film Assemblies of Gold Nanoparticles. *J. Mater. Chem.* **2007**, *17* (5), 457-462.

(43) Moreno-Moreno, M.; Ares, P.; Moreno, C.; Zamora, F.; Gómez-Navarro, C.; Gómez-Herrero, J. AFM Manipulation of Gold Nanowires to Build Electrical Circuits. *Nano Lett.* **2019**, *19* (8), 5459-5468.

(44) Gong, S.; Zhao, Y.; Yap, L. W.; Shi, Q.; Wang, Y.; Bay, J. A. P. B.; Lai, D. T. H.; Uddin, H.; Cheng, W. Fabrication of Highly Transparent and Flexible NanoMesh Electrode via Self-Assembly of Ultrathin Gold Nanowires. *Adv. Electron. Mater.* **2016**, *2* (7), 1600121.

(45) Gong, S.; Schwalb, W.; Wang, Y.; Chen, Y.; Tang, Y.; Si, J.; Shirinzadeh, B.; Cheng, W. A Wearable and Highly Sensitive Pressure Sensor with Ultrathin Gold Nanowires. *Nat. Commun.* **2014**, *5* (1), 3132.

(46) Kim, K. K.; Hong, S.; Cho, H. M.; Lee, J.; Suh, Y. D.; Ham, J.; Ko, S. H. Highly Sensitive and Stretchable Multidimensional Strain Sensor with Prestrained Anisotropic Metal Nanowire Percolation Networks. *Nano Lett.* **2015**, *15* (8), 5240-5247.

(47) Lonjon, A.; Laffont, L.; Demont, P.; Dantras, E.; Lacabanne, C. Structural and Electrical Properties of Gold Nanowires/P(VDF-TrFE) Nanocomposites. *J. Phys. Appl. Phys.* **2010**, *43* (34), 345401.

(48) Ebrahimpour, Z.; Mansour, N. Annealing Effects on Electrical Behavior of Gold Nanoparticle Film: Conversion of Ohmic to Non-Ohmic Conductivity. *Appl. Surf. Sci.* **2017**, *394*, 240-247.

(49) Gong, S.; Lai, D. T. H.; Su, B.; Si, K. J.; Ma, Z.; Yap, L. W.; Guo, P.; Cheng, W. Highly Stretchy Black Gold E-Skin Nanopatches as Highly Sensitive Wearable Biomedical Sensors. *Adv. Electron. Mater.* **2015**, *1* (4), 1400063.

(50) Yao, S., Swetha, P. and Zhu, Y., Nanomaterial-enabled wearable sensors for healthcare. *Adv. Healthc. Mater.* **2018**, *7*(1), 1700889.

(51) Klinkova, A., Thérien-Aubin, H., Ahmed, A., Nykypanchuk, D., Choueiri, R.M., Gagnon, B., Muntyanu, A., Gang, O., Walker, G.C. and Kumacheva, E., Structural and optical properties of self-assembled chains of plasmonic nanocubes. *Nano lett.* **2014**, *14*(11), 6314-6321.

(52) Du, Y.; Sheng, H.; Astruc, D.; Zhu, M. Atomically Precise Noble Metal Nanoclusters as Efficient Catalysts: A Bridge between Structure and Properties. *Chem. Rev.* **2020**, *120* (2), 526-622.

(53) Zhang, Y.; Cui, X.; Shi, F.; Deng, Y. Nano-Gold Catalysis in Fine Chemical Synthesis. *Chem. Rev.* **2012**, *112* (4), 2467-2505.

(54) Xie, L.; Liu, Q.; Shi, X.; Asiri, A. M.; Luo, Y.; Sun, X. Superior Alkaline Hydrogen Evolution Electrocatalysis Enabled by an Ultrafine PtNi Nanoparticle-Decorated Ni Nanoarray with Ultralow Pt Loading. *Inorg. Chem. Front.* **2018**, *5* (6), 1365-1369.

(55) Yu, Z. Y.; Duan, Y.; Liu, J. D.; Chen, Y.; Liu, X. K.; Liu, W.; Ma, T.; Li, Y.; Zheng, X. S.; Yao, T.; Gao, M. R.; Zhu, J. F.; Ye, B. J.; Yu, S. H. Unconventional CN Vacancies Suppress Iron-Leaching in Prussian Blue Analogue Pre-Catalyst for Boosted Oxygen Evolution Catalysis. *Nat. Commun.* **2019**, *10* (1), 2799.

(56) Li, N.; Zhao, P.; Astruc, D. Anisotropic Gold Nanoparticles: Synthesis, Properties, Applications, and Toxicity. *Angew. Chem. Int. Ed.* **2014**, *53* (7), 1756-1789.

(57) Kang, H.; Buchman, J. T.; Rodriguez, R. S.; Ring, H. L.; He, J.; Bantz, K. C.; Haynes, C. L. Stabilization of Silver and Gold Nanoparticles: Preservation and Improvement of Plasmonic Functionalities. *Chem. Rev.* **2019**, *119* (1), 664-699.

(58) Nag, A.; Mukhopadhyay, S. C.; Kosel, J. Wearable Flexible Sensors: A Review. *IEEE Sens. J.* **2017**, *17* (13), 3949-3960.

(59) Bao, C.; Zhu, W.; Yang, J.; Li, F.; Gu, S.; Wang, Y.; Yu, T.; Zhu, J.; Zhou, Y.; Zou, Z. Highly Flexible Self-Powered Organolead Trihalide Perovskite Photodetectors with Gold Nanowire Networks as Transparent Electrodes. *ACS Appl. Mater. Interfaces* **2016**, *8* (36), 23868-23875.

(60) Efimov, A. A.; Arsenov, P. V.; Borisov, V. I.; Buchnev, A. I.; Lizunova, A. A.; Kornyushin, D. V.; Tikhonov, S. S.; Musaev, A. G.; Urazov, M. N.; Shcherbakov, M. I.; Spirin, D. V.; Ivanov, V. V. Synthesis of Nanoparticles by Spark Discharge as a Facile and Versatile Technique of Preparing Highly Conductive Pt Nano-Ink for Printed Electronics. *Nanomaterials* **2021**, *11* (1), 234.

(61) Ding, Y.; Cui, Y.; Liu, X.; Liu, G.; Shan, F. Welded Silver Nanowire Networks as High-Performance Transparent Conductive Electrodes: Welding Techniques and Device Applications. *Appl. Mater. Today* **2020**, *20*, 100634.

(62) Ryu, C. H.; Joo, S. J.; Kim, H. S. Intense Pulsed Light Sintering of Cu Nano Particles/Micro Particles-Ink Assisted with Heating and Vacuum Holding of Substrate for Warpage Free Printed Electronic Circuit. *Thin Solid Films* **2019**, *675*, 23-33.

(63) Li, W.; Chen, M. Synthesis of Stable Ultra-Small Cu Nanoparticles for Direct Writing Flexible Electronics. *Appl. Surf. Sci.* **2014**, *290*, 240-245.

(64) Li, Z.; Wang, G.; Li, Z.; Cheng, Z.; Zhou, G.; Li, S. Flexible Transparent Electrodes Based on Gold Nanomeshes. *Nanoscale Res. Lett.* **2019**, *14* (1), 132.

(65) Li, W.; Xiong, L.; Pu, Y.; Quan, Y.; Li, S. High-Performance Paper-Based Capacitive Flexible Pressure Sensor and Its Application in Human-Related Measurement. *Nanoscale Res. Lett.* **2019**, *14* (1), 183.

(66) Bachmann, B.; Adly, N. Y.; Schnitker, J.; Yakushenko, A.; Rinklin, P.; Offenhäusser, A.; Wolfrum, B. All-Inkjet-Printed Gold Microelectrode Arrays for Extracellular Recording of Action Potentials. *Flex. Print. Electron.* **2017**, *2* (3), 035003.

(67) Liu, Z.; Xu, J.; Chen, D.; Shen, G. Flexible Electronics Based on Inorganic Nanowires. *Chem. Soc. Rev.* **2014**, *44* (1), 161-192.

(68) Chen, M.; Luo, W.; Xu, Z.; Zhang, X.; Xie, B.; Wang, G.; Han, M. An Ultrahigh Resolution Pressure Sensor Based on Percolative Metal Nanoparticle Arrays. *Nat. Commun.* **2019**, *10* (1), 4024.

(69) You, I.; Kim, B.; Park, J.; Koh, K.; Shin, S.; Jung, S.; Jeong, U. Stretchable E-Skin Apexcardiogram Sensor. *Adv. Mater.* **2016**, *28* (30), 6359-6364.

(70) Heller, I.; Chatoor, S.; Männik, J.; Zevenbergen, M. A. G.; Dekker, C.; Lemay, S. G. Influence of Electrolyte Composition on Liquid-Gated Carbon Nanotube and Graphene Transistors. *J. Am. Chem. Soc.* **2010**, *132* (48), 17149-17156.

(71) Pu, L.; Abbas, A. S.; Maheshwari, V. Electrochemical Synthesis on Nanoparticle Chains to Couple Semiconducting Rods: Coulomb Blockade Modulation Using Photoexcitation. *Adv. Mater.* **2014**, *26* (37), 6491-6496.

(72) Pu, L.; Fan, H.; Maheshwari, V. Formation of Microns Long Thin Wire Networks with a Controlled Spatial Distribution of Elements. *Catal. Sci. Technol.* **2020**, *10* (7), 2020-2028.

(73) Peng, Z.; Yang, H. Designer Platinum Nanoparticles: Control of Shape, Composition in Alloy, Nanostructure and Electrocatalytic Property. *Nano Today* **2009**, *4* (2), 143-164.

(74) Lin, T. H.; Lin, C. W.; Liu, H. H.; Sheu, J. T.; Hung, W. H. Potential-Controlled Electrodeposition of Gold Dendrites in the Presence of Cysteine. *Chem. Commun.* **2011**, *47* (7), 2044-2046.

(75) Bao, W. S.; Meguid, S. A.; Zhu, Z. H.; Weng, G. J. Tunneling Resistance and Its Effect on the Electrical Conductivity of Carbon Nanotube Nanocomposites. *J. Appl. Phys.* **2012**, *111* (9), 093726.

(76) Ohnishi, H.; Kondo, Y.; Takayanagi, K. Quantized Conductance through Individual Rows of Suspended Gold Atoms. *Nature* **1998**, *395* (6704), 780-783.

(77) Berven, C. A.; Wybourne, M. N. Effect of Self-Capacitance on the Tunneling Thresholds in Linear Arrays of Nanoparticles. *Appl. Phys. Lett.* **2001**, *78* (24), 3893-3895.

(78) Parthasarathy, R.; Lin, X. M.; Jaeger, H. M. Electronic Transport in Metal Nanocrystal Arrays: The Effect of Structural Disorder on Scaling Behavior. *Phys. Rev. Lett.* **2001**, *87* (18), 186807.

(79) Tran, T. B.; Beloborodov, I. S.; Hu, J.; Lin, X. M.; Rosenbaum, T. F.; Jaeger, H. M. Sequential Tunneling and Inelastic Cotunneling in Nanoparticle Arrays. *Phys. Rev. B* **2008**, *78* (7), 075437.

(80) Zabet-Khosousi, A.; Dhirani, A. A. Charge Transport in Nanoparticle Assemblies. *Chem. Rev.* **2008**, *108* (10), 4072-4124.

(81) Cordan, A. S.; Leroy, Y.; Goltzené, A.; Pépin, A.; Vieu, C.; Mejias, M.; Launois, H. Temperature Behavior of Multiple Tunnel Junction Devices Based on Disordered Dot Arrays. *J. Appl. Phys.* **1999**, *87* (1), 345-352.

(82) Amjadi, M.; Kyung, K. U.; Park, I.; Sitti, M. Stretchable, Skin-Mountable, and Wearable Strain Sensors and Their Potential Applications: A Review. *Adv. Funct. Mater.* **2016**, *26* (11), 1678-1698.

(83) Ramachandran, L.; Lonjon, A.; Demont, P.; Dantras, E.; Lacabanne, C. Conduction Mechanisms in P(VDF-TrFE)/Gold Nanowire Composites: Tunnelling and Thermally-Activated Hopping Process near the Percolation Threshold. *Mater. Res. Express* **2016**, *3* (8), 085027.

(84) Huang, J. C. Carbon Black Filled Conducting Polymers and Polymer Blends. *Adv. Polym. Technol.* **2002**, *21* (4), 299-313.

(85) Parthasarathy, R.; Lin, X. M.; Elteto, K.; Rosenbaum, T. F.; Jaeger, H. M. Percolating through Networks of Random Thresholds: Finite Temperature Electron Tunneling in Metal Nanocrystal Arrays. *Phys. Rev. Lett.* **2004**, *92* (7), 076801.

(86) Yao, S.; Swetha, P.; Zhu, Y. Nanomaterial-Enabled Wearable Sensors for Healthcare. *Adv. Healthc. Mater.* **2018**, *7* (1), 1700889.

(87) Webb, R. C.; Bonifas, A. P.; Behnaz, A.; Zhang, Y.; Yu, K. J.; Cheng, H.; Shi, M.; Bian, Z.; Liu, Z.; Kim, Y. S.; Yeo, W. H.; Park, J. S.; Song, J.; Li, Y.; Huang, Y.; Gorbach, A. M.; Rogers, J. A. Ultrathin Conformal Devices for Precise and Continuous Thermal Characterization of Human Skin. *Nat. Mater.* **2013**, *12* (10), 938-944.

(88) K, R. R.; Gandla, S.; Gupta, D. Highly Sensitive, Rugged, and Wearable Fabric Strain Sensor Based on Graphene Clad Polyester Knitted Elastic Band for Human Motion Monitoring. *Adv. Mater. Interfaces* **2019**, *6* (16), 1900409.

(89) Trung, T. Q.; Ramasundaram, S.; Hwang, B. U.; Lee, N. E. An All-Elastomeric Transparent and Stretchable Temperature Sensor for Body-Attachable Wearable Electronics. *Adv. Mater.* **2016**, *28* (3), 502-509.

(90) Luo, C.; Jia, J.; Gong, Y.; Wang, Z.; Fu, Q.; Pan, C. Highly Sensitive, Durable, and Multifunctional Sensor Inspired by a Spider. *ACS Appl. Mater. Interfaces* **2017**, *9* (23), 19955-19962.

(91) Honda, W.; Harada, S.; Arie, T.; Akita, S.; Takei, K. Wearable, Human-Interactive, Health-Monitoring, Wireless Devices Fabricated by Macroscale Printing Techniques. *Adv. Funct. Mater.* **2014**, *24* (22), 3299-3304.

(92) Chen, F.; Li, X.; Hihath, J.; Huang, Z.; Tao, N. Effect of Anchoring Groups on Single-Molecule Conductance: Comparative Study of Thiol-, Amine-, and Carboxylic-Acid-Terminated Molecules. *J. Am. Chem. Soc.* **2006**, *128* (49), 15874-15881.

(93) Amjadi, M.; Pichitpajongkit, A.; Lee, S.; Ryu, S.; Park, I. Highly Stretchable and Sensitive Strain Sensor Based on Silver Nanowire-Elastomer Nanocomposite. *ACS Nano* **2014**, *8* (5), 5154-5163.

(94) Park, J.; Lee, Y.; Hong, J.; Lee, Y.; Ha, M.; Jung, Y.; Lim, H.; Kim, S. Y.; Ko, H. Tactile-Direction-Sensitive and Stretchable Electronic Skins Based on Human-Skin-Inspired Interlocked Microstructures. *ACS Nano* **2014**, *8* (12), 12020-12029.

(95) Park, Y.; Shim, J.; Jeong, S.; Yi, G. R.; Chae, H.; Bae, J. W.; Kim, S. O.; Pang, C. Microtopography-Guided Conductive Patterns of Liquid-Driven Graphene Nanoplatelet Networks for Stretchable and Skin-Conformal Sensor Array. *Adv. Mater.* **2017**, *29* (21), 1606453.

(96) Kang, D.; Pikhitsa, P. V.; Choi, Y. W.; Lee, C.; Shin, S. S.; Piao, L.; Park, B.; Suh, K. Y.; Kim, T.; Choi, M. Ultrasensitive Mechanical Crack-Based Sensor Inspired by the Spider Sensory System. *Nature* **2014**, *516* (7530), 222-226.

(97) Park, J.; Kim, M.; Lee, Y.; Lee, H. S.; Ko, H. Fingertip Skin-Inspired Microstructured Ferroelectric Skins Discriminate Static/Dynamic Pressure and Temperature Stimuli. *Sci. Adv.* **2015**, *1* (9), e1500661.

(98) Drotlef, D. M.; Amjadi, M.; Yunusa, M.; Sitti, M. Bioinspired Composite Microfibers for Skin Adhesion and Signal Amplification of Wearable Sensors. *Adv. Mater.* **2017**, *29* (28), 1701353.

(99) Kohara, K.; Tabara, Y.; Oshiumi, A.; Miyawaki, Y.; Kobayashi, T.; Miki, T. Radial Augmentation Index: A Useful and Easily Obtainable Parameter for Vascular Aging. *Am. J. Hypertens.* **2005**, *18* (S1), 11S-14S.

(100) Munir, S.; Jiang, B.; Guilcher, A.; Brett, S.; Redwood, S.; Marber, M.; Chowienczyk, P. Exercise Reduces Arterial Pressure Augmentation through Vasodilation of Muscular Arteries in Humans. *Am. J. Physiol. Heart Circ. Physiol.* **2008**, *294* (4), H1645-H1650.

(101) Huang, C. M.; Chang, H. C.; Kao, S. T.; Li, T. C.; Wei, C. C.; Chen, C.; Liao, Y. T.; Chen, F. J. Radial Pressure Pulse and Heart Rate Variability in Heat- and Cold-Stressed Humans. *Evid. Based Complement. Alternat. Med.* **2010**, *2011*, e751317.

(102) Myers, A. C.; Huang, H.; Zhu, Y. Wearable Silver Nanowire Dry Electrodes for Electrophysiological Sensing. *RSC Adv.* **2015**, *5* (15), 11627-11632.

(103) Ashley, E. A.; Niebauer, J. *Cardiology Explained*; Remedica, 2004.

(104) Chen, J.; Liu, J.; Thundat, T.; Zeng, H. Polypyrrole-Doped Conductive Supramolecular Elastomer with Stretchability, Rapid Self-Healing, and Adhesive Property for Flexible Electronic Sensors. *ACS Appl. Mater. Interfaces* **2019**, *11* (20), 18720-18729.

(105) Yamamoto, Y.; Harada, S.; Yamamoto, D.; Honda, W.; Arie, T.; Akita, S.; Takei, K. Printed Multifunctional Flexible Device with an Integrated Motion Sensor for Health Care Monitoring. *Sci. Adv.* **2016**, *2* (11), e1601473.

(106) Yamamoto, Y.; Yamamoto, D.; Takada, M.; Naito, H.; Arie, T.; Akita, S.; Takei, K. Efficient Skin Temperature Sensor and Stable Gel-Less Sticky ECG Sensor for a Wearable Flexible Healthcare Patch. *Adv. Healthc. Mater.* **2017**, *6* (17), 1700495.

(107) Cai, Y.; Shen, J.; Dai, Z.; Zang, X.; Dong, Q.; Guan, G.; Li, L. J.; Huang, W.; Dong, X. Extraordinarily Stretchable All-Carbon Collaborative Nanoarchitectures for Epidermal Sensors. *Adv. Mater.* **2017**, *29* (31), 1606411.

(108) Zhang, B.; Lei, J.; Qi, D.; Liu, Z.; Wang, Y.; Xiao, G.; Wu, J.; Zhang, W.; Huo, F.; Chen, X. Stretchable Conductive Fibers Based on a Cracking Control Strategy for Wearable Electronics. *Adv. Funct. Mater.* **2018**, *28* (29), 1801683.

(109) Trung, T. Q.; Lee, N. E. Recent Progress on Stretchable Electronic Devices with Intrinsically Stretchable Components. *Adv. Mater.* **2017**, *29* (3), 1603167.

(110) Kim, D. C.; Shim, H. J.; Lee, W.; Koo, J. H.; Kim, D. H. Material-Based Approaches for the Fabrication of Stretchable Electronics. *Adv. Mater.* **2020**, *32* (15), 1902743.

(111) Choi, S.; Han, S. I.; Kim, D.; Hyeon, T.; Kim, D. H. High-Performance Stretchable Conductive Nanocomposites: Materials, Processes, and Device Applications. *Chem. Soc. Rev.* **2019**, *48* (6), 1566-1595.

(112) Wu, Y.; Liu, H.; Chen, S.; Dong, X.; Wang, P.; Liu, S.; Lin, Y.; Wei, Y.; Liu, L. Channel Crack-Designed Gold@PU Sponge for Highly Elastic Piezoresistive Sensor with Excellent Detectability. *ACS Appl. Mater. Interfaces* **2017**, *9*(23), 20098-20105.

(113) Song, E.; Kang, B.; Choi, H. H.; Sin, D. H.; Lee, H.; Lee, W. H.; Cho, K. Stretchable and Transparent Organic Semiconducting Thin Film with Conjugated Polymer Nanowires Embedded in an Elastomeric Matrix. *Adv. Electron. Mater.* **2016**, *2* (1), 1500250.

(114) Jheng, W. W.; Su, Y. S.; Hsieh, Y. L.; Lin, Y. J.; Tzeng, S. D.; Chang, C. W.; Song, J. M.; Kuo, W. Gold Nanoparticle Thin Film-Based Strain Sensors for Monitoring Human Pulse. *ACS Appl. Nano Mater.* **2021**, *4* (2), 1712-1718.

(115) Herrmann, J.; Müller, K. H.; Reda, T.; Baxter, G. R.; Raguse, B.; de Groot, G. J. J. B.; Chai, R.; Roberts, M.; Wieczorek, L. Nanoparticle Films as Sensitive Strain Gauges. *Appl. Phys. Lett.* **2007**, *91* (18), 183105.

(116) A Tunable Palladium Nanoparticle Film-Based Strain Sensor in a Mott Variable-Range Hopping Regime. *Sens. Actuators Phys.* **2018**, *272*, 161-169.

(117) Zhang, Y.; Sheehan, C. J.; Zhai, J.; Zou, G.; Luo, H.; Xiong, J.; Zhu, Y. T.; Jia, Q. X. Polymer-Embedded Carbon Nanotube Ribbons for Stretchable Conductors. *Adv. Mater.* **2010**, *22* (28), 3027-3031.

(118) Hannigan, B. C.; Cuthbert, T. J.; Geng, W.; Tavassolian, M.; Menon, C. Understanding the Impact of Machine Learning Models on the Performance of Different Flexible Strain Sensor Modalities. *Front. Mater.* **2021**, *8*, 44.

(119) Saraf, R.; Fan, H.; Maheshwari, V. Porous Perovskite Films Integrated with Au-Pt Nanowire-Based Electrodes for Highly Flexible Large-Area Photodetectors. *Npj Flex. Electron.* **2020**, *4* (1), 1-8.

(120) Seh, Z. W.; Kibsgaard, J.; Dickens, C. F.; Chorkendorff, I.; Nørskov, J. K.; Jaramillo, T. F. Combining Theory and Experiment in Electrocatalysis: Insights into Materials Design. *Science* **2017**, *355* (6321).

(121) Mohammed-Ibrahim, J.; Sun, X. Recent Progress on Earth Abundant Electrocatalysts for Hydrogen Evolution Reaction (HER) in Alkaline Medium to Achieve Efficient Water Splitting - A Review. *J. Energy Chem.* **2019**, *34*, 111-160.

(122) Wang, J.; Yue, X.; Yang, Y.; Sirisomboonchai, S.; Wang, P.; Ma, X.; Abudula, A.; Guan, G. Earth-Abundant Transition-Metal-Based Bifunctional Catalysts for Overall Electrochemical Water Splitting: A Review. *J. Alloys Compd.* **2020**, *819*, 153346.

(123) Kumar, A.; Bhattacharyya, S. Porous NiFe-Oxide Nanocubes as Bifunctional Electrocatalysts for Efficient Water-Splitting. *ACS Appl. Mater. Interfaces* **2017**, *9* (48), 41906-41915.

(124) Danilovic, N.; Subbaraman, R.; Strmcnik, D.; Chang, K. C.; Paulikas, A. P.; Stamenkovic, V. R.; Markovic, N. M. Enhancing the Alkaline Hydrogen Evolution Reaction Activity through the Bifunctionality of $Ni(OH)_2$/Metal Catalysts. *Angew. Chem.* **2012**, *124* (50), 12663-12666.

(125) Lim, D.; Kim, S.; Kim, N.; Oh, E.; Shim, S. E.; Baeck, S. H. Strongly Coupled $Ni/Ni(OH)_2$ Hybrid Nanocomposites as Highly Active Bifunctional Electrocatalysts for Overall Water Splitting. *ACS Sustain. Chem. Eng.* **2020**, *8* (11), 4431-4439.

(126) Sun, H.; Yan, Z.; Liu, F.; Xu, W.; Cheng, F.; Chen, J. Self-Supported Transition-Metal-Based Electrocatalysts for Hydrogen and Oxygen Evolution. *Adv. Mater.* **2020**, *32* (3), 1806326.

(127) Tahir, M.; Pan, L.; Idrees, F.; Zhang, X.; Wang, L.; Zou, J. J.; Wang, Z. L. Electrocatalytic Oxygen Evolution Reaction for Energy Conversion and Storage: A Comprehensive Review. *Nano Energy* **2017**, *37*, 136-157.

(128) Ledezma-Yanez, I.; Wallace, W. D. Z.; Sebastián-Pascual, P.; Climent, V.; Feliu, J. M.; Koper, M. T. Interfacial Water Reorganization as a PH-Dependent Descriptor of the Hydrogen Evolution Rate on Platinum Electrodes. *Nat. Energy* **2017**, *2* (4), 1-7.

(129) Suryanto, B. H. R.; Wang, Y.; Hocking, R. K.; Adamson, W.; Zhao, C. Overall Electrochemical Splitting of Water at the Heterogeneous Interface of Nickel and Iron Oxide. *Nat. Commun.* **2019**, *10* (1), 5599.

(130) Yin, H.; Zhao, S.; Zhao, K.; Muqsit, A.; Tang, H.; Chang, L.; Zhao, H.; Gao, Y.; Tang, Z. Ultrathin Platinum Nanowires Grown on Single-Layered Nickel Hydroxide with High Hydrogen Evolution Activity. *Nat. Commun.* **2015**, *6* (1), 6430.

(131) Jiao, S.; Fu, X.; Wang, S.; Zhao, Y. Perfecting Electrocatalysts via Imperfections: Towards the Large-Scale Deployment of Water Electrolysis Technology. *Energy Environ. Sci.* **2021**, *14* (4), 1722-1770.

(132) Yu, X.; Zhao, J.; Zheng, L. R.; Tong, Y.; Zhang, M.; Xu, G.; Li, C.; Ma, J.; Shi, G. Hydrogen Evolution Reaction in Alkaline Media: Alpha- or Beta-Nickel Hydroxide on the Surface of Platinum? *ACS Energy Lett.* **2018**, *3* (1), 237-244.

(133) Cao, Z.; Chen, Q.; Zhang, J.; Li, H.; Jiang, Y.; Shen, S.; Fu, G.; Lu, B.; Xie, Z.; Zheng, L. Platinum-Nickel Alloy Excavated Nano-Multipods with Hexagonal Close-Packed Structure and Superior Activity towards Hydrogen Evolution Reaction. *Nat. Commun.* **2017**, *8* (1), 15131.

(134) Zhang, C.; Liang, X.; Xu, R.; Dai, C.; Wu, B.; Yu, G.; Chen, B.; Wang, X.; Liu, N. H2 In Situ Inducing Strategy on Pt Surface Segregation Over Low Pt Doped $PtNi_5$ Nanoalloy with Superhigh Alkaline HER Activity. *Adv. Funct. Mater.* **2021**, *31* (14), 2008298.

(135) Xie, Y.; Cai, J.; Wu, Y.; Zang, Y.; Zheng, X.; Ye, J.; Cui, P.; Niu, S.; Liu, Y.; Zhu, J.; Liu, X.; Wang, G.; Qian, Y. Boosting Water Dissociation Kinetics on Pt-Ni Nanowires by N-Induced Orbital Tuning. *Adv. Mater.* **2019**, *31* (16), 1807780.

(136) Hong, Y.; Choi, C. H.; Choi, S. I. Catalytic Surface Specificity of $Ni(OH)_2$-Decorated Pt Nanocubes for the Hydrogen Evolution Reaction in an Alkaline Electrolyte. *ChemSusChem* **2019**, *12* (17), 4021-4028.

(137) Zeng, Y.; Chen, G. F.; Jiang, Z.; Ding, L. X.; Wang, S.; Wang, H. Confined Heat Treatment of a Prussian Blue Analogue for Enhanced Electrocatalytic Oxygen Evolution. *J. Mater. Chem. A* **2018**, *6* (33), 15942-15946.

(138) Lin, Y. C.; Chuang, C. H.; Hsiao, L. Y.; Yeh, M. H.; Ho, K. C. Oxygen Plasma Activation of Carbon Nanotubes-Interconnected Prussian Blue Analogue for Oxygen Evolution Reaction. *ACS Appl. Mater. Interfaces* **2020**, *12* (38), 42634-42643.

(139) You, B.; Qiao, S. Z. Destabilizing Alkaline Water with 3d-Metal (Oxy)(Hydr)Oxides for Improved Hydrogen Evolution. *Chem. - Eur. J.* **2021**, *27* (2), 553-564.

(140) Liu, H.; Yan, Z.; Chen, X.; Li, J.; Zhang, L.; Liu, F.; Fan, G.; Cheng, F. Electrodeposition of Pt-Decorated $Ni(OH)_2/CeO_2$ Hybrid as Superior Bifunctional Electrocatalyst for Water Splitting. *Research* **2020**, *2020*.

(141) Zhang, X.; Liang, Y. Nickel Hydr(Oxy)Oxide Nanoparticles on Metallic MoS_2 Nanosheets: A Synergistic Electrocatalyst for Hydrogen Evolution Reaction. *Adv. Sci.* **2018**, *5* (2), 1700644.

(142) Vegard, L. Die Konstitution Der Mischkristalle Und Die Raumfüllung Der Atome. *Z. Für Phys.* **1921**, *5* (1), 17-26.

(143) Ma, L.; Zhang, Q.; Wu, C.; Zhang, Y.; Zeng, L. PtNi Bimetallic Nanoparticles Loaded MoS_2 Nanosheets: Preparation and Electrochemical Sensing Application for the Detection of Dopamine and Uric Acid. *Anal. Chim. Acta* **2019**, *1055*, 17-25.

(144) Yadav, A.; Pandey, R.; Liao, T. W.; Zharinov, V. S.; Hu, K. J.; Vernieres, J.; Palmer, R. E.; Lievens, P.; Grandjean, D.; Shacham-Diamand, Y. A Platinum-Nickel Bimetallic Nanocluster Ensemble-on-Polyaniline Nanofilm for Enhanced Electrocatalytic Oxidation of Dopamine. *Nanoscale* **2020**, *12* (10), 6047-6056.

(145) Grosvenor, A. P.; Biesinger, M. C.; Smart, R. St. C.; McIntyre, N. S. New Interpretations of XPS Spectra of Nickel Metal and Oxides. *Surf. Sci.* **2006**, *600* (9), 1771-1779.

(146) Chen, L.; Lu, L.; Zhu, H.; Chen, Y.; Huang, Y.; Li, Y.; Wang, L. Improved Ethanol Electrooxidation Performance by Shortening Pd-Ni Active Site Distance in Pd-Ni-P Nanocatalysts. *Nat. Commun.* **2017**, *8* (1), 14136.

(147) Zhu, T.; Song, H.; Li, F.; Chen, Y. Hydrodeoxygenation of Benzofuran over Bimetallic Ni-Cu/γ-Al_2O_3 Catalysts. *Catalysts* **2020**, *10* (3), 274.

(148) Soo Kim, D.; Chul Lee, H. Nickel Vacancy Behavior in the Electrical Conductance of Nonstoichiometric Nickel Oxide Film. *J. Appl. Phys.* **2012**, *112* (3), 034504.

(149) Liu, S. Q.; Wen, H. R.; Ying-Guo; Zhu, Y. W.; Fu, X. Z.; Sun, R.; Wong, C. P. Amorphous $Ni(OH)_2$ Encounter with Crystalline CuS in Hollow Spheres: A Mesoporous Nano-Shelled Heterostructure for Hydrogen Evolution Electrocatalysis. *Nano Energy* **2018**, *44*, 7-14.

(150) Chen, L.; Chang, J.; Zhang, Y.; Gao, Z.; Wu, D.; Xu, F.; Guo, Y.; Jiang, K. Fluorine Anion-Enriched Nickel Hydroxyl Oxide as an Efficient Oxygen Evolution Reaction Electrocatalyst. *Chem. Commun.* **2019**, *55* (23), 3406-3409.

(151) Ruqia, B.; Choi, S. I. Pt and Pt-$Ni(OH)_2$ Electrodes for the Hydrogen Evolution Reaction in Alkaline Electrolytes and Their Nanoscaled Electrocatalysts. *ChemSusChem* **2018**, *11* (16), 2643-2653.

(152) Li, Y.; Bao, X.; Chen, D.; Wang, Z.; Dewangan, N.; Li, M.; Xu, Z.; Wang, J.; Kawi, S.; Zhong, Q. A Minireview on Nickel-Based Heterogeneous Electrocatalysts for Water Splitting. *ChemCatChem* **2019**, *11* (24), 5913-5928.

(153) Shinagawa, T.; Garcia-Esparza, A. T.; Takanabe, K. Insight on Tafel Slopes from a Microkinetic Analysis of Aqueous Electrocatalysis for Energy Conversion. *Sci. Rep.* **2015**, *5* (1), 13801.

(154) Mahmood, N.; Yao, Y.; Zhang, J. W.; Pan, L.; Zhang, X.; Zou, J. J. Electrocatalysts for Hydrogen Evolution in Alkaline Electrolytes: Mechanisms, Challenges, and Prospective Solutions. *Adv. Sci.* **2018**, *5* (2), 1700464.

(155) Zhang, W.; Song, H.; Cheng, Y.; Liu, C.; Wang, C.; Khan, M. A. N.; Zhang, H.; Liu, J.; Yu, C.; Wang, L.; Li, J. Core-Shell Prussian Blue Analogs with Compositional Heterogeneity and Open Cages for Oxygen Evolution Reaction. *Adv. Sci.* **2019**, *6* (7), 1801901.

(156) Subbaraman, R.; Tripkovic, D.; Strmcnik, D.; Chang, K. C.; Uchimura, M.; Paulikas, A. P.; Stamenkovic, V.; Markovic, N. M. Enhancing Hydrogen Evolution Activity in Water Splitting by Tailoring Li^+-$Ni(OH)_2$-Pt Interfaces. *Science* **2011**, *334* (6060), 1256-1260.

(157) Rossmeisl, J.; Logadottir, A.; Nørskov, J. K. Electrolysis of Water on (Oxidized) Metal Surfaces. *Chem. Phys.* **2005**, *319* (1), 178-184.

(158) Stevens, M. B.; Trang, C. D. M.; Enman, L. J.; Deng, J.; Boettcher, S. W. Reactive Fe-Sites in Ni/Fe (Oxy)Hydroxide Are Responsible for Exceptional Oxygen Electrocatalysis Activity. *J. Am. Chem. Soc.* **2017**, *139* (33), 11361-11364.

(159) Yan, J.; Kong, L.; Ji, Y.; White, J.; Li, Y.; Zhang, J.; An, P.; Liu, S.; Lee, S. T.; Ma, T. Single Atom Tungsten Doped Ultrathin α-$Ni(OH)_2$ for Enhanced Electrocatalytic Water Oxidation. *Nat. Commun.* **2019**, *10* (1), 2149.

(160) Dou, Y.; Zhang, L.; Xu, J.; He, C. T.; Xu, X.; Sun, Z.; Liao, T.; Nagy, B.; Liu, P.; Dou, S. X. Manipulating the Architecture of Atomically Thin Transition Metal (Hydr)Oxides for Enhanced Oxygen Evolution Catalysis. *ACS Nano* **2018**, *12* (2), 1878-1886.

(161) Hall, D. S.; Lockwood, D. J.; Bock, C.; MacDougall, B. R. Nickel Hydroxides and Related Materials: A Review of Their Structures, Synthesis and Properties. *Proc. R. Soc. Math. Phys. Eng. Sci.* **2015**, *471* (2174), 20140792.

(162) Kirubasankar, B.; Palanisamy, P.; Arunachalam, S.; Murugadoss, V.; Angaiah, S. 2D $MoSe_2$-$Ni(OH)_2$ Nanohybrid as an Efficient Electrode Material with High Rate Capability for Asymmetric Supercapacitor Applications. *Chem. Eng. J.* **2019**, *355*, 881-890.

(163) Feng, Y.; Wang, X.; Dong, P.; Li, J.; Feng, L.; Huang, J.; Cao, L.; Feng, L.; Kajiyoshi, K.; Wang, C. Boosting the Activity of Prussian-Blue Analogue as Efficient Electrocatalyst for Water and Urea Oxidation. *Sci. Rep.* **2019**, *9* (1), 15965.

(164) Su, X.; Wang, Y.; Zhou, J.; Gu, S.; Li, J.; Zhang, S. Operando Spectroscopic Identification of Active Sites in NiFe Prussian Blue Analogues as Electrocatalysts: Activation of Oxygen Atoms for Oxygen Evolution Reaction. *J. Am. Chem. Soc.* **2018**.

(165) Guo, C.; Jiao, Y.; Zheng, Y.; Luo, J.; Davey, K.; Qiao, S. Z. Intermediate Modulation on Noble Metal Hybridized to 2D Metal-Organic Framework for Accelerated Water Electrocatalysis. *Chem* **2019**, *5* (9), 2429-2441.

(166) Lao, M.; Rui, K.; Zhao, G.; Cui, P.; Zheng, X.; Dou, S. X.; Sun, W. Platinum/Nickel Bicarbonate Heterostructures towards Accelerated Hydrogen Evolution under Alkaline Conditions. *Angew. Chem. Int. Ed.* **2019**, *58* (16), 5432-5437.

(167) Zhang, Y.; Shao, Q.; Pi, Y.; Guo, J.; Huang, X. A Cost-Efficient Bifunctional Ultrathin Nanosheets Array for Electrochemical Overall Water Splitting. *Small* **2017**, *13* (27), 1700355.

(168) Fu, M.; Zhang, Q.; Sun, Y.; Ning, G.; Fan, X.; Wang, H.; Lu, H.; Zhang, Y.; Wang, H. Ni-Fe Nanocubes Embedded with Pt Nanoparticles for Hydrogen and Oxygen Evolution Reactions. *Int. J. Hydrog. Energy* **2020**, *45* (41), 20832-20842.

(169) Singh, B.; Prakash, O.; Maiti, P.; Menezes, P. W.; Indra, A. Electrochemical Transformation of Prussian Blue Analogues into Ultrathin Layered Double Hydroxide Nanosheets for Water Splitting. *Chem. Commun.* **2020**, *56* (95), 15036-15039.

(170) Ren, Y.; Chim, W. K.; Guo, L.; Tanoto, H.; Pan, J.; Chiam, S. Y. *Sol. Energy Mater. Sol. Cells* **2013**, *116*, 83.

(171) Hall, D. S.; Lockwood, D. J.; Poirier, S.; Bock, C.; MacDougall, B. R. *J. Phys. Chem. A* **2012**, *116*, 6771.

(172) Bantignies, J. L.; Deabate, S.; Righi, A.; Rols, S.; Hermet, P.; Sauvajol, J. L.; Henn, F. *J. Phys. Chem. C* **2008**, *112*, 2193.

(173) Hall, D. S.; Lockwood, D. J.; Bock, C.; MacDougall, B. R. *Proc. R. Soc. Math. Phys. Eng. Sci.* **2015**, *471*, 20140792.

(174) Jackowska, K.; Krysinski, P. New Trends in the Electrochemical Sensing of Dopamine. *Anal. Bioanal. Chem.* **2013**, *405* (11), 3753-3771.

(175) Xu, T. Q.; Zhang, Q. L.; Zheng, J. N.; Lv, Z. Y.; Wei, J.; Wang, A. J.; Feng, J. J. Simultaneous Determination of Dopamine and Uric Acid in the Presence of Ascorbic Acid Using Pt Nanoparticles Supported on Reduced Graphene Oxide. *Electrochimica Acta* **2014**, *115*, 109-115.

(176) Sun, C. L.; Lee, H. H.; Yang, J. M.; Wu, C. C. The Simultaneous Electrochemical Detection of Ascorbic Acid, Dopamine, and Uric Acid Using Graphene/Size-Selected Pt Nanocomposites. *Biosens. Bioelectron.* **2011**, *26* (8), 3450-3455.

(177) Mahshid, S.; Li, C.; Mahshid, S. S.; Askari, M.; Dolati, A.; Yang, L.; Luo, S.; Cai, Q. Sensitive Determination of Dopamine in the Presence of Uric Acid and Ascorbic Acid Using TiO_2 Nanotubes Modified with Pd, Pt and Au Nanoparticles. *Analyst* **2011**, *136* (11), 2322-2329.

(178) Sajid, M.; Nazal, M. K.; Mansha, M.; Alsharaa, A.; Jillani, S. M. S.; Basheer, C. Chemically Modified Electrodes for Electrochemical Detection of Dopamine in the Presence of Uric Acid and Ascorbic Acid: A Review. *TrAC Trends Anal. Chem.* **2016**, *76*, 15-29.

(179) Hsu, M. S.; Chen, Y. L.; Lee, C. Y.; Chiu, H. T. Gold Nanostructures on Flexible Substrates as Electrochemical Dopamine Sensors. *ACS Appl. Mater. Interfaces* **2012**, *4* (10), 5570-5575.

(180) Thiagarajan, S.; Chen, S. M. Preparation and Characterization of PtAu Hybrid Film Modified Electrodes and Their Use in Simultaneous Determination of Dopamine, Ascorbic Acid and Uric Acid. *Talanta* **2007**, *74* (2), 212-222.

(181) Ratnam, K. V.; Manjunatha, H.; Janardan, S.; Babu Naidu, K. C.; Ramesh, S. Nonenzymatic Electrochemical Sensor Based on Metal Oxide, MO (M= Cu, Ni, Zn, and Fe) Nanomaterials for Neurotransmitters: An Abridged Review. *Sens. Int.* **2020**, *1*, 100047.

(182) Gao, J.; He, P.; Yang, T.; Zhou, L.; Wang, X.; Chen, S.; Lei, H.; Zhang, H.; Jia, B.; Liu, J. Electrodeposited NiO/Graphene Oxide Nanocomposite: An Enhanced Voltammetric Sensing Platform for Highly Sensitive Detection of Uric Acid, Dopamine and Ascorbic Acid. *J. Electroanal. Chem.* **2019**, *852*, 113516.

(183) Shen, Y.; Sheng, Q.; Zheng, J. A High-Performance Electrochemical Dopamine Sensor Based on a Platinum-Nickel Bimetallic Decorated Poly(Dopamine)-Functionalized Reduced Graphene Oxide Nanocomposite. *Anal. Methods* **2017**, *9* (31), 4566-4573.

(184) Nancy, T. E. M.; Kumary, V. A. Synergistic Electrocatalytic Effect of Graphene/Nickel Hydroxide Composite for the Simultaneous Electrochemical Determination of Ascorbic Acid, Dopamine and Uric Acid. *Electrochimica Acta* **2014**, *133*, 233-240.

(185) Zhang, S.; Fu, Y.; Sheng, Q.; Zheng, J. Nickel-Cobalt Double Hydroxide Nanosheets Wrapped Amorphous $Ni(OH)_2$ Nanoboxes: Development of Dopamine Sensor with Enhanced Electrochemical Properties. *New J. Chem.* **2017**, *41* (21), 13076-13084.

(186) Yang, C.; Sun, X.; Zhang, C.; Liu, M. Green Synthesis of Co-Ni Hollow Spheres for Its Electrochemical Detection of Dopamine. *J. Nanoparticle Res.* **2020**, *22* (3), 55.

(187) Liu, X.; Liu, J. Biosensors and Sensors for Dopamine Detection. *View* **2021**, *2* (1), 20200102.

(188) Xu, C.; Wang, J.; Zhou, J. Nanoporous PtNi Alloy as an Electrochemical Sensor for Ethanol and H_2O_2. *Sens. Actuators B Chem.* **2013**, *182*, 408-415.

(189) Lipani, L.; Dupont, B. G. R.; Doungmene, F.; Marken, F.; Tyrrell, R. M.; Guy, R. H.; Ilie, A. Non-Invasive, Transdermal, Path-Selective and Specific Glucose Monitoring via a Graphene-Based Platform. *Nat. Nanotechnol.* **2018**, *13* (6), 504-511.

(190) Trafela, Š.; Zavašnik, J.; Šturm, S.; Žužek Rožman, K. Controllable Voltammetric Formation of a Structurally Disordered $NiOOH/Ni(OH)_2$ Redox Pair on Ni-Nanowire Electrodes for Enhanced Electrocatalytic Formaldehyde Oxidation. *Electrochimica Acta* **2020**, *362*, 137180.

(191) Kalyva, M.; Wragg, D. S.; Fjellvåg, H.; Sjåstad, A. O. Engineering Functions into Platinum and Platinum-Rhodium Nanoparticles in a One-Step Microwave Irradiation Synthesis. *ChemistryOpen* **2017**, *6* (2), 273-281.

(192) Beden, B.; Largeaud, F.; Kokoh, K.; Lamy, C. Fourier Transform Infrared Reflectance Spectroscopic Investigation of the Electrocatalytic Oxidation of D-Glucose: Identification of Reactive Intermediates and Reaction Products. *Electrochimica Acta* **1996**, *41* (5), 701-709.

(193) Gisbert, R.; García, G.; Koper, M. T. M. Adsorption of Phosphate Species on Poly-Oriented Pt and Pt(111) Electrodes over a Wide Range of PH. *Electrochimica Acta* **2010**, *55* (27), 7961-7968.

(194) Hwang, D. W.; Lee, S.; Seo, M.; Chung, T. D. Recent Advances in Electrochemical Non-Enzymatic Glucose Sensors - A Review. *Anal. Chim. Acta* **2018**, *1033*, 1-34.

(195) Do, U. P.; Seland, F.; Wang, K.; Johannessen, E. A. Raney-Platinum Thin Film Electrodes for the Catalysis of Glucose in Abiotically Catalyzed Micro-Glucose Fuel Cells. *J. Mater. Sci.* **2019**, *54* (22), 14143-14156.

(196) Yang, H.; Wang, Z.; Zhou, Q.; Xu, C.; Hou, J. Nanoporous Platinum-Copper Flowers for Non-Enzymatic Sensitive Detection of Hydrogen Peroxide and Glucose at near-Neutral PH Values. *Microchim. Acta* **2019**, *186* (9), 631.

(197) Garcia, A. C.; Touzalin, T.; Nieuwland, C.; Perini, N.; Koper, M. T. M. Enhancement of Oxygen Evolution Activity of Nickel Oxyhydroxide by Electrolyte Alkali Cations. *Angew. Chem.* **2019**, *131* (37), 13133-13137.

(198) Zhu, Q.; Bao, J.; Huo, D.; Yang, M.; Hou, C.; Guo, J.; Chen, M.; Fa, H.; Luo, X.; Ma, Y. 3D Graphene Hydrogel - Gold Nanoparticles Nanocomposite Modified Glassy Carbon Electrode for the Simultaneous Determination of Ascorbic Acid, Dopamine and Uric Acid. *Sens. Actuators B Chem.* **2017**, *238*, 1316-1323.

(199) Daubinger, P.; Kieninger, J.; Unmüssig, T.; A. Urban, G. Electrochemical Characteristics of Nanostructured Platinum Electrodes - a Cyclic Voltammetry Study. *Phys. Chem. Chem. Phys.* **2014**, *16* (18), 8392-8399.

(200) Ou, C.; Yuan, R.; Chai, Y.; Tang, M.; Chai, R.; He, X. A Novel Amperometric Immunosensor Based on Layer-by-Layer Assembly of Gold Nanoparticles-Multi-Walled Carbon Nanotubes-Thionine Multilayer Films on Polyelectrolyte Surface. *Anal. Chim. Acta* **2007**, *603* (2), 205-213.

(201) Bacil, R. P.; Chen, L.; Serrano, S. H. P.; Compton, R. G. Dopamine Oxidation at Gold Electrodes: Mechanism and Kinetics near Neutral PH. *Phys. Chem. Chem. Phys.* **2020**, *22* (2), 607-614.

(202) Wang, X.; Liu, X.; Tong, C. J.; Yuan, X.; Dong, W.; Lin, T.; Liu, L. M.; Huang, F. An Electron Injection Promoted Highly Efficient Electrocatalyst of $FeNi_3$@GR@Fe-NiOOH for Oxygen Evolution and Rechargeable Metal-Air Batteries. *J. Mater. Chem. A* **2016**, *4* (20), 7762-7771.

(203) Lu, S.; Hummel, M.; Chen, K.; Zhou, Y.; Kang, S.; Gu, Z. Synthesis of Au@ZIF-8 Nanocomposites for Enhanced Electrochemical Detection of Dopamine. *Electrochem. Commun.* **2020**, *114*, 106715.

(204) Lei, Y.; Butler, D.; Lucking, M. C.; Zhang, F.; Xia, T.; Fujisawa, K.; Granzier-Nakajima, T.; Cruz-Silva, R.; Endo, M.; Terrones, H.; Terrones, M.; Ebrahimi, A. Single-Atom Doping of MoS2 with Manganese Enables Ultrasensitive Detection of Dopamine: Experimental and Computational Approach. *Sci. Adv.* **2020**, *6* (32), eabc4250.

(205) Biella, S.; Prati, L.; Rossi, M. Selective Oxidation of D-Glucose on Gold Catalyst. *J. Catal.* **2002**, *206* (2), 242-247.

(206) Su, Y.; Guo, H.; Wang, Z.; Long, Y.; Li, W.; Tu, Y. Au@Cu_2O Core-Shell Structure for High Sensitive Non-Enzymatic Glucose Sensor. *Sens. Actuators B Chem.* **2018**, *255*, 2510-2519.

(207) Zhao, C.; Shao, C.; Li, M.; Jiao, K. Flow-Injection Analysis of Glucose without Enzyme Based on Electrocatalytic Oxidation of Glucose at a Nickel Electrode. *Talanta* **2007**, *71* (4), 1769-1773.

(208) Ni, G.; Wang, F.; Pan, Z.; Zhang, R. Bimetallic CuCo Derived from Prussian Blue Analogue for Nonenzymatic Glucose Sensing. *Electroanalysis* **2021**, *33* (4), 845-853.

(209) Dung, N. Q.; Duong, T. T. T.; Lam, T. D.; Dung, D. D.; Huy, N. N.; Thanh, D. V. Communication-A Simple Empirical Method for Determination of CuOOH/CuO Redox Couple in Electrochemical Nonenzymatic Glucose Sensing. *J. Electrochem. Soc.* **2021**, *168* (1), 017506.

(210) Liu, S.; Zeng, W.; Guo, Q.; Li, Y. Metal Oxide-Based Composite for Non-Enzymatic Glucose Sensors. *J. Mater. Sci. Mater. Electron.* **2020**, *31* (19), 16111-16136.

(211) Sun, S.; Shi, N.; Liao, X.; Zhang, B.; Yin, G.; Huang, Z.; Chen, X.; Pu, X. Facile Synthesis of $CuO/Ni(OH)_2$ on Carbon Cloth for Non-Enzymatic Glucose Sensing. *Appl. Surf. Sci.* **2020**, *529*, 147067.

(212) Gumilar, G.; Valentino Kaneti, Y.; Henzie, J.; Chatterjee, S.; Na, J.; Yuliarto, B.; Nugraha, N.; Patah, A.; Bhaumik, A.; Yamauchi, Y. General Synthesis of Hierarchical Sheet/Plate-like M-BDC (M = Cu, Mn, Ni, and Zr) Metal-Organic Frameworks for Electrochemical Non-Enzymatic Glucose Sensing. *Chem. Sci.* **2020**, *11* (14), 3644-3655.

(213) Guan, P.; Li, Y.; Zhang, J.; Li, W. Non-Enzymatic Glucose Biosensor Based on CuO-Decorated CeO_2 Nanoparticles. *Nanomaterials* **2016**, *6* (9), 159.

(214) Zou, L.; Yang, C.; Lei, Y.; Zakharov, D.; Wiezorek, J. M. K.; Su, D.; Yin, Q.; Li, J.; Liu, Z.; Stach, E. A.; Yang, J. C.; Qi, L.; Wang, G.; Zhou, G. Dislocation Nucleation Facilitated by Atomic Segregation. *Nat. Mater.* **2018**, *17* (1), 56-63.

(215) Casaletto, M. P.; Longo, A.; Martorana, A.; Prestianni, A.; Venezia, A. M. XPS Study of Supported Gold Catalysts: The Role of Au^0 and $Au^{+\delta}$ Species as Active Sites. *Surf. Interface Anal.* **2006**, *38* (4), 215-218.

(216) Raimondi, F.; Geissler, K.; Wambach, J.; Wokaun, A. Hydrogen Production by Methanol Reforming: Post-Reaction Characterisation of a $Cu/ZnO/Al_2O_3$ Catalyst by XPS and TPD. *Appl. Surf. Sci.* **2002**, *189* (1), 59-71.

(217) Krumpolec, R.; Homola, T.; Cameron, D. C.; Humlíček, J.; Caha, O.; Kuldová, K.; Zazpe, R.; Přikryl, J.; Macak, J. M. Structural and Optical Properties of Luminescent Copper(I) Chloride Thin Films Deposited by Sequentially Pulsed Chemical Vapour Deposition. *Coatings* **2018**, *8* (10), 369.

(218) Nandanwar, S.; Borkar, S.; Cho, J. H.; Kim, H. J. Microwave-Assisted Synthesis and Characterization of Solar-Light-Active Copper-Vanadium Oxide: Evaluation of Antialgal and Dye Degradation Activity. *Catalysts* **2021**, *11* (1), 36.

(219) Biesinger, M. C.; Payne, B. P.; Lau, L. W. M.; Gerson, A.; Smart, R. S. C. X-Ray Photoelectron Spectroscopic Chemical State Quantification of Mixed Nickel Metal, Oxide and Hydroxide Systems. *Surf. Interface Anal.* **2009**, *41* (4), 324-332.

(220) Ratcliff, E. L.; Meyer, J.; Steirer, K. X.; Garcia, A.; Berry, J. J.; Ginley, D. S.; Olson, D. C.; Kahn, A.; Armstrong, N. R. Evidence for Near-Surface NiOOH Species in Solution-Processed NiO_x Selective Interlayer Materials: Impact on Energetics and the Performance of Polymer Bulk Heterojunction Photovoltaics. *Chem. Mater.* **2011**, *23* (22), 4988-5000.

(221) Akri, M.; Zhao, S.; Li, X.; Zang, K.; Lee, A. F.; Isaacs, M. A.; Xi, W.; Gangarajula, Y.; Luo, J.; Ren, Y.; Cui, Y. T.; Li, L.; Su, Y.; Pan, X.; Wen, W.; Pan, Y.; Wilson, K.; Li, L.; Qiao, B.; Ishii, H.; Liao, Y. F.; Wang, A.; Wang, X.; Zhang, T. Atomically Dispersed Nickel as Coke-Resistant Active Sites for Methane Dry Reforming. *Nat. Commun.* **2019**, *10* (1), 5181.

(222) Shah, A., Qureshi, R., Khan, S. B., Asiri, A. M., Shah, A. U. H. A., Ishaq, M., Khan, M. S., Lunsford, S. K. and Zia, M. A., Spectroscopic analysis of Au-Cu alloy nanoparticles of various compositions synthesized by a chemical reduction method. *Adv. Mater. Sci. Eng.* **2015**.

(223) Shin, K. S.; Kim, J. H.; Kim, I. H.; Kim, K. Novel Fabrication and Catalytic Application of Poly(Ethylenimine)-Stabilized Gold-Silver Alloy Nanoparticles. *J. Nanoparticle Res.* **2012**, *14* (3), 735.

(224) Liu, G.; Zhao, J.; Qin, L.; Liu, S.; Zhang, Q.; Li, J. Synthesis of an Ordered Nanoporous Cu/Ni/Au Film for Sensitive Non-Enzymatic Glucose Sensing. *RSC Adv.* **2020**, *10* (22), 12883-12890.

(225) Wang, X.; Liu, E.; Zhang, X. Non-Enzymatic Glucose Biosensor Based on Copper Oxide-Reduced Graphene Oxide Nanocomposites Synthesized from Water-Isopropanol Solution. *Electrochimica Acta* **2014**, *130*, 253-260.

(226) Wei, H.; Sun, J. J.; Guo, L.; Li, X.; Chen, G. N. Highly Enhanced Electrocatalytic Oxidation of Glucose and Shikimic Acid at a Disposable Electrically Heated Oxide Covered Copper Electrode. *Chem. Commun.* **2009**, No. 20, 2842-2844.

(227) Mishra, A. K.; Mukherjee, B.; Kumar, A.; Jarwal, D. K.; Ratan, S.; Kumar, C.; Jit, S. Superficial Fabrication of Gold Nanoparticles Modified CuO Nanowires Electrode for Non-Enzymatic Glucose Detection. *RSC Adv.* **2019**, *9* (4), 1772-1781.

(228) Wang, B.; Luo, Y.; Gao, L.; Liu, B.; Duan, G. High-Performance Field-Effect Transistor Glucose Biosensors Based on Bimetallic Ni/Cu Metal-Organic Frameworks. *Biosens. Bioelectron.* **2021**, *171*, 112736.

(229) Archana, V.; Xia, Y.; Fang, R.; Gnana kumar, G. Hierarchical CuO/NiO-Carbon Nanocomposite Derived from Metal Organic Framework on Cello Tape for the Flexible and High Performance Nonenzymatic Electrochemical Glucose Sensors. *ACS Sustain. Chem. Eng.* **2019**, *7* (7), 6707-6719.

(230) Velmurugan, M.; Karikalan, N.; Chen, S. M. Synthesis and Characterizations of Biscuit-like Copper Oxide for the Non-Enzymatic Glucose Sensor Applications. *J. Colloid Interface Sci.* **2017**, *493*, 349-355.

(231) SoYoon, S.; Ramadoss, A.; Saravanakumar, B.; Kim, S. J. Novel Cu/CuO/ZnO Hybrid Hierarchical Nanostructures for Non-Enzymatic Glucose Sensor Application. *J. Electroanal. Chem.* **2014**, *717-718*, 90-95.

(232) Zhu, J.; Yin, H.; Gong, J.; Al-Furjan, M. S. H.; Nie, Q. In Situ Growth of Ni/NiO on N-Doped Carbon Spheres with Excellent Electrocatalytic Performance for Non-Enzymatic Glucose Detection. *J. Alloys Compd.* **2018**, *748*, 145-153.

(233) Gao, X.; Du, X.; Liu, D.; Gao, H.; Wang, P.; Yang, J. Core-Shell Gold-Nickel Nanostructures as Highly Selective and Stable Nonenzymatic Glucose Sensor for Fermentation Process. *Sci. Rep.* **2020**, *10* (1), 1365.

(234) Oh, S. Y.; Hong, S. Y.; Jeong, Y. R.; Yun, J.; Park, H.; Jin, S. W.; Lee, G.; Oh, J. H.; Lee, H.; Lee, S. S.; Ha, J. S. Skin-Attachable, Stretchable Electrochemical Sweat Sensor for Glucose and PH Detection. *ACS Appl. Mater. Interfaces* **2018**, *10* (16), 13729-13740.

(235) Germain, A. Sleep Disturbances as the Hallmark of PTSD: Where Are We Now? *Am. J. Psychiatry* **2013**, *170* (4), 372-382.

(236) Blaskovich, B.; Reichardt, R.; Gombos, F.; Spoormaker, V. I.; Simor, P. Cortical Hyperarousal in NREM Sleep Normalizes from Pre- to Post- REM Periods in Individuals with Frequent Nightmares. *Sleep* **2020**, *43* (1).

(237) Jones, H. R. EMG Evaluation of the Floppy Infant: Differential Diagnosis and Technical Aspects. *Muscle Nerve* **1990**, *13* (4), 338-347.

(238) Siddicky, S. F.; Bumpass, D. B.; Krishnan, A.; Tackett, S. A.; McCarthy, R. E.; Mannen, E. M. Positioning and Baby Devices Impact Infant Spinal Muscle Activity. *J. Biomech.* **2020**, *104*, 109741.

Appendix

UNIVERSITY OF WATERLOO

Notification of Ethics Clearance to Conduct Research with Human Participants

---

Principal Investigator: Vivek Maheshwari (Chemistry)

Student investigator: Hua Fan (Chemistry)

File #: 43352

Title: Electrode patch for measuring electrophysiological signals

---

The Clinical Research Ethics Committee is pleased to inform you this study has been reviewed and given ethics clearance.

Initial Approval Date: 06/22/21 (m/d/y)

University of Waterloo Research Ethics Committees are composed in accordance with, and carry out their functions and operate in a manner consistent with, the institution's guidelines for research with human participants, the Tri-Council Policy Statement for the Ethical Conduct for Research Involving Humans (TCPS, 2nd edition), International Conference on Harmonization: Good Clinical Practice (ICH-GCP), the Ontario Personal Health Information Protection Act (PHIPA), the applicable laws and regulations of the province of Ontario. Both Committees are registered with the U.S. Department of Health and Human Services under the Federal Wide Assurance, FWA00021410, and IRB registration number IRB00002419 (HREC) and IRB00007409 (CREC).

This study is to be conducted in accordance with the submitted application and the most recently approved versions of all supporting materials.

Expiry Date: 06/23/22 (m/d/y)

Multi-year research must be renewed at least once every 12 months unless a more frequent review has otherwise been specified. Studies will only be renewed if the renewal report is received and approved before the expiry date. Failure to submit renewal reports will result in the investigators being notified ethics clearance has been suspended and Research Finance being notified the ethics clearance is no longer valid.

Level of review: Delegated Review

Signed on behalf of the Clinical Research Ethics Committee

Heather Root, Senior Manager, Ethics, heather.root@uwaterloo.ca, 519-888-4567, ext. 30469

This above named study is to be conducted in accordance with the submitted application and the most recently approved versions of all supporting materials.

Documents reviewed and received ethics clearance for use in the study and/or received for information:

file: SOP_version1_EMG_20210618.pdf

file: SOP_version1_EOG_20210618.pdf

file: SOP_version1_ECG_20210618.pdf

file: Recuritment_letter_version1_20210511.pdf

file: Approval-safety-office_version1_20210511.pdf

file: SOP_version1_patch_electrode_20210510.pdf

file: bitalino-revolution-user-manual.pdf

file: ConsentLetter_version1_20210511.pdf

Approved Protocol Version 2 in Research Ethics System

This is an official document. Retain for your files.

You are responsible for obtaining any additional institutional approvals that might be required to complete this study.